APPLIED COMPUTATIONAL ELECTROMAGNETICS SOCIETY JOURNAL

July 2020
Vol. 35 No. 7
ISSN 1054-4887

The ACES Journal is abstracted in INSPEC, in Engineering Index, DTIC, Science Citation Index Expanded, the Research Alert, and to Current Contents/Engineering, Computing & Technology.

The illustrations on the front cover have been obtained from the research groups at the Department of Electrical Engineering, The University of Mississippi.

JULY 2020 REVIEWERS: REGULAR PAPERS

Banupriya Annadurai
Ahmed Attiya
Mehdi Bahadorzadeh
Toure Baidy
Mehmet Belen
Kejian Chen
Tijana Dimitrijevic
Alistair Duffy
Grant Ellis
Jun Fan
Ahmed Hassan
Mourad Ibrahim
Ian Jeffrey
Michael Johnson
Arjun Kumar
Antonio Lazaro
Yingsong Li
Peyman Mahouti
Ronald Marhefka
Abdolkhalegh Mohammadi
Kumutha N.
Yuvaraj N.
Paolo Nepa
Xiao-Min Pan
Mohammd Pourbagher
Zbynek Raida
Kesavamoorthy Rajamannar
Phillippe Ratajczak
Niladri Sarkar
Khalil Sayidmarie
Mustafa Secmen
Christopher Trueman
Mustafa Hikmet Bilgehan Ucar
Fan Yang
Huanhuan Yang
Lei Zhao

THE APPLIED COMPUTATIONAL ELECTROMAGNETICS SOCIETY JOURNAL

Vol. 35 No. 7 July 2020

TABLE OF CONTENTS – REGULAR PAPERS

Fast Monostatic RCS Computation Using the Near-Field Sparse Approximate Inverse and the Multilevel Fast Multipole Algorithm

Carlos Delgado and Felipe Cátedra

Department of Computer Science
University of Alcalá, Alcalá de Henares, Madrid, Spain
carlos.delgado@uah.es, felipe.catedra@uah.es

Abstract ─ This paper describes an iteration-free numerical approach for the analysis of the monostatic Radar Cross Section of arbitrary scenarios. The proposed method is based on a combination of the Sparse Approximate Inverse of the near-field coupling matrix and the Multilevel Fast Multipole Algorithm, and allows to bypass the iterative solution process maintaining a good degree of accuracy.

Index Terms ─ Computational electromagnetics, inverse matrices, moment method, radar cross section.

I. INTRODUCTION

The computation of the Radar Cross Section (RCS) of complex objects has raised the interest of the academic and industrial sectors due to a wide range of applications involved. Efficient RCS computation methods can be used in approach systems, automatic vehicle identification and traffic management, collision-avoidance systems, meteorology, military applications and others. However, the calculation of the RCS of electrically large and complex objects is often restricted to the use of high-frequency methods [1] due to the relaxation of their computational requirements compared to full-wave techniques such as the Method of Moments (MoM) [2]. The use of high-frequency approaches imposes certain geometrical restrictions in order to guarantee accurate results that may not be fulfilled in some cases. Hybrid techniques [3,4,5] have typically been proposed in order to mitigate this limitation.

There has been a surge in the development of efficient full-wave approaches based on the MoM that allow to address larger problems. Some of these techniques rely on the idea of avoiding the storage of the full coupling matrix and, instead, retain only its near-field matrix, computing the interactions between distant elements using efficient matrix-vector products [6,7]. One of the most popular approaches within this group [6] is the Multilevel Fast Multipole Algorithm (MLFMA), based on the aggregation of the fields radiated by the currents over regions of the geometry to form multipole expansions that can then be translated to different points and disaggregated in order to account for distant interactions. A different strategy is based on the reduction of the number of unknowns using an extended set of basis and testing functions called macro-basis functions, which, in turn, can be seen as aggregations of the low-level functions used by the conventional MoM [8,9].

The prediction of monostatic RCS values of complex scenarios using rigorous approaches is an especially demanding task in terms of CPU-time, since it requires the solution of the matrix system for as many excitations as observation directions, although some methods have been developed in order to decrease this number using a low-rank reduction of the set of excitations [10], or the approximation of close angular monostatic values using bistatic computations [11]. A fast numerical approach developed using the two-dimensional RCS via the MLFMA combined with a low-rank spectral preconditioner and the compression of the excitation vectors using ACA is described in [12]. An alternative application of ACA for the fast computation of the monostatic RCS is shown in [13]. In [14] the authors propose a fast technique for the analysis of the monostatic RCS using Interpolative Decomposition (ID) and the skeletonization of the excitation matrix. The same algorithm is used for the analysis of wide angular sweeping in [15], overcoming the high memory requirements of the skeletonization by applying an algorithm parallelized using the Message Passing Interface (MPI) paradigm. In [16,17] extrapolations based on the Asymptotic Waveform Extraction technique (AWE) are presented for an efficient monostatic RCS computation. A Bayesian Compressive Sensing method for monostatic scattering analysis is detailed in [18]. The Best Uniform Approximation method combined with the Singular Value Decomposition (SVD) is proposed in [19] to reduce the CPU-time required for monostatic RCS computations.

We propose in this work a novel approach for the fast computation of the monostatic RCS based on the combination of the Sparse Approximate Inverse (SAI) of the near-field coupling matrix, which allows to obtain an

Submitted On: January 23, 2020
Accepted On: May 5, 2020

approximation of the currents produced by the near-field interactions between basis functions, and the MLFMA in order to take into consideration the far-field interactions. This strategy allows to bypass an iterative solution process, which generally involves most of the computing time when using a conventional full-wave solver. The accuracy obtained, as seen in the test cases provided, can be considered good for many applications while allowing to analyze problems that fall out of the scope of high-frequency techniques.

II. COMPUTATION OF THE SPARSE APPROXIMATE INVERSE

The Sparse Approximate Inverse is generally used for the generation of preconditioners in MoM-based approaches [20,21,22]. In this document we propose an alternative application, using the SAI matrix to obtain directly an initial current distribution due to the near-field interactions between basis functions. Following the conventional application of the MLFMA we assume a partitioning of the scenario in terms of cubical regions with a typical side length of λ/4.

As a starting point for the description of the analysis technique it is convenient to consider the MoM matrix equation:

$$[Z][J] = [V], \tag{1}$$

where [Z] is a non-sparse coupling matrix, [J] denotes the current density distribution to be determined and [V] is the excitation vector. It is possible to separate matrix [Z] into two parts, containing respectively the near- and far-field interactions:

$$([Z_{NF}] + [Z_{FF}])[J] = [V]. \tag{2}$$

Matrix $[Z_{NF}]$ contains the coupling terms between basis functions located in the same or in adjacent regions, which are, in turn, the coefficients with more significant magnitude. This allows to make the following approximation in order to compute its approximate inverse:

$$[Z_{NF}][J] \approx [V], \tag{3}$$

and, assuming that [M] is an approximation of the inverse of $[Z_{NF}]$, the following relation stands after performing the right multiplication of both sides by [M] in (3):

$$[J] \approx [M][V]. \tag{4}$$

In order to find [M] we impose a sparsity pattern, i.e., restrict the positions of the non-null coefficients of [M], and use a Linear Least Squares (LLS) approximation to determine the best solution that satisfies such constraint. It is common to use the same block structure of $[Z_{NF}]$ for [M] [21], although we have proposed an enlarged version of this structure based on a sparsity distance parameter [22]. The SAI matrix is computed, therefore, minimizing the norm of the difference between the identity matrix [I] and the product of [M] and $[Z_{NF}]$:

$$min\|[I] - [M][Z_{NF}]\|. \tag{5}$$

The Frobenius norm is generally applied in (5), because it allows to separate the computation of each row of the SAI matrix from the rest, which involves very good scalability properties using modern multi-core computers. By following this procedure, (5) can be decomposed into N_s independent LLS problems:

$$min\|[I] - [M][Z_{NF}]\|_F^2 = \sum_{t=1}^{N_s} min\left\|\boldsymbol{i_t} - \boldsymbol{m_t}[Z_{NF}^{(t)}]\right\|_F^2, \tag{6}$$

where N_s is the number of unknowns of the problem, $\mathbf{i_t}$ is the t-th column of the identity matrix and $\mathbf{m_t}$ makes reference to the t-th row of the SAI matrix, determined after solving the LLS problem. Matrix $[Z_{NF}^{(t)}]$ is a submatrix of $[Z_{NF}]$ obtained by discarding the coefficients that are not involved in the LLS problem. By following this procedure, after solving the N_s problems described by (6) the full SAI matrix can be obtained.

A. Filtering strategies in the SAI matrix generation

Taking into account the previous considerations regarding the matrix generation, it is possible to improve its computational efficiency as well as the memory footprint [23]. We can, on one hand, substitute matrix $[Z_{NF}^{(t)}]$ in (6) with a filtered version $[\tilde{Z}_{NF}^{(t)}]$, where the coefficients with a magnitude lower than τ times the largest self-impedance term within each MLFMA first-level region are set to 0. The τ parameter will be denoted in this work as *impedance filtering threshold*. As a result, it is possible to eliminate a number of columns in the matrix that defines each LLS problem, reducing the effective size of these problems and speeding up the SAI generation. Typical τ values of around 10^{-2} offer a noticeable CPU-time reduction while maintaining a performance comparable to that of the unfiltered version. The second filtering strategy that can be considered addresses the $\mathbf{m_t}$ solution vector in (6) that determines the t-th row of the SAI matrix. This vector, in turn, can be substituted by its filtered version $\tilde{\boldsymbol{m}}_{\boldsymbol{t}}$ in order to be stored using a reduced amount of data. In this case the filtering parameter ξ is used, denoted as *row filtering threshold*. Only the elements of the computed row with a magnitude equal or larger than ξ times that of the dominant element are to be retained, while the rest are approximated to 0. Values of 10^{-2} to $3{\cdot}10^{-2}$ have been proven in the existing literature [22,23] to keep good performance while requiring a fraction of the memory needed by the non-filtered SAI matrix.

III. COMPUTATION OF FAR-FIELD INTERACTIONS USING MLFMA

While the SAI matrix can be used to obtain an approximation of the current distribution on the scenario due to the near-field interactions, the MLFMA provides an operator to account for those between distant functions.

The working principle of the MLFMA consists of

aggregating the contributions of multiple basis functions to the center of their parent region. The aggregation of the j-th basis function $T_j(\vec{r'})$ to the multipole located at the center of the m-th region can be performed as follows:

$$V_{jm}^{AGG}(\hat{k}) = \int_S e^{-j\hat{k}\vec{r}_{jm}} \left(\bar{I} - \hat{k}\hat{k}\right) T_j(\vec{r'}) dS', \quad (7)$$

and, analogously, the disaggregation term of a multipole centered at the m'-th region to the i-th testing function $R_i(\vec{r'})$ can be written:

$$V_{m'i}^{DIS}(\hat{k}) = \int_S e^{j\hat{k}\vec{r}_{im'}} \left(\bar{I} - \hat{k}\hat{k}\right) R_i(\vec{r'}) dS'. \quad (8)$$

After aggregating the currents to the center of the corresponding parent regions, the multipoles can be aggregated to higher-level regions in a similar fashion and translated to other same-level regions. The translation operator $\tau_{mm'}(\hat{k}, \vec{r}_{mm'})$ allows to express the multipole expansion aggregated to the center of m as a modified multipole centered at m':

$$\tau_{mm'}(\hat{k}, \vec{r}_{mm'}) = \frac{jk}{4\pi} \sum_{l=0}^{L} j^l (2l+1) \; h_l^{(1)}(kr_{mm'}) P_l(\vec{r}_{mm'} \cdot \hat{k}), \quad (9)$$

where $h_l^{(1)}(kr_{mm'})$ is a spherical Hankel function of the first kind and $P_l(\vec{r}_{mm'} \cdot \hat{k})$ is a Legendre polynomial.

Using the aggregation of the fields radiated by the basis functions into their first-level multipoles and subsequently into their higher-level ones, the translation of the centers of these multipoles and the disaggregation it is possible perform very efficiently the matrix-vector multiplication between the far-field coupling matrix and the current vector. We will denote in this work Ψ_{FF} to the operator that allows to carry out this computation:

$$\Psi_{FF}([J]) = [Z_{FF}][J]. \quad (10)$$

IV. DESCRIPTION OF THE PROPOSED APPROACH

With the previous considerations, and after computing the SAI matrix [M] as indicated in (6), it is possible to obtain a first approximation of the current distribution on the scenario [$J^{(1)}$] multiplying the SAI matrix and the incident field vector [$V^{(1)}$]:

$$\left[J^{(1)}\right] \approx [M][V^{(1)}]. \quad (11)$$

Vector [$V^{(1)}$] in (11) is the excitation restricted to the visible zone of the geometry:

$$v_i^{(1)} = \begin{cases} v_i, if\ \hat{n}_i \cdot \hat{k} \le 0 \\ 0, if\ \hat{n}_i \cdot \hat{k} > 0 \end{cases}, \ for\ i=1..Ns, \quad (12)$$

where $v_i^{(1)}$ and v_i make reference to the i-th coefficient of [$V^{(1)}$] and [V], respectively, $\hat{k}$ is the direction of the impinging plane wave and $\hat{n}_i$ stands for the normal vector evaluated at the center of the i-th subdomain.

The field scattered by [$J^{(1)}$] can be associated, in the terminology of high-frequency approaches, to first order effects, and can be sufficient to analyze problems that do not present interactions between separate geometrical regions (such as double reflections, double diffraction or combined effects). However, in order to offer a solution for more general cases, and after obtaining [$J^{(1)}$], it is possible to calculate the field induced by this current distribution over the scenario due to the far-field contributions:

$$[V_{FF}] = \Psi_{FF}\left(\left[J^{(1)}\right]\right). \quad (13)$$

It is important to remark that [V_{FF}] requires a modification before obtaining the final induced currents. Analogously to the procedure followed in (12) it is necessary to illuminate only the visible part of the scenario, generating a new excitation vector [$V^{(2)}$] as follows:

$$v_i^{(2)} = \begin{cases} v_i^{FF}, if\ \hat{n}_i \cdot \hat{k} \le 0 \\ 0, if\ \hat{n}_i \cdot \hat{k} > 0 \end{cases}, \ for\ i=1..Ns, \quad (14)$$

where v_i^{FF} denotes the i-th coefficient of $[V_{FF}]$. It is worthwhile to remark that the current distribution [$J^{(1)}$] is equivalent to considering only the near-field coupling matrix [Z_{NF}] shown in (2), and can be refined by obtaining [$J^{(2)}$] after the introduction of the correction voltage [$V^{(2)}$] including near and far field contributions as follows:

$$[Z_{NF}]\left[J^{(2)}\right] + \left[V^{(2)}\right] = \left[V^{(1)}\right], \quad (15)$$

and an approximation of the resulting current distribution can be obtained using the SAI matrix:

$$\left[J^{(2)}\right] \approx [M]\left([V^{(1)}] - [V^{(2)}]\right). \quad (16)$$

A. SAI matrix storage and matrix-vector product strategies

In addition to the theoretical efficiency of modern computational analysis approaches, their scalability is very important in order to handle complex problems. It is necessary to make use of appropriate data structures for the concurrent generation and storage of the matrices and vectors used in the analysis. The LLS problems represented in (6) can be, thanks to the application of the Frobenius norm, distributed among a number of threads or nodes in shared-memory and distributed-memory architectures, respectively. The solution of each problem gives rise to a row of the SAI matrix. However, when distributed memory systems such as computer clusters are taken into account, there are two alternatives for the storage of this matrix: (i) each node can store the set of rows of the preconditioner that has previously computed or (ii) each row can be processed and its elements distributed to the nodes that store the corresponding parts of the current and excitation vectors. Note that the first alternative does not require exchanging messages in the SAI generation process, but needs to exchange the excitation vectors between nodes in the matrix-vector multiplications. This is the approach taken in the present work, since it requires a lesser amount of data exchanged between nodes. Figure 1 shows the matrix-vector product data distributed between a number of nodes *P* in order to clarify this situation, where each processor stores the data represented with the same color.

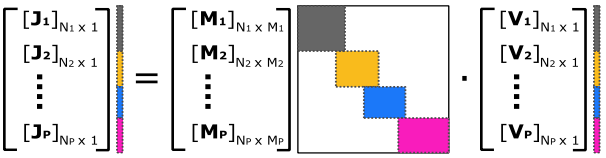

Fig. 1. Scheme illustrating the distribution of the current vector, SAI matrix and excitation vector among computing nodes, represented by blocks with different colors. N_i represents the number of rows assigned to the i-th node, while M_i corresponds to the maximum number of columns corresponding to the i-th node after applying the *row filtering threshold*.

B. Basis and testing functions applied

The scenarios considered in the present work are described by means of Non-Uniform Rational B-Spline (NURBS) surfaces defined by their (u,v) parametric coordinates. We make use of a curved mesh based on quadrangles defined on the parametric space of these patches. The basis and testing functions are rooftops and razor-blade functions defined in the parametric space. The resulting elements and functions, therefore, are curved and conformed to the surface in the real space. This scheme offers a good degree of accuracy modeling the original geometry and avoiding facetization errors. The basis functions are introduced between pairs of adjacent subdomains for the u and v components. Figure 2 depicts an example of the definition of these functions for the Electric Field Integral Equation (EFIE) formulation.

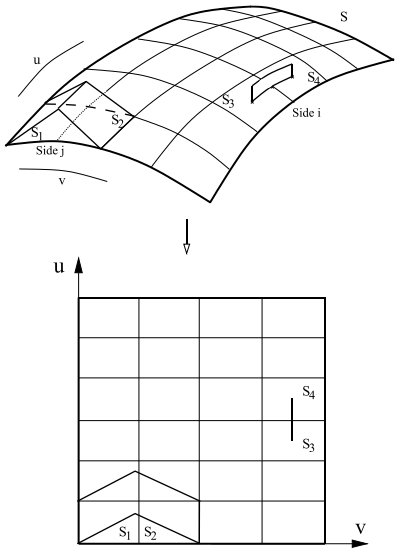

Fig. 2. Illustration of the basis (curved rooftops) and testing (curved razor-blades) functions used in the presented approach over NURBS patches, in the real space (top) and parametric space (bottom). Each junction between consecutive patches is denoted as a *side* and associated with a basis and a testing function.

V. NUMERICAL RESULTS

We present in this section some examples in order to validate the performance and efficiency of the proposed approach. The hardware platform used to obtain the results contains 2 Intel Xeon processors with a base clock speed of 2.9 GHz, 16 physical cores and 256 GB of RAM. The first test case considered is a cube with a side length of 1 m, coated with 2 mm of a material with an electric permittivity ε_r=2. The base of the cube rests on the XY plane, with its sides parallel to the reference axes. The center of the cube is located at (0.5, 0.5, 0.5), with all the units in meters. The monostatic RCS has been obtained for the θ-θ polarization considering the Electric Field Integral Equation at a frequency of 3 GHz for φ=0º and θ ranging from 0º to 90º in 0.5º steps. The results obtained with the presented technique have been compared with those returned by the full-wave MoM-MLFMA approach using the Biconjugate Stabilized Gradient solver (BiCGStab) [24] with a residual of 10^{-3} and using the same SAI matrix as a preconditioner. The *impedance filtering threshold* used in this case has been $\tau = 10^{-2}$, obtaining an average reduction of 25.2% for the size of the LLS problems required to retrieve the SAI rows. Using the same value for the *row filtering threshold* ($\xi = 10^{-2}$) we have obtained a reduction of the total size of the SAI matrix of 67.3%. Figure 3 shows good agreement between both approaches. In this case there are predominantly near-field interactions and therefore only the SAI matrix has been necessary to obtain the current distribution using the proposed approach, which means calculating the scattering field from the $[J^{(1)}]$ current distribution obtained as shown in (11). The total number of basis and testing functions has been 249,696. The CPU-time required for this computation has been 21,288 seconds in the case of the MoM-MLFMA and 894 seconds with the proposed technique, including an identical setup time of 541 seconds to obtain the near-field coupling matrix, the SAI matrix and the multipole data.

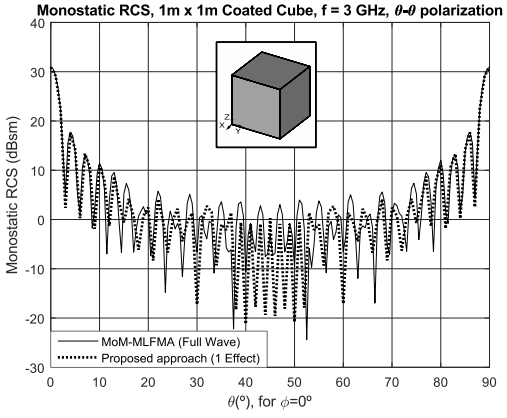

Fig. 3. Monostatic RCS results for the scenario containing a coated cube.

The second test case considered includes an additional cube, with the same characteristics as that previously described, with its center located at (-1.5, 0.5, 2.5), where all the units are expressed in meters. This case has been analyzed considering the same frequency, polarization and observation directions and includes second order effects in addition to reflection. To illustrate the difference between both we have separated the results obtained considering only the SAI matrix (1 effect) and the SAI-MLFMA contribution (2 effects). These results are shown in Fig. 4 and compared to those obtained using MoM-MLFMA, showing very good agreement. The impedance filtering threshold τ and the row filtering threshold ξ, as in the previous example, have been set to 10^{-2}, obtaining a reduction of the size of the LLS problems involved in the SAI matrix computation of 19.5% and a reduction of the total SAI matrix size of 72.3%. The number of basis functions has been 499,392. The total CPU-time with MoM-MLFMA using the same solver as in the previous case has been 53,940 seconds, while the proposed approach has required 6,122 seconds computing both effects and 5,240 seconds when considering only the near-field contribution. This time includes a setup stage of 3,513 seconds for both approaches. We have differentiated the results for both effects in Fig. 4 with the sole purpose of illustrating the contribution carried by each stage of the approach.

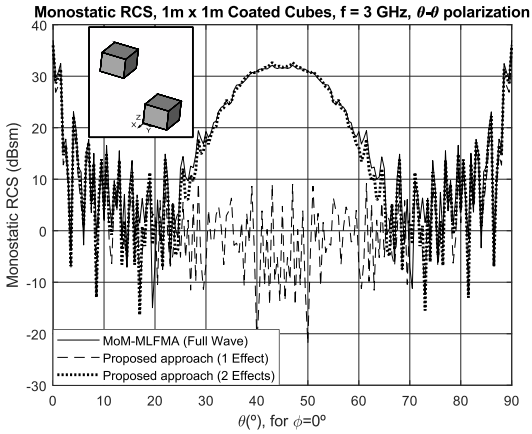

Fig. 4. Monostatic RCS results for the scenario containing two coated cubes.

VI. CONCLUSION

A novel analysis method for the computation of the monostatic RCS of arbitrary scenarios has been described in this letter. This approach presents very good efficiency compared to full-wave approaches because it does not require to make use of an iterative solver. The parametric Sparse Approximate Inverse of the near-field coupling matrix is used to obtain the induced currents considering the near-field interactions, and the Multilevel Fast Multipole Algorithm takes into account the far-field effects using the near-field derived currents in order to compute the final current distribution. Good performance and accuracy is observed in the test cases provided.

ACKNOWLEDGMENT

The work described in this letter has been supported in part by the Spanish Ministry of Economy and Competitiveness (Project Ref. TEC2017-89456-R), by the Junta de Comunidades de Castilla-La Mancha (Project Ref. SBPLY/17/180501/000433) and by the University of Alcalá (Project Ref. CCG2018/EXP-048).

REFERENCES

[1] E. F. Knott, "A progression of high-frequency RCS prediction techniques," *Proc. IEEE*, vol. 73, no. 2, pp. 252-264, Feb. 1985.

[2] R. F. Harrington, *Field Computation by Moment Methods*. New York, McMillan, 1968.

[3] D. P. Bouche, F. A. Molinet, and R. Mittra, "Asymptotic and hybrid techniques for electromagnetic scattering," *Proc. IEEE*, vol. 81, no. 12, pp. 1658-1684, Dec. 1993.

[4] L. N. Medgyesi-Mitschang and D.-S. Wang, "Hybrid methods in computational electromagnetics: A review," *Computer Physics Communications*, vol. 68, no. 1-3, pp. 76-94, Nov. 1991.

[5] C. Delgado, E. Garcia, and F. Catedra, "Hybrid iterative approach combined with domain decomposition for the analysis of large electromagnetic problems," *Proc. IEEE*, vol. 101, no. 2, pp. 320-331, Aug. 2012.

[6] W. C. Chew, J. Jin, E. Michielssen, J. Song, Ed., *Fast and Efficient Algorithms in Computational Electromagnetics*. Artech House Inc., 2001.

[7] K. Zhao, M. N. Vouvakis, J.-F. Lee, "The adaptive cross approximation algorithm for accelerated method of moments computations of EMC problems," *IEEE Trans. Electromagnetic Compat.*, vol. 14, iss. 4, pp. 763-773, Nov. 2005.

[8] E. Suter and J. R. Mosig, "A subdomain multilevel approach for the efficient MoM analysis of large planar antennas," *Micr. Opt. Technol. Letters*, vol. 26, no. 4, pp. 270-277, Aug. 2000.

[9] C. Delgado, R. Mittra, and M. F. Cátedra, "Accurate representation of the edge behavior of current when using PO-derived Characteristic Basis Functions," *IEEE Antennas and Wireless Propagation Letters*, vol. 7, no. 5, pp. 43-45, Mar. 2008.

[10] Z.-Q. Lu and X. An, "Fast monostatic radar cross-section computation for perfectly electric conducting targets using low-rank compression and adaptive integral method," *IEEE Trans. Antennas Propagat.*, vol. 52, no. 2, pp. 605-607,

Feb. 2004.
[11] M. J. Schuh, A. C. Woo, and M. P. Simon, "The monostatic/bistatic approximation," *Electromagnetics*, vol. 36, no. 4, pp. 76-78, Aug. 2004.
[12] A. Schroder, H. D. Brüns, and C. Schuster, "A hybrid approach for rapid computation of two-dimensional monostatic radar cross section problems with the multilevel fast multipole algorithm," *IEEE Trans. Antennas Propag*., vol. 60, no. 12, pp. 6058-6061, Dec. 2012.
[13] Z. Liu, R. Chen, J. Chen, and Z. Fan, "Using adaptive cross approximation for efficient calculation of monostatic scattering with multiple incident angles," *Appl. Comput. Electrom*., vol. 26, no. 4, pp. 325-333, 2011.
[14] X. M. Pan and X. Q. Sheng, "Accurate and efficient evaluation of spatial electromagnetic responses of large scale targets," *IEEE Trans. Antennas Propag*., vol. 62, no. 9, pp. 4746-4753, 2014.
[15] X. M. Pan, S. L. Huang, and X. Q. Sheng, "Wide angular sweeping of dynamic electromagnetic responses from large targets by MPI parallel skeletonization," *IEEE Trans. Antennas Propag*., vol. 66, no. 3, pp. 1619-1623, Mar. 2018.
[16] Y. E. Erdemli, J. Gong, C. J. Reddy, and J. L. Volakis, "Fast RCS pattern fill using AWE technique," *IEEE Trans. Antennas Propagat*., vol. 46, pp. 1752-1753, Nov. 1998.
[17] X. C. Wei, Y. J. Zhang, and E. P. Li, "The hybridization of fast multipole method with asymptotic waveform evaluation for the fast monostatic RCS computation," *IET Microw. Antennas Propag*., vol. 8, no. 1, pp. 46-51, Jan. 2014.
[18] H.-H. Zhang, X.-W. Zhao, Z.-C. Lin, and W. E. I. Sha, "Fast monostatic scattering analysis based on Bayesian compressive sensing," *Appl. Comput. Electrom*., vol. 31, no. 11, pp. 1279-1285, 2016.
[19] Z. Liu, S. He, X. Zhang, Y. Liu, and Y. Zhang, "Using the best uniform approximation with compression for efficient computation of monostatic scattering," *Appl. Comput. Electrom*., vol. 29, no. 11, pp. 856-863, 2014.
[20] J. Lee, J. Zhang, and C.-C. Lu, "Sparse inverse preconditioning of multilevel fast multipole algorithm for hybrid integral equations in electromagnetics," *IEEE Trans. Antennas Propagat.*, vol. 52, no. 9, pp. 2277-2287, Sept. 2004.
[21] T. Malas and L. Gürel, "Accelerating the multilevel fast multipole Algorithm with the Sparse-Approximate-Inverse (SAI) preconditioning," *SIAM J. Sci. Comput.*, vol. 31, no. 3, pp. 1968-1984, Mar. 2009.
[22] C. Delgado and M. F. Cátedra, "Sparse approximate inverse preconditioner with parametric sparsity pattern applied to Macro Basis Function methods," *IEEE Antennas and Wireless Propagation Letters*, vol. 17, no. 5, pp. 849-852, May 2018.
[23] C. Delgado, E. García, A. Somolinos, and M. F. Cátedra, "Hybrid parallelisation scheme for the application of distributed near-field sparse approximate inverse preconditioners on high-performance computing clusters," *IET Microw. Antennas Propag*., vol. 14, no. 4, pp. 320-328, Mar. 2020.
[24] G. L. G. Sleijpen and D. R. Fokkema, "Bi-CGSTAB(l) for linear equations involving unsymmetric matrices with complex spectrum," *Elec. Trans. Numer. Anal.*, vol. 1, pp. 11-32, 1993.

Carlos Delgado received the M.S. and Ph.D. degrees in Telecommunications Engineering from the University of Alcalá, Alcalá de Henares, Spain, in 2002 and 2006, respectively. He was a Visiting Scholar in 2005 and a Visiting Post-Doctoral Fellow in 2007 with the Electromagnetic Communication Laboratory, Pennsylvania State University, State College, PA, USA. He is currently an Associate Professor with the Computer Science Department, University of Alcalá. He is also a Co-Founder of newFASANT, a company that develops and commercializes electromagnetic simulation software using a wide range of numerical approaches. His current research interests include numerical methods applied to scattering and radiation problems, hybridization of high-frequency and full-wave methods, and fast computational techniques applied to electromagnetics.

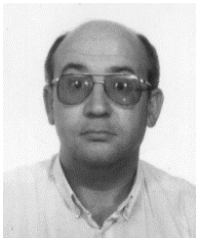

Manuel Felipe Cátedra received the M.S. and Ph.D. degrees in Telecommunications Engineering from the Polytechnic University of Madrid (UPM), Madrid, Spain, in 1977 and 1982, respectively. From 1976 to 1989 he was with the Radiocommunication and Signal Processing Department, UPM. He has been a Professor with the University of Cantabria, Santander, Spain, from 1989 to 1998. He is currently a Professor with the University of Alcalá, Madrid. He has worked on about a 100 research projects solving problems of electromagnetic compatibility in radio and telecommunication equipment, antennas, microwave components and radar cross section, and mobile communications. He has developed and applied CAD tools for radio-equipment systems such as Navy ships, aircrafts, helicopters, or satellites,

and the main contractors being EADS, ALCATEL, CNES, ALENIA, DASA, SAAB, INTA, BAZAN, INDRA, the Spanish Defense Department, CAICYT, DGICYT, CICYT, CEE (ESPRIT), European Space Agency (ESA), Ericsson, MATRA SPACE, CSELT, KTH, INAVI, Texas University, Drexel University, Singapore University, Mitsubishi, Kawasaki Heavy Industries, BOSCH, CASA, RYMSA, IRSA, INDRA, ISDEFE, TELEFONICA, ENSA, Instituto Geográfico Nacional, TELEVES, GMV, and ACCIONA. Recently, he promoted the creation of a technology-based company of the University of Alcalá called newFASANT (http://www.fasant.com) for a better transfer of techniques developed by the group.

An Analytical Method of Minimizing the Crosstalk of Curved Cable and Determining the Optimal Wiring

Dan Ren [1], Wan W. Ruan [2], Pei Xiao [2], Ping A. Du [2], Jian H. Deng [1], and Kai M. Zhou [1]

[1] Institute of Electronic Engineering
China Academy of Engineering Physics, Mianyang 621900, China
rendan_IEE@163.com, 292219937@qq.com, zhkm50121@126.com

[2] School of Mechanical and Electrical Engineering
University of Electronic Science and Technology of China, Chengdu 611731, China
rww4gz@163.com, xiaopei_uestc@sina.cn, dupingan@uestc.edu.cn

Abstract ─ Crosstalk is an easily occurred electromagnetic interference between adjacent cables. Previous research on crosstalk mainly focused on straight cables, and seldom works are reported for bended cables which happens most often in applications. Thus, we propose an analytic method to minimize the crosstalk between curved cables and determine the optimal wiring rules within a specified frequency range. The procedure of the proposed method can be described as the following steps: Firstly, the theoretical crosstalk model of curved cables is deduced and verified by numerical simulation. Then, an "σ area" is defined as the evaluation parameter of crosstalk effects, which is devoted to obtaining the law of S_σ with the bending degree. On this basis, an optimal wiring is presented and a physical explanation through the coupling mechanism is given. Finally, an experiment is carried out to further validate the proposed method.

Index Terms ─ Crosstalk, curved cables, σ area, optimal wiring rules.

I. INTRODUCTION

Interconnection cables are widely used to transmit energy and signals in electronic and electrical systems. The common mode current along the cable take the primary responsibility for the electromagnetic radiation, which induce the crosstalk on adjacent cables through the distribution parameters. Crosstalk between cables may lead to electromagnetic compatibility (EMC) and TEMPEST problems [1-2], so the research on the mechanism and the suppression methods of crosstalk between cables is of great significance in engineering applications.

Based on the propagation principle of crosstalk, researchers developed some interference suppression methods from three aspects: interference source, propagation path and receiver. The previous works showed that differential mode excitation gives a better case of crosstalk compared with common mode excitation [3]. Since interference source limited by circuit topology are not easy to change, many suppression techniques have been developed on propagation path and receiver, and the widely used way is changing wiring. The common methods used for guiding wiring to prevent crosstalk include keeping the cables farther apart, enlarging the angle between cables, reducing the height to ground, adding shielding layer to terminals and using guard traces [4-9], etc. In addition, some newly studies have been proposed to reduce crosstalk by using input and output configuration [10], mode velocity equalization [11], matched loads [12], the partial phase shift network [13], etc.

The research on crosstalk suppression approach should account for suppression effect, solution complexity, practical constraints and other issues. Obviously, changing wiring is still the simplest and most effective way. Some wiring rules have been used to prevent crosstalk in industrial application, but the technical rationale is not clear. This paper aims at proposing an analytical method of minimizing the crosstalk of curved cable and determining the optimal wiring. In this paper, we'll take the single core cable as example to establish the crosstalk coupling model of curved cables and study the wiring rules. Especially, in order to determine the optimal wiring between two points, we presented the definition of "σ area" on the frequency crosstalk curve to evaluate the impact of crosstalk. On this basis, an analytic method to determinate the minimum crosstalk within a specified frequency range is proposed so that an optimal wiring can be formed.

Submitted On: December 16, 2019
Accepted On: May 17, 2020

II. CROSSTALK COUPLING MODEL OF CURVED CABLE

A. Derivation of crosstalk analytic calculation

Coupling between circuits is a common electromagnetic phenomenon, and the crosstalk is a typical form of the coupling effects, as illustrated in Fig. 1.

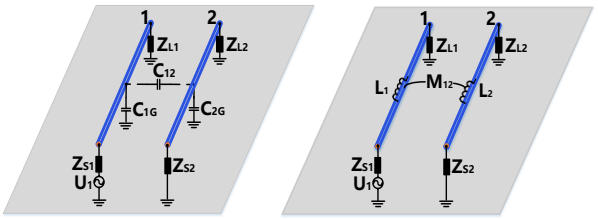

(a) (b)

Fig. 1. Schematic for crosstalk coupling of two conductors: (a) capacitive coupling; (b) inductive coupling.

Multi-conductor transmission line (MTL) theory is often used to analyze the crosstalk between cables. The electrical behaviors of MTL equations in matrix form described in frequency domain can be given as:

$$\frac{d\hat{\boldsymbol{V}}(x)}{dx}+\hat{\boldsymbol{Z}}\hat{\boldsymbol{I}}(x)=0, \tag{1}$$

$$\frac{d\hat{\boldsymbol{I}}(x)}{dx}+\hat{\boldsymbol{Y}}\hat{\boldsymbol{V}}(x)=0. \tag{2}$$

For lossless transmission lines, $\hat{\boldsymbol{Z}}=j\omega\boldsymbol{L}$, $\hat{\boldsymbol{Y}}=j\omega\boldsymbol{C}$ with $\boldsymbol{L}$, $\boldsymbol{C}$ represents per-unit-length inductance matrix and capacitance matrix, respectively.

For non-uniform transmission line, the calculation formula of inductance matrix $\boldsymbol{L}$ can be defined as [14]:

$$\boldsymbol{L}=\begin{bmatrix} \frac{\mu_0}{2\pi}\ln\left(\frac{2h_1}{r_1}\right) & \frac{\mu_0}{4\pi}\ln\left(1+\frac{4h_1h_2}{s_{12}^{\ 2}}\right) \\ \frac{\mu_0}{4\pi}\ln\left(1+\frac{4h_1h_1}{s_{12}^{\ 2}}\right) & \frac{\mu_0}{2\pi}\ln\left(\frac{2h_2}{r_2}\right) \end{bmatrix}, \tag{3}$$

where, r_1 and r_2 are the radius of two adjacent cables, h_1 and h_2 are the heights to the ground, s_{12} is the spacing between two cables, μ_0 is the permeability for free space.

To solve capacitance matrix $\boldsymbol{C}$, the electric potential coefficient M is introduced, which can be written as:

$$\boldsymbol{C}=\begin{bmatrix} C_{1G}+C_{12} & -C_{12} \\ -C_{21} & C_{2G}+C_{12} \end{bmatrix}=\boldsymbol{M}^{-1}, \tag{4}$$

$$\begin{cases} M_{11}=\dfrac{1}{2\pi\varepsilon_0}\left(\dfrac{1}{\varepsilon_r}\ln\dfrac{1}{r_1}+\varepsilon_e\ln\dfrac{1}{r_1+\Delta r_1}-\ln\dfrac{1}{2h_1}\right) \\ M_{12}=S_{21}=\dfrac{1}{4\pi\varepsilon_0}\ln\left(1+\dfrac{4h_1h_2}{s_{12}^{\ 2}}\right) \\ M_{22}=\dfrac{1}{2\pi\varepsilon_0}\left(\dfrac{1}{\varepsilon_r}\ln\dfrac{1}{r_2}+\varepsilon_e\ln\dfrac{1}{r_2+\Delta r_2}-\ln\dfrac{1}{2h_2}\right) \end{cases}, \tag{5}$$

where, ε_0 is the permittivity for free space and ε_r the relative dielectric constant, ε_e the effective dielectric constant which can be defined by $\varepsilon_e=(\varepsilon_r-1)/\varepsilon_r$, Δr_1 and Δr_2 the dielectric thickness.

By differentiating the coupled, first-order phasor MTL equations in (1), (2) with respect to line position *x* and substituting each other, the y can be replaced in the form of uncoupled, second-order ordinary differential equations which are coupled together. To solve these equations, it is necessary to decouple the min to *n* separate MTL equations with a similarity transformation [15-18]. By solving each set of separate equation, the calculated results can be transformed back to the original voltages and currents through variable transformation. Therefore, we define the relationships between the actual phasor line voltages $\hat{\boldsymbol{V}}$ and current $\hat{\boldsymbol{I}}$, and the mode voltages $\hat{\boldsymbol{V}}_m$ and currents $\hat{\boldsymbol{I}}_m$ by using the transformational matrices $\hat{\boldsymbol{T}}_V$, $\hat{\boldsymbol{T}}_I$, then we can obtain the decoupled equations of second-order MTL as follows:

$$\frac{d^2}{dx^2}\hat{\boldsymbol{V}}_m(x)=\hat{\boldsymbol{T}}_V^{-1}\hat{\boldsymbol{Z}}\hat{\boldsymbol{Y}}\hat{\boldsymbol{T}}_V\hat{\boldsymbol{V}}_m(x)=\hat{\gamma}^2\hat{\boldsymbol{V}}_m(x), \tag{6}$$

$$\frac{d^2}{dx^2}\hat{\boldsymbol{I}}_m(x)=\hat{\boldsymbol{T}}_I^{-1}\hat{\boldsymbol{Y}}\hat{\boldsymbol{Z}}\hat{\boldsymbol{T}}_I\hat{\boldsymbol{I}}_m(x)=\hat{\gamma}^2\hat{\boldsymbol{I}}_m(x). \tag{7}$$

By solving $\hat{\boldsymbol{T}}_V$ and $\hat{\boldsymbol{T}}_I$, the mode voltages and currents on the basis of the sum of forward- and backward-travelling wave can be obtained. According to the transformation relationship, they can be transformed back to the actual voltages and currents along with the transmission lines:

$$\hat{\boldsymbol{V}}(x)=\hat{\boldsymbol{T}}_V\left(\boldsymbol{e}^{-\hat{\gamma}x}\hat{\boldsymbol{V}}_m^{+}+\boldsymbol{e}^{\hat{\gamma}x}\hat{\boldsymbol{V}}_m^{-}\right), \tag{8}$$

$$\hat{\boldsymbol{I}}(x)=\hat{\boldsymbol{T}}_I\left(\boldsymbol{e}^{-\hat{\gamma}x}\hat{\boldsymbol{I}}_m^{+}-\boldsymbol{e}^{\hat{\gamma}x}\hat{\boldsymbol{I}}_m^{-}\right). \tag{9}$$

For uniform transmission lines, the phasor voltages and currents are related to the chain-parameter matrix, that is:

$$\begin{pmatrix}\hat{\boldsymbol{V}}(L)\\ \hat{\boldsymbol{I}}(L)\end{pmatrix}=\hat{\boldsymbol{\Phi}}(L)\begin{pmatrix}\hat{\boldsymbol{V}}(0)\\ \hat{\boldsymbol{I}}(0)\end{pmatrix}=\begin{bmatrix}\hat{\phi}_{11}(L) & \hat{\phi}_{12}(L)\\ \hat{\phi}_{21}(L) & \hat{\phi}_{22}(L)\end{bmatrix}\begin{pmatrix}\hat{\boldsymbol{V}}(0)\\ \hat{\boldsymbol{I}}(0)\end{pmatrix}, \tag{10}$$

where, the chain-parameter in (10) can be equivalent to:

$$\hat{\phi}_{11}(L) = 0.5\boldsymbol{Y}^{-1}\boldsymbol{T}_I(\boldsymbol{e}^{\gamma L} + \boldsymbol{e}^{-\gamma L})\boldsymbol{T}_I^{-1}\boldsymbol{Y}, \quad (11)$$

$$\hat{\phi}_{12}(L) = -0.5\boldsymbol{Y}^{-1}\boldsymbol{T}_I\boldsymbol{\gamma}(\boldsymbol{e}^{\gamma L} - \boldsymbol{e}^{-\gamma L})\boldsymbol{T}_I^{-1}, \quad (12)$$

$$\hat{\phi}_{21}(L) = -0.5\boldsymbol{T}_I(\boldsymbol{e}^{\gamma L} - \boldsymbol{e}^{-\gamma L})\boldsymbol{\gamma}^{-1}\boldsymbol{T}_I^{-1}\boldsymbol{Y}, \quad (13)$$

$$\hat{\phi}_{22}(L) = 0.5\boldsymbol{T}_I(\boldsymbol{e}^{\gamma L} + \boldsymbol{e}^{-\gamma L})\boldsymbol{T}_I^{-1}. \quad (14)$$

For curved non-uniform cables, non-uniformity is mainly manifested by the variation of parasitic parameters at each point along the cables. To solve crosstalk in this case, a simple method is to treat it as a discretely uniform MTL [18]. This method requires to divide a cable into cascade sections, each of them can be approximated as a uniform sub-segment with chain-parameter $\hat{\phi}_k$, as shown in Fig. 2.

Then the chain-parameter matrix of the entire non-uniform cable can be obtained by multiplying the chain-parameter matrix of each uniform sub-segments, that is:

$$\hat{\Phi}(L) = \hat{\phi}_n(\Delta x_n)\times\ldots\times\hat{\phi}_i(\Delta x_i)\times\ldots\times\hat{\phi}_1(\Delta x_1). \quad (15)$$

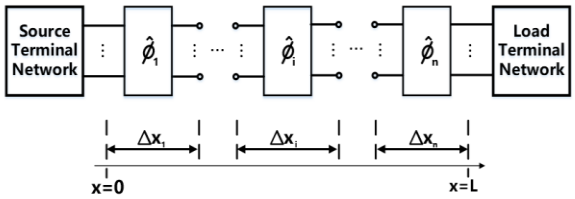

Fig. 2. Chain-parameter cascade of curved non-uniform transmission lines.

The relationship between the phasor voltages and currents of the curved non-uniform cable at both ends can also be expressed by a chain parameter matrix. With the terminal conditions in the form of Thevenin equivalents, we obtain:

$$\begin{aligned}&\left(\hat{\Phi}_{12} - \hat{\Phi}_{11}\hat{\boldsymbol{Z}}_S - \hat{\boldsymbol{Z}}_L\hat{\Phi}_{22} + \hat{\boldsymbol{Z}}_L\hat{\Phi}_{21}\hat{\boldsymbol{Z}}_S\right)\hat{\boldsymbol{I}}(0)\\ &= \hat{\boldsymbol{V}}_L - \left(\hat{\Phi}_{11} - \hat{\boldsymbol{Z}}_L\hat{\Phi}_{21}\right)\hat{\boldsymbol{V}}_S,\end{aligned} \quad (16)$$

$$\hat{\boldsymbol{I}}(L) = \hat{\Phi}_{21}\hat{\boldsymbol{V}}_S + \left(\hat{\Phi}_{22} - \hat{\Phi}_{21}\hat{\boldsymbol{Z}}_S\right)\hat{\boldsymbol{I}}(0), \quad (17)$$

where, $\hat{\boldsymbol{Z}}_S$ and $\hat{\boldsymbol{Z}}_L$ are the impedance matrices of the near and far terminals, $\hat{\boldsymbol{V}}_S$ and $\hat{\boldsymbol{V}}_L$ the excitation source matrices of the near and far terminals, respectively. Terminal current $\hat{\boldsymbol{I}}(0)$ and $\hat{\boldsymbol{I}}(L)$ can be obtained from equations (16) and (17). Finally, we can obtain the crosstalk $\hat{\boldsymbol{V}}(0)$ and $\hat{\boldsymbol{V}}(L)$ at both ends of curved non-uniform cables through Thevenin equivalents, which will be used to derive optimal wiring rules.

B. Numerical validation of crosstalk analytic calculation

A validation model is designed to validate the calculation method above, as shown in Fig. 3. The model consists of two curved cables with a radius of 0.9mm and a dielectric thickness of 0.95 mm. The spacing is 25mm, and the height to the ground satisfies $h = 100 + 70sin(\pi x/1000 + \pi)$ mm. The aggressor cable is excited by a V_S =1V voltage over frequency (0,500MHz), all terminal impedance are 50Ω.

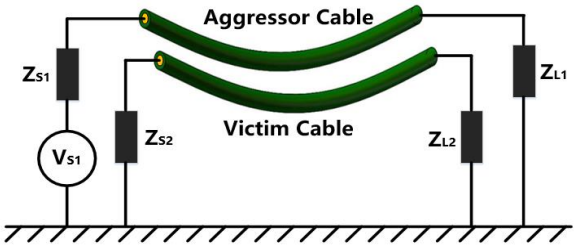

Fig. 3. Electrical connection of a two curved cables model above a ground plane

In this paper, we use a full-analysis commercial software CST based on the transmission line matrix (TLM) technique to validate the proposed method. By using 2D (TL) modeling technique, the equivalent circuit model of cables is obtained and then the crosstalk is calculated by using AC combine results solver. The AC simulation task provides three different ways for cable field coupling, and we choose the first type which ignores the radiation effects. Also, the loss effect can be set in the 2D (TL) modeling settings.

The calculated crosstalk voltages on victim cable by the proposed method and CST are drawn in Fig. 4. It can be seen that the induced voltage at near and far end of the victim cable calculated from our proposed method is well in accordance with that from CST in a wider frequency range.-However, it should be noted that there is a slight difference at higher frequency. The main reason is the difference in the extraction accuracy of the distributed parameters. Table 1 summarizes the calculation time and required memory of our method and the CST. We can see that our method consumes less memory and performs better efficiency.

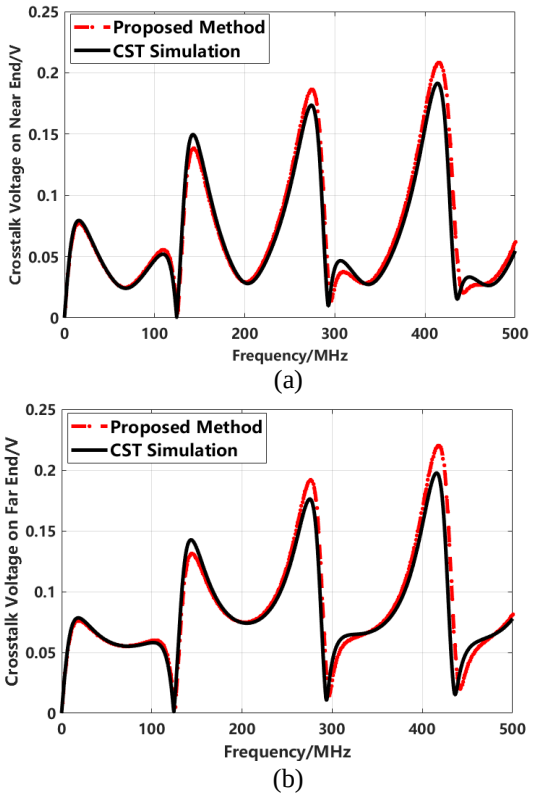

Fig. 4. Comparison of crosstalk voltage on victim cable: (a) near end; (b) far end.

Table 1: Comparison of two methods

	Proposed Method (by MATLAB)	CST Simulation
Computation Time	0.86s	2.7 Mins
Required Memory	3KB	2.08MB

III. THEORETICAL DERIVATION OF OPTIMAL WIRING RULES IN FIXED WORKING FREQUENCY

A. Definition of "σ area"

Sensitive devices often operate within a specific frequency range, and crosstalk generated in this range may cause greater harm. Therefore, the smaller the sum of crosstalk in this frequency range, the lower probability of performance degradation and breakdown happen to the interfered sensitive device. In this paper, a "σ area" is presented to evaluate the impact of crosstalk, which is defined as the area enclosed by the crosstalk waveform and the coordinate axis, as illustrated in Fig. 5, and calculated by:

$$S_\sigma = \int_{F_1}^{F_2} f(x)dx, \tag{18}$$

where, $f(x)$ is the relationship of the induced voltage and the frequency.

According to equations (3) and (4), the waveform of induced voltage is related to the values of inductance matrix and capacitance matrix, and varies with the wiring parameters, such as length, height to the ground, spacing and so on, which will lead to the variation of σ area. Therefore, we can minimize S_σ by changing the wiring of cables and obtain the best routing.

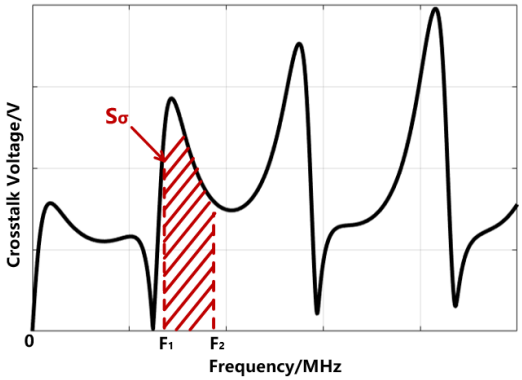

Fig. 5. Definition of "σ area".

B. Relationship between "σ area" and wiring

In applications, the interconnected cables between devices are usually in a relaxed state, as shown in Fig. 6. The cable wiring can be expressed with an approximate function as follows:

$$h = h_0 + a\sin(\pi x/\Delta s + \pi)\text{mm},$$

where, h defines the height to the ground of cable with respect to cable position$x$, h_0 the height of mounting points which means an initial height above the ground, Δs the spacing between two fixed mounting points, a the degree of bending of cable. Since h_0 and Δs usually have fixed values, the cables wiring depends mainly on the value of parameter a, and the probability can be characterized by a function of $S_\sigma(a)$.

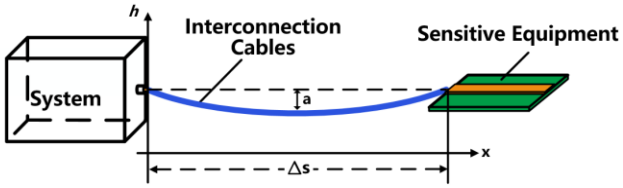

Fig. 6. Wiring of interconnection cables between devices.

Assuming h_0=80mm, Δs=500mm, and the working frequency of sensitive device ranges from 250MHz to 270MHz. The relationship curve between $S_\sigma(a)$ and parameter a can be drawn by changing a from 0 mm to 75 mm, as shown in Fig. 7. The curve shows that σ area decreases first and then increases with increased a.

As shown in Fig. 7, the value of σ area get the minimum when the parameter are aches point P, which means that the crosstalk sum value in the frequency range is minimum. Thus, it is determined that the wiring in this case is the optimal one under a given working conditions.

The optimal wiring analysis calculation process between two fixed points can be summarized as following steps:

1) Define the"σ area";

2) Draw the relation curve of S_σ about independent variables under certain conditions;

3) Determine the minimum crosstalk and optimal wiring on the basis of the above curve.

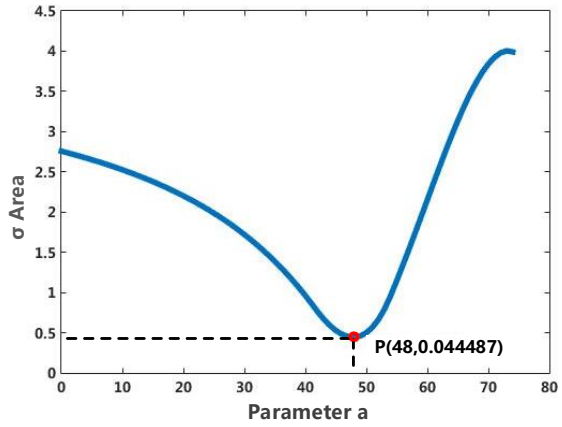

Fig. 7. Relationship between σ area and parameter a.

C. Physical interpretation of optimal wiring

The resonance point is an inherent characteristic of a system network containing inductive and capacitive components. The per-unit-length equivalent circuit for MTL, shown in Fig. 8, indicates that resonance exists among transmission lines.

When the length of transmission line is equal to half of the wavelength, the current distribution along line enhances significantly, known as generalized resonance. Letting L represents the length of transmission lines, the crosstalk voltage on the interfered lines will exhibit the same frequency rules due to the resonance of the transmission lines system in the vicinity and its multiplication of the frequency:

$$f_0=c/2L. \quad (19)$$

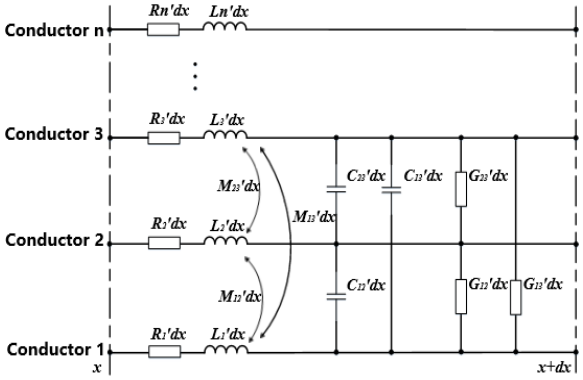

Fig. 8. The per-unit-length equivalent circuit for MTL.

So, the length of the interconnection cable will also change with the parameter a, which will cause the resonance point to move. When resonant frequency does not fall within the operating frequency, the value of σ area can be greatly reduced.

On the other hand, the value of parameter a determines the bending degree of a cable, the larger the parameter a, the smaller the height of each uniform sub-segment to the ground based on the cascade of curved cables. According to the calculation formula of capacitance matrix, the equivalent capacitance decreases as the height to the ground decreases, thus the capacitive coupling is weakened. In addition, the inductive coupling will be weakened as well due to the reduction of closed loop area enclosed by the interference circuit.

However, it doesn't mean that the larger the parameter a, the better the effect of interference rejection. There are multiple resonance points of a transmission lines system, the increasing in length will bring a new resonance point in the operating frequency range of the sensitive equipment.

IV. EXPERIMEMNTAL VALIDATION OF OPTIMAL WIRING

To validate the analytic calculation of the optimal wiring rules, we build a well-controlled cables crosstalk testing plat form by using Vector Network Analyzer as shown in Fig. 9. The core radius of tested cables is 0.9 mm, the insulation layer thickness is 0.95 mm, the spacing between two cables is 25mm and 80 mm high above a ground reference which is a finite metallic plane with a length of 1m and a width of 0.5 m, the distance between two fixed mount points is 500mm. Two cables are connected to the analyzer through SMA connectors, where the red one connected to Port1 is the aggressor cable, and the blue one connected to Port2 is the victim cable. Each terminal of the cables is matched to a 50Ω impedance.

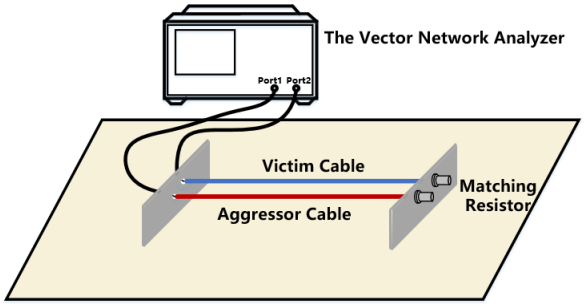

Fig. 9. Schematic diagram of two-cables coupling experiment

The output signal from Port 1 return to Port 2 via the cables and the conduction coupling path between them, so the tested cables can be regarded as a two-port network from Port 1 to Port 2. Therefore, once the S_{21} is measured, the near-end crosstalk of the victim cable can be obtained when the 1V voltage is injected into the aggressor cable.

The experimental testing device is shown in Fig. 10 (a). By increasing the length, the cables are naturally bended and sag between the two mounting points, as illustrated in Fig. 10 (b). The lengths of the cables in three groups of experiments are 500mm, 510mm, 525mm. Measurements were performed over (30KHz, 500MHz) and S_{21} of three experiments were recorded.

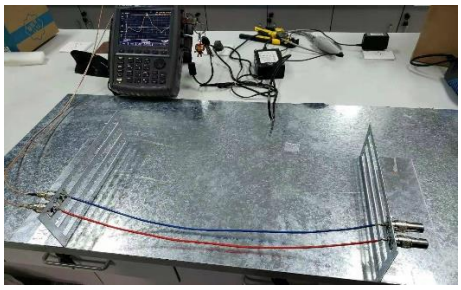

(a)

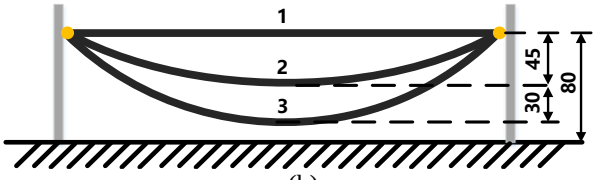

(b)

Fig. 10. Coupling experiments: (a) experimental test picture of S_{21}; (b) three groups of experiments.

The measured results of S_{21} with different parameter a are shown in Fig. 11. It obviously shows that the relationship between resonance points and the length of cables is in good consistent with equation (19), the longer the length, the resonant frequencies shift to the left. The resonance point of the blue solid curve is not the fundamental frequency point, but the peak point of the second waveform after the resonant points shift as the length of cables increases and the bending changes.

Table 2 shows three experimental results of σ area by calculating the region enclosed by the measured waveform of S_{21} and the coordinate axis from 200MHz to 400MHz, which demonstrates the relationship between S_σ and parameter a. When parameter a equals 45 in the No.2 experiment, the value of σ area is minimum. So compared with the analysis result, there is a consentaneous conclusion that $S_\sigma$decreases first and then increases with the increased a, and crosstalk has the minimum impact on system when a takes a value around 48. Consequently, the conclusion and the proposed calculation method of the optimal wiring can be validated through the experiments.

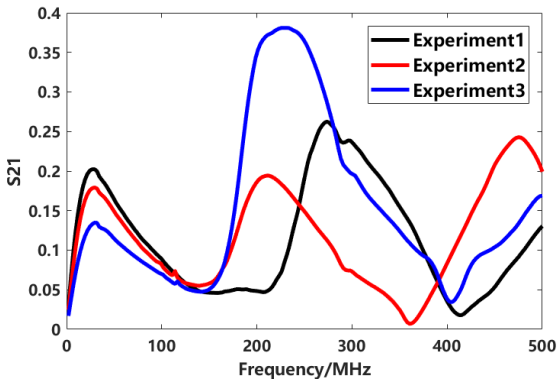

Fig. 11. Measurement waveform of S_{21} for each test.

Table 2: Calculation results of S_σ from 200 to 400MHz

Experiments	**No.1**	**No.2**	**No.3**
	a=0	a=45	a=75
S_σ	3.1262	1.8469	4.4576

V. CONCLUSION

To solve the relationship between curved cables wiring and crosstalk impacts, an analytical method to minimize curved cables crosstalk and determine the optimal wiring rules in a fixed frequency range is proposed. Firstly, a theoretical calculation model for crosstalk of curved cables is derived based on similarity transformation and chain-parameter matrix cascade, and validated by numerical simulation. Then, by defining the"σ area" to evaluate the impact of crosstalk the relation curve between crosstalk and bending degree of cables is obtained. On this basis, an optimal wiring is determined via the inflection point of the curve and a physical explanation is given by use of the generalized resonance and the crosstalk coupling mechanism. Finally, a measurements of parameter S_{21} are carried out to

validate the proposed calculation method of the optimal wiring for curved cables. This work is contributed to guiding the wiring of cables in industrial application. However, the method still has some limitations. Our work takes single core cables as the object, for shielded or twisted pair cables, the calculation model needs to be further modified to analyze wiring rules due to the change of basic structure.

ACKNOWLEDGMENT

This project is supported by the National Natural Science Foundation of China (Grant No. 51675086) and the Equipment Pre-research Foundation of China and National Defense Basic Scientific Research Project of China (Grant No. JCKY2016212B034).

REFERENCES

[1] V. Solak, H. S. Efendioglu, B. Colak, et al., "Analysis and simulation of cable crosstalk," *IEEE IV International Electromagnetic Compatibility Conference*, pp. 1-4, 2017.

[2] M. S. Halligan and D. G. Beetner, "Maximum crosstalk estimation in weakly coupled transmission lines," *IEEE Transactions on Electromagnetic Compatibility*, vol. 56, no. 3, pp. 736-744, 2014.

[3] D. E. Bockelman and W. R. Eisenstadt, "Direct measurement of crosstalk between integrated differential circuits," *IEEE Transactions on Microwave Theory and Techniques*, vol. 48, no. 8, pp. 1410-1413, 2000.

[4] P. Xiao, W.-W. Ran, and P.-A. Du, "An analytic method of determining a critical cable spacing for acceptable crosstalk," *ACES Journal*, vol. 35, no. 2, pp. 237-244, 2020.

[5] R. H. Voelker, "Transposing conductors in signal buses to reduce nearest-neighbor crosstalk," *IEEE Transactions on Microwave Theory & Techniques*, vol. 43, no. 5, pp. 1095-1099, 2002.

[6] F. D. Mbairi, W. P. Siebert, and H. Hesselbom, "High-frequency transmission lines crosstalk reduction using spacing rules," *IEEE Transactions on Components and Packaging Technologies*, vol. 31, no. 3, pp. 601-610, 2008.

[7] S. Caniggia and F. Maradei, *Signal Integrity and Radiated Emission of High-speed Digital Systems*, New Jersey: John Wiley & Sons, Inc. New York, 2008.

[8] C. Jullien, J. Genoulaz, and M. Dunand, "Extremity crosstalk protection analysis on twisted cables," *IEEE International Symposium on Electromagnetic Compatibility*, pp. 391-395, 2015.

[9] K. Prachumrasee, A. Siritaratiwat, V. Ungvichian, et al., "A methodology to identify crosstalk contributor from 6-line suspension assembly interconnect of ultra-high capacity hard disk drives," *ACES Journal*, vol. 27, no. 1, pp. 22-27, 2012.

[10] T. Ciamulski and W. K. Gwarek, "Coupling compensation concept applied to crosstalk cancelling in multiconductor transmission lines," *IEEE Transactions on Electromagnetic Compatibility*, vol. 50, no. 2, pp. 437-441, 2008.

[11] J. Lee, S. Lee, and S. Nam, "A crosstalk reduction technique for microstrip MTL using mode velocity equalization," *IEEE Transactions on Electromagnetic Compatibility*, vol. 53, no. 2, pp. 366-371, 2011.

[12] Y. X. Sun, Q. Li, W. H. Yu, et al., "Study on crosstalk between space transient interference microstrip lines using finite difference time domain method," *ACES Journal*, vol. 30, no. 8, pp. 891-897, 2015.

[13] Q. C. Lou, S. S. Wang, X. X. Gao, et al., "Far-end crosstalk cancellation of transmission lines based on partial phase shift network cascade," *Transaction of China Electrotechnical Society*, vol. 33, no. 17, pp. 3965-3974, 2018.

[14] R. B. Wang, *Ph.D. dissertation*. Jilin: Jilin University, 2011.

[15] K. Ogata, *States Space Analysis of Control Systems*. Prentice-Hall, Englewood Cliffs, New Jersey, 1967.

[16] C. T. Chen, *Linear System Theory and Design*. Holt, Rinehart and Winston, New York, 1984.

[17] F. E. Hohn, *Elementary Matrix Algebra*. 2nd edition, Macmillan, New York, 1964.

[18] A. Ralston, *A First Course in Numerical Analysis*. Mcgraw-Hill, New York, 1965.

[19] C. R. Paul, *Analysis of Multi-conductor Transmission Lines*. Wiley, 1994.

Dan Ren was born in Huainan, Anhui Province, China, in 1986. He received the doctoral degree of Mechanical Engineering from UESTC, Chengdu, China, in 2017. He is currently a Research Assistant at Institute of Electronic Engineering, China Academy of Engineering Physics. His research interests include numerical computation, electromagnetic measurement, electromagnetic environment effective.

Wan-Wei Ruan was born in Yiwu, Zhejiang Province, China, in 1994. She received the B.E. from Huazhong Agricultural University in 2016. She is currently a Master student of UESTC. Her research interest is numerical methods of electromagnetic radiation and crosstalk.

Pei Xiao was born in Shaoyang, Hunan Province, China, in 1989. He received the Bachelor and Ph.D. degrees in Mechanical Engineering from UESTC, Chengdu, China, in 2013 and 2019 respectively.

He is currently a Postdoctoral Research Fellow in Hunan University. His research interests are numerical computation, theoretical electromagnetic analysis including the EMT method, and EMC/EMI in Multi-conductor transmission line, power electronic device and electric vehicle.

Ping-An Du received the M.S. and the doctoral degrees in Mechanical Engineering from Chongqing University, Chongqing, China, in 1989 and 1992, respectively. He is currently a Full Professor of Mechanical Engineering at the University of Electronic Science and Technology of China, Chengdu, China. His research interests include numerical simulation in EMI, vibration, temperature, and so on.

Jian-Hong Deng was born in Tianmen, Hubei Province, China, in 1970. He received the bachelor degree of Optical Engineer from HUST, Wuhan, China, in 1991 and the master degree of Nuclear Technology and Applications from Graduate School of China Academy of Engineering Physics, Mianyang, China, in 2000.

He is currently a Senior Engineer at Institute of Electronic Engineering, China Academy of Engineering Physics. His research interests include electromagnetic effective, electromagnetic measurement and electromagnetic defend.

Kai-Ming Zhou was born in Hechuan, Chongqing Province, China, in 1967. He received the bachelor degree of Applied Physical from UESTC, Chengdu, China, in 1994. He is currently a Senior Engineer at Institute of Electronic Engineering, China Academy of Engineering Physics. His research interests include electromagnetic conceive, electromagnetic measurement.

A Novel PO Solver for Uncertainty EM Computation of Electrically Large Targets

Yong Chen [1,2], Zhao-Guo Hou [2], Hong-Cheng Yin [2], and Ru-Shan Chen [3]

[1] School of Physics, Beijing Institute of Technology, Beijing, 100081, China
yonche@163.com

[2] Science and Technology on Electromagnetic Scattering Laboratory, Beijing, 100854, China
houzg@139.com, yinhc207@126.com

[3] Nanjing University of Science and Technology, Nanjing, 210094, China
eerschen@njust.edu.cn

Abstract ─ A novel PO method is proposed to analyze the uncertain scattering problems. The algorithm starts with modeling the target with a variable shape by using the non-uniform rational B-spline (NURBS) scheme. Then the scattering far-field is expressed in terms of the variable parameters in NURBS. It should be noted that the perturbation approach is applied to describe the uncertainty of the varying shapes. Compared with the traditional Monte Carlo (MC) method, only a few matrix equations are needed to be solved, so the efficiency will increase greatly. At last, several numerical examples are given to validate the accuracy and efficiency of the proposed method.

Index Terms ─ Electromagnetic scattering, perturbation approach, PO, varying geometric shape.

I. INTRODUCTION

In the field of computational electromagnetic, the methods to obtain EM scattering characteristics for certain targets have been well studied [1-6]. However, the uncertainty for modeling electromagnetic scattering of real targets also needs to be focused due to the manufacturing tolerance, environmental influence or insufficient information. Furthermore, the uncertainty of EM scattering characteristics is a key point of radar system design for target detection. In fact, the uncertainty of the target geometry is often difficult to describe. It is hard to get the EM scattering characteristic for the target with a variable shape. Therefore, it is significant to develop an efficient method for solving the scattering problems of targets with uncertain geometry structures.

A lot of works have been done in the past decades to analyze the uncertainty problems [7-22]. The Monte Carlo (MC) simulation is one of the most popular methods to evaluate the impact of uncertainty [15-16]. In this method, a series of samplings are chosen to describe the variation of the uncertain problems, thus an uncertain problem can be divided into several certain problems, which is easy and direct. Based on this, the computational efficiency of the MC method will become worse with the number of sampling points increasing [17]. Then a generalized polynomial chaos method [18] is proposed to further accelerate the convergence, in which the random variables can be expanded by a series of orthogonal polynomials. There are two common schemes in this method, namely Stochastic Galerkin (SG) approach [9-11,21-22] and stochastic collocation (SC) approach [14,19,20]. When the order of polynomial becomes higher, both the SG and SC method will result in a huge coupling system. In [26], a surrogate modeling technique for electromagnetic scattering analysis of objects with variable shapes is presented by using the method of moments, but this method is not easy to be realized due to the huge consumption of computational resources [27-32]. Therefore, it is urgent and necessary to develop an efficient tool to analyze the uncertain scattering problems for three-dimensional objects.

In this paper, the perturbation method is introduced into the physical optics (PO) method [27] to solve the uncertainty in scattering problems. Firstly, the varying shape on the surface of the target is modeled by using the non-uniform rational B-spline (NURBS) scheme [23-24]. In this way, the geometric uncertainty can be described in terms of several random variables. Then the scattering far-fields can be rewritten by the Taylor series, which is constructed by the random variables. As a result, the geometry can be easily changed by adjusting the variables. Numerical results are compared with the traditional MC method, which demonstrates the accuracy and efficiency of the proposed method.

The remainder of this paper is organized as follows. In Section 2, the theory and the formulations are given.

Submitted On: January 18, 2020
Accepted On: May 4, 2020

Three numerical experiments are presented in Section 3 to show the efficiency of the proposed method. Section 4 concludes this paper.

II. THEORY AND FORMULATIONS

A. NURBS surface modeling

A plane with 0.74m*1.15m is considered. The number of control points in the u direction (i.e., the x-axis) is set to seven, and the number of control points in the v direction (i.e., the y-axis) is set to nine. All the control points are numbered. The first control point is labeled P_{00}, and the last control point is labeled P_{68}. So the NURBS surface can be redrawn by MATLAB as shown in Fig. 1.

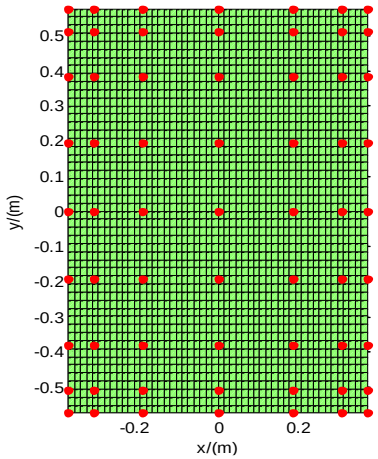

Fig. 1. NURBS surface with controlling points.

A new plane can be got by turning the z coordinate of $P_{3,2}$ to -0.4 and the z coordinate of $P_{3,6}$ to 0.4, which is shown in Fig. 2. It can be seen that as the two points of $P_{3,2}$ and $P_{3,6}$ changes, the surface shape closer to the two control points is bent. But the other parts far away from the two points on the plane are not deformed.

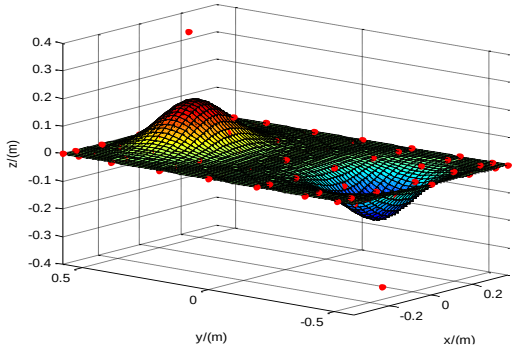

Fig. 2. Reconstructed surface with varying shapes.

Because of the influence of the external environment or the other factors, the geometrical shape of the target is uncertainty. The varying geometrical shape will directly cause the varying of target's EM scattering characteristics. As shown in Fig. 3, the side length of the cube model varies in the interval of $[l-\Delta l, l+\Delta l]$.

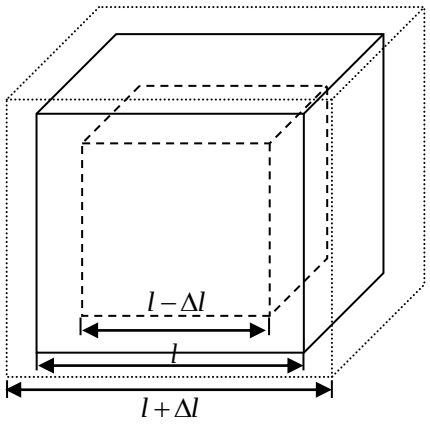

Fig. 3. The cube model with uncertainty geometrical shape.

B. Relationship between variables and equations

An object with a certain size of $\boldsymbol{\alpha}^c$ is considered. The largest varied size is assumed as $\Delta\alpha$. That is, the range of the size for the object is $[\boldsymbol{\alpha}^c-\nabla\alpha, \boldsymbol{\alpha}^c+\nabla\alpha]$. The far-field scattering field of a PEC object can be calculated as follows:

$$\mathbf{E}_s(\mathbf{r}) = \frac{jk\eta}{4\pi R_0} e^{-jkR_0} \int_s \hat{k}_s \times \left[\hat{k}_s \times (2n \times H_i)\right] e^{jk\bullet(\hat{k}_s-\hat{k}_i)\mathbf{r}'} ds' . \quad (1)$$

The above formula can be written as:

$$\mathbf{E}(\boldsymbol{\alpha}^I) = \mathbf{b}(\boldsymbol{\alpha}^I), \quad (2)$$

where $\boldsymbol{\alpha}^I$ represents any point in $[\boldsymbol{\alpha}^c-\nabla\alpha, \boldsymbol{\alpha}^c+\nabla\alpha]$. And then the equation (3) can be obtained by using the first-order Taylor series to expand the equation (1) at the point $\boldsymbol{\alpha}^c$:

$$\begin{aligned}\mathbf{b}(\boldsymbol{\alpha}^I) &= \mathbf{b}(\boldsymbol{\alpha}^c) + \sum_{i=1}^{n} \frac{\partial \mathbf{b}(\boldsymbol{\alpha}^c)}{\partial \alpha_i} \Delta\alpha_i , \quad (3)\\ &= \mathbf{b}(\boldsymbol{\alpha}^c) + \Delta\mathbf{b}^I\end{aligned}$$

where n is the number of random variables and $\Delta\alpha_i$ is largest varied size in the i-th random variable, there is:

$$\mathbf{E}^c + \Delta\mathbf{E}^I = \mathbf{b}(\boldsymbol{\alpha}^c) + \Delta\mathbf{b}^I, \quad (4)$$

where $\Delta\mathbf{E}^I$ represents the change of the far-field scattering field. $\mathbf{E}^c$ represents the far-field scattering field of the model with the size of $\boldsymbol{\alpha}^c$, namely:

$$\mathbf{E}^c = \mathbf{b}(\boldsymbol{\alpha}^c). \quad (5)$$

Then the change of the far-field scattering field can be expressed as:

$$\Delta\mathbf{E}^I = \sum_{i=1}^{n} \left(\frac{\partial \mathbf{b}\left(\boldsymbol{\alpha}^c\right)}{\partial \alpha_i}\right) \Delta\alpha_i , \tag{6}$$

where $\partial \mathbf{b}\left(\boldsymbol{\alpha}^c\right) / \partial \alpha_i$ is always the same for different varied sizes, thus the system just needs to be solved once. Compared with the Monte Carlo method, much more time can be saved by the proposed method in this paper.

When an object is modeled with a NURBS surface, any point on the object can be represented by:

$$\mathbf{S}(u,v) = \sum_{i=0}^{n}\sum_{j=0}^{m} R_{i,j}(u,v) P_{ij}, \tag{7}$$

where $R_{i,j}(u,v)$ is a piecewise rational basis function. P_{ij} is a control point, and the x, y, and z coordinates of the control point are represented by $P_{ijx}, P_{ijy}, P_{ijz}$ respectively. Then the relationship between the coordinates of the point on the object and the coordinates of the control point is:

$$\begin{aligned} S_x &= \sum_{i=0}^{N}\sum_{j=0}^{M} R_{i,j} P_{ijx} \\ S_y &= \sum_{i=0}^{N}\sum_{j=0}^{M} R_{i,j} P_{ijy} \\ S_z &= \sum_{i=0}^{N}\sum_{j=0}^{M} R_{i,j} P_{ijz}, \end{aligned} \tag{8}$$

where S_x, S_y, S_z represent the x, y, z coordinates of the point on the object. And then the shape of the object can be controlled by adjusting the coordinates of the control points. All the x, y, and z coordinates of the control points are mutually independent. In the paper, the x, y, and z coordinates of the control point $P_{ijx}, P_{ijy}, P_{ijz}$ are can be seen as random variables. The derivative of the equation (1) can be written as:

$$\begin{aligned} \frac{\partial \mathbf{b}\left(\boldsymbol{\alpha}^c\right)}{\partial \alpha_i} &= jk\eta \frac{e^{-jkR_0}}{4\pi R_0} \frac{\partial \int_s \hat{k}_s \times \left[\hat{k}_s \times (2\hat{n} \times H_i)\right] e^{jk\left(\hat{k}_s - \hat{k}_i\right)\cdot \mathbf{r}'} ds'}{\partial \alpha_i} \\ &= jk\eta \frac{e^{-jkR_0}}{4\pi R_0} \frac{\hat{k}_s \times \left[\hat{k}_s \times (2\hat{n} \times H_i)\right] \partial \left[e^{jk\left(\hat{k}_s - \hat{k}_i\right)\cdot \mathbf{r}'} \cdot A\right]}{\partial \alpha_i} \\ &= jk\eta \frac{e^{-jkR_0}}{4\pi R_0} \hat{k}_s \times \left[\hat{k}_s \times (2\hat{n} \times H_i)\right] \left(\frac{\partial \left[e^{jk\left(\hat{k}_s - \hat{k}_i\right)\cdot \mathbf{r}'}\right]}{\partial \alpha_i} \cdot A + \frac{\partial A}{\partial \alpha_i} \cdot e^{jk\left(\hat{k}_s - \hat{k}_i\right)\cdot \mathbf{r}'} \right) \end{aligned} \tag{9}$$

where $\partial \alpha_i$ represents the random variable $P_{ijx}, P_{ijy}, P_{ijz}$, and A is the area of the triangle. The derivation of area $\frac{\partial A}{\partial \alpha_i}$ can be derived as:

$$\frac{\partial A}{\partial P_{ijx}} = \frac{1}{4} \cdot \frac{1}{2\sqrt{\left[4a^2b^2 - (a^2+b^2-c^2)^2\right]}} \cdot \begin{bmatrix} 4b^2 \cdot \dfrac{\partial a^2}{\partial P_{ijx}} + 4a^2 \cdot \dfrac{\partial b^2}{\partial P_{ijx}} \\ -2(a^2+b^2-c^2) \cdot \left(\dfrac{\partial a^2}{\partial P_{ijx}} + \dfrac{\partial b^2}{\partial P_{ijx}} - \dfrac{\partial c^2}{\partial P_{ijx}}\right) \end{bmatrix}, \tag{10}$$

$$\frac{\partial A}{\partial P_{ijy}} = \frac{1}{4} \cdot \frac{1}{2\sqrt{\left[4a^2b^2 - (a^2+b^2-c^2)^2\right]}} \cdot \begin{bmatrix} 4b^2 \cdot \dfrac{\partial a^2}{\partial P_{ijy}} + 4a^2 \cdot \dfrac{\partial b^2}{\partial P_{ijy}} \\ -2(a^2+b^2-c^2) \cdot \left(\dfrac{\partial a^2}{\partial P_{ijy}} + \dfrac{\partial b^2}{\partial P_{ijy}} - \dfrac{\partial c^2}{\partial P_{ijy}}\right) \end{bmatrix}, \tag{11}$$

$$\frac{\partial A}{\partial P_{ijy}} = \frac{1}{4} \cdot \frac{1}{2\sqrt{\left[4a^2b^2 - (a^2+b^2-c^2)^2\right]}} \cdot \begin{bmatrix} 4b^2 \cdot \dfrac{\partial a^2}{\partial P_{ijz}} + 4a^2 \cdot \dfrac{\partial b^2}{\partial P_{ijz}} \\ -2(a^2+b^2-c^2) \cdot \left(\dfrac{\partial a^2}{\partial P_{ijz}} + \dfrac{\partial b^2}{\partial P_{ijz}} - \dfrac{\partial c^2}{\partial P_{ijz}}\right) \end{bmatrix}, \tag{12}$$

where a,b,c is the side length of the triangle mesh. $\partial a^2 / \partial \alpha_i$, $\partial b^2 / \partial \alpha_i$ and $\partial c^2 / \partial \alpha_i$ are derived as:

$$\begin{aligned} \frac{\partial a^2}{\partial \alpha_i} &= 2(S_1 - S_2) \cdot \left(\frac{\partial S_1}{\partial \alpha_i} - \frac{\partial S_2}{\partial \alpha_i}\right) \\ &= 2\left(\sum_{i=0}^{N}\sum_{j=0}^{M} R_{i,j}^1 P_{ij} - \sum_{i=0}^{N}\sum_{j=0}^{M} R_{i,j}^2 P_{ij}\right) \cdot \left(\sum_{i=0}^{N}\sum_{j=0}^{M} R_{i,j}^1 - \sum_{i=0}^{N}\sum_{j=0}^{M} R_{i,j}^2\right) \end{aligned} \tag{13}$$

$$\begin{aligned} \frac{\partial b^2}{\partial \alpha_i} &= 2(S_2 - S_3) \cdot \left(\frac{\partial S_2}{\partial \alpha_i} - \frac{\partial S_3}{\partial \alpha_i}\right) \\ &= 2\left(\sum_{i=0}^{N}\sum_{j=0}^{M} R_{i,j}^2 P_{ij} - \sum_{i=0}^{N}\sum_{j=0}^{M} R_{i,j}^3 P_{ij}\right) \cdot \left(\sum_{i=0}^{N}\sum_{j=0}^{M} R_{i,j}^2 - \sum_{i=0}^{N}\sum_{j=0}^{M} R_{i,j}^3\right) \end{aligned} \tag{14}$$

$$\begin{aligned} \frac{\partial c^2}{\partial \alpha_i} &= 2(S_3 - S_1) \cdot \left(\frac{\partial S_3}{\partial \alpha_i} - \frac{\partial S_1}{\partial \alpha_i}\right) \\ &= 2\left(\sum_{i=0}^{N}\sum_{j=0}^{M} R_{i,j}^3 P_{ij} - \sum_{i=0}^{N}\sum_{j=0}^{M} R_{i,j}^1 P_{ij}\right) \cdot \left(\sum_{i=0}^{N}\sum_{j=0}^{M} R_{i,j}^3 - \sum_{i=0}^{N}\sum_{j=0}^{M} R_{i,j}^1\right) \end{aligned} \tag{15}$$

where S_1, S_2 and S_3 are the three vertices of triangle mesh. In this way, the deviation of the scattering field $\Delta\mathbf{E}$ can be obtained by:

$$\begin{aligned} \Delta\mathbf{E} &= \sum_{i=1}^{n} \left(\frac{\partial \mathbf{b}(\boldsymbol{\alpha}^c)}{\partial \alpha_i}\right) \Delta\alpha_i \\ &= \sum_{i=1}^{n} \left(jk\eta \frac{e^{-jkR_0}}{4\pi R_0} \frac{\partial \int_s \hat{k}_s \times [\hat{k}_s \times (2\hat{n} \times H_i)] e^{jk(\hat{k}_s - \hat{k}_i)\cdot \mathbf{r}'} ds'}{\partial \alpha_i} \right) \Delta\alpha_i \end{aligned} \tag{16}$$

It should be noted the first-order Taylor series is used to expand the formula of far-field scattering field at the mean value. Therefore, the error will be introduced into the approximate calculation formula. More specifically, the error will increase with varying interval of the shape becomes bigger. The experience indicates that the interval should be less then 0.4λ. As shown in Eq. (4), the change of the far-field scattering field should be calculated only once for each $\Delta\alpha_i$. Therefore, the computation complexity has a linear relation to the number of random variables. In other words, the equation should be solved *n* (number of random variables) times totally for the uncertain problems. However, for the MC

method, the computational efficiency will decrease as the number of sampling points increases. Generally, the number of sampling points in the MC method is far greater than the number of random variables in the proposed method. Therefore, the computational time can be saved a lot when compared with the traditional MC method.

III. NUMERICAL RESULTS

In this section, a series of examples are presented to demonstrate the efficiency of the proposed method.

A. The bistatic RCS for a PEC slab

Firstly, a slab model with uncertain side length is analyzed with the proposed method at the frequency of 1GHz. The side length of the slab model is set as [1.91m, 2.09m], as shown in Fig. 4. To verify the accuracy of the proposed method for uncertainty problems, the result simulated by the MC method with 1000 sampling points is used as a reference [39-40]. The incident angle of plane wave is set at $\theta_i = 0^\circ$, $\varphi_i = 180^\circ$. The bistatic RCS results are compared in Fig. 5 between the MC method and the proposed method. It can be seen that there is a good agreement between them. Moreover, the comparisons of CPU time cost between the proposed method and MC method with 1000 samples are listed in Table 1.

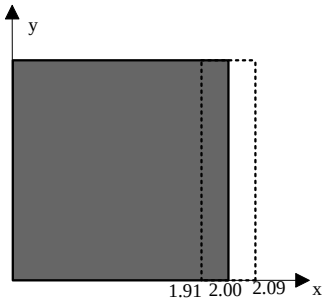

Fig. 4. The slab model with uncertain side length.

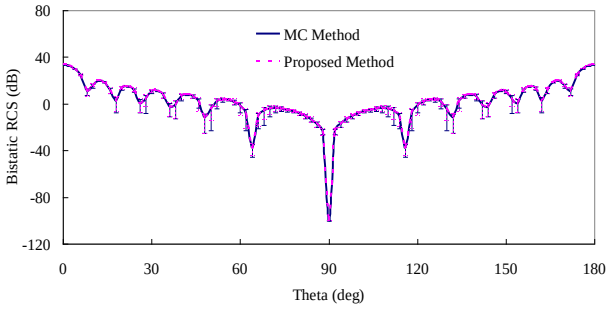

Fig. 5. Bistatic RCS of a slab model with uncertain side length.

Table 1: Comparisons of CPU Time between the Proposed Method and MC Method with 1000 Samples

Method	CPU Time (s)
Proposed method	41
Monte Carlo	1158

B. The monostatic RCS for a PEC aircraft

Secondly, the analysis of monostatic RCS is taken for a PEC aircraft at the frequency of 1.0 GHz. As shown in Fig. 6 (a), the nose of aircraft is along y axis. The varying length of wings is set as the uncertain scattering property of the aircraft model with the variation of $[-0.09m, 0.09m]$. It can be seen from Fig. 6 (b) that there are eight control points to describe the varying shape of this aircraft. The incident angle of plane wave is set at $\theta_i = 90^\circ$, $\varphi_i = 0-180^\circ$. As shown in Fig. 7, the monostatic RCS results are given and it can be found that there is a good agreement between the MC method and the proposed method. Moreover, the comparisons of CPU time cost between the proposed method and MC method with 1000 samples are listed in Table 2.

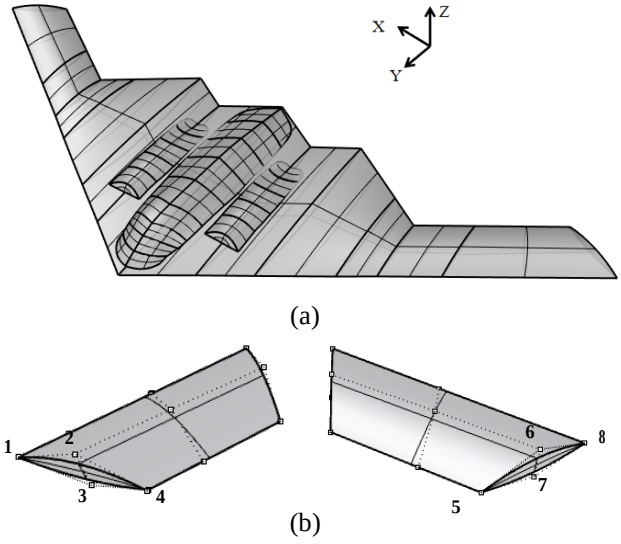

Fig. 6. (a)The aircraft model with varying length of wings. (b) The aircraft model constructed by NURBS Approach (Points 1-8 are used to control the varying of the wings length).

Table 2: Comparisons of CPU time between the proposed method and MC method with 1000 samples

Method	CPU Time (s)
Proposed method	2817
Monte Carlo	81095

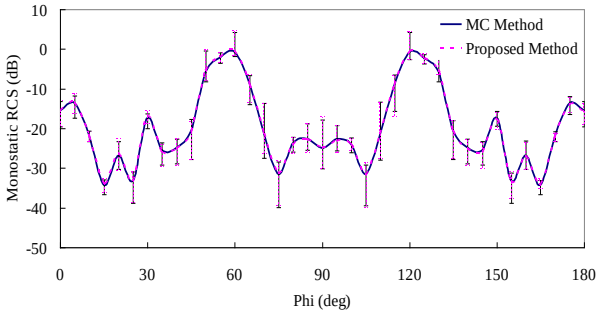

Fig. 7. Monostatic RCS of an aircraft model with varying length of wings.

C. The monostatic RCS for a PEC missile over a rough medium sea surface

At last, we consider the scattering from a missile over a rough medium sea surface at the frequency of 1 GHz. As shown in Fig. 8 (a), the nose of missile is along z axis. The varying length of wings is set as the uncertain scattering property of the missile model with the variation of [2.9m, 3.1m]. As shown in Fig. 8 (b), there are eight control points to describe the varying shape of this missile. The incident angle of plane wave is set at $\theta_i = -90^\circ \sim 90^\circ$, $\varphi_i = 180^\circ$. As shown in Fig. 9, the monostatic RCS results are given and it can be found that there is a good agreement between the MC method and the proposed method. Moreover, the comparisons of CPU time cost between the proposed method and MC method with 1000 samples are listed in Table 3.

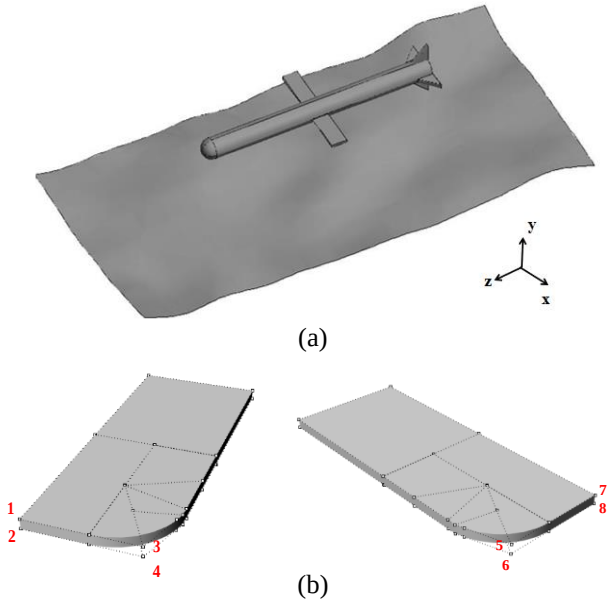

Fig. 8. (a) The missile model with varying length of wings over a rough medium sea surface. (b) The aircraft model constructed by NURBS Approach (Points 1-8 are used to control the varying of the wings length).

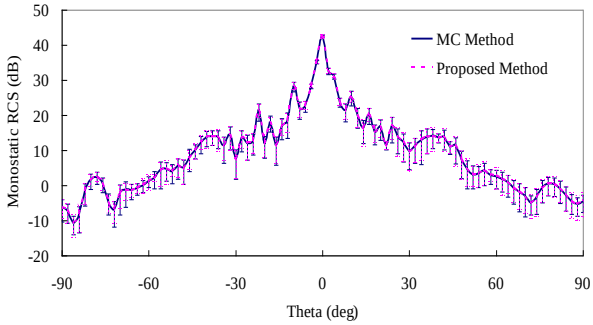

Fig. 9. Monostatic RCS of a missile model with varying length of wings.

Table 3: Comparisons of CPU time between the proposed method and MC method with 1000 samples

Method	CPU Time (s)
Proposed method	502
Monte Carlo	18459

IV. CONCLUSION

In this paper, the perturbation approach is used to analyze the uncertain scattering from electrically large targets. By using the non-uniform rational B-spline (NURBS) scheme, the varying geometrical shape can be modeled with several variables. In this way, the scattering far-fields can be calculated by the PO method. Less matrix equations are needed to be solved when compared with the traditional Monte Carlo method.

ACKNOWLEDGMENT

The authors gratefully acknowledge the financial supports by the National Key Research and Development Program of China under Grant 2016YFC1401001.

REFERENCES

[1] W. C. Chew, J. M. Jin, E. Midielssen, and J. M. Song, *Fast and Efficient Algorithms in Computational Electromagnetics*. Boston, MA: Artech House, 2001.

[2] M. Chen, R. S. Chen, D. Z. Ding, Z. H. Fan "Accelerating the multilevel fast multipole method with parallel preconditioner for large-scale scattering problems," *Applied Computational Electromagnetic Society*, vol. 26, no. 10, pp. 815-822, Oct. 2011.

[3] Z. He and R. S. Chen, "A vector meshless parabolic equation method for three-dimensional electromagnetic scatterings," *IEEE Trans. Antennas and Propagation*, vol. 63, no. 6, pp. 2595-2603, 2015.

[4] W. C. Chew, T. J. Cui, and J. M. Song, "A FAFFA-MLFMA algorithm for electromagnetic scattering," *IEEE Trans. Antennas Propag.*, vol. 50, no. 11, pp. 1641-1649, 2002.

[5] Z. He, Z. H. Fan, D. Z. Ding, and R. S. Chen, "Efficient radar cross-section computation of electrically large targets with ADI-PE method,"

Electronics Letters, vol. 51, no. 4, pp. 360-362, 2015.

[6] Z. He and R. S. Chen, "Frequency-domain and time-domain solvers of parabolic equation for rotationally symmetric geometries," *Computer Physics Communication*, vol. 220, pp. 181-187, 2017.

[7] C. Chauviere, J. S. Hesthaven, and L. C. Wilcox, "Efficient computation of RCS from scatterers of uncertain shapes," *IEEE Trans. Antennas Propagat*., vol. 55, no. 5, pp. 1437-1448, May 2007.

[8] A. C. M. Austin and C. D. Sarris, "Efficient analysis of geometrical uncertainty in the FDTD method using polynomial chaos with application to microwave circiuts," *IEEE Trans. Microw. Theory Techn*., vol. 61, no. 12, pp. 4293-4301, Dec. 2013.

[9] Z. Zubac, D. D. Zutter, and D. V. Ginste, "Scattering from two-dimensional objects of varying shape combining the method of moments with the stochastic Galerkin method," *IEEE Trans. Antennas Propagat*., vol. 62, no. 9, pp. 4852-4856, Sep. 2014.

[10] Z. Zubac, D. D. Zutter, and D. V. Ginste, "Scattering from two-dimensional objects of varying shape combining the multilevel fast multipole method (MLFMM) with the stochastic galerkin method (SGM)," *IEEE Antennas Wireless Propagat. Lett*., vol. 14, pp. 843-846, 2015.

[11] Z. Zubac, L. Daniel, D. D. Zutter, and D. V. Ginste, "A cholesky-based SGM-MLFMM for stochastic full-wave problems described by correlated random variables," *IEEE Antennas Wireless Propagat. Lett*., vol. 16, pp. 776-779, 2017.

[12] B. T. Nguyen, C. Furse, and J. J. Simpson, "A 3-D stochastic FDTD model of electromagnetic wave propagation in magnetized ionosphere plasma," *IEEE Trans. Antennas Propagat*., vol. 63, no. 1, pp. 304-313, Jan. 2015.

[13] T. Tan, A. Taflove, and V. Backman, "Single realization stochastic FDTD for weak scattering waves in biological random media," *IEEE Trans. Antennas Propagat*., vol. 61, no. 2, pp. 818-828, Feb. 2013.

[14] H. Bagci, A. C. Yucel, J. Hesthaven, and E. Michielssen, "A fast stroud-based collocation method for statistically characterizing EMI/EMC phenomena on complex platforms," *IEEE Trans. Electromagn. Compat*., vol. 51, no. 2, pp. 301-311, May 2009.

[15] P. Li and L. J. Jiang, "Uncertainty quantification for electromagnetic system using ASGC and DGTD method," *IEEE Trans. Electromagn. Compat*., vol. 57, no. 4, pp. 754-763, Aug. 2015.

[16] G. Fishman, *Monte Carlo: Concepts, Algorithms, and Applications*. ch. 3, New York, NY, USA: Springer-Verlag, 1996.

[17] O. P. Le Maitre and O. M. Knio, *Spectral Methods for Uncertainty Quantification with Applications to Computational Fluid Dynamics*. Heidelberg, Germany: Springer-Verlag, pp. 7-10, 2010.

[18] D. Xiu, "Fast numerical methods for stochastic computations: A review," *Commun. Comput. Phys*., vol. 5, no. 2-4, pp. 242-272, 2009.

[19] D. Xiu, "Efficient collocational approach for parametric uncertainty analysis," *Commun. Comput. Phys*., vol. 2, no. 2, pp. 293-309, 2007.

[20] A. C. Yucel, H. Bagci, and E. Michielssen, "An adaptive multi-element probabilistic collocation method for statistical EMC/EMI characterization," *IEEE Trans. Electromagn. Compat*., vol. 55, no. 6, pp. 1154-1168, Dec. 2013.

[21] R. G. Ghanem and P. D. Spanos, *Stochastic Finite Elements. A Spectral Approach*. ch. 3, New York, NY, USA: Springer-Verlag, 1991.

[22] C. Chauviere, J. S. Hesthaven, and L. Lurati, "Computational modeling of uncertainty in time-domain electromagnetics," *SIAM J. Sci. Comput*., vol. 28, no. 2, pp. 751-775, Feb. 2006.

[23] F. Z. Shi, *Computer-aided Geometric Design and Nonuniform Rational B-Spline*. ch. 14, Beijing, China: Higher Education Express, 2001.

[24] H. B. Yuan, N. Wang, and C. H. Liang, "Combining the higher order method of moments with geometric modeling by NURBS surfaces," *IEEE Trans. Antennas Propagat.*, vol. 57, no. 11, pp. 3558-3563, Nov. 2009.

[25] S. M. Rao, D. R. Wilton, and A. W. Glisson, "Electromagnetic scattering by surfaces of arbitrary shape," *IEEE Trans. Antennas Propagat*., vol. AP-30, no. 3, May 1982.

[26] Z. P. Qiu and I. Elishakoff, "Antioptimization of structures with large uncertain-but-non-random parameters via interval analysis," *Computer Methods in Applied Mechanics and Engineering*, vol. 152, no. 3, pp. 361-372, 1998.

[27] B. Z. Xia, D. J. Yu, and J. Liu, "Interval and subinterval perturbation methods for a structural-acoustic system with interval parameters," *Journal of Fluids and Structures*, vol. 38, pp. 146-163, 2013.

[28] C. Wang, Z. P. Qiu, X. J. Wang, and D. Wu, "Interval finite element analysis and reliability-based optimization of coupled structural-acoustic system with uncertain parameters," *Finite Elements in Analysis and Design*, vol. 91, pp. 108-114, 2014.

[29] R. F. Harrington, *Field Computation by Moment Method. Malabar*. FL: Krieger, 1982.

[30] Y. Saad and M. Schultz. "GMRES: A generalized minimal residual algorithm for solving non-symmetric linear systems," *SIAM J. Sci. Stat. Comput*., vol. 7, pp. 856-869, 1986.

[31] P. Arcioni, M. Bressan and L. Perregrini, "On the evaluation of the double surface integrals arising in the application of the boundary integral method to 3-D problems," *IEEE Transactions on Microwave Theory and Techniques*, vol. 45, no. 3, pp. 436-439,

Mar. 1997.
[32] K. C. Wang, D. Z. Ding, and R. S. Chen, "A surrogate modeling technique for electromagnetic scattering analysis of 3-D objects with varying shape," *IEEE Antennas Wireless Propagat. Lett*., vol. 17, pp. 1524-1527, 2018.
[33] Y. Y. An, D. X. Wang, and R. S. Chen, "Improved multilevel physical optics algorithm for fast computation of monostatic radar cross section," *IET Microw. Antennas Propag*., vol. 8, iss. 2, pp. 93-98, 2014.
[34] Y. Y. An, D. X. Wang, and R. S. Chen, "A fast numerical algorithm for calculating electromagnetic scattering from an object above a rough surface," *Electromagnetics*, vol. 33, no. 1, pp. 10-22, 2013
[35] Y. Y. An, R. S. Chen, P. P. Xu, Z. W. Liu, and L. P. Zha, "Analysis of composite scattering from a target above/below a dielectric rough surface using higher order basis functions," *Appl. Comput. Electromagn. Society J*., vol. 27, no. 7, pp. 541-549, 2012.
[36] D. Z. Ding, Y. Shi, Z. N. Jiang, and R. S. Chen, "Application of hierarchical two-level spectral preconditioning method for electromagnetic scattering from the rough surface," *Int. J. Antennas Propag*., vol. 2014, Article ID 752418, 10 pages, July 2014.
[37] Z. H. Fan, Z. He, D. Z. Ding, and R. S. Chen, "The parallel ray propagation fast multipole algorithm with curve asymptotic phase basis function for large-scale EM scatterings," *Appl. Comput. Electromagn. Soc. J*., vol. 30, no. 4, pp. 415-422, 2015.
[38] M. Chen, R. S. Chen, D. Z. Ding, and Z. H. Fan, "Accelerating the multilevel fast multipole method with parallel preconditioner for large-scale scattering problems," *Appl. Comput. Electromagn. Society J*., vol. 26, no. 10, pp. 815-822, Oct. 2011.
[39] K. C. Wang, Z. He, D. Z. Ding, and R. S. Chen, "An uncertainty scattering analysis of 3-D objects with varying shape based on method of moments," *IEEE Transactions on Antennas and Propagation*, vol. 67, no. 4, pp. 2835-2840, 2019.
[40] K. C. Wang, D. Z. Ding, and R. S. Chen, "A surrogate modeling technique for electromagnetic scattering analysis of 3-D objects with varying shape," *IEEE Antennas and Wireless Propagat. Letter*, vol. 17, no. 8, pp. 1524-1527, 2018.

Yong Chen was born in Tianmen, Hubei Province, China, in 1983. He received the B.S. degree from WuHan University in 2005, and the M.S. degree in Electromagnetic Field and Microwave Technology from the graduate school of Second Academy, China Aerospace Science &Industry Corporation in 2008. He is currently working towards the Ph.D. degree in Physics at Beijing Institute of Technology.

He is a Senior Engineer at Science and Technology on Electromagnetic Scattering Laboratory. His research interest includes the electromagnetic scattering modeling and radar signal simulation.

Zhaoguo Hou was born in Dingxi, Gansu Province, China, in 1983. He received the B.S. degree from Beijing Institute of Technology in 2005, the M.S. degree in condensed matter Physics from Beijing Institute of Technology in 2007, and the Ph.D. degree in Electromagnetic Field and Microwave Technology from Communication University of China in 2011.

He is a Senior Engineer at Science and Technology on Electromagnetic Scattering Laboratory. His research interests include computational electromagnetics and radar signal simulation.

Hong-Cheng Yin was born in Jiangxi, China. He received the B.S. degree from Northwest Telecommunication Engineering Institute, Xi'an, China, in 1986, the M.S. degree from Beijing Institute of Environmental Features (BIEF), Beijing, China, in 1989, and the Ph.D. degree from Southeast University, Nanjing, China, in 1993, all in Electromagnetic Field and Microwave Technique. He is currently a Researcher at the Science and Technology on Electromagnetic Scattering Laboratory, BIEF. His research interests include numerical methods in electromagnetic fields, electromagnetic scattering and inverse scattering, radar target recognition. Yin is a Fellow of Chinese Institute of Electronics.

Ru Shan Chen was born in Jiangsu, China. He received the B.Sc. and M.Sc. degrees from the Department of Radio Engineering, Southeast University, China, in 1987 and 1990, respectively, and the Ph.D. degree from the Department of Electronic Engineering, City University of Hong Kong, in 2001.

He joined the Department of Electrical Engineering, Nanjing University of Science and Technology (NJUST), China, where he became a Teaching Assistant in 1990 and a Lecturer in 1992. Since September 1996, he has been a Visiting Scholar with the Department of Electronic Engineering, City University of Hong Kong, first as Research Associate, then as a Senior Research

Associate in July 1997, a Research Fellow in April 1998, and a Senior Research Fellow in 1999. From June to September 1999, he was also a Visiting Scholar at Montreal University, Canada. In September 1999, he was promoted to Full Professor and Associate Director of the Microwave and Communication Research Center in NJUST, and in 2007, he was appointed as the Head of the Department of Communication Engineering, NJUST. He was appointed as the Dean in the School of Communication and Information Engineering, Nanjing Post and Communications University in 2009. And in 2011 he was appointed as Vice Dean of the School of Electrical Engineering and Optical Technique, NJUST. Currently, he is a principal investigator of more than 10 national projects. His research interests mainly include computational electromagnetics, microwave integrated circuit and nonlinear theory, smart antenna in communications and radar engineering, microwave material and measurement, RF-integrated circuits, etc. He has authored or coauthored more than 260 papers, including over 180 papers in international journals.

Source Enumeration Method Combining Gerschgorin Circle Transform and Generalized Bayesian Information Criterion in Large-scale Antenna Array

Chuanchuan Wang, Yonghu Zeng, and Liandong Wang

State Key Laboratory of Complex Electromagnetic Environment Effects on Electronics and Information System
Luoyang, 471003, China
wangchuan1083@126.com, 471680179@qq.com, 874353112@qq.com

Abstract ─ A new source enumeration method based on gerschgorin circle transform and generalized Bayesian information criterion is devised, for the case that the antenna array observed signals are overlapped with spatial colored noise, and the number of antennas compared with that of snapshots meet the requirement of general asymptotic regime. Firstly, the sample covariance matrix of the observed signals is calculated, and then gerschgorin circle transformation is carried out on the sample covariance matrix. With the help of the more obvious distinction between the transformed signal gerschgorin circle radius and the noise gerschgorin circle radius, the observation statistic used to establish the likelihood function of the information theoretic criterion is constructed, by using the estimated values of the transformed sample covariance matrix's eigenvalues, and according to the idea of corrected Rao's score test, the observed statistics used to establish the likelihood function of the ITC are constructed. Based on the statistics, the source number is estimated by employing the generalized Bayesian information criterion (GBIC). The effectiveness of the proposed method is validated by experiments. Compared with the information theoretic criterion (ITC) methods and gerschgorin circle method (GDE), in Gaussian white noise, at the time $M/N \geq 1$, that is the relationship between the number of antennas and that of snapshots meets the requirement of the general asymptotic regime, the proposed method can accurately estimate the source number with 100% probability, the other methods failed. Compared with the ITC methods based on eigenvalue diagonal loading and GDE, in colored noise, at the time $M/N \geq 1$, the proposed method can accurately estimate the source number with 100% probability, the other methods failed. Compared with the methods based on random matrix theory, in colored noise, the proposed method can estimate the source number with 100% probability, but the estimation of other methods failed. The proposed method has wide applicability, in terms of the relationship between the numbers of antennas and snapshots, it is suitable for both general asymptotic regime and classical asymptotic system, and in terms of noise characteristics, it is suitable for both Gaussian white noise environment and colored noise environment.

Index Terms ─ Colored noise, corrected Rao's score test, general asymptotic regime, Gerschgorin circle transform, source enumeration.

I. INTRODUCTION

The estimation of the emitters' number has important applications in many fields, such as phased array radar, communications, brain imaging, neural networks, speech signal separation and direction of arrival estimation [1-8]. The classical methods for source enumeration are essentially based on the statistical analysis theory of observed data and their moment functions. For example, the hypothesis testing methods and information theoretic criterion (ITC) methods are commonly used for source enumeration, which mainly make use of the statistical distribution of observed data and the statistics of sample eigenvalues [9]. Among the classical source enumeration methods, the hypothesis testing methods include spherical test [10] and eigenvalue detection [11], which are mainly used to construct the observation statistics for hypothesis testing and set the decision threshold by using the statistical distribution law of sample eigenvalues. The ITC methods include Akaike information criterion (AIC) [12], Bayesian information criterion (BIC) [13], minimum description length (MDL) [14] and Predictive description length (PDL) [15], etc., usually assume that the observed data are Gaussian distribution, and then establish a criterion for estimating the number of sources according to the likelihood function of the joint probability distribution of the observed data. The expression of source enumeration is a function of the sample eigenvalues. A new source enumeration method based on higher-order tensors is presented in [16]. All these methods are applicable to Gaussian white noise environment [1-2, 16-17]. The main methods for source enumeration in colored noise environment are gerschgorin circle method [18] and

Submitted On: March 30, 2020
Accepted On: May 17, 2020

ITC methods based on diagonal loading [2, 19]. The performance of ITC methods have been studied in [17], results show that the methods are suitable for small-scale array signals whose sample number is much larger than the number of antennas. The above source enumeration methods are mainly based on the classical asymptotic system, that is, the dimension of the observed data matrix is fixed and the number of snapshots tends to be infinite.

However, in large-scale antenna arrays such as phased array radar and Multiple Input Multiple Output (MIMO) systems, due to the limitation of data storage space and the real-time requirement of signal processing, the observed data is often difficult to meet the condition that the number of snapshots is much larger than that of antennas, and it usually belongs to high-dimensional limited sampling data or even small sampling data. That is, the number of snapshots is in the same order of magnitude as that of antennas, or even less than the number of antennas. As to large-scale array observed data, the proportional relationship between the number of snapshots and that of antennas often does not meet the requirements of classical statistical theory, so the emergence of large-scale array brings new challenges to the classical source enumeration methods [20-21].

At present, the source enumeration in general asymptotic regime is mainly based on random matrix theory, including RMT-AIC method [4], BN-AIC method [5], BIC-variant method [6], LS-MDL method [7], the estimation method based on spike model [22], etc., and these methods are applicable when the number of antennas is less than that of snapshots. As to the estimation method based on spherical test and the estimation method based on modified Rao score test [22], they are applicable when the number of antennas is more than, less than or equal to the number of snapshots. All these methods are not only suitable for source enumeration in general asymptotic regime, but also suitable for classical asymptotic system. However, these methods are only applicable to white noise environment, but fail in colored noise environment [1, 4-7, 22].

Comprehensive analysis shows that at this stage, there is a lack of source enumeration method which is suitable for both classical asymptotic system and general asymptotic regime, whether there is white noise or colored noise environment. Considering that in the actual signal environment, the proportional relationship between the number of antennas and the number of snapshots, and whether the noise of observed signal overlapped by Gaussian white noise or colored noise is unknown, therefore, it is necessary to develop a source enumeration method which is suitable for both classical asymptotic system and general asymptotic regime, and is applicable to both Gaussian white noise and colored noise. In this paper, a source enumeration method based on gerschgorin circle transform and generalized Bayesian information criterion is devised, which does not need to prejudge the relationship between the number of antennas and that of snapshots (applying conditions must be satisfied, the relationship between the number of antenna elements M, the number of sources K, and the number of snapshots N is: $M-K\geq 1$, $K<N$, M can be larger than, equal to or less than N), and whether the observed signal overlapped noise is Gaussian white noise or colored noise. The number of narrowband signal sources such as communications can be blindly estimated in the complex electromagnetic environment.

The remainder of the paper is organized as follows. Section II presents the model of source enumeration problem. Section III gives the proposed source enumeration method. Section IV describes experiment results that validate the proposed method. Finally, the conclusions are drawn in Section V.

II. MATHEMATICAL MODEL OF SOURCE ENUMERATION

Suppose there are far-field signals whose number is K incidenting from the directions $\theta_1,\theta_2,\cdots,\theta_K$ onto an antenna array, and the number of antennas is M. at the sampling time t, the observed signals by the array is expressed as,

$$\boldsymbol{X}(\mathrm{t})=\sum_{k=1}^{K}a(\theta_k)\,s_k(t)+\boldsymbol{w}(t)=\boldsymbol{A}(\boldsymbol{\theta})\boldsymbol{s}(\mathrm{t})+\boldsymbol{w}(t), \tag{1}$$

where $\boldsymbol{X}(\mathrm{t})=[\boldsymbol{X}_1(t),\boldsymbol{X}_2(t),\ldots,\boldsymbol{X}_M(t)]^{\mathrm{T}}$ (the superscript T represents transpose) is the observed signal vector, $a(\theta_k)$ is the array direction vector, $\boldsymbol{A}(\boldsymbol{\theta})=[a(\theta_1),a(\theta_2),\cdots,a(\theta_K)]$ is the matrix composed of direction vectors, $\theta=[\theta_1,\theta_2,\cdots,\theta_K]^{\mathrm{T}}$ is the incoming wave angle parameter vector of the signals, $\boldsymbol{s}(t)=[s_1(t),s_2(t),\cdots,s_K(t)]^{\mathrm{T}}$ is the incident signal vector, $\boldsymbol{w}(t)=[w_1(t),w_2(t),\cdots,w_M(t)]^{\mathrm{T}}$ is the additive noise vector, the sampling time is $t=1,2,\cdots,N$, and N is the number of snapshots. The basic assumptions of the array observed signal model shown in formula (1) are as follows [22]:

(1) The incident signals are narrowband stationary signals independent of each other, which satisfy the mean $\mathrm{E}\{\boldsymbol{s}(t)\}=0$ and covariance matrix $\mathrm{E}\{\boldsymbol{s}(t)\boldsymbol{s}^H(t)\}=diag\{p_{s_1},p_{s_2},\cdots,p_{s_K}\}\triangleq P_{\boldsymbol{s}}\in R^{K\times K}$, where p_{s_k} is the power of the $k-$th signal;

(2) The superimposed noise in the observed signal vector is additive noise (Gaussian white noise or colored noise);

(3) The number of incident signals is less than that of antennas and snapshots at the same time, that is $K<\min(M,N)$;

(4) The incident signals propagate in ideal space, and the antennas have omni-directional consistency.

III. THE PROPOSED SOURCE ENUMERATION METHOD

A. The principle of the proposed method

In practice, the sample data received by antenna array contains noise, and it may not be an ideal Gaussian white noise, but a complex spatial colored noise. In the complex spatial colored noise environment, the noise eigenvalue part of the covariance matrix of the received data will become very divergent and will not vibrate near the noise power like the Gaussian white noise's eigenvalue part. This problem caused by colored noise will invalidate various algorithms for source enumeration using hypothesis testing and ITC. As to the source enumeration method based on gerschgorin circle theorem, and the methods based on eigenvalue diagonal loading combined with ITC are usually only applicable to the classical asymptotic system, that is, the relationship between the number of antennas M and that of snapshots N is: M is fixed and $M/N \ll 1$. While under the general asymptotic regime, the relationship between the number of antennas and that of signal samples is that M and N tend to infinity at the same rate, $M, N \to \infty$ and $M/N \to c \in (0, \infty)$, the above methods usually fail to estimate the source number, regardless of whether the noise is Gaussian white noise or colored noise.

The existing source enumeration methods based on random matrix theory cannot be applied to estimate the source number, in the case of observed signal overlapped with colored noise in general asymptotic regime [1, 4-7, 22]. Through the analysis of the eigenvalues of the observed signals' covariance matrix, it is found that the noise eigenvalues are very divergent in the colored noise environment. As to the source enumeration methods based on gerschgorin circle theorem, they can be used to estimate the source number in Gaussian white noise or colored noise in the classical asymptotic system. When applying these methods, it is necessary to make a special transformation of the observed signals' covariance matrix. And after the transformation, there will be a more obvious distinction between the signal gerschgorin circle radius and the noise gerschgorin circle radius. In order to estimate the source number under the condition of observed signals overlapping with colored noise in general asymptotic regime, with the help of the idea of gerschgorin circle transformation, the sample covariance matrix of the observed signals is calculated first, and makes the gerschgorin circle transformation to the sample covariance matrix, then we get the more obvious distinguishing between the signal gerschgorin circle radius and the noise gerschgorin circle radius after the transformation. According to the idea of corrected Rao's score test (CRST), it can be used to detect the structural characteristics of large-dimensional covariance matrix [23]. The spherical test statistics in CRST can test whether the covariance matrix of the observed data's noise part is proportional to the unit matrix. According to this principle, based on the estimated eigenvalues of the transformed sample covariance matrix, the observed statistics used to establish the likelihood function of the ITC are constructed, and on this basis the source number is estimated by the generalized Bayesian information criterion (GBIC). The conventional BIC yields unsatisfactory results, especially in some difficult conditions, such as small sample sizes, low signal-to-noise ratios (SNRs), close spacing and high correlation between the sources. To improve its performance, Lu et al. [24] proposed a generalized Bayesian information criterion, by incorporating the density of the sample eigenvalues or corresponding statistics.

The proposed method improves the existing source enumeration method based on corrected Rao's score test [22], which can be used not only in the classical asymptotic system, but also in the general asymptotic regime, whether the observed signals are overlapped with Gaussian white noise or colored noise.

B. Specific steps of the proposed method

The specific steps of the proposed method are as follows.

Step 1: assume that the antenna array has M elements, and the observed signals obtained by one measurement can be expressed as $\boldsymbol{X}(\mathrm{t}) = [\boldsymbol{X}_1(t), \boldsymbol{X}_2(t), \ldots, \boldsymbol{X}_M(t)]^{\mathrm{T}}$ (superscript T represents transpose). The sampling time is $t = 1,2,\cdots, N$, N is the number of snapshots, and the covariance matrix of the observed signals is calculated as $\boldsymbol{R}(t) = \frac{\boldsymbol{X}(t)\cdot\boldsymbol{X}^H(t)}{N}$.

Step 2: block the sample covariance matrix $\boldsymbol{R}(t)$ as follows:

$$\boldsymbol{R}(t) = \begin{bmatrix} \boldsymbol{R}^{'}(t) & \hat{r} \\ \hat{r}^H & \hat{r}_{MM} \end{bmatrix}.$$

The $M-1$-dimensional square matrix $\boldsymbol{R}^{'}(t)$ is the covariance matrix of the observed data $\boldsymbol{X}^{'}(t)$ obtained by removing the last element of the antenna array. For convenience, the following $\boldsymbol{R}(t)$ and $\boldsymbol{R}^{'}(t)$ will be abbreviated as $\boldsymbol{R}$ and $\boldsymbol{R}^{'}$. Take the characteristic matrix of $\boldsymbol{R}$, and it is recorded as $\boldsymbol{V}$, then we construct a unitary transformation matrix $\boldsymbol{T}$:

$$\boldsymbol{T} = \begin{bmatrix} \boldsymbol{V} & \boldsymbol{0} \\ \boldsymbol{0}^H & \boldsymbol{1} \end{bmatrix}. \tag{2}$$

The covariance matrix of the observed signals is unitary transformed by the constructed unitary transformation matrix $\boldsymbol{T}$,

$$\boldsymbol{R}_T=\boldsymbol{T}^H\boldsymbol{R}\boldsymbol{T}=\begin{bmatrix}\boldsymbol{V}^H\boldsymbol{R}'\boldsymbol{V} & \boldsymbol{V}^{\boldsymbol{H}}\hat{\boldsymbol{r}}\\ \hat{\boldsymbol{r}}^H\boldsymbol{V} & \hat{\boldsymbol{r}}_{MM}\end{bmatrix}=\begin{bmatrix}\gamma_1 & 0 & \cdots & 0 & \rho_1\\ 0 & \gamma_2 & \cdots & 0 & \rho_2\\ \vdots & \vdots & \ddots & \vdots & \vdots\\ 0 & 0 & \cdots & \gamma_{M-1} & \rho_{M-1}\\ \rho_1^* & \rho_2^* & \cdots & \rho_{M-1}^* & \hat{\boldsymbol{r}}_{MM}\end{bmatrix}. \quad (3)$$

Step 3: write the spectral decomposition of M-dimensional observed data covariance matrix $\boldsymbol{R}$, and $M-1$-dimensional observed data covariance matrix $\boldsymbol{R}^{'}$ as: $\boldsymbol{R}=\sum_{i=1}^{M}\lambda_i\boldsymbol{u}_i\boldsymbol{u}_i^H$, $\boldsymbol{R}^{'}=\sum_{i=1}^{M-1}\gamma_i\boldsymbol{v}_i\boldsymbol{v}_i^H$.

Step 4: do Eigen-Decomposition to the M-dimensional observed data covariance matrix $\boldsymbol{R}$ and the $M-1$-dimensional observed data covariance matrix $\boldsymbol{R}^{'}$, which are respectively expressed as:

$$\boldsymbol{R}=\boldsymbol{U}\boldsymbol{\Sigma}_\lambda\boldsymbol{U}^H,\boldsymbol{R}^{'}=\boldsymbol{V}\boldsymbol{\Sigma}_\lambda'\boldsymbol{V}^H.$$

Divide $\boldsymbol{U},\boldsymbol{V}$ and $\boldsymbol{\Sigma}_\lambda$ into blocks:

$$\boldsymbol{U}=\begin{bmatrix}u_{11} & \cdots & u_{1M}\\ \vdots & \ddots & \vdots\\ u_{M1} & \cdots & u_{MM}\end{bmatrix}=\begin{bmatrix}\boldsymbol{U}' & \boldsymbol{u}_M'\\ \boldsymbol{e}^H & u_{MM}\end{bmatrix}$$

$$\boldsymbol{V}=[\boldsymbol{v}_1\ \boldsymbol{v}_2\ \cdots\ \boldsymbol{v}_{M-1}]$$

$$\boldsymbol{\Sigma}_\lambda=\begin{bmatrix}\boldsymbol{\Sigma}_\lambda' & \cdots & \\ \vdots & \ddots & \vdots\\ & \cdots & \lambda_M\end{bmatrix},$$

where $\boldsymbol{U}'=[\boldsymbol{u}_1'\ \boldsymbol{u}_2'\cdots\boldsymbol{u}_{M-1}']$,$\boldsymbol{u}_i'=\left[\boldsymbol{u}_{1i}\ \boldsymbol{u}_{2i}\cdots\ \boldsymbol{u}_{(M-1)i}\right]^H$ $(i=1,2,\ldots,M)$, $\boldsymbol{e}=\left[\boldsymbol{u}_{M1}\ \boldsymbol{u}_{M2}\ \cdots\ \boldsymbol{u}_{M(M-1)}\right]^H$, $\boldsymbol{\Sigma}_\lambda'=\mathrm{diag}(\lambda_1,\lambda_2,\ldots,\lambda_{M-1})$.

Step 5: as in formula (2), by applying the unitary transformation matrix $\boldsymbol{T}$, the block matrix $\boldsymbol{U}$ and $\boldsymbol{V}$ to do unitary transformation of $\boldsymbol{\Sigma}_\lambda$, the following can be obtained:

$$\boldsymbol{R}_T=\boldsymbol{T}^H\boldsymbol{U}\boldsymbol{\Sigma}_\lambda\boldsymbol{U}^H\boldsymbol{T}=$$
$$\begin{bmatrix}\boldsymbol{V} & \boldsymbol{0}\\ \boldsymbol{0}^H & \boldsymbol{1}\end{bmatrix}^H\begin{bmatrix}\boldsymbol{U}' & \boldsymbol{u}_M'\\ \boldsymbol{e}^H & u_{MM}\end{bmatrix}\begin{bmatrix}\boldsymbol{\Sigma}_\lambda' & \\ & \lambda_M\end{bmatrix}\begin{bmatrix}\boldsymbol{U}' & \boldsymbol{u}_M'\\ \boldsymbol{e}^H & u_{MM}\end{bmatrix}\begin{bmatrix}\boldsymbol{V} & \boldsymbol{0}\\ \boldsymbol{0}^H & \boldsymbol{1}\end{bmatrix}=$$
$$\begin{bmatrix}\boldsymbol{V}^H\boldsymbol{U}'\boldsymbol{\Sigma}_\lambda'\boldsymbol{U}'^H\boldsymbol{V}+\lambda_M\boldsymbol{V}^H\boldsymbol{u}_M'\boldsymbol{u}_M'^H\boldsymbol{V} & \boldsymbol{V}^H\boldsymbol{U}'\boldsymbol{\Sigma}_\lambda'\boldsymbol{e}+\lambda_M\boldsymbol{V}^H\boldsymbol{u}_M'u_{MM}\\ \boldsymbol{e}^H\boldsymbol{\Sigma}_\lambda'\boldsymbol{U}'^H\boldsymbol{V}+\lambda_Mu_{MM}\boldsymbol{u}_M'^H\boldsymbol{V} & \boldsymbol{e}^H\boldsymbol{\Sigma}_\lambda'\boldsymbol{e}+\lambda_Mu_{MM}u_{MM}^*\end{bmatrix}. \quad (4)$$

Step 6: similar to the formula (3) in **Step 2**, take the first to the $M-1$ rows and the M column of the formula (4) in **Step 5**, and it is expressed as ρ_i' $(i=1,2,\cdots,M-1)$, then we take its absolute value $|\rho|_i'$ $(i=1,2,\cdots,M-1)$, write it as $r_i=|\rho|_i'$, and it can be regarded as the estimated values of the $M-1$ eigenvalue of the covariance matrix $\boldsymbol{R}^{'}$.

Step 7: as to r_i $(i=1,2,\cdots,M-1)$, ordering that $r_M=r_{M-1}$, expressing r_i and r_M as a sequence $r_i'=r_i$ $(i=1,2,\cdots,M)$, judging whether the values of r_i' are arranged in the order of $r_1'\geq r_2'\geq\cdots\geq r_M'$, if yes, the sequence r_i' is retained and proceed to the next step; if the values of r_i' are arranged in the order of $r_1'\leq r_2'\leq\cdots\leq r_M'$, the values of r_i' would be in reverse order, that is, the values of r_i' would be arranged in the order from the largest to the smallest, and they are expressed as $r_i'^f$, the serial number is $i=1,2,\cdots,M$. For convenience, we express r_i' or $r_i'^f$ as $r_i'^{new}=r_i'$ or $r_i'^f$.

Step 8: according to the eigenvalue sequence $r_i'^{new}$, the modified Rao score test method is introduced to estimate the number of sources. Defining $\widehat{\mathbf{R}}_W^{(k)}=\mathrm{diag}\{r_{k+1}'^{new},\cdots,r_M'^{new}\}$, and $\boldsymbol{T}^{(k)}$ is calculated by the following formula:

$$\boldsymbol{T}^{(k)}=\frac{1}{\sqrt{\tilde{\tau}^{(k)}}}Tr\left[\left(\frac{1}{\hat{\sigma}_k^2}\widehat{\mathbf{R}}_W^{(k)}-\mathbf{I}_{M-k}\right)^2\right]-(M-k)\tilde{c}_N^{(k)}, \quad (5)$$

where, $\tilde{\tau}^{(k)}=2(\tilde{c}_N^{(k)})^2\ \ (1+2\ \tilde{c}_N^{(k)})$, $\tilde{c}_N^{(k)}=(M-k)/(N-1)$, $\hat{\sigma}_k^2=\frac{1}{M-k}\sum_{i=k+1}^{M}r_i'^{new}$.

Step 9: define the formula of Source Enumeration based on gerschgorin circle theorem and modified Rao score test as following:

$$\mathrm{GDE-CRSTGBIC}(k)=\left(\boldsymbol{T}^{(k)}\right)^2+(k+1)\log N. \quad (6)$$

Step 10: estimate the source number by the following formula:

$$\hat{K}=\arg\max\ \mathrm{GDE-CRSTGBIC}(k),\quad k=1,2,\cdots,M-1. \quad (7)$$

IV. EXPERIMENTS AND ANALYSIS

The validation of the proposed method is carried out under the simulation

condition of the DELL9020MT personal computer, Intel (R) Core (TM) i7mur4770 CPU @ 3.40GHz Windows 64-bit operating system, and the simulation software is MATLAB R2010a. In order to fully verify the effectiveness of the proposed method (we name it as GDE-CRSTGBIC), the calculation results of the proposed method and the reference methods are compared, and three groups of tests are carried out.

Experiment 1: Comparison between the proposed method (GDE-CRSTGBIC) and the ITC methods (BIC, AIC, MDL, KIC), gerschgorin circle method (GDE), in the environment of Gaussian white noise. The experimental conditions are set as follows:

1) s_1 is a BPSK signal with a subpulse width of 3×10^{-7}s and a carrier frequency of 10MHz.

2) s_2 is a CW signal with a subpulse width of 1.5×10^{-5}s and a carrier frequency of 10MHz.

3) s_3 is a LFM signal with a carrier frequency of 10MHz and pulse repetition rate of 0.1MHz.

4) s_4 is a FSK signal with a subpulse width of 10^{-7}s. The carrier frequency varies with the binary baseband signal between 25MHz and 50MHz.

5) s_5 is a MPSK signal with a subpulse width of 4×10^{-7}s and a carrier frequency of 50MHz.

If the number of sources is set as $K = 4$, the source signals are composed of s_1, s_2, s_3 and s_5. If the number of sources is set as K=5, the source signals are composed of s_1~s_5. Set different number of array antenna elements M, and mixing matrix $\boldsymbol{A}$ is generated by random function, the sampling frequency is 120MHz, snapshots is N, the observed signals are overlapped with white Gaussian noise, the variation range of signal-to-noise ratio (SNR) is -10dB~30dB, step size is 2dB, 1000 Monte Carlo simulations are carried out on each SNR. The experimental results are shown in Figs. 1 (a)-(d). In addition, when $M = 340, K = 5, N = 300$, the histogram of the estimated source number at SNR $= 15$dB is shown in Figs. 2 (a)-(f).

Figure 1 shows the comparison of results by the GDE-CRSTGBIC method and the ITC methods (BIC, AIC, MDL, KIC), gerschgorin circle method (GDE), in the Gaussian white noise environment. As can be seen from Fig. 1 (a), at this time $M/N \ll 1$, the relationship between the number of antennas and that of snapshots meets the requirements of the classical asymptotic system. Under the condition of Gaussian white noise, when the SNR is larger than 3dB, the GDE-CRSTGBIC method, MDL method and BIC method can accurately estimate the source number with 100% probability, but the gerschgorin circle method needs more than 26dB of the SNR to reach 100% probability. In Fig. 1 (b), Fig. 1 (c) and Fig. 1 (d), $\frac{M}{N} \geq 1$, so the relationship between the number of antennas and that of snapshots meets the requirement of the general asymptotic regime. Under the condition of Gaussian white noise, the GDE-CRSTGBIC method can accurately estimate the source number with 100% probability when the SNR is larger than 14dB, 8dB, and 7dB, respectively. Other ITC and GDE methods failed to estimate the source number.

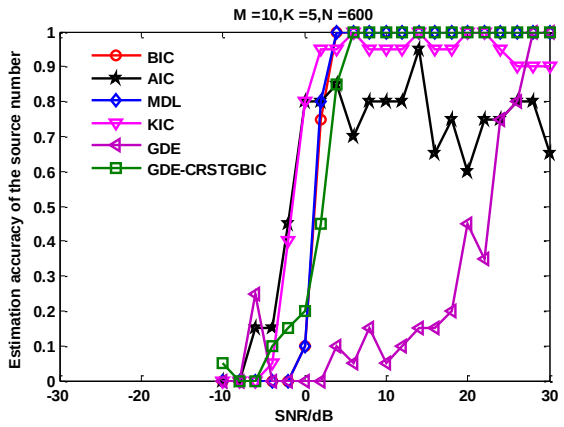

(a)

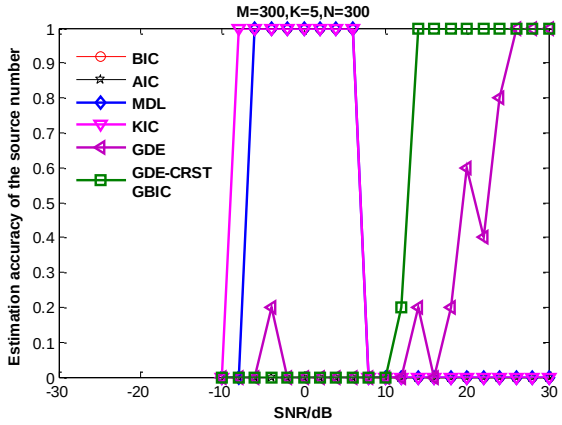

(b)

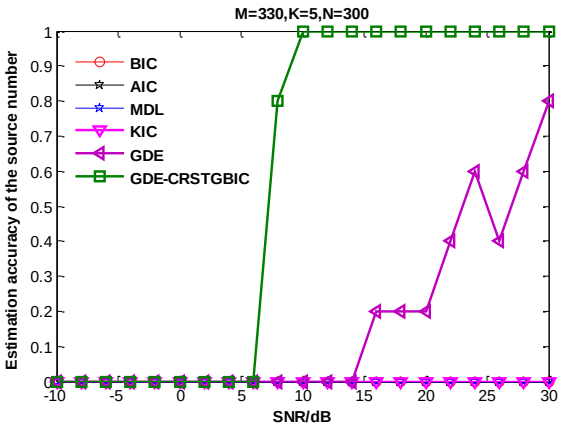

(c)

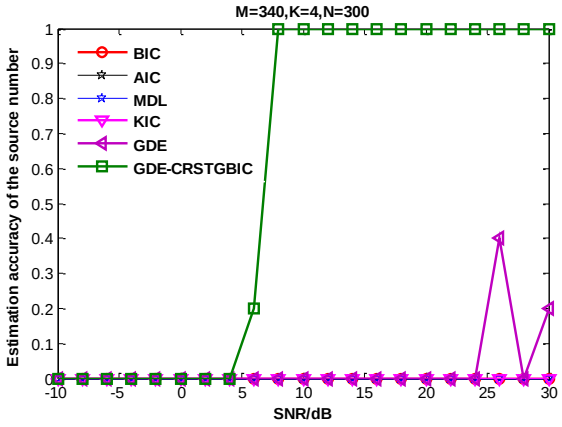

(d)

Fig. 1. The source number estimation results by proposed method are compared with those of the ITC methods and the GDE method under the condition of white noise.

Figure 2 shows, when $M = 340, K = 5, N = 300$, that is the relationship between the number of antennas and that of snapshots meets the requirement of the general asymptotic regime. In Gaussian white noise, the

GDE-CRSTGBIC method can accurately estimate the source number with 100% probability when the SNR is 15dB. Other ITC and GDE methods failed to estimate the source number.

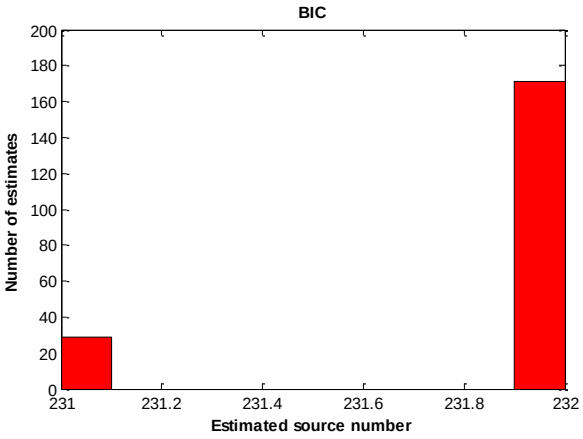

(a)

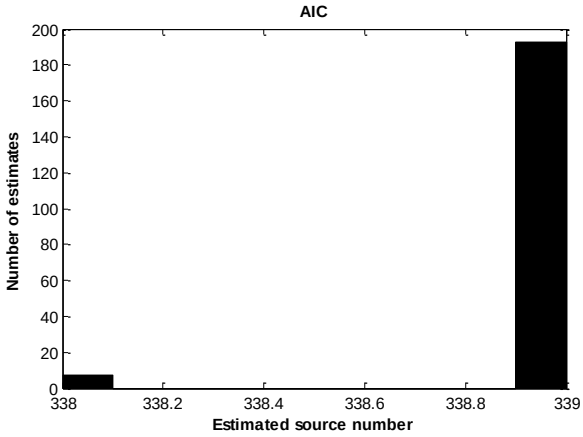

(b)

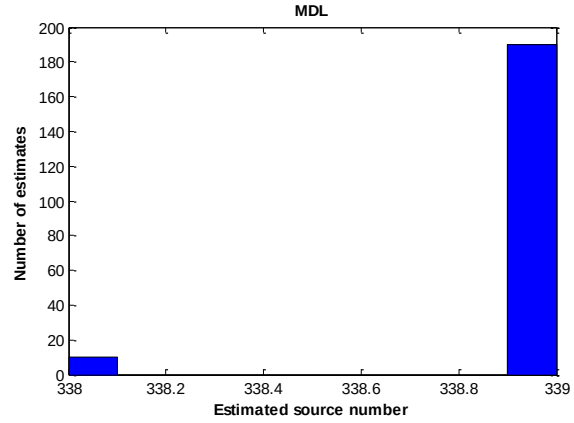

(c)

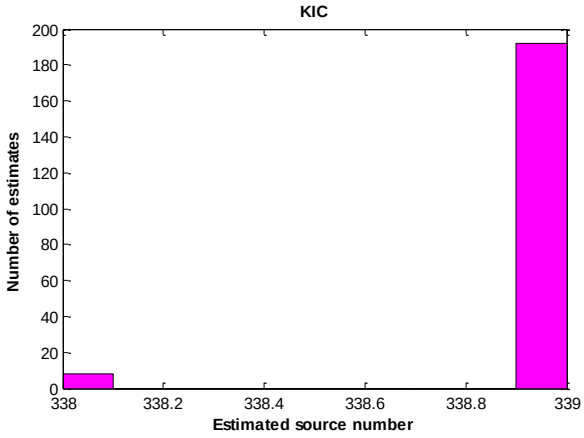

(d)

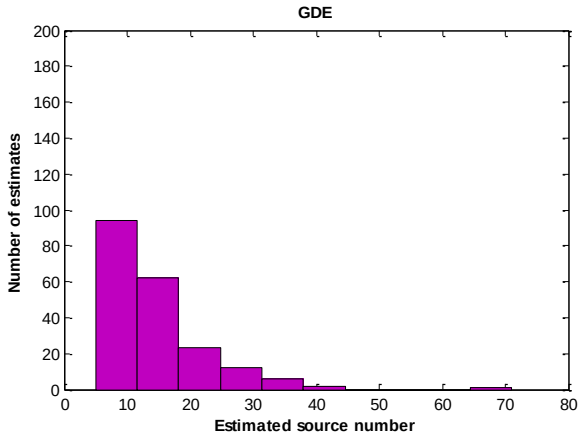

(e)

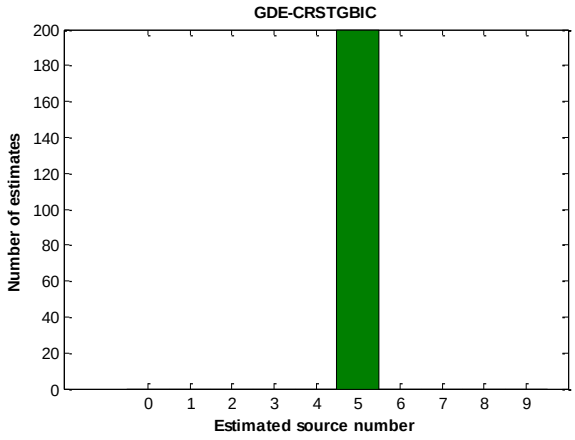

(f)

Fig. 2. Histogram of estimated source number at SNR = 15dB when $M = 340, K = 5, N = 300$.

Experiment 2: The proposed method (GDE-

CRSTGBIC) is compared with the ITC methods (BIC, AIC, MDL, KIC) based on eigenvalue diagonal loading and gerschgorin circle method (GDE) in colored noise. The source signals are the same with those in ***Experiment 1***.

If the number of sources is set as $K = 4$, the source signals are composed of s_1, s_2, s_3 and s_5. If the number of sources is set as K=5, the source signals are composed of s_1~s_5. Set different number of array antenna elements M, mixing matrix $\boldsymbol{A}$ is generated by random function, sampling frequency is 120MHz, snapshots is N, observed signals are overlapped with spatial color noise, the elements of its covariance matrix are expressed as $n_{ik} = \sigma_n^2 0.9^{|i-k|}\exp[(j(i\text{-}k)\pi/2)]$, $i,k = 1,2,\cdots,M$. σ_n is an adjustable parameter, which is used to set the SNRs of observed signals, the variation range of signal-to-noise ratio (SNR) is -10dB~30dB , step size is 2dB, 1000 Monte Carlo simulations are carried out on each SNR. The experimental results are shown in Figs. 3 (a)-(d). In addition, when $M = 340, K = 5, N = 300$, the histogram of the estimated source number at SNR $=$ 20dB is shown in Figs. 4 (a)-(f).

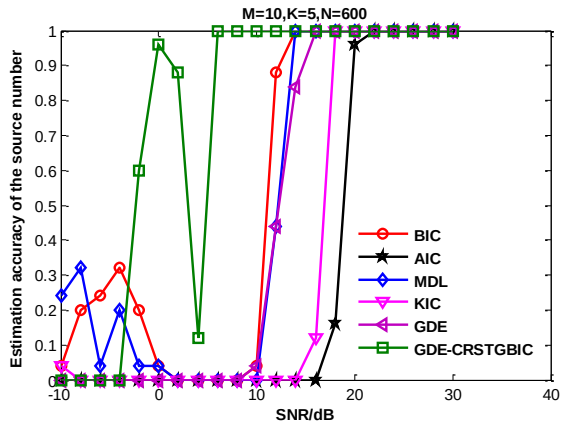

(a)

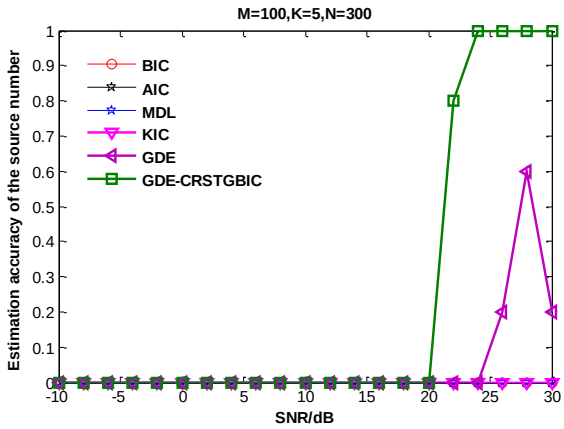

(b)

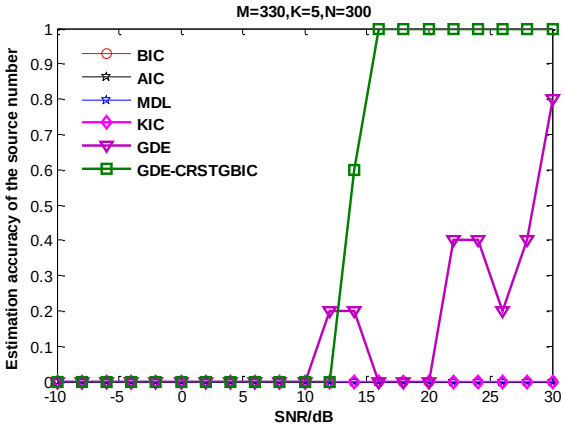

(c)

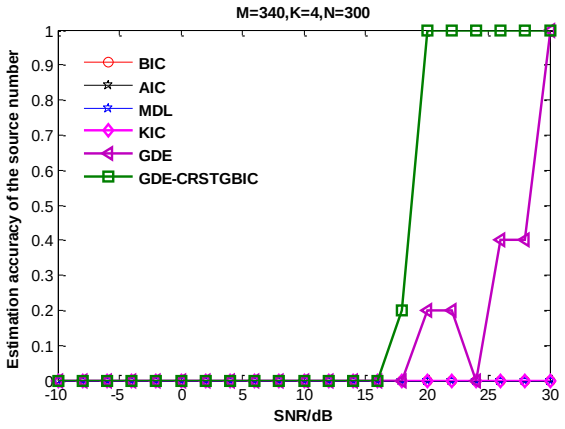

(d)

Fig. 3. Comparison of the results by the proposed method with those of the ITC methods and the GDE method in colored noise environment.

Figure 3 shows the comparison of results between the proposed method (GDE-CRSTGBIC method) and the ITC methods based on eigenvalue diagonal loading (BIC, AIC, MDL, KIC), gerschgorin circle method (GDE), in colored noise environment. In Fig. 3 (a), at this time $M/N \ll 1$, the relationship between the number of antennas and that of snapshots meets the requirements of the classical asymptotic system. Under the condition of colored noise, when the SNR is larger than 5dB, the GDE-CRSTGBIC method can accurately estimate the source number with 100% probability, and other methods need larger SNR. In Fig. 3 (b), Fig. 3 (c) and Fig. 3 (d), $\frac{M}{N} \geq 1$, so the relationship between the number of antennas and that of snapshots meets the requirements of general asymptotic regime. Under the condition of colored noise, when the SNRs are larger than 9 dB , 15 dB and 19 dB respectively, the source number can be estimated accurately with 100%

probability by the proposed method, while other methods failed.

Figure 4 shows, when $M = 340, K = 5, N = 300$, that is the relationship between the number of antennas and that of snapshots meets the requirement of the general asymptotic regime. In colored noise, the GDE-CRSTGBIC method can accurately estimate the source number with 100% probability when the SNR is 20dB. Other ITC and GDE methods failed to estimate the source number.

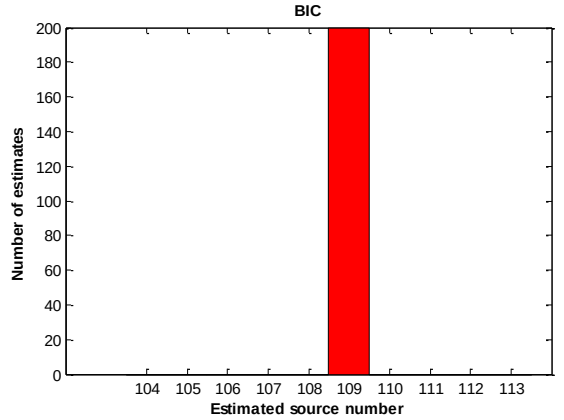

(a)

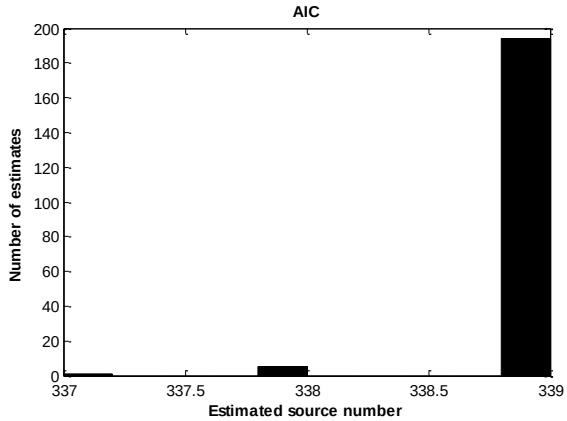

(b)

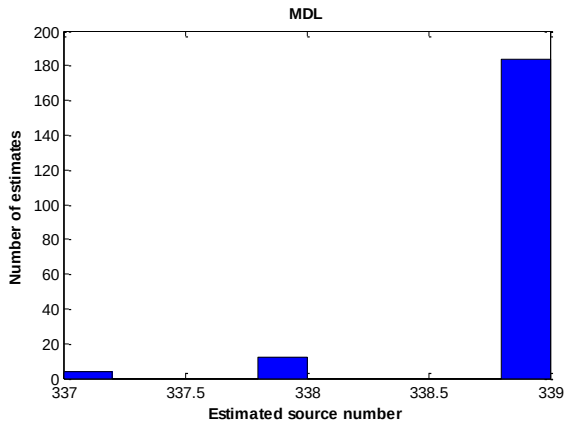

(c)

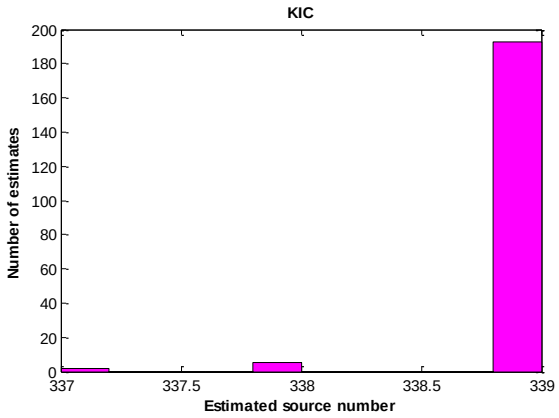

(d)

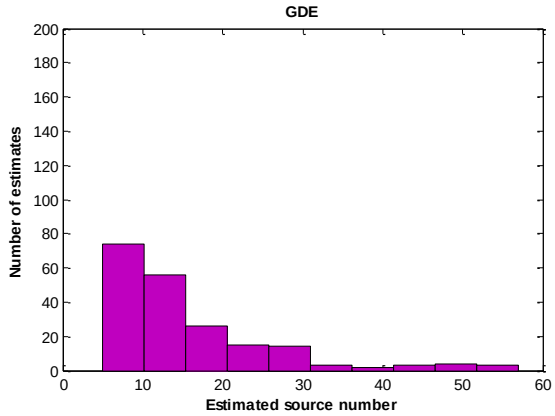

(e)

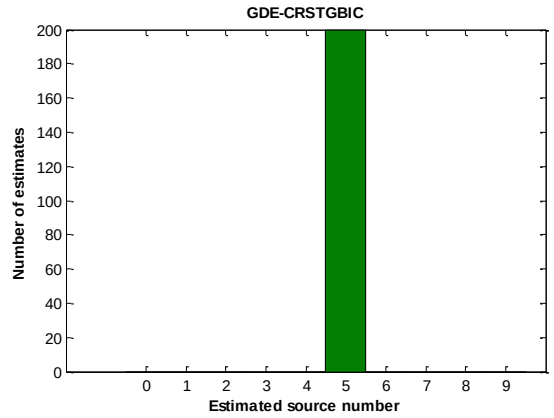

(f)

Fig. 4. Histogram of estimated source number at SNR $=$ 20dB when $M = 340, K = 5, N = 300$.

Experiment 3: Comparison of the results between the proposed method and methods based on random matrix theory (BN-AIC, RMT-AIC, BIC-variant, LS-MDL, CRST-GBIC), in colored noise environment.

The source signals used in this experiment are the same as those in ***Experiment 1***, and the number of source signals is 5. Set different number of the antennas M, mixing matrix $\boldsymbol{A}$ is generated by random function,

sampling frequency is 120MHz, the number of snapshots is N, observed signals are overlapped with spatial color noise, the elements of its covariance matrix are expressed as $n_{ik} = \sigma_n^2 0.9^{|i-k|} \exp[(\mathrm{j}(i\text{-}k)\pi/2)]$, $i,k = 1,2,\cdots,M$. σ_n is used to set the signal-to-noise ratio (SNR) of observed signals, the variation range of SNR is $-10\mathrm{dB}\sim 30\mathrm{dB}$, step size is 2dB, 1000 Monte Carlo simulations are carried out on each SNR. The experimental results are shown in Figs. 5(a)-(d). In addition, when $M = 340, K = 5, N = 300$, the histogram of the estimated source number at SNR $= 20$dB is shown in Figs. 6 (a)-(f).

Figure 5 are the comparison of the results between the proposed method (GDE-CRSTGBIC) and the methods based on random matrix theory (BN-AIC, RMT-AIC, BIC-variant, LS-MDL, CRST-GBIC) in colored noise environment. As can be seen from Fig. 5 (a), at this time $M/N \ll 1$, the relationship between the number of antennas and that of snapshots meets the requirements of the classical asymptotic system. Under the condition of colored noise, the GDE-CRSTGBIC method compared with a variety of source enumeration methods based on random matrix theory, the former can accurately estimate the source number with 100% probability when SNR is larger than 23dB, but the other methods fail. In Fig. 5 (b), Fig. 5 (c) and Fig. 5 (d), $\frac{M}{N} \approx$ or ≥ 1, the relationship between the number of antennas and that of snapshots belongs to the classical asymptotic system. In colored noise, the proposed method can estimate the source number with 100% probability when SNRs are larger than 10dB, 15dB and 13dB respectively, but the estimation of other methods failed.

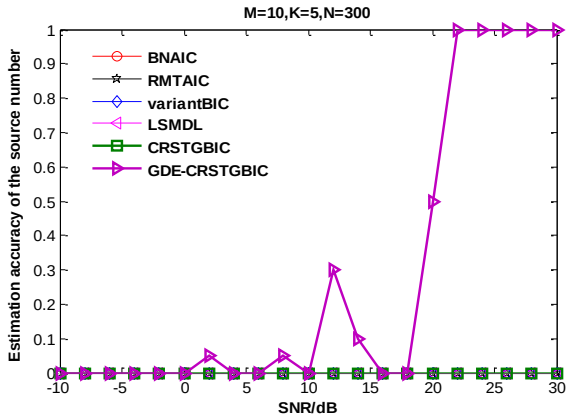

(a)

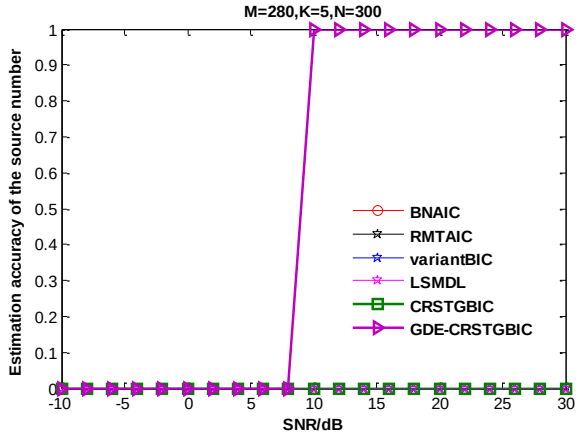

(b)

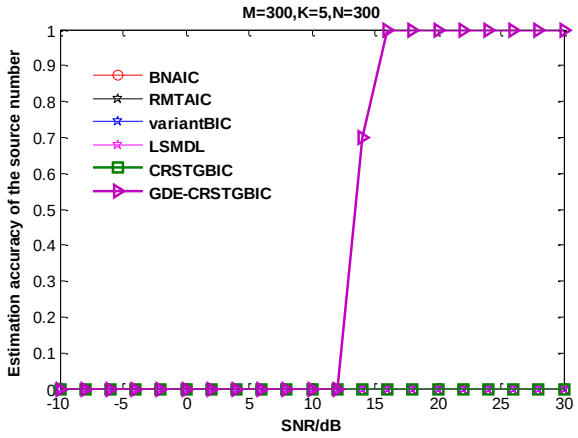

(c)

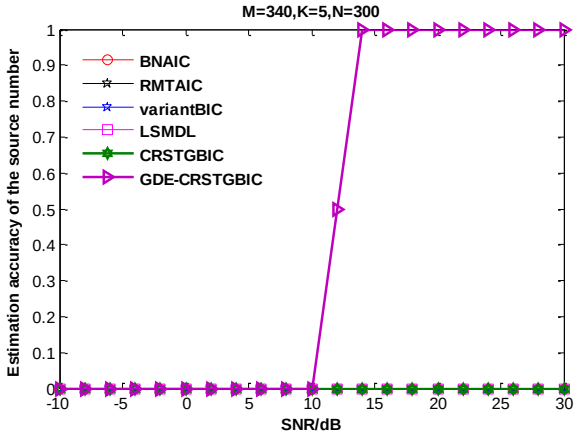

(d)

Fig. 5. Comparison of the results between the proposed method and the methods based on random matrix theory in colored noise environment.

Figure 6 shows, when $M = 340, K = 5, N = 300$, that is the relationship between the number of antennas and that of snapshots meets the requirement of the general asymptotic regime. In colored noise, the GDE-CRSTGBIC method can accurately estimate the source number with 100% probability when the SNR is 20dB. Other RMT methods failed to estimate the source number.

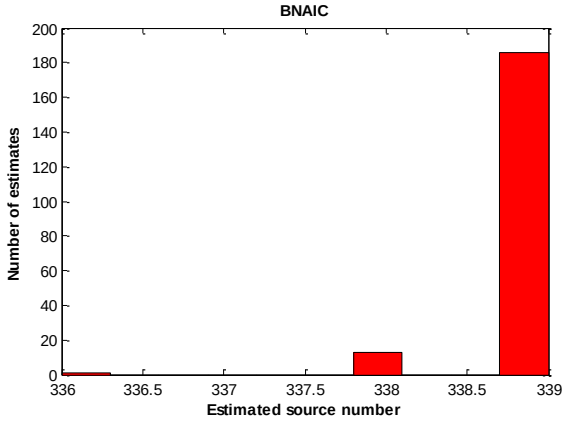

(a)

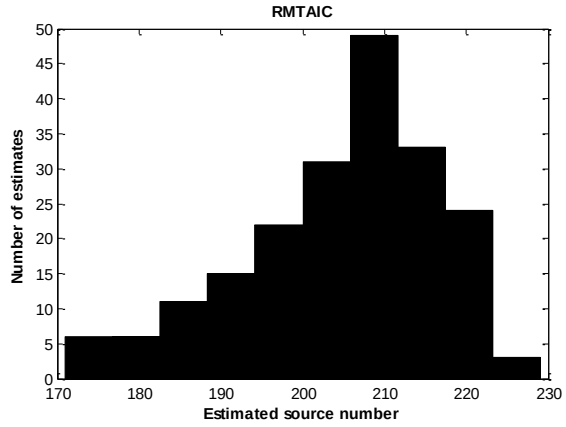

(b)

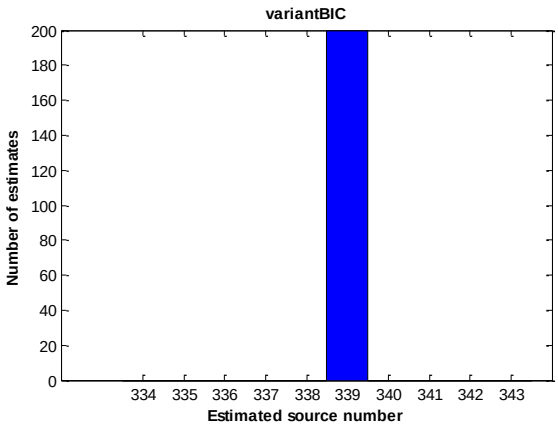

(c)

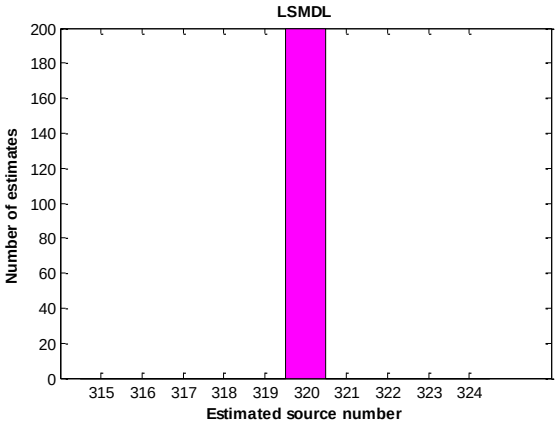

(d)

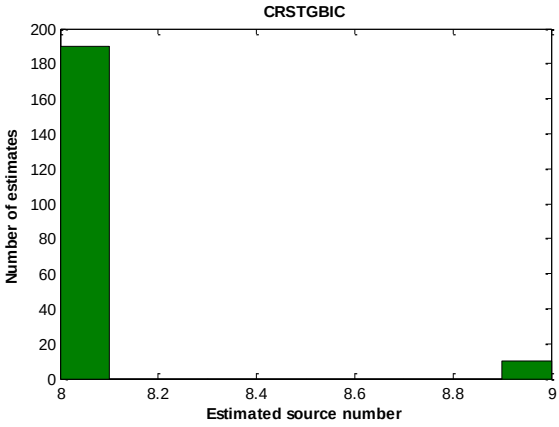

(e)

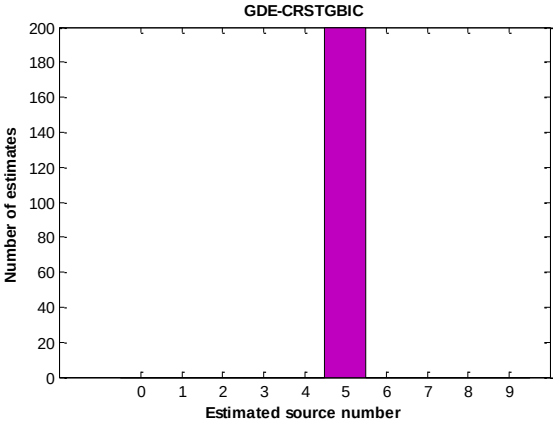

(f)

Fig. 6. Histogram of estimated source number at SNR $=$ 20dB when $M = 340, K = 5, N = 300$.

V. CONCLUSION

A new method is proposed for source enumeration, under the condition that the observed signals are overlapped with spatial colored noise, and the number of

antennas and that of snapshots meet the requirements of general asymptotic regime. The proposed method does not need to presuppose or assume the relationship between the number of antennas and that of snapshots, that is, it is applicable to the classical asymptotic system (the number of antennas is fixed and much smaller than the number of snapshots), and also suitable in a general asymptotic regime (the number of antennas is equal to or larger than that of snapshots). At the same time, the proposed method can be used to estimate the source number not only in the Gaussian white noise environment, but also in the colored noise environment. In view of the lack of source enumeration method in the general asymptotic regime, and the observed signals overlapping with colored noise, an effective approach is provided by us.

ACKNOWLEDGMENT

This research was funded by the National Natural Science Foundation of China (Grant No. 61801480).

REFERENCES

[1] H. Asadi and B. Seyfe, "Signal enumeration in Gaussian and non-Gaussian noise using entropy estimation of eigenvalues," *Digital Signal Process.*, vol. 78, pp. 163-174, Mar. 2018.

[2] M. J. Chen, G. Q. Long, and Z. R. Huang, "Source number estimation in the presence of nonuniform noise," *J. Signal Process.*, vol. 34, no. 2, pp. 134-139, Feb. 2018.

[3] C. C. Wang, Y. H. Zeng, W. H. Fu, and L. D. Wang, "Estimation method for an underdetermined mixing matrix based on maximum density point searching," *J. Xidian University*, vol. 46, no. 1, pp. 106-111, Feb. 2019.

[4] R. Nadakuditi and A. Edelman, "Sample eigenvalue based detection of high-dimensional signals in white noise using relatively few samples," *IEEE Trans. Signal Process.*, vol. 56, no. 7, pp. 2625-2638, July 2008.

[5] B. Nadler, "Nonparametric detection of signals by information theoretic criteria: performance analysis and an improved estimator," *IEEE Trans. Signal Process.*, vol. 58, no. 5, pp. 2746-2756, May 2010.

[6] L. Huang, Y. Xiao, K. Liu, H. C. So, and J. K. Zhang, "Bayesian information criterion for source enumeration in large-scale adaptive antenna array," *IEEE Trans. Vehicular Technology*, vol. 65, no. 5, pp. 3018-3032, May 2016.

[7] L. Huang and H.C. So, "Source enumeration via MDL criterion based on linear shrinkage estimation of noise subspace covariance matrix," *IEEE Trans. Signal Process.*, vol. 61, no. 19, pp. 4806-4821, Oct. 2013.

[8] C. C. Wang and R. Jia, "A source signal recovery method for underdetermined blind source separation based on shortest path," *Applied Computational Electromagnetics Society Journal*, vol. 35, no. 4, pp. 406-414, Apr. 2020.

[9] B. Jiang, A. N. Lu, and J. Xu, "An improved signal number estimation method based on information theoretic criteria in array processing," *2019 IEEE 11th International Conference on Communication Software and Networks*, Chongqing, China, pp. 193-197, June 12-June 15, 2019.

[10] P. Cung, J. Bohme, C. Mecklenbrauker, and A. Hero, "Detection of the number of signals using the Benjamini-Hochberg procedure," *IEEE Trans. Signal Process.*, vol. 55, no. 6, pp. 2497-2508, June 2007.

[11] H. Akaike, "A new look at the statistical model identification," *IEEE Trans. Automatic Control*, vol. AC-19(6), pp. 716-723, 1974.

[12] M. Max and T. Kailath, "Detection of signals by information theoretic criteria," *IEEE Trans. Acoustics, Speech and Signal Process.*, vol. 33, no. 2, pp. 387-392, Apr. 1985.

[13] G. Schwarz, "Estimating the dimension of a model," *Annals Statistic*, vol. 6, no. 2, pp. 461-464, 1978.

[14] M. Wax, "Detection and localization of multiple sources via the stochastic signals model," *IEEE Trans. Signal Process.*, vol. 39, no. 11, pp. 2450-2456, Nov. 1991.

[15] S. Valaee and P. Kabal, "An information theoretic approach to source enumeration in array signal processing," *IEEE Trans. Signal Process.*, vol. 52, no. 5, pp. 1171-1178, May 2004.

[16] Y. Xie, K. Xie, and S. L. Xie, "Source number estimation and effective channel order determination based on higher-order tensors," *Circuits, Systems, and Signal Process.*, published online: Apr. 2019.

[17] W. Cheng, Z. S. Zhang, and Z. J. He, "Information criterion-based source enumeration methods with comparison," *J. Xi'an Jiaotong University*, vol. 49, no. 8, pp. 38-44, Aug. 2015.

[18] H. T. Wu, J. F. Yang, and F. K. Chen, "Source number estimators using transformed gerschgorin Radii," *IEEE Trans. Signal Process.*, vol. 43, no. 6, pp. 1325-1333, June 1995.

[19] Q. T. Zhang and K. M. Wong, "Information theoretic criteria for the determination of the number of signals in spatially correlated noise," *IEEE Trans. Signal Process.*, vol. 41, no. 4, pp. 1652-1663, Apr. 1993.

[20] Y. Y. Liu, X. Y. Sun, and G. H. Liu, "Source enumeration in large arrays using corrected Rao's score test and relatively few samples," *2017 25th European Signal Processing Conference (EUSIPCO)*, Kos Kilkis, Greece, pp. 1405-1409, Aug. 28-Sep. 2, 2017.

[21] Z. D. Bai, S. R. Zheng, and D. D. Jiang, *Large Dimensional Statistical Analysis*. Beijing: Higher Education Press, 2012.
[22] Y. Y. Liu, "Applications of large random matrix theory to array signal parameters estimation," Ph.D. dissertation, *Communication Engineering Dep., Jilin Univ.*, Changchun, China, 2017.
[23] D. D. Jiang, "Tests for large-dimensional covariance structure based on Rao's score test," *Journal of Multivariate Analysis*, no. 152, pp. 28-39, Aug. 2016.
[24] Z. H. Lu and A. M. Zoubir, "Generalized Bayesian information criterion for source enumeration in array processing," *IEEE Trans. Signal Process*., vol. 61, no. 6, pp. 1470-1480, Mar. 2013.

Chuanchuan Wang received the B.A., M. S. and Ph.D. degrees from Shi Jia Zhuang, Mechanical Engineering College, China, in 2007, 2009, and 2013, respectively.

Since 2014, he has been a Research Assistant with the State Key Laboratory of Complex Electromagnetic Environment Effects on Electronics and Information System. He is the author of more than 40 articles, and co-authored 21 inventions. His research interests include blind signal processing and effectiveness evaluation theory.

Yonghu Zeng received the B.S., M.S. and Ph.D. degrees from National University of Defense Technology of China, in 1994, 1997, and 2004 respectively. Since 2012, he has been a Researcher with the State Key Laboratory of Complex Electromagnetic Environment Effects on Electronics and Information System. He has co-authored more than 60 articles, 6 books, and 26 inventions.

His research interests include radar signal processing and effectiveness evaluation theory.

Liandong Wang received the B.S., M.S. and Ph.D. degrees from National University of Defense Technology of China, in 1989, 1993, and 2000 respectively. Since 2012, he has been a Researcher with the State Key Laboratory of Complex Electromagnetic Environment Effects on Electronics and Information System. He has co-authored more than 100 articles, 10 books, and 30 inventions.

His research interests include radar signal processing, electromagnetic environment effects and effectiveness evaluation theory.

Performance of MATLAB and Python for Computational Electromagnetic Problems

Alec J. Weiss and Atef Z. Elsherbeni

Department of Electrical Engineering
Colorado School of Mines, Golden, Colorado, 80120, United States
aweiss@mines.edu, aelsherb@mines.edu

Abstract ─ MATLAB and Python are two common programming languages commonly used in computational electromagnetics. Both provide simple syntax and debugging tools to make even complicated tasks relatively simple. This paper studies how these programming languages compare in throughput for a variety of tasks when utilizing complex numbers which are common in electromagnetics applications. The compared tasks include basic operations like addition, subtraction, multiplication, and division, along with more complex operations like exponentiation, summation, Fourier transforms, and matrix solving. Each of these tests is performed for both single and double precision on the CPU. A 2D finite difference frequency domain problem and a planar array beamforming problem are also presented for comparison of throughput for realistic simulations.

Index Terms ─ Computational electromagnetics, MATLAB, python.

I. INTRODUCTION

Programming languages such as Python and MATLAB are popular in computational electromagnetics. They provide abstract constructs when compared to lower level compiled programming languages such as C/C++ and FORTRAN. Both Python and MATLAB provide platforms for quickly developing and testing a variety computational electromagnetics (CEM) problems. MATLAB and Python provide optimized libraries that can be leveraged to create computationally efficient programs with a minimal amount of programming. This environment is ideal for the testing of new technologies because users can quickly prototype ideas without worrying about memory management and data types.

A. Current work

Speeds between MATLAB and Python have been previously compared for areas of scientific computing. [1] provided some benchmark tests to compare runtimes on a number of linear algebra routines for real numbers in both Python and MATLAB while articles like [2] and [3] have covered general usage of Python as an alternative to MATLAB for scientific computing. Even further, [4] investigates and discusses the usage of Python for computational electromagnetics (CEM). A vast amount of research has looked specifically on the usage of MATLAB for CEM for general applications like [5] and for more application specific acceleration like in [6].

Unlike MATLAB, Python is a free and open source programming language that is community supported. Python and many scientific computing libraries can be downloaded as a single package like Anaconda [7]. The Anaconda package also includes integrated development environments (IDEs) like Spyder [8] to provide an experience similar to that of working in MATLAB's IDE. For those who are not familiar with Python syntax, there exists many free resources to help learn the intricacies of the programming language and help quickly get a user started. Some resources like [9] even provide direct command translations from MATLAB to Python allowing those familiar with MATLAB to learn how to use numerical libraries in Python even faster.

While MATLAB and Python have both been studied and utilized for a variety of electromagnetic problems, MATLAB still dominates this area of research. *IEEEXplore* has about 3,000 paper matches for the keyword *Python* and over 56,000 for the keyword *MATLAB*. Here we will take an in depth look at how Python matches up as a competitor to MATLAB specifically in CEM problems.

B. Comparison for scientific computing

CEM problems commonly deal in double and single precision complex numbers. To the knowledge of the authors, comparisons of MATLAB and Python for computation using complex numbers has not previously been investigated. Because CEM problems vary so widely in application and implementation, a generic approach to comparison of speeds between MATLAB and Python was taken. For this approach, a large variety of math operations were tested that gradually increase in complexity. These operations are the building blocks for many CEM problems and can be used to estimate the

Submitted On: April 2, 2020
Accepted On: May 21, 2020

relative runtimes between programming languages.

Basic operations (e.g., add, subtract, multiply, divide) are first tested to provide a good baseline for elementary math operations performed on complex numbers. This is then stepped up to include more complex operations like exponentiation, summation, and a combination of elementary operations (specifically $c = a + b * exp(a)$). Past this, matrix operations such as matrix-matrix multiplication and LU decomposition are performed, along with solving of both dense and sparse systems of linear equations. With runtime comparisons for basic operations, relative runtimes can then be estimated for more realistic CEM problems. To test these runtimes, a realistic finite difference frequency domain (FDFD) problem and a beamforming simulation written in both MATLAB and Python were compared.

II. MATLAB AND PYTHON FOR CEM

As previously mentioned, both MATLAB and Python have been used on a variety of applications. Both provide a large range of pre-written optimized functions that the users do not need to rewrite from scratch. In many cases for linear algebra operations, Python and MATLAB can both be configured to use the Intel Math Kernel Library (MKL) [10]. This library provides highly optimized basic linear algebra subprograms (BLAS) and linear algebra package (LAPACK) library for common linear algebra problems. With both programming languages using these subroutines, many linear algebra operations utilize the same precompiled code and therefore would be expected have near identical runtimes.

A. MATLAB

MATLAB arguably provides an easier and more beginner friendly approach for people not experienced in programming. This is because MATLAB does not typically require external libraries. This means that all commands that need to be used in MATLAB are either available from the core installation, or a toolbox. Once a toolbox is installed, the commands from that toolbox are always available to the user. MATLAB also is built specifically for matrix operations. This means that for many CEM applications, the code will be optimized and require less verbose syntax than its Python counterpart.

B. Python

Unlike MATLAB, Python requires libraries to be imported for a variety of tasks. While this provides an extra step by calling the *import* command in Python, it increases the flexibility of the programming language by allowing the user to easily include third party packages without the concern of overlapping function and class names.

While a vast number of Python libraries exist online, three well developed libraries are utilized in this paper. These are *NumPy*, *SciPy*, and *Numba*. These three libraries cover most of the core functionality that MATLAB contains and can therefore be used to solve many CEM problems. *NumPy* and *SciPy* provide functionality such as array and matrix operations, along with access to linear algebra subroutines found in the compiled BLAS backend. *Numba* provides an additional layer of acceleration for Python allowing vector operations to be partially compiled and run around the typical Python interpreter.

C. Further acceleration

Beyond using prebuilt libraries, MATLAB and Python both provide further acceleration capabilities. Both can access functions written and compiled from C/C++ and FORTRAN. In MATLAB, mex file wrappers are written to take MATLAB data types and pass them to these lower level functions. Python on the other hand can typically directly call these compiled functions. This is because at its core, Python typically uses a runtime built in the C programming language. Integration with lower level libraries can therefore be done through a Cython interface, or by loading the functions as a shared library through the ctypes interface.

Python code can also be compiled to native machine code with Cython. This allows users to include additional keywords to specify information such as data types and sizes. This additional information information allows the Cython compiler to optimize the compiled code to provide further acceleration over equivalent native Python code.

While it is important to know these low-level interfaces exist, prototype code will typically be written directly in Python or MATLAB and therefore these interfaces are not quantitatively compared in this paper.

III. MEASUREMENT OF COMPUTATIONAL SPEEDS IN PYTHON AND MATLAB

A. Accurate timing of code

Both MATLAB and Python provide methods to perform some timing analysis on different code snippets with tic()/toc() in MATLAB and timeit() in Python. Extensions of both of these functions were written with new *OperationTimer* classes. The version of this class in MATLAB and Python leveraged the existing timing capabilities but extended upon them to provide more in-depth timing statistics. These classes provided the user with an adjustable number of repeat measurements. In most cases 100 repeat measurements were made.

Repeat measurements are vital as they allow the generation of uncertainty bounds on the data. Bounding the uncertainties of the runtimes helps remove any outliers that may occur due to system inconsistencies (such as operating system scheduling). These uncertainties also provide insight into how variable these runtimes may be over multiple uses. In the case of this paper, these uncertainties were generated as the standard

deviation of the repeat measurements.

Along with producing repeat measurements, the *OperationTimer* classes had several other features. This included allowing the user to run a sweep of input data which in turn allowed the testing of runtimes as a function of element count for each operation. Functionality for generating statistics on the data was also included in each class. These classes also provided a consistent interface and data format between both MATLAB and Python to ensure consistency in the post-processing of the results.

B. Testing the functions

With a consistent class for timing of the code in both MATLAB and Python, each of the functions to be compared could then be tested. MATLAB and Python scripts were created that pass the function handles for each operation to test to the *OperationTimer* class. These scripts also set up parameters such as the number of repeat measurements and the sweep dimensions to run for each function. With the scripts set up, each function could then be timed and compared.

IV. CPU RESULTS

CPU results were obtained for the aforementioned operations on an AMD Threadripper 2990WX 32 Core processors with 64 logical processors and 128 GB of RAM. These results were obtained using MATLAB R2018a and Python 3.7 with NumPy 1.17.4, SciPy 1.3.2, and Numba 0.46. Each of the tests was run for both single and double precision complex data. Uncertainty bars were generated using the standard deviation of each of the recorded times.

A. Basic operations

The first set of results were basic add, subtract, multiply, and divide. Each of these operations was repeated 100 times for arrays with a number of elements ranging from 1 all the way to 100 million. The addition operation can be seen in Fig. 1, subtraction in Fig. 2, multiplication in Fig. 3, and division in Fig. 4.

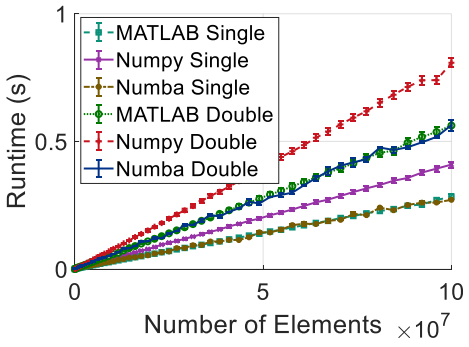

Fig. 1. Runtime vs. number of elements for addition with single and double precision using MATLAB, NumPy, and Numba.

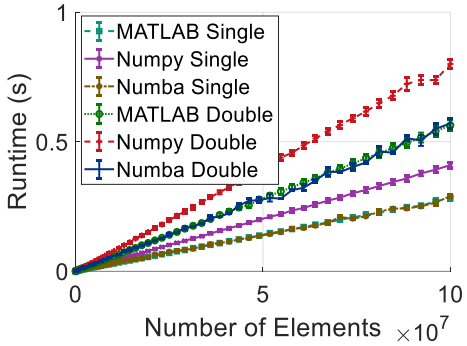

Fig. 2. Runtime vs. number of elements for subtraction with single and double precision using MATLAB, NumPy, and Numba.

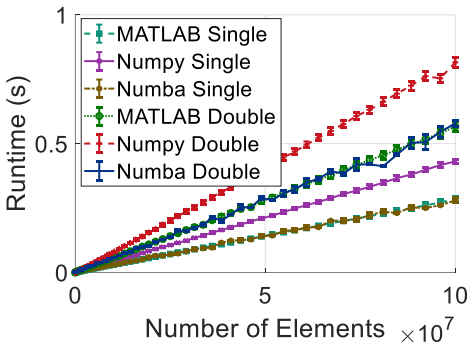

Fig. 3. Runtime vs. number of elements for multiplication with single and double precision using MATLAB, NumPy, and Numba.

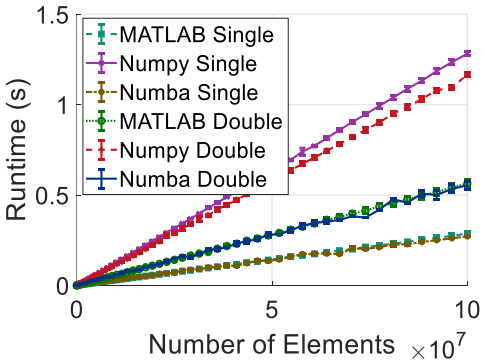

Fig. 4. Runtime vs. number of elements for division with single and double precision using MATLAB, NumPy and Numba.

In each of these cases, both single and double precision for MATLAB and the Python Numba library have almost identical computation time. Numba performs just in time (JIT) compilation of the code to approach speeds of programming languages like C and FORTRAN. MATLAB also reaches these same speeds without any special operations. NumPy on the other hand is much

slower with each of these operations. This is most likely because there are number of abstracted steps and calls to the Python interpreter that must be performed on top of the typical computation, causing a slowdown. It is also important to note that both Numba and MATLAB provide a form of parallelization almost no user input (the 'parallel' keyword must be specified for Numba). Depending on the size of the dataset, this also will factor into the speedup of MATLAB and Numba over the Numpy Library.

B. Extended operations

Extended Operations were then tested including exponentiation, a combination of basic operations ($c = a + b * e^a$), summation, and the fast fourier transform (FFT). Each of these operations was again run 100 times for a variety of different numbers of elements. All operations except the FFT were run with sizes from 1 to 100 million elements while the FFT was run on arrays of size 1 to 5 million elements. The timed result comparisons of exponentiation and combined operations can be seen in Fig. 5 and Fig. 6 with the sum and FFT seen in Fig. 7 and Fig. 8.

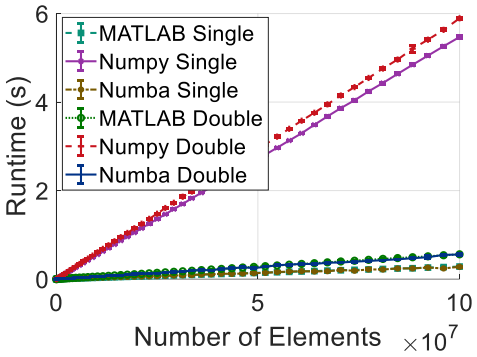

Fig. 5. Runtime vs. number of elements for exponentiation with single and double precision using MATLAB, NumPy, and Numba.

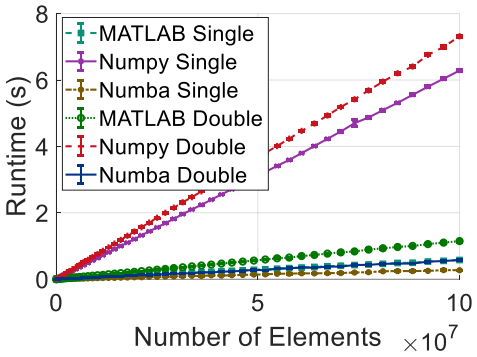

Fig. 6. Runtime vs. number of elements for combined $a + b * exp(a)$ with single and double precision using MATLAB, NumPy, and Numba.

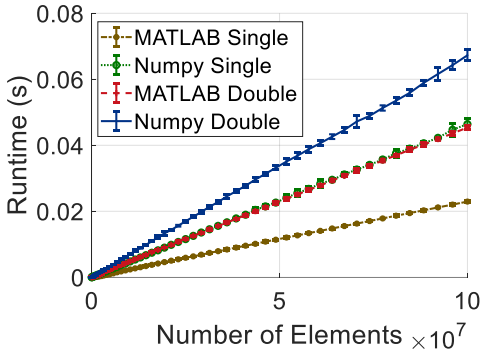

Fig. 7. Runtime vs. number of elements for summation with single and double precision using MATLAB and NumPy.

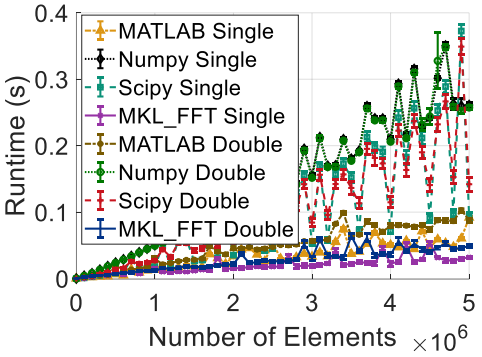

Fig. 8. Runtime vs. number of elements for fft(a) with single and double precision using MATLAB, NumPy, SciPy, and MKL_FFT.

Again, we can see that for exponentiation, MATLAB and Python using Numba provide near identical run times while NumPy proves much slower than the other two. Surprisingly, for the combined operation, Numba outperformed MATLAB for both double and single precision operations. This is most likely because the compiled Numba function does not interact with the Python interpreter, whereas the MATLAB code must return control to its interpreter between each operation. MATLAB again outperforms NumPy in all cases. The FFT operations exemplifies the usage of other libraries in Python, which can be both a strength and weakness. NumPy and SciPy have their own FFT functions while another library called MKL_FFT has yet another implementation. While this increases the difficulty for the user to know exactly what function to use, quick web searches can help find application specific Python libraries that may be faster than those used in MATLAB. It can be seen that while SciPy and NumPy are slower than MATLAB, the MKL_FFT library outperforms MATLAB in terms of speed when performing *fft(a)*.The open source nature also allows the slower libraries to implement parts of the

faster ones. In the future, SciPy plans to directly integrate MKL_FFT [11].

C. Matrix operations

The final set of basic operations performed were a set of common linear algebra matrix routines. These routines included matrix-matrix multiplication and LU decomposition along with solving of both dense and sparse linear equations. Matrix multiplication, LU decomposition, and dense matrix solving are all called from the underlying MKL BLAS library and therefore would be expected to perform the same between MATLAB and Python. In Python, the MKL library is used through an interface provided by the NumPy library. The runtime comparisons for matrix multiplication, LU decomposition, and dense matrix solving can be seen in Fig. 9, Fig. 10, and Fig. 11 respectively. As expected, both MATLAB and Python run at almost the exact same speeds for these three operations. In most cases and for most sizes, the runtimes even lie within the uncertainty bounds of one another.

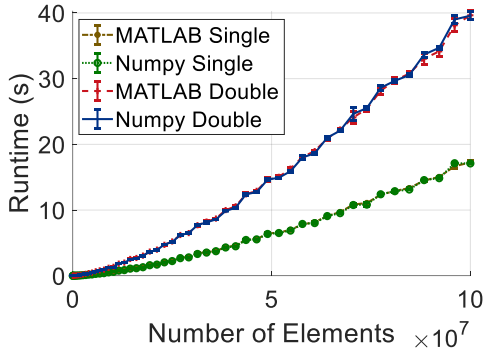

Fig. 9. Runtime vs. number of elements for matrix multiplication with single and double precision using MATLAB and NumPy/SciPy.

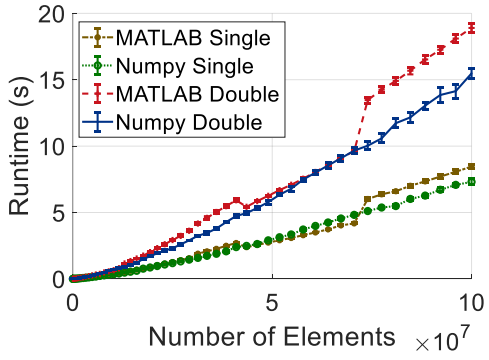

Fig. 10. Runtime vs. number of elements for LU decomposition with single and double precision using MATLAB and NumPy/SciPy.

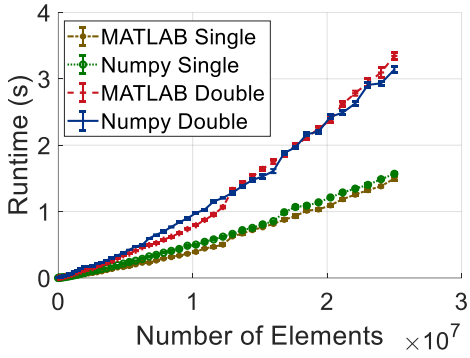

Fig. 11. Runtime vs. number of elements for dense linear equation solving with single and double precision using MATLAB and NumPy/SciPy.

The sparse solving did not fall under the BLAS libraries and therefore there were no expectations for runtime comparisons. MATLAB does not support single precision sparse matrices and therefore only times for double precision for MATLAB are provided. Figure 12 shows the runtimes for a variety of different sizes of sparse matrices. From this plot it can clearly be seen that MATLAB drastically outperforms Python for sparse matrix solving.

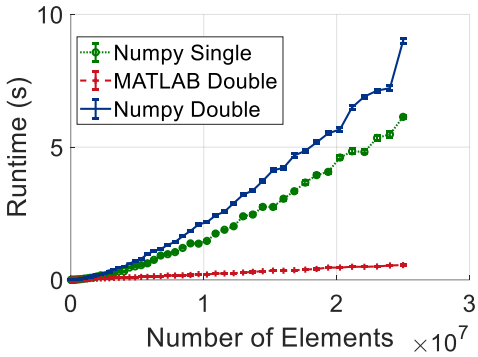

Fig. 12. Runtime vs. number of elements for sparse linear equation solving with single and double precision using MATLAB and NumPy/SciPy.

D. Finite difference frequency domain simulation

While the basic operations tested provide a good basis set of data for runtime comparison between MATLAB and Python, a real FDFD simulation was implemented and the runtimes compared. The FDFD simulation performed calculates the scattering from a 2D cylinder. Because FDFD relies on solving a sparse set of linear equations, it is expected that MATLAB will drastically outperform the runtime of Python because of the runtime comparison of sparse equation solving. The magnitude of the total electric field produced by this

simulation can be seen in Fig. 13. These results were produced and verified by both a MATLAB and Python code. The number of cells in the x and y directions were then swept to compare runtimes of the simulations. The runtime as a function of the total number of elements ($cells_x * cells_y$) was then plotted. The runtime comparisons for both single and double precision are given in Fig. 14. Again, MATLAB is not capable of single precision sparse datatypes and therefore this metric is not included.

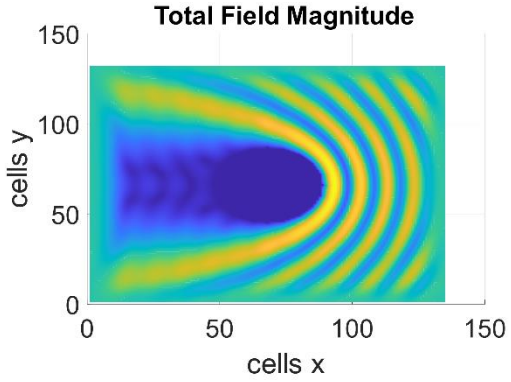

Fig. 13. Total electric field from FDFD scattering from a cylinder problem.

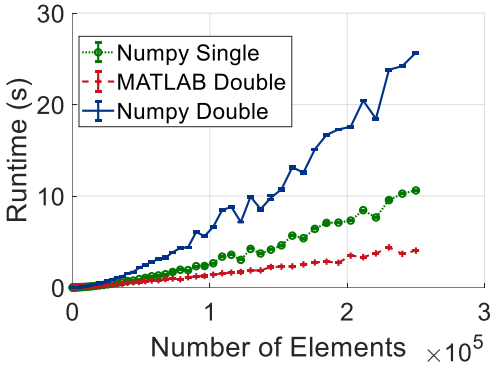

Fig. 14. Runtime vs. number of elements for an FDFD simulation with single and double precision using MATLAB and NumPy/SciPy.

As expected, this data shows that MATLAB drastically outperforms even the single precision version of Python. MATLAB also seems to exhibit a linear increase in runtime ($O(n)$) as the number of cells are increased whereas NumPy exhibits a squared ($O(n^2)$) runtime increase. Because of this it is assumed that for much larger domains, Python FDFD simulations will only become slower compared to MATLAB.

E. Beamforming angle of arrival estimation

A final test was performed with a basic angle of arrival beamforming algorithm. For this test, a large 35 by 35 element antenna array is simulated. An incident plane wave is simulated at a $\pi/4$ radians azimuthal angle and $\pi/4$ radians elevation angle. The output of the beamformed data can be seen in Fig. 15. Beamforming was then performed and times recorded for an increasing number of steering angles. It is expected that because beamforming consists of matrix multiplication and combined elementary operations that Python would outperform MATLAB in this task. The speeds in both MATLAB and Python for a varying number of angles can be seen in Fig. 16.

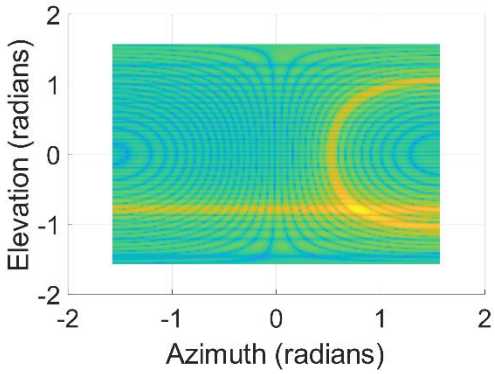

Fig. 15. Beamformed values between -pi/2 and pi/2 radians with 181 calculated angles with an incident plane wave at pi/4 and -pi/4 azimuth and elevation.

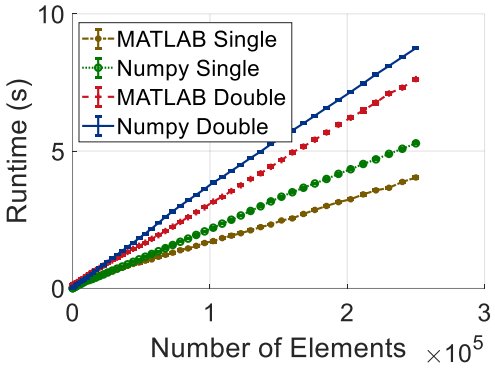

Fig. 16. Runtime vs. number of elements for an antenna array beamforming simulation with single and double precision using MATLAB and NumPy.

Surprisingly, MATLAB still outperformed the Python implementation in this scenario for more than about 20,000 elements. The simulations included setup and array allocation in the timing which may have played a role in the unexpected result. While this is true for large sizes, many times beamforming simulations may be interested in a smaller number of angles and for these cases, Python outperforms MATLAB.

V. CONCLUSION

Although MATLAB is faster for many complex number-based calculations and simulations, other factors come into play when choosing a programming language. For the highest possible speeds in simulations, compiled code written in C or FORTRAN will be the fastest choice. As mentioned earlier, while MATLAB provides accessibility to these lower level functions, Python provides great tools for this integration with ctypes and Cython. Python can also provide acceleration through direct compilation with Cython.

While they were the focus of this paper, runtimes are not the only thing to focus on in a programming language. Python provides a free alternative with many community supported libraries for a variety of different scientific and non-scientific applications. These libraries extend the capabilities of Python to provide everything from easy documentation with sphinx or pydoc, to control of instruments using the pyvisa, pyserial, and socket libraries. While all of these capabilities exist within MATLAB, they typically come as an additional cost in a MATLAB toolbox.

While all of these factors should be taken into consideration before deciding on a programming language, MATLAB clearly outperforms Python in the majority of complex math operations and all CEM simulations tested. That being said, Python can provide a well-supported alternative to MATLAB for usage in CEM problems.

REFERENCES

[1] J. Unpingco, "Some comparative benchmarks for linear algebra computations in Matlab and Scientific Python," in *2008 DoD HPCMP Users Group Conference*, pp. 503-505, 2008. doi: 10.1109/DoD.HPCMP.UGC.2008.49.

[2] R. Python, "MATLAB vs Python: Why and how to make the switch – Real Python," [Online]. Available: https://realpython.com/matlab-vs-python/. [Accessed: 30-Dec-2019].

[3] J. Ranjani, A. Sheela, and K. P. Meena, "Combination of NumPy, SciPy and Matplotlib/ Pylab - A good alternative methodology to MATLAB - A comparative analysis," in *2019 1st International Conference on Innovations in Information and Communication Technology (ICIICT)*, pp. 1-5, 2019 doi: 10.1109/ICIICT1.2019.8741475.

[4] N. Kinayman, "Python for microwave and RF engineers [Application Notes]," *IEEE Microwave Magazine*, vol. 12, no. 7, pp. 113-122, Dec. 2011. doi: 10.1109/MMM.2011.942704.

[5] M. Capek, P. Hazdra, J. Eichler, P. Hamouz, and M. Mazanek, "Acceleration techniques in Matlab for EM community," in *2013 7th European Conference on Antennas and Propagation (EuCAP)*, pp. 2639-2642, 2013.

[6] A. J. Weiss, A. Z. Elsherbeni, V. Demir, and M. F. Hadi, "Using MATLAB's parallel processing toolbox for multi-CPU and multi-GPU accelerated FDTD simulations," vol. 34, no. 5, p. 7, 2019.

[7] "Anaconda | The world's most popular data science platform," *Anaconda*. [Online]. Available: https://www.anaconda.com/. [Accessed: 14-Jan-2020].

[8] "Spyder Website." [Online]. Available: https://www.spyder-ide.org/. [Accessed: 14-Jan-2020].

[9] V. Gundersen, "NumPy for MATLAB users." 2006.

[10] ajolleyx, "Intel® Math Kernel Library (Intel® MKL)," 00:00:14 UTC. [Online]. Available: https://software.intel.com/en-us/mkl. [Accessed: 13-Jan-2020].

[11] "SciPy Roadmap — SciPy v1.4.1 Reference Guide." [Online]. Available: https://docs.scipy.org/doc/scipy/reference/roadmap.html. [Accessed: 16-Jan-2020].

Alec J. Weiss received his B.S. degree in Electrical and Computer Engineering from the University of Colorado, Boulder, Colorado, USA in 2017 and his M.S. in Electrical Engineering from the Colorado School of Mines, Golden, Colorado, USA in 2018 where he is currently pursuing his Ph.D. in Electrical Engineering. He joined the National Institute of Standards and Technology (NIST) Communications Technology Laboratory (CTL) in 2017 as a graduate student researcher. His research interests include millimeter-wave measurements, 5G communications systems, and high performance computing for electromagnetic applications.

Atef Z. Elsherbeni received an honor B.Sc. degree in Electronics and Communications, an honor B.Sc. degree in Applied Physics, and an M.Eng. degree in Electrical Engineering, all from Cairo University, Cairo, Egypt, in 1976, 1979, and 1982, respectively, and a Ph.D. degree in Electrical Engineering from Manitoba University, Winnipeg, Manitoba, Canada, in 1987. He started his engineering career as a part time Software and System Design Engineer from March 1980 to December 1982 at the Automated Data System Center, Cairo, Egypt. From January to August 1987, he was a Post-Doctoral Fellow at Manitoba University. Elsherbeni joined the faculty at the University of Mississippi in

August 1987 as an Assistant Professor of Electrical Engineering. He advanced to the rank of Associate Professor in July 1991, and to the rank of Professor in July 1997. He was the Associate Dean of the College of Engineering for Research and Graduate Programs from July 2009 to July 2013 at the University of Mississippi. He then joined the Electrical Engineering and Computer Science (EECS) Department at Colorado School of Mines in August 2013 as the Dobelman Distinguished Chair Professor. He was appointed the Interim Department Head for (EECS) from 2015 to 2016 and from 2016 to 2018 he was the Electrical Engineering Department Head. In 2009 he was selected as Finland Distinguished Professor by the Academy of Finland and TEKES. Elsherbeni is a Fellow member of IEEE and ACES. He is the Editor-in-Chief for ACES Journal, and a past Associate Editor to the Radio Science Journal. He was the Chair of the Engineering and Physics Division of the Mississippi Academy of Science, the Chair of the Educational Activity Committee for IEEE Region 3 Section, the General Chair for the 2014 APS-URSI Symposium, the president of ACES Society from 2013 to 2015, and the IEEE Antennas and Propagation Society (APS) Distinguished Lecturer for 2020-2022.

Design Optimization of a Dual-band Microstrip SIW Antenna using Differential Evolutionary Algorithm for X and K-Band Radar Applications

Aysu Belen [1], Filiz Güneş [1], and Peyman Mahouti [2]

[1] Department of Electronics and Communication Engineering
University of Yıldız Technical, Istanbul, TURKEY
aysu.yldrm07@gmail.com, gunes@yildiz.edu.tr

[2] Department of Electronic and Automation,
Istanbul Cerrahpaşa University, Istanbul/TURKEY
pmahouti@istanbul.edu.tr

Abstract ─ In this work, design optimization and fabrication of a high performance microstrip dual-band antenna are presented using Substrate Integrated Waveguide (SIW) technology with Roger 4350 (ε_r=3.48 and h=1.52mm). Firstly, the SIW antenna design is considered as a multi-objective multi-dimensional optimization problem for a simple microstrip geometry and its geometrical parameters are optimized efficiently using Differential Evolutionary Algorithm (DEA) in the 3D CST Microwave studio environment based on the gain and return loss characteristics at 12 GHz and 24 GHz. In the second step, for justification of the proposed design method, the optimally designed dual band microstrip SIW antenna has been prototyped. Furthermore, the experimental results are compared with the performance measures of other counterpart designs in literature. Thus, based on the obtained results and comparisons, it can be concluded that the proposed microstrip SIW antenna model and its optimization procedure, is a sufficient and low-cost solution for X and K band radar applications.

Index Terms ─ Differential evolutionary algorithm, dual band, microstrip, optimization, substrate integrated waveguide.

I. INTRODUCTION

Substrate-Integrated Waveguide (SIW) is a novel and efficient solution counterpart of the traditionally waveguide designs [1-3]. Since a SIW structure can easily realized on a planar substrate, its integration with other planar microwave systems is possible. In SIW designs, an equivalent electrical walls that can confined EM waves are created via the use of metallized holes where the top and bottom metal layers of PCB substrate would provide the other sides of the waveguide.

The SIW design is a family member of substrate integrated circuits that include other substrate integrated structures such as substrate integrated image guides and substrate integrated non-radiative dielectric guides [1]. SIW components are popular thanks to being easy to design and realized, and have the combined advantages of planar printed circuits and metallic waveguides. Just like microstrip and coplanar transmission lines, SIW components are compact, flexible, and cost efficient. Furthermore, SIW design also have the advantages of conventional metallic waveguides, such as shielding, low-loss, high quality-factor and high-power handling [1]. In this way, the concept of system in Packet (SiP) can be extended to the System on- Substrate (SoS). SoS represents the ideal platform for developing cost-effective, easy-to-fabricate and high performance mm-wave systems.

Recently, especially antenna designs with SIW technology are becoming a trending topic for novel, high performance, low-cost antenna design [4-10]. Antennas designed with SIW technology have excellent performance due to the ability of suppressing surface wave propagation, wider operation band, decreased end-fire radiation and cross-polarization radiation. Typically, in [4-5], the effect of adding SIW structure to the proposed antenna was presented and gain was measured to be enhanced up to 4 dBi.

In this work, SIW technology is applied to design a microstrip dual-band antenna for X and K band radar applications. An antenna model given in Fig. 1 [5] is considered as an efficient antenna model for the aimed operation frequencies. Roger 4350 (ε_r=3.48) with 1.52mm height is used as a low-cost substrate of the SIW. The design optimization process of the proposed SIW antenna model is achieved via the use of Differential Evolutionary Algorithm (DEA) in 3D CST Microwave studio environment. For this purpose, the microstrip SIW antenna design problem is converted to an optimization problem by defining optimization variables and objectives based on the antenna

Submitted On: December 6, 2019
Accepted On: May 4, 2020

performance criteria such as gain and return loss characteristics. Then, in order to prove the success of the design optimization of SIW antenna, a prototype is built with the optimal design parameters obtained from the DEA process and measured its performance. The measurements verify that the proposed microstrip SIW antenna model is a sufficient solution for X and K band radar applications and the DEA algorithm is an efficient algorithm for design optimization of microstrip SIW antennas.

II. DESIGN OPTIMIZATION OF DUAL BAND MICROSTRIP SIW ANTENNA USING DIFFERENTIAL EVOLUTIONARY ALGORITHM

Meta-heuristic algorithm is an advance procedure to form a heuristic that can find an efficient solution to a given problem, especially in case of problems with incomplete or imperfect information. Examples for these methods are: Methods that inspired from the behavior of animal and microorganism, such as particle swarm optimization, artificial immune systems, and insect colonies like Ant or Bees. Most of the mentioned methods have been utilized in design optimization of microwave device and antennas [11-17].

DEA is a method of multidimensional mathematical optimization which belongs to the class of Evolutionary Algorithm (EA). DEA is originated by Kenneth Price and Rainer M. Storn and first publication of idea of this method was published as a technical report in [18-19].

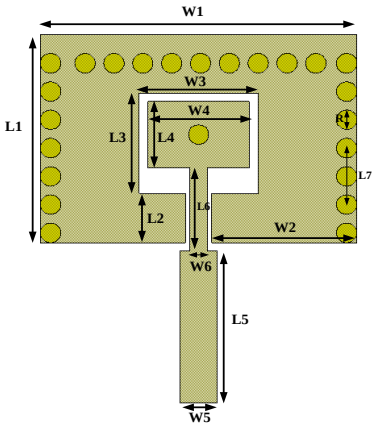

Fig. 1. Parametric layout of SIW antenna.

Roger 4350 (ε_r=3.48) with 1.52mm height is used as substrate of the SIW antenna and the optimization variables are dimensions of the rectangular microstrip patch, feedline size, the total number of metallized via's and their gaps as given with their limitations in Table 1.

The geometrical design parameters can be increased or decreased based on the request of designer, furthermore design parameters such as distance of via's, diameter of via's or other parameters such as dielectric constant or height of substrate can be added. But it should be noted that with the increase in number of optimization variables the search space would become more complex and requires more function evaluations which would drastically decreases the computationally efficiency of the design process. Also it should be taken into consideration that decreasing number of variables might prevent the algorithm to find the optimal solutions in the limited search space.

The flow chart of the optimization process is given in Fig. 2. According to this flow chart, it can be observed the DEA working in MATLAB environment send the optimization parameter values to CST suit environment to start a 3D electromagnetic simulation process. Then the simulation results in CST environment are sent to MATLAB environment in order to evaluate the cost function of the optimization process:

$$\text{Cost}_i = \frac{C_1}{Directivity_i} + \frac{C_2}{\left|S_{11_i}\right|}, \qquad (1)$$

where, C is weighted constrained determined by user (Here in C_1=0.9, C_2= 0.3 which is determined with trial and error method), both S_{11} and directivity are only taken into account at the requested operation frequencies, 12 and 24 GHz; ***i*** is the index of the current member of DEA population. The performance results are obtained after 10 independent runs of the optimization process and the specification criteria of the objective function are:

$$S_{11}dB \le -10 \qquad f = 10GHz\ and\ 24GHz\ , \qquad (2)$$

$$Max(Directivity) \qquad f = 10\text{GHz and } 24\text{GHz}\ . \qquad (3)$$

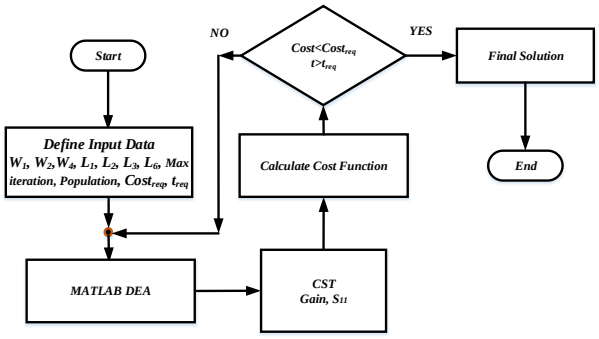

Fig. 2. Flow chart of the SIW antenna design optimization.

In Tables 2-3, the performance results of DEA algorithm for 10 different runs are presented. In Table 2, the best, worst and mean performance results of DEA for these 10 runs are given. As it can be observed, when the population size is taken as 20, the optimization process cannot converge to the required cost value and are trapped in a local minima in the search domain. However when the population size is increased the overall performance of the DEA is also increased. However it

should be noted that although the increased number of population might also increases the performance it also would decrease the computationally efficiency of the whole process. This can be observed from Tables 2 and 3, where the minimal cost value obtained from run with 30 population size is reached to the value of 0.307 the run with 50 population size had achieved 0.278. However, even though the mean performance result of 50 population run is much better than the run with 30 population, the required function evaluation for 50 population is much higher than 30 populated run which will drastically decreases the computational efficiency of optimization process.

Table 1: Constraints of the variables in (mm)

Parameter	Constraint	Parameter	Constraint
W_1	10~20	L_1	5~15
W_2	1~10	L_2	1~10
W_4	1~10	L_3	1~10
		L_6	1~10

Table 2: Performance results of DEA*

Population	Cost		
	Maximum	Minimum	Mean
20	7.54	2.54	3.88
30	2.26	0.307	0.916
50	1.34	0.278	0.613

*Mean results obtained from 10 different runs at 20 iteration.

Table 3: Number of function evaluations of DEA*

Population	Iteration			
	5	10	15	20
20	107	198	289	380
30	161	297	433	570
50	268	495	722	950

*Mean results obtained from 10 different runs.

Table 4: Optimal parameter list in (mm)

W_1	15.4	L_1	10.7
W_2	7	L_2	2.5
W_3	5.75	L_3	5.1
W_4	4.95	L_4	3.4
W_5	$2xW_6$	L_5	7.8
W_6	0.85	L_6	4.2
R	0.8	L_7	3.35

The parameters given in Table 4 are obtained via DEA with 50 population size after a 20 iteration where the minimal cost was found as 0.278 with respect to the limitations given in Table 1 and Eq. 1.

The simulated and measured results of the prototyped SIW antenna design (Fig. 3) are presented in Figs. 4-6. The measurement results are obtained using the measurement setup given [20]. The simulated radiation pattern of the optimally designed SIW antenna are given in Fig. 4 where the designed antenna achieves a simulated gain level of 7 and 7.13 dBi at 12 and 24 GHz respectively.

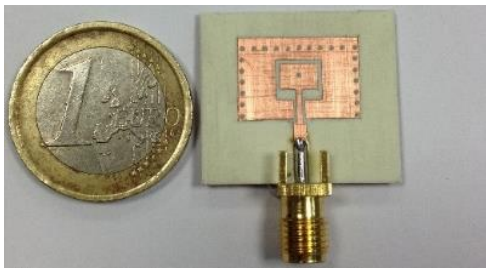

Fig. 3. Fabricated antenna.

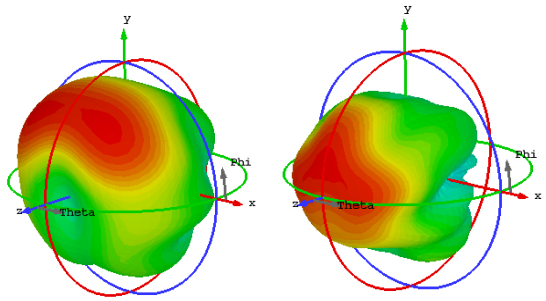

(a) (b)

Fig. 4. Simulated gain patterns (a) 12GHz and (b) 24 GHz.

For further investigation of the effect of SIW structure on the performance results of antenna designs two additionally simulation cases had been added. (i) An antenna design similar in Fig. 1 which does not have any SIW structure with the same geometrical design parameters in Table 4 (NO SIW design), (ii) the same No SIW antenna design that is optimized via the DEA (NO SIW OPT). In Fig. 5, the simulated performance of antenna design with and without SIW structure had been presented alongside of both simulated and measured performance of the optimally design SIW antenna. Here it should be noted that optimized antenna not only is have resonance frequency in 12 and 24 GHz but also is resonated in middle frequencies. This can be prevented by simply adding these frequencies to the cost function or it is also possible to make the antenna has better performance measures in these frequencies by adding them to the cost function. However in this work simply only performance measures at 12 and 24 GHz are provided to the cost function and optimization process for design optimization of a dual band antenna.

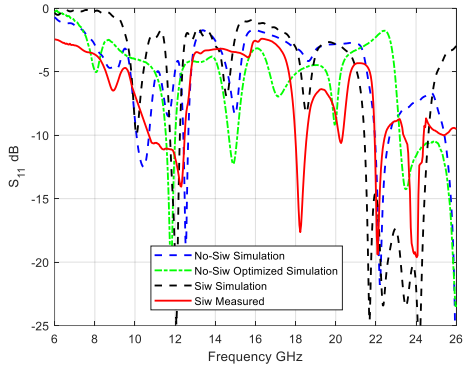

Fig. 5. Simulated and measured return losses.

In Table 5 and Fig. 6, the simulated and measured gain performance results of the antenna designs are presented. As it can be seen, the best gain performance results obtained from the design without SIW structure, even though an optimization process is applied, is around 6 dB for the selected operation frequencies while after the application of SIW design the gain is increased almost 2 dB. Furthermore, for extending the performance enhancement of SIW structure a comparison analysis with recently published works with SIW designs in literature [21-26] is presented in Table 6. As it can be seen from Table 6, the proposed design optimization process has achieved an antenna model that not only have better or similar performance results (Gain and S_{11}), but also have realized this performance measure with smaller size compared to counterpart designs even though one of its operation band is at 12 GHz.

Table 5: Comparison of the realized gains

Model		Realized Gain (dB)		Die Size in (mm)
		12GHz	24GHz	
SIW Measured		6.7	7	25.5x22.5
Simulated	**SIW DEA**	7.01	7.13	25.38x22.45
	No SIW	4.8	5.8	25.38x22.45
	No SIW DEA	5.1	6.2	23.85x22.45

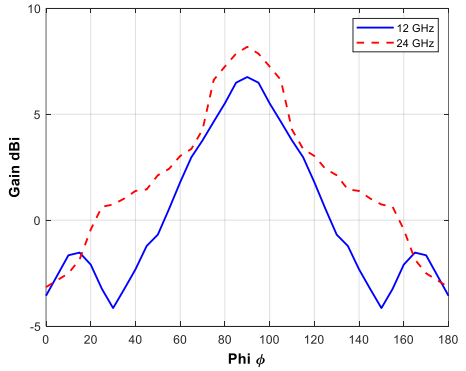

Fig. 6. Measured far field gain.

Table 6: Comparison of antenna with literature

Models	f (GHz)	S_{11} (dB)	Realized Gain dB	Substrate	Die Size (mm)
Here	12 / 24	-10 / -19	6.7 / 7	Roger 4350	25.5x22.5
[6]	10	-25	9.8		30x30
[21]	15	-15	7.5	---	30x30
[22]	25	-20	---	Arlon 25N	15x27
[23]	10 / 12	-30 /-30	8 / 9	Taconic TLY	40x56
[24]	18.2-23.8	<-15	9.5	Droid 5880	20x25
[25]	25.8-31.5	<-15	>6	RT/Duroid 5880	---
[26]	8-15	<-17	>6	Arlon IsoClad 917	55 × 46.8

V. CONCLUSION

In this work, a high performance, miniature, novel antenna is designed and fabricated on a low-cost substrate for X and K band radar applications. For this purpose, design optimization and fabrication of a high performance microstrip dual band antenna using Substrate Integrated Waveguide technology is worked out. Thus firstly, an efficient design optimization of a microstrip SIW antenna has been carried out on a low-cost substrate Roger 4350 with a possible simple geometry as a multi-objective, multi-dimensional optimization problem using the Differential Evolutionary Algorithm (DEA) within 3-D CST Microwave studio environment. At the same time, effects of the SIW structures are investigated on the radiation and return loss characteristics of the antenna design by simulation in different cases and optimized using DEA. In simulated results, the optimized antenna with SIW structure achieves the simulated gain level of 7 and 7.13 dB at 12 and 24 GHz respectively, while other two cases of antenna design without SIW design can only achieves 6 dB at most. In the second step, for justification of the proposed design method, the optimally designed dual band SIW antenna has been prototyped. Finally it has been reached a conclusion that the competitive performance has been achieved with this miniature, simple microstrip SIW antenna design as compared with the counterpart designs in the literature.

ACKNOWLEDGMENT

We would like to express our special thanks of gratitude to the Aktif Neser Elektronik, for providing researcher license of CST, Microwave and Antenna Laboratory of Yıldız Technical University. This work was supported by 100/2000 YÖK and TÜBITAK-BIDEB 2011/A International PhD Fellowship Program.

REFERENCES

[1] M. Bozzi, L. Perregrini, K. Wu, and P. Arcioni, "Current and future research trends in substrate

integrated waveguide technology," *Radioengineering*, vol. 18, no. 2, 2009.

[2] W. Jiang, K. Huang, and C. Liu, "Ka-band dual-frequency single-slot antenna based on substrate integrated waveguide," *IEEE Antennas and Wireless Propagation Letters*, vol. 17, no. 2, pp. 221-224, 2017.

[3] T. Cheng, W. Jiang, S. Gong, and Y. Yu, "Broadband SIW cavity-backed modified dumbbell-shaped slot antenna," *IEEE Antennas and Wireless Propagation Letters*, vol. 18, no. 5, pp. 936-940, 2019.

[4] M. A. Belen, P. Mahouti, A. Çalışkan, and A. Belen, "Modeling and realization of cavity-backed dual-band SIW antenna," *Applied Computational Electromagnetics Society Journal*, vol. 32, no. 11, pp. 974-978, 2017.

[5] A. Belen and F. Güneş, "Design and realization of dual band microstrip SIW antenna," *Sigma Journal of Engineering and Natural Sciences*, vol. 37, no. 4, pp. 1083-1092, 2019,

[6] M. A. Belen, F. Güneş, A. Çalışkan, P. Mahouti, S. Demirel, and A. Yıldırım, "Microstrip SIW patch antenna design for X band application," *MIKON 21st International Conference on Microwaves, Radar and Wireless Communications*, Krakow Poland, 2016.

[7] J. Lacik, "Circularly polarized SIW square ring-slot antenna for X-band applications," *Microw. Opt. Technol. Lett.*, vol. 54, pp. 2590-2594, 2012.

[8] S. Moitra and P. S. Bhowmik, "Effect of various slot parameters in single layer substrate integrated waveguide (SIW) slot array antenna for Ku-band applications," *Applied Computational Electromagnetics Society Journal*, vol. 30, no. 8, 2015.

[9] N. Tiwari and T. R Rao, "Antipodal linear tapered slot antenna with dielectric loading using substrate integrated waveguide technology for 60 GHz communications," *Applied Computational Electromagnetics Society Journal*, vol. 32, no. 4, 2017.

[10] E. Baghernia and M. H. Neshati, "Development of a broadband substrate integrated waveguide cavity backed slot antenna using perturbation technique," *Applied Computational Electromagnetics Society Journal*, vol. 29, no. 11, 2014.

[11] F. Glover and G. A. Kochenberger, "Handbook of metaheuristics," Springer, *International Series in Operations Research & Management Science*, 2003.

[12] E. G. Talbi, *Metaheuristics: From Design to Implementation*. Wiley, 2009.

[13] F. Güneş, S. Demirel, and P. Mahouti, "Design of a front–end amplifier for the maximum power delivery and required noise by HBMO with support vector microstrip model," *Radioengineering*, vol. 23, 2014.

[14] F. Güneş, S. Demirel, and P. Mahouti, "A simple and efficient honey bee mating optimization approach to performance characterization of a microwave transistor for the maximum power delivery and required noise," *Int. J. Numer. Model.* 2015, doi: 10.1002/jnm.2041.

[15] K. Güney and M. Onay, "Bees algorithm for design of dual-beam linear antenna arrays with digital attenuators and digital phase shifters," *Int. J. RF and Microwave CAE*, vol. 18, pp. 337-347, 2008.

[16] A. Galehdar, D. V. Thiel, A. Lewis, and M. Randall, "Multi objective optimization for small meander wire dipole antennas in a fixed area using ant colony system," *Int. J. RF and Microwave CAE*, vol. 19, pp. 592-597, 2009.

[17] A. Yildirim, F. Güneş, and M. A. Belen, "Differential evolution optimization applied to the performance analysis of a microwave transistor," *Sigma Journal of Engineering and Natural Sciences*, vol. 8, no. 2, pp.135-144, 2017.

[18] F. Güneş, M. A. Belen, and P. Mahouti, "Competitive evolutionary algorithms for building performance database of a microwave transistor," *Int. J. Circ. Theor. Appl.*, vol. 46, pp. 244-258, 2018.

[19] K. Price, R. M. Storn, and J. A. Lampinen, *Differential Evolution*. Springer-Verlag Berlin Heidelberg, 2005.

[20] F. Güneş, Z. Sharipov, M. A. Belen, and P. Mahouti, "GSM filtering of horn antennas using modified double square frequency selective surface," *Int. J. RF Microw. Comput. Aided Eng.*, vol. 27, 2017.

[21] M. Esquius-Morote, B. Fuchs, J.-F. Zürcher, and J. R. Mosig, "Novel thin and compact H-plane SIW horn antenna," *IEEE Transactions on Antennas and Propagation*, vol. 61, no. 6, 2013.

[22] A. Collado and A. Georgiadis, "24 GHz substrate integrated waveguide (SIW) rectenna for energy harvesting and wireless power transmission," *IEEE MTT-S International Microwave Symposium Digest (MTT)*, Seattle, WA, pp. 1-3, 2013. doi: 10.1109/MWSYM.2013.6697772

[23] L. Sabri, N. Amiri, and K. Forooraghi, "Dual-band and dual-polarized SIW-fed microstrip patch antenna," *IEEE Antennas and Wireless Propagation Letters*, vol. 13, pp. 1605-1608, 2014. doi: 10.1109/LAWP.2014.2339363

[24] T. Cheng, W. Jiang, S. Gong, and Y. Yu, "Broadband SIW cavity-backed modified dumbbell-shaped slot antenna," *IEEE Antennas and Wireless Propagation Letters*, vol. 18, no. 5, pp. 936-940, 2019. doi: 10.1109/LAWP.2019.2906119.

[25] W. Jiang, K. Huang, and C. Liu, "Ka-band dual-frequency single-slot antenna based on substrate

integrated waveguide," *IEEE Antennas and Wireless Propagation Letters*, vol. 17, no. 2, 2018.

[26] Y. Wu, K. Ding, B. Zhang, D. Wu, and J. Li, "SIW-tapered slot antenna for broadband MIMO Applications," *IET Microw. Antennas Propag.*, vol. 12, no. 4, pp. 612-616, 2018.

Aysu Belen received her M.Sc. degree in Electronics and Communication Engineering from the Yıldız Technical University in 2016. She has been currently in the Ph.D. program of Yıldız Technical University. Her main research areas are optimization of microwave circuits, circuits, device modeling, and computer aided circuit design and microwave amplifiers.

Filiz Güneş received her M.Sc. degree in Electronics and Communication Engineering from the Istanbul Technical University. She attained her Ph.D. degree in Communication Engineering from the Bradford University in 1979. She is currently a Full Professor in Yıldız Technical University. Her current research interests are in the areas of multivariable network theory, device modeling, computer-aided microwave circuit design, monolithic microwave integrated circuits, and antenna designs.

Peyman Mahouti received his Ph.D. degree in Electronics and Communication Engineering from the Yıldız Technical University in 2016. The main research areas are analytical and numerical modelling of microwave devices, optimization techniques for microwave stages, and application of artificial intelligence based algorithms.

A Broadband Reflectarray Based on Vivaldi Antenna Elements

Fan Qin, Lihong Li, Yi Liu, and Hailin Zhang

State Key Laboratory of Integrated Services Networks (ISN)
Xidian University, Xi'an 710071, China
fqin@xidian.edu.cn, lhli_06@stu.xidian.edu.cn, yliu@xidian.edu.cn, and hlzhang@xidian.edu.cn

Abstract — In this paper, a novel broadband reflectarray (RA) is presented. For achieving broadband performance, the unit cell is realized using Vivaldi antenna element, where the feeding line acts as phase delay-line for adjusting the reflection phase. By simply changing the length of phase delay-line, a full 360° phase coverage is obtained. Additionally, the phase response curves are nearly parallel within a broad bandwidth, leading to a wideband operation. To verify this design, a prototype consisting of 10×22 unit cells is designed, fabricated and measured. The measured results show that the maximum gain reaches 21.50 dBi with 20.15% 1-dB gain bandwidth and 30.38% 3-dB gain bandwidth, respectively. Simulated and measured results agree very well with the proposed design scheme.

Index Terms — Broadband, high gain, reflectarray, Vivaldi antenna array.

I. INTRODUCTION

Nowdays, it becomes more and more challenging to satisfy the ever-lasting capacity-growing and users-boosting demands in wireless networks. For example, many electronic devices in civil and military areas are preferred to be connected using wireless technology. To support these connections with high date rate, mobility and stability in wireless systems, antennas are highly required to have the properties of high gain, broad bandwidth and stable radiation characteristics [1-2]. In addition, for commercial applications, it is important to reduce the complexity of antenna structures and have low cost.

Reflectarrays (RAs) have been considered as promising alternative to traditional high-gain antennas because of their high gain, compact structure, lightweight, low cost, easy beam forming, etc. Compared to conventional antenna arrays and parabolic reflectors, RAs do not need complicated feeding network and have planar structure [3-5]. However, the RAs have a severe drawback of narrow bandwidth performance mainly due to the inherent narrow bandwidth for microstrip antenna unit cell and the differential spatial phase delay caused by different path lengths from feed source to each unit cell [6-7]. In recent years, many methods have been proposed to increase the bandwidth of the reflectarray, including the use of multilayer structures [8-10], subwavelength element [11], dual-frequency phase synthesis [12], and true - time delay technique [13]. In [14], a three-layer printed reflectarray with patches of variable size was designed, whose 1-dB bandwidth reaches to 10%. In [15], double-layer subwavelength elements with variable size were employed to enlarge the gain bandwidth of the reflectarray antennas. Besides, by employing tightly coupled technique, an ultra-wide-band reflectarray antenna was reported in [16].

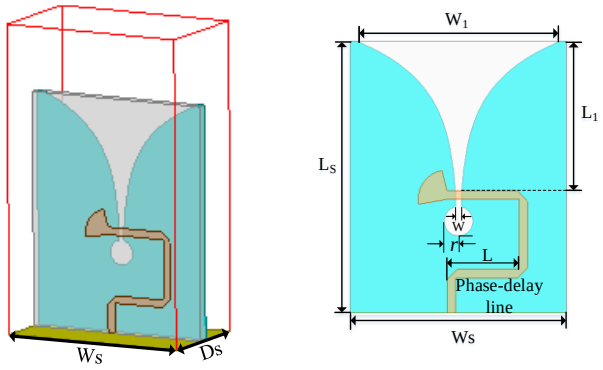

Fig. 1. The unit cell of this reflectarray: (a) periodic structure view; (b) front view.

As a kind of exponential tapered slot antenna, Vivaldi antennas provide a wide impedance bandwidth and stable gain. They are fabricated using low-cost planar fabricating technology. Hence, they are used in many applications which demand wide or ultra-wide bandwidth and directional radiation properties, such as ultra-wideband (UWB) imaging systems and emerging 5G systems [17]. However, one serious problem of Vivaldi antenna arrays is that it requires a complicated, bulky feed network consisting a number of power dividers, which will introduce significant losses at high frequency above X-band. Moreover, the perpendicular structure between Vivaldi array and feeding network

Submitted On: December 31, 2019
Accepted On: May 10, 2020

improves the fabrication complexity seriously. These drawbacks extremely limit the applications of large Vivaldi antenna arrays.

Inspired by the concept of RAs and wideband property of Vivaldi antennas, a wideband unit cell based on Vivaldi antenna is proposed to enhance the bandwidth performance of reflectarray in this paper. The feeding line in the Vivaldi element is used as phase-delay line to control the reflection phase response. By varying the length of the delay line, a full 360° linear phase range within a broad bandwidth is obtained. Within its operating frequency, the reflection magnitude maintains above -0.5 dB. To verify the design, a wideband reflectarray consisting of 10×22 unit cells is designed, fabricated and measured. The maximum gain of the proposed reflectarray is approximately 21.50 dBi with the 1-dB gain bandwidth of 20.15% and 3-dB gain bandwidth of 30.38%, respectively.

Table 1: Optimized parameters of the Vivaldi antenna

Parameter	L_S	W_S	W
Value (mm)	18.6	15	0.4
Parameter	*r*	L_1	W_1
Value (mm)	1	7.3	14

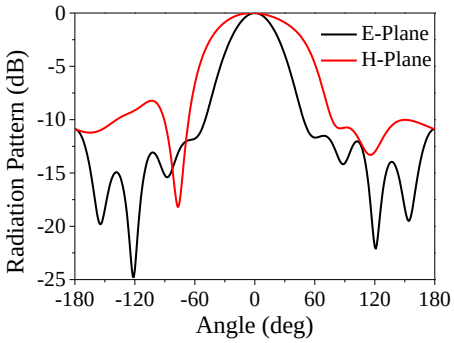

Fig. 2. The simulated radiation patterns of unit cell at 13GHz.

II. DESIGN OF UNIT CELL

The geometry of the proposed unit cell is shown in Fig. 1, which is composed of a conventional taper-slot Vivaldi antenna and a metallic reflect plane. As can be seen, the taper-slot with a circle-end is printed on the ground of the Vivaldi antenna element. The phase-delay line beginning with a fan-shape is etched on the other side of the substrate for coupling electromagnetic (EM) signals through the taper-slot. This structure can provide a stable radiation patterns and good impedance matching over a wide frequency range. A metallic plane with the dimension of 15×6.8 mm^2 is placed at the end of the Vivaldi antenna element for reflecting EM signals. This proposed unit cell is printed on a 0.8 mm Rogers 4003C substrate with dielectric constant of 3.55 and loss tangent of 0.0027.

The operating principle of the proposed unit cell can be described as follows. The incident waves illumining the unit cell is received by Vivaldi antenna element and transmit through the delay line. Because the delay line is metallic ended, the waves will be reflected and radiated by the Vivaldi element. During this process, the functions of the delay line are signal transmitting and phase controlling. By varying the length of the delay line on each unit cell, the corresponding reflection phase can be simply controlled. It is worth noting that in order to obtain a more compact configuration and increase the length of the delay line, the delay line is bent and stretched. The unit cell has been optimized to operate at Ku-band. The optimized parameters are reported in Table 1.

To investigate the reflection coefficient of the unit cell, numerical simulations are carried out by using ANSYS HFSS software. The infinite array model is built by placing master- slave boundary around the unit cell with Floquet port excitation.

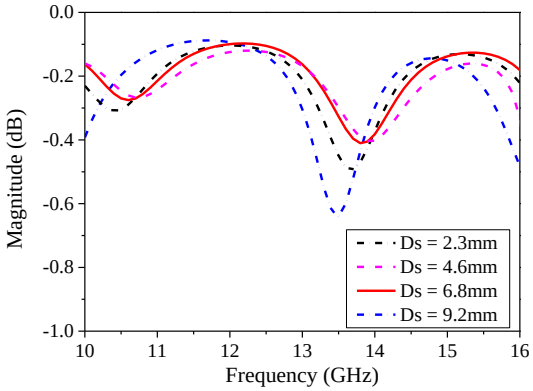

Fig. 3. The reflection magnitudes of the unit cell with different Ds.

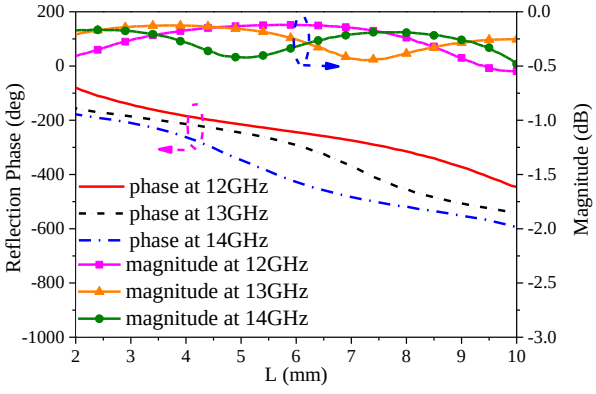

Fig. 4. Simulated element phase shifts and magnitudes at different frequencies.

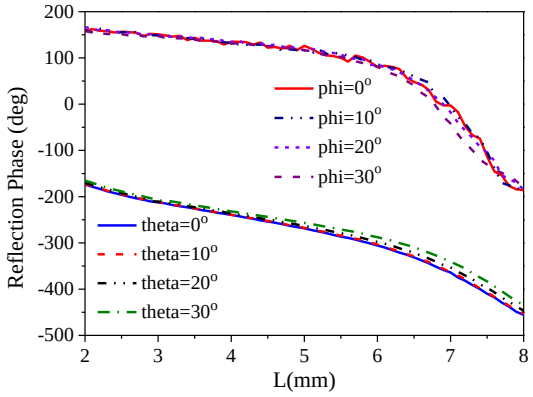

Fig. 5. The reflection phase of the unit cell with different oblique incidence.

Figure 2 shows the simulated radiation patterns of unit cell at 13GHz. The 3-dB beamwidth of the radiation pattern on the E-plane and H-plane is 28° and 49°, respectively. The simulated magnitudes of unit cell with different Ds is presented in Fig. 3. As can be seen, the unit cell has good reflection performance when Ds is 6.8mm (0.3 λ), whose magnitude is lower than -0.4dB within 10GHz to 16GHz. Therefore, the optimized Ds is finally chosen as 6.8 mm in this paper. Figure 4 shows the simulated reflection phase and magnitude for a normal incident wave at different frequencies. It can be observed that the reflection phase covers a full 360° phase range as the delay line varies from 2 mm to 10 mm. Besides, within 12 GHz to 14 GHz, the phase response curves maintain parallelism with each other, which imply that the unit cell has a good wideband response. The magnitude curves show a good reflection performance, whose values are above -0.5 dB in the operating band.

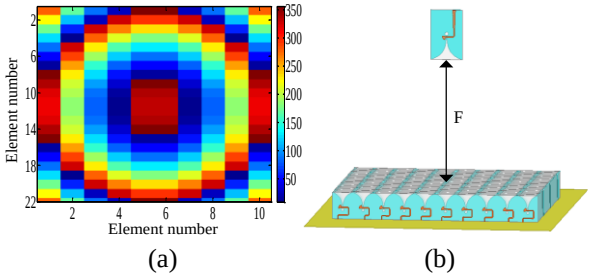

Fig. 6. (a) The phase distribution of the reflectarray. (b) The 3-D structure of the reflectarray.

In general, most of the unit cells are not located in the center of the reflectarray and they are obliquely illuminated by the incident waves, so it is necessary to consider the performance of the reflection phase when the incident angle is different. Figure 5 simulated the phase response of the unit cell under different incident angles. It is clearly seen that compared to normal incident illumination, the unit cell illuminated by 30° (theta or phi) incident waves still can maintain a very stable performance with little phase variation. Hence, according to the above analysis, the proposed unit cell has the properties of broadband operation, high reflection magnitude, full phase range, low sensitive of incident angle, which is desired to constitute a wideband reflectarray.

III. SIMULATION AND MEASUREMENT

To obtain high-gain performance, the reflection phase for each unit cell must be designed to compensate for different path lengths from the illuminating feed, and achieve a uniform phase on the array aperture. The required reflection phase φ_i for the i[th] unit cell is calculated as:

$$\varphi_i = k_0(R_i - \vec{r}_i \cdot \hat{r}_0) + \varphi_0, \quad (1)$$

where k_0 is the propagation constant in free space, R_i is the distance from feed antenna to the i[th] unit cell, $\vec{r}_i$ is the position vector of the i^{th} unit cell, and $\hat{r}_0$ is the main beam unit vector. For generating the far-field at the broadside direction, $\vec{r}_i \cdot \hat{r}_0 = 0$, where φ_0 is a phase constant that is selected to drive the reference phase at the aperture center phase to a certain value. Once the required phase at each unit cell is determined, the corresponding length of delay line in unit cell, namely the parameter of '*L*', can be obtained from Fig. 3.

When feed antenna non-uniformly illuminates the reflectarray consisting of M×N unit cells, the reradiated field from the array in an arbitrary direction can be represented by:

$$\vec{E}(\vec{u}) = \sum_{i=1}^{n}\sum_{j=1}^{m} F_f(\vec{R}_{ij} \cdot \vec{R}_f) F(\vec{R}_{ij} \cdot R_0) F(\vec{R}_0 \cdot \vec{R}) F(\vec{R}_0 \cdot \vec{R}) \cdot \exp\left\{-jK_0\left[\left|\vec{R}_{ij} - \vec{R}_f\right| - \vec{R}_{ij} \cdot \vec{R}\right] + j\varphi_{ij}\right\}, \quad (2)$$

where F_f is the radiation pattern function of the feed antenna, F is the radiation pattern function of the Vivaldi element, $\vec{R}_{ij}$ is the position vector of the ij$_{th}$ element, $\vec{R}_f$ is the position vector of the feed, k_0 is the free-space wavenumber, and φ_{ij} is the required phase delay of the ij$_{th}$ element.

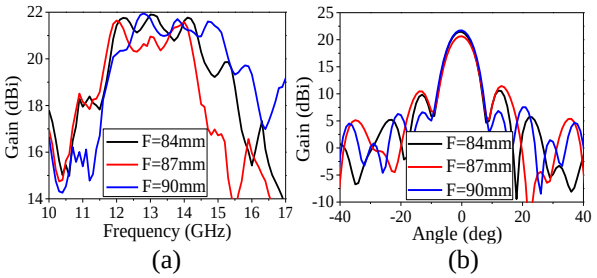

Fig. 7. (a) The bandwidth of the RAs with varying F at the broadside direction; (b) the radiation pattern of the RAs with varying F at the broadside direction.

Table 2: Simulated results with different F

Focal Length	84mm	87mm	90mm
Unit numbers	10*22	10*22	10*22
Maximum gain/dBi	21.90	21.64	21.94
1-dB bandwidth	17.7%	17.3%	20.7%
3-dB bandwidth	29.6%	22.7%	33.4%

According to function (1), the phase distribution for generating narrow beams along broadside direction is presented in Fig. 6 (a). As can be seen, the phase distribution shows a symmetric distribution around the array center. To validate the wideband performance of the reflectarray unit cell, a reflectarray antenna operating at 13 GHz is designed and simulated. This reflectarray consists of 10×22 unit cells with the dimension of 150×149.6mm^2. Based on the calculated phase distribution, the proposed wideband RA is built and shown in Fig. 6 (b).

Three different focal lengths are chosen to study the effects of F/D on gain performance, where *D* is the aperture size of the proposed reflectarray. Figure 7 presents the antenna gain and radiation patterns by changing F with fixed aperture dimension. It can be seen that the proposed reflectarray can successfully generate high-gain radiation patterns, where all of the maximum gain with different F/D are above 20 dBi. Meanwhile, the value of F/D impacts on the gain performance and gain bandwidth. Both of the maximum gain and gain bandwidth show growth trend with the increase of F/D. Table 2 reports the maximum gain, 1-dB gain bandwidth and 3-dB gain bandwidth with different focal lengths. According to the results, the focal length is finally chosen as 90 mm.

The simulated radiation pattern at 13 GHz is plotted in Fig. 8. The focusing pencil beam is produced successfully. With accurate phase distribution, the reflectarray has a high gain performance, whose maximum gain reaches 21.73 dBi at 13GHz. Figure 9 shows the side view of E-fields. As we can see, the proposed reflectarray has good focusing effects on EM waves. The incident spherical wave generated by the feed antanna is transmitted through the Vivaldi elements and reflected by the metallic plane, which is converted into plane wave. To verify the design, a prototype is fabricated, assembled and measured, as shown in Fig. 10. The overall dimension of the reflectarray is 220×220 mm^2 with the effective area of 150×180mm^2, which is covered by 10×22 unit cells. To assemble the proposed reflectarray and feed antenna, a frame and two supporters are designed, which are also considered during the simulations.

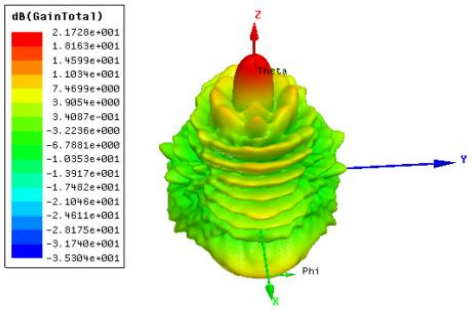

Fig. 8. The simulated radiation pattern at 13 GHz.

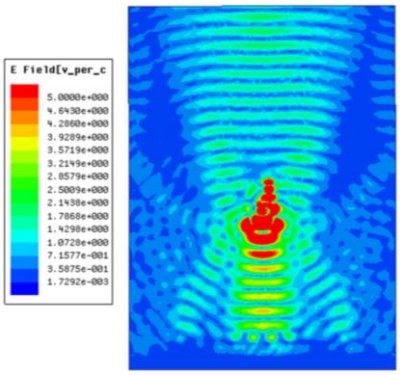

Fig. 9. The side view of E-fields.

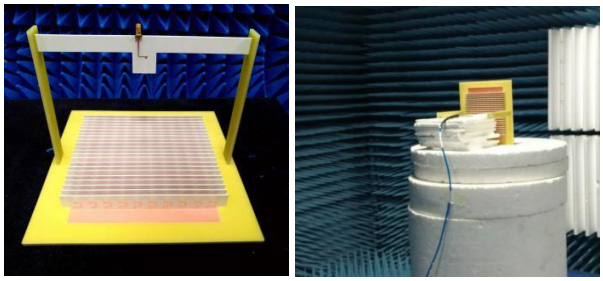

(a) (b)

Fig. 10. The fabricated prototype: (a) the proposed reflectarray; (b) the E-field measurement in microwave chamber.

Vivaldi antenna is also selected as the feed antenna. It is placed above the reflectarray surface at the distance of 90 mm. Figure 11 (a) shows the simulated radiation patterns of feed antenna at 13GHz. The measured S parameters of the feed antenna is plotted in Fig. 11 (b), showing that the proposed feed antenna can work from 10 GHz to 18 GHz.

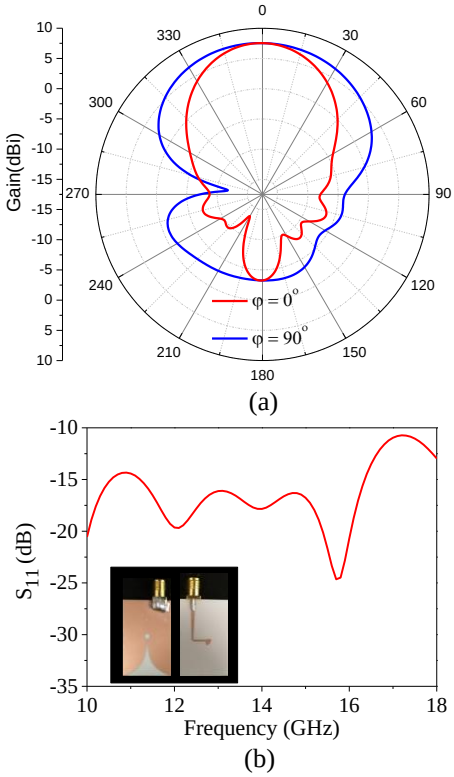

Fig. 11. The measured S parameter of the feed antenna.

Radiation patterns are measured in anechoic chamber. Figure 12 presents the measured E-plane and H-plane radiation patterns at 12 GHz, 13 GHz and 14 GHz, respectively. The simulated radiation patterns are also plotted as comparison. It can be observed that the simulated and measured results show a good agreement. Due to outstanding focused effects, pencil beams are generated. The 3-dB beamwidth of the radiation patterns is around 5°. Meanwhile, good cross-polarization lower than -20 dB is also achieved. Most of the side lobe level (SLL) are below -13 dB. Some measured SLL are slightly higher compared to these of the simulation. This can be the result of manufacturing tolerances and the manipulation setup. The measured gain is plotted in Fig. 12 to showing that the 1-dB gain bandwidth is 20.15% from 12 GHz to 14.6 GHz and 3-dB gain bandwidth is 30.38% from 11.54 GHz to 15.48 GHz, respectively. The measured maximum gain reaches to 21.5 dBi at 12.7 GHz. Clearly, the proposed reflectarray antenna is with outstanding high-gain and wideband characteristics. Moreover, the gain of feed antenna and the measurement results for aperture efficiency are also shown in Fig. 13. As we can see, the gain of feed antenna is stable at Ku-band, which is higher than 7.5dBi from11GHz to18GHz. The maximum aperture efficiency by the measurement is 23.1% at 12.6GHz.

Table 3 compares the proposed reflectarray based on Vivaldi antenna elements with other reported reflectarrays. The comparison mainly focuses on center frequency, maximum gain, aperture efficiency, 1-dB gain bandwidth and 3-dB gain bandwidth. As we can see, the proposed reflectarray based on Vivaldi antenna elements shows the superiority of wide gain bandwidth compared to those reported reflectarrays.

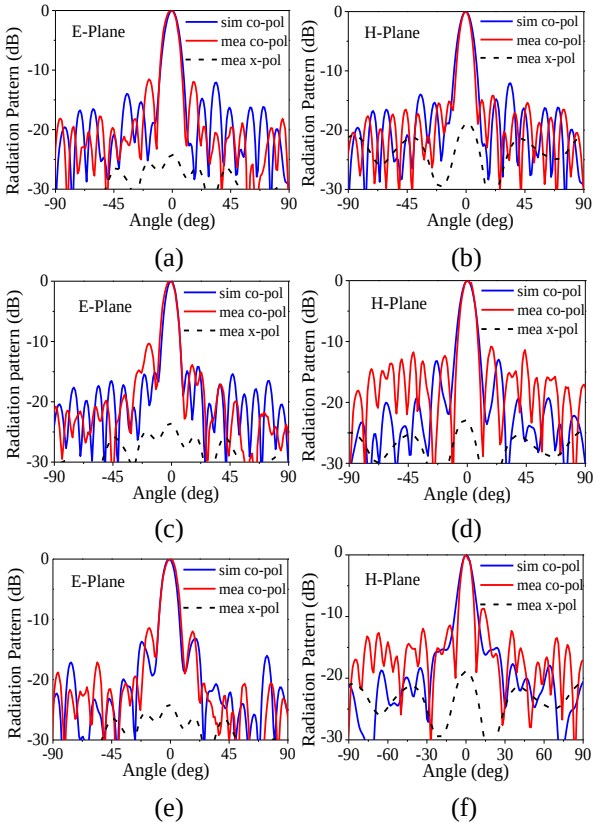

Fig. 12. The simulated and measured radiation patterns at: 12GHz (a), (b); 13GHz (c), (d); 14GHz (e),(f).

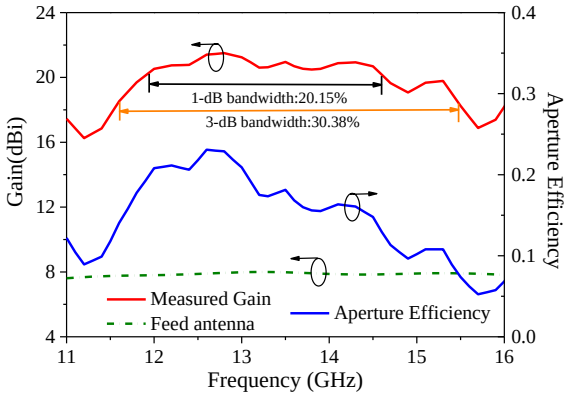

Fig. 13. The measured gain, aperture efficiency at the broadside direction and feed antenna gain.

Table 3: Comparison with other reported reflectarray

Ref.	[5]	[7]	[10]	This Work
Center frequency (GHz)	42.5	10	13.5	13
Maximum gain (dBi)	32.83	26.38	32.76	21.5
Aperture efficiency	51.11%	51.3%	--	23.1%
1-dB Gain bandwidth	12.94%	20%	14.8%	20.15%
3-dB Gain bandwidth	16%	28%	--	30.38%

IV. CONCLUSION

In conclusion, a wideband reflectarray operating at Ku-band is designed by employing Vivaldi unit cells. By adjusting the delay lines, the required phase compensation can be simply achieved for producing high-band pencil beams. Arranging unit cells with different delay line length according to the calculated phase distribution, we have designed a reflectarray radiating along broadside direction with a focal distance of 90 mm. The measured results are in a good agreement with the simulated ones, which demonstrates a 20.15% 1-dB gain bandwidth and a 30.38% 3-dB gain bandwidth, respectively, with maximum gain of 21.5 dBi.

ACKNOWLEDGMENT

This work is supported by the National Key Research and Development Program of China (Grant No. 2016YFE020700), partly supported by the Fundamental Research Funds for the Central Universities (Grant No. JB190101) and the National Natural Science Foundation of China (Grant No. 61701362).

REFERENCES

[1] X. Y. Xia, Q. Wu, H. M. Wang, and C. Yu, "Wideband millimeter-wave microstrip reflectarray using dual-resonance unit cells," *IEEE Antennas Wireless Propag. Lett.*, vol. 16, pp. 4-7, 2017.

[2] Q. Y. Chen, S. W. Qu, X. Q. Zhang, and M. Y. Xia, "Low-profile wideband reflectarray by novel elements with linear phase response," *IEEE Antennas Wireless Propag. Lett*., vol. 11, pp. 1545-1547, 2012.

[3] G. B. Wu, S. W. Qu, S. W. Yang, and C. H. Chan, "Broadband, single-layer dual circularly polarized reflectarrays with linearly polarized feed," *IEEE Trans. Antennas Propag.*, vol. 64, no. 10, pp. 4235-4241, Oct. 2016.

[4] Y. Z. Li, M. E. Bialkowski, and A. M. Abbosh, "Single layer reflectarray with circular rings and open-circuited stubs for wideband operation," *IEEE Trans. Antennas Propag*., vol. 60, no. 9, pp. 4183-4189, Sep. 2012.

[5] Z. W. Miao and Z. C. Hao, "A wideband reflectarray antenna using substrate integrated coaxial true-time delay lines for QLink-Pan applications," *IEEE Antennas Wireless Propag. Lett.*, vol. 16, pp. 2582-2585, 2017.

[6] L. Zhang, S. Gao, Q. Luo, and W. T. Li, "Single-layer wideband circularly polarized high-efficiency reflectarray for satellite communications," *IEEE Trans. Antennas Propag*., vol. 65, no. 9, pp. 4529-4538, Sep. 2017.

[7] C. H. Han, Y. T. Zhang, and Q. S. Yang, "A novel single-layer unit structure for broadband reflectarray Antenna," *IEEE Antennas Wireless Propag. Lett.*, vol. 16, pp. 681-684, 2017.

[8] M. H. A. S. M. Amin, K Ghaemi, and N. Behdad, "Ultra-wideband, true-time-delay reflectarray antennas using ground-plane-backed, miniaturized-element frequency selective surfaces," *IEEE Trans. Antennas Propag*., vol. 63, no. 2, pp. 534-542, Feb. 2015.

[9] M. Mohammadirad, N. Komjani, Abdel R. Sebak and Mohammad R. Chaharmir, "A broadband reflectarray antenna using the triangular array configuration," *Applied Computational Electromagnetics Society Journal*, vol. 26, no. 8, pp. 640-650, Aug. 2011.

[10] A. Tayebi, J. Gomez, J. R. Almagro, and F. Catedra, "Broadband high efficiency single-layer reflectarray antenna based on spiral crosses," *Applied Computational Electromagnetics Society Journal*, vol. 28, no. 1, pp. 1-7, Jan. 2013.

[11] P. Y. Qin, Y. J. Guo, and A. R. Weily, "Broadband reflectarray antenna using subwavelength elements based on double square meander-line rings," *IEEE Trans. Antennas Propag*., vol. 64, no. 1, pp. 378-383, Jan. 2016.

[12] Y. L. Mao, S. H. Xu, F. Yang, and A. Elsherbeni, "A novel phase synthesis approach for wideband reflectarray design," *IEEE Trans. Antennas Propag*., vol. 63, no. 9, pp. 4189-4193, Sep. 2015.

[13] E. Carrasco, J. A. Encinar, and M. Barba, "Bandwidth improvement in large reflectarrays by using true-time delay," *IEEE Trans. Antennas Propag*., vol. 56, no. 8, pp. 2496-2503, Aug. 2008.

[14] J. A. Encinar and J. A. Zornoza, "Broadband design of three-layer printed reflectarrays," *IEEE Trans. Antennas Propag*., vol. 51, no. 7, pp. 1662-1664, July 2003.

[15] P. Nayeri, F. Yang, and A. Z. Elsherbeni, "Broadband reflectarray antennas using double-layer subwavelength patch elements," *IEEE Antennas Wireless Propag. Lett*., vol. 9, pp. 1139-1142, 2010.

[17] W. T. Li, S. Gao, L. Zhang, and Q. Luo, "An ultra-wide-band tightly coupled dipole reflectarray

antenna," *IEEE Trans. Antennas Propag*., vol. 66, no. 2, pp. 533-540, Feb. 2018.

[18] Y. H. Xu, J. P. Wang, L. Ge, and X. D. Wang, "Design of a notched-band Vivaldi antenna with high selectivity," *IEEE Antennas Wireless Propag. Lett*., vol. 17, pp. 62-65, Jan. 2018.

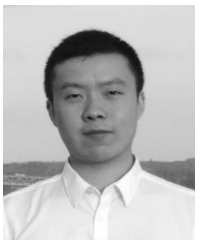

Fan Qin received the B.S. degree in Electronic Information Engineering and the Ph.D. degree in Electromagnetic Wave and Microwave Technology from Northwestern Polytechnical University, Xi'an, China, in 2010 and 2016, respectively. He is currently a Lecturer with the State Key Laboratory of Integrated Services Networks (ISN), Xidian University. His research interests include OAM antenna design, circularly polarized antennas, dual-band/multiband antenna arrays, metamaterials antennas and transmitarrays.

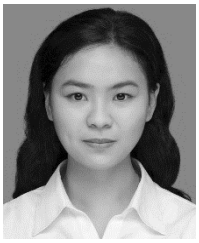

Li-hong Li is currently pursuing the Ph.D. degree in State Key Laboratory of Integrated Services Networks (ISN), Xidian University, Xi'an, China. Her research interests include high-gain Wideband reflectarray antennas, metasurface antenna and OAM antenna design.

Yi Liu (M'09–SM'17) received the B.S. degree from Dalian Jiaotong University, Dalian, China, in 2002, and the M.S. and Ph.D. degrees from Xidian University, Xi'an, China, in 2005, and 2007, respectively, all in communication engineering. Since January 2008, he has been in the State Key Laboratory of Integrated Service Network, Xidian University, where he is currently a Professor. From March 2011 to February 2012, he was a Visiting Scholar in the University of Delaware, Newark, DE, USA. His research interests include signal processing for wireless communications, MIMO and OFDM wireless communications, and cooperative communications.

Hai-lin Zhang (M'97) received B.S. and M.S. degrees from Northwestern Polytechnic University, Xi'an, China, in 1985 and 1988 respectively, and the Ph.D. from Xidian University, Xi'an, China, in 1991. In 1991, he joined School of Telecommunications Engineering, Xidian University, where he is a Senior Professor and the Dean of this school. He is also currently the Director of Key Laboratory in Wireless Communications Sponsored by China Ministry of Information Technology, a key member of State Key Laboratory of Integrated Services Networks, one of the state government specially compensated scientists and engineers, a field leader in Telecommunications and Information Systems in Xidian University, an Associate Director of National 111 Project. Zhang's current research interests include key transmission technologies and standards on broadband wireless communications for 5G and 5G-beyond wireless access systems. He has published more than 150 papers in journals and conferences.

Low Profile High-gain Antenna for Broadband Indoor Distributed Antenna System

Lu Xu and Yong Jin Zhou

Key Laboratory of Specialty Fiber Optics and Optical Access Networks
Shanghai University, Shanghai 200444, China
yjzhou@shu.edu.cn

Abstract ─ Here an improved folded patch antenna with low profile and high gain is proposed. By loading slow-wave metamaterials structure and metal pillars, the antenna operates from 0.6 GHz to 2.1 GHz (111% fractional bandwidth) with the VSWR<2. The profile height is 48.5 mm and 0.095λ at 0.6 GHz. The measured gain is 4 dBi at 0.6 GHz. The average gain is 7.43 dBi over the entire bandwidth. Hence, it is an excellent candidate for the emerging multiband indoor base station application such as 700 MHz, CDMA800, GSM900, DCS1800, PCS1900, UMTS, and IMT2000, etc.

Index Terms ─ 5G, broadband, folded patch, high gain, metamaterials.

I. INTRODUCTION

The demands for high speed and broadband data services for mobile users are growing dramatically and more than 80% mobile data traffic is originated in the indoor environments, for instance, commercial buildings and airports [1]. Thus, the indoor distributed antenna systems (IDAS) which are employed to provide wireless communication coverage in high-traffic indoor areas are becoming more and more important [2]. Since most of the antennas for IDAS are mounted on the ceilings or wall of indoor areas, they are required to have a low profile and a high gain [1]. Furthermore, more frequency bands have been commercially allocated for different communication systems to provide better communication services, such as 2nd generation (2G), 3G, 4G, and 5G. The most widely used 2G-5G frequency spectrum in the world today is 700, 800, 1800, 1900, 2100, and 2600 MHz. Recently, 700 MHz was allocated to China Broadcasting Network Corporation Ltd. (CBN). 700 MHz frequency will save the investment of 5G network deployment because it uses fewer sites because of its large-area network coverage. In addition, the 700 MHz frequency also offers good signal penetration in buildings, basements and elevators. Hence low-profile broadband antennas which can simultaneously cover multiple service bands are in great demand [1], especially those antennas covering 700 MHz.

The printed patch antenna is a good choice due to its low-profile feature, but it inherently suffers from the weakness of narrow bandwidth [3]. To improve the bandwidth for broadband applications, different kinds broadband printed antennas have been proposed, such as modified fractal antenna [4,5], planar elliptical antenna [6-8], notched trapezoidal monopole antenna [9], dual band-notched circular ring antenna [10], a half-disc and a half-ellipse antenna [11], and a back-to-back triangular shaped patch antenna [12]. However, the previous antennas suffer from low gain at low frequency, for example, the peak gain is ~ 0 dBi at 650 MHz for the antenna in [13] and the peak gain is 0 dBi at 1 GHz for the antenna in [14].

Since the antennas for IDAS are mounted on the ceilings or wall, there is always a big ground plane. To obtain high gain, the monopole or dipole antenna with a perpendicular ground plane is a good choice. However, such antennas suffer from high profile at low frequencies. A loop-loaded dipole antenna ranging from 880-2700 MHz [2], a low-profile sleeve monopole ranging from 750-2660 MHz [15], a dual-sleeve monopole antenna ranging from 730 to 3880 MHz [16] and a triple-band folded patch antenna with a shorting wall from 720 MHz [17] have been achieved. Their heights are 50 mm, 29 mm, 29 mm, and 39 mm, respectively. But all the above antennas cannot still cover 700 MHz. By incorporating a shorted coupling top loading structure over two cross-connected monopole antennas, an enhanced bandwidth ranging from 650 to 4500 MHz (152%) for a reflection coefficient <−15 dB is achieved. The achieved gain is 2 dBi for the 650-960 MHz band [3]. However, its profile height is 85 mm.

Wideband folded feed *L*-slot folded patch antenna ranging from 0.72 to 3.6 GHz was proposed and analyzed [18-20]. It has been shown that by loading slow-wave metamaterials structure, the miniaturization of the antennas can be realized [21-22]. Compared to the original antenna in Ref. [18], two metallic pillars are added onto the upper folded part to miniaturize the antenna and a slow-wave metamaterials structure is loaded to improve further the gain at higher frequency

Submitted On: December 31, 2019
Accepted On: May 13, 2020

band. The improved folded patch antenna with low profile and high gain ranging from 0.6 GHz to 2.1 GHz for VSWR < 2 has been fabricated. The gain is 4 dBi at 0.6 GHz. The average gain is 7.43 dBi over the entire bandwidth. Hence, it is an excellent candidate for the emerging multiband indoor base station application such as 700MHz, CDMA800, GSM900, DCS1800, PCS1900, UMTS, and IMT2000, etc.

II. ANTENNA DESIGN

Figure 1 shows the 3D perspective view and configuration of Antenna 1, which is mounted in the middle of a square ground plane with the dimensions of 290 mm × 290 mm. The patch antenna consists of a vertical wall shorted to the ground plane, a horizontal patch cut with an *L*-shaped slot, a vertical metallic wall, and the upper horizontal patch. The coaxial probe is used to excite the antenna which is connected to the lower folded part. First, in order to make the operating frequency shift to the lower frequency, two metallic pillars shown in Fig. 1 (a) are loaded to the upper folded patch. The detailed sizes are l_1 = 90 mm, l_2 = 113 mm, l_3 = 36 mm, l_4 = 16 mm, w_1 = 52 mm, w_2 = 55.5 mm, w_3 = 18 mm, w_4 = 31 mm, w_5 = 5 mm, h_1 = 18 mm, h_2 = 40 mm, h_3 = 2.5 mm, h_4 = 8.5 mm, and d_1 = 4 mm.

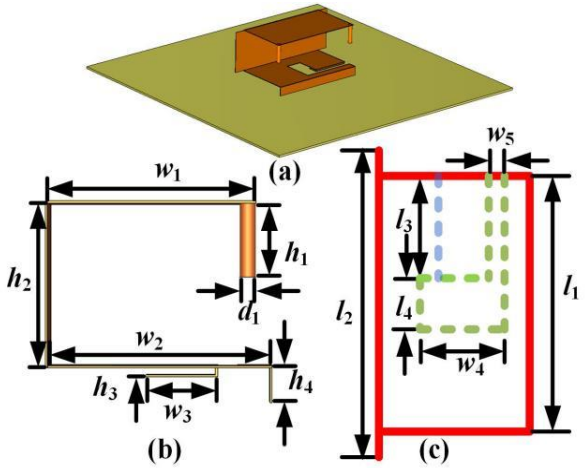

Fig. 1. (a) 3D perspective view, (b) side view, and (c) bottom view of Antenna 1.

To improve the gain at higher frequency band, a slow-wave metamaterials structure is loaded, which is shown in Fig. 2 and denoted by Antenna 2. The optimized parameters of the slow-wave structure are l_5 = 90 mm, w_6 = 6.5 mm, h_5 = 2.5 mm, and h_6 = 6 mm, respectively.

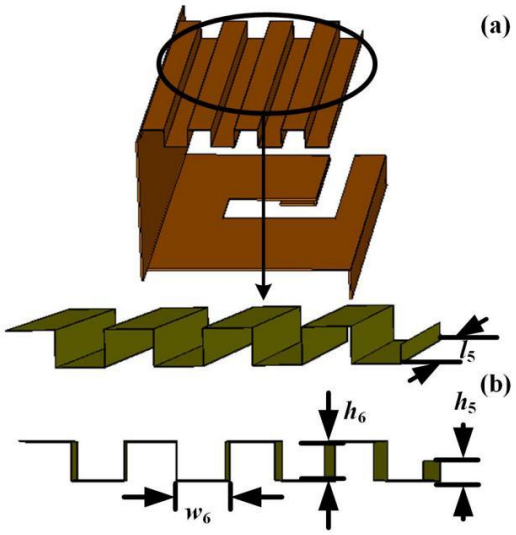

Fig. 2. (a) The structure of Antenna 2, and (b) the details of the slow-wave metamaterials structure.

III. RESULTS AND DISCUSSIONS

A. Simulated results

The reflection coefficients and VSWR of Antenna 1 are obtained by using the commercial software HFSS 15.0, which is based on finite element method (FEM). The results are shown in Fig. 3. It can be seen that the operating frequency of Antenna 1 is from 0.6 GHz to 2.1 GHz when S_{11} is lower than -10 dB or VSWR < 2. Hence, the relative impedance bandwidth reaches up to 111%. However, it can be seen that the gain decreases for Antenna 1 at higher frequency band (larger than 1.6 GHz). A slow-wave metamaterials structure is loaded to improve further the gain at higher frequency band.

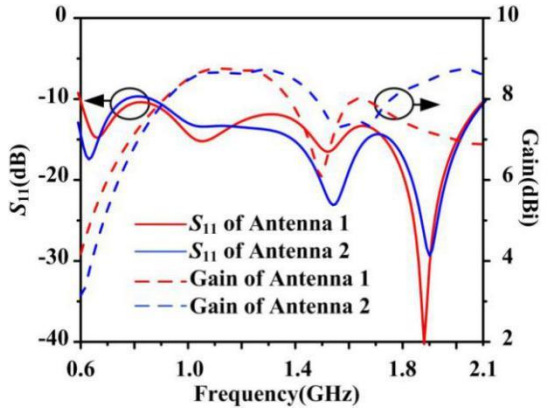

Fig. 3. Simulated reflection coefficients and gains of Antenna 1 and Antenna 2.

One unit cell of the slow-wave structure is used and the boundary conditions in the simulation are illustrated in Fig. 4 (a), where periodic boundary condition (PBC) is used in x direction and perfect electric conductor condition (PEC) is used in the other directions. The eigenmode solver of the commercial software CST microwave studio is adopted. From the dispersion curves shown in Fig. 4 (b), it can be seen that the dispersion curve is on the right side of the light line, which is the slow wave zone. The dispersion curve becomes lower when groove height h_6 increases. For the same operating frequency, the corresponding wave vector β would be larger for the lower dispersion curve.

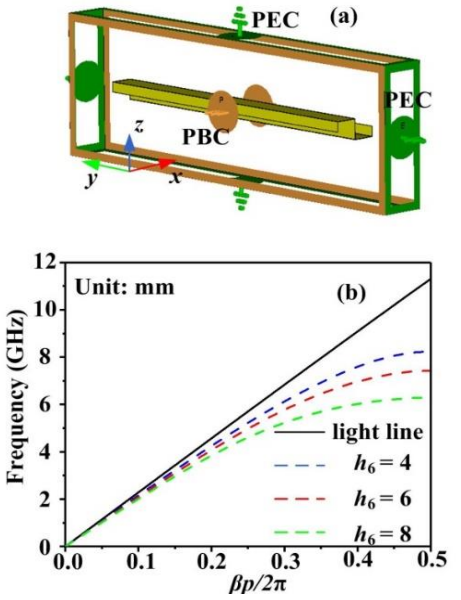

Fig. 4. (a) The boundary conditions in the numerical simulations, and (b) dispersion curves of the slow-wave structure.

B. Experimental results

The fabricated antenna (the material is aluminum) is shown in Fig. 5, whose thickness is 0.5 mm. The radiation pattern and gain measurements were conducted in the commercial chamber, whose minimum operating frequency is 600 MHz.

The measured reflection coefficients and gain are shown in Fig. 6. From Fig. 6 (a), it can be seen that the measurement results agree well with the simulation results. From Fig. 6 (b), we can see that the measured gain is a little lower than the simulation results. The measured average gain is 6.11 dBi over the entire bandwidth. It may be caused by the manual welding of the coaxial probe to the lower patch.

The simulated and measured radiation patterns at 1.1 GHz, 1.6GHz, and 2.1 GHz are shown in Fig. 7. It can be seen that the measured results agree well with the simulation results. Due to the asymmetry of the antenna structure, the radiation patterns are a little asymmetric. Finally, the performances of the proposed antenna are compared with other antennas in Table 1. Compared to the printed antenna, the proposed antenna has a high gain. It is 4 dBi at 0.6 GHz. Compared to the antennas [14-16, 18] from Table 1, the profile height is not more than 0.1λ and the operating frequency is ranging from 0.6 GHz to 2.1 GHz, covering the 700 MHz. Specially, the measured average gain is highest (7.43 dBi) over the entire bandwidth.

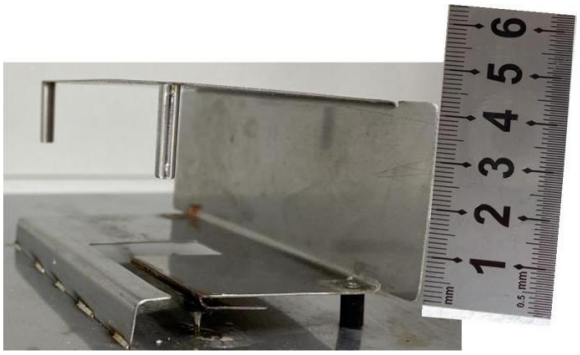

Fig. 5. The sample of the fabricated antenna.

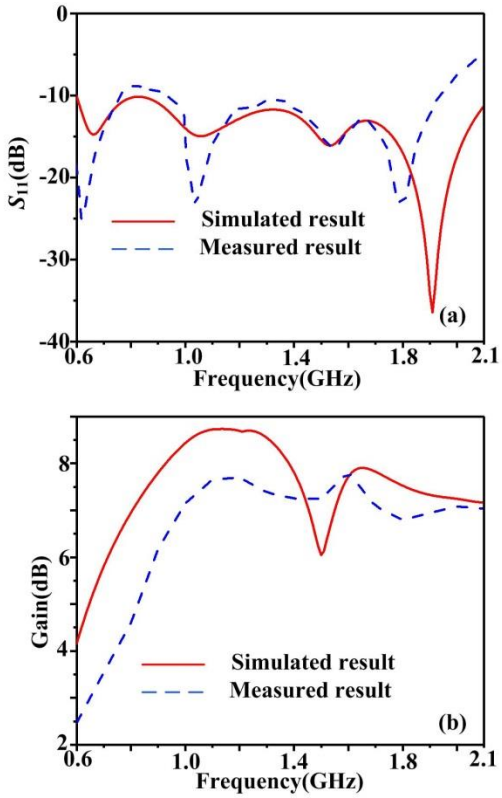

Fig. 6. Simulated and measured (a) reflection coefficients and (b) gain of Antenna 1.

Table 1: Comparison of the related researches

Antenna	Dimensions (mm)	Electrical Size (λ: Wavelength at the Lowest Frequency)	%	f_L (GHz)	Gain
[2]	120 × 120 × 50	0.352 λ × 0.352 λ × 0.15 λ	102	0.88	/
[3]	150 × 150 × 85	0.325 λ × 0.325 λ × 0.18 λ	161	0.65	1.9 dBi @ 1.7 GHz
[5]	19.2 × 14.4 ×1	0.032 λ × 0.024 λ × 0.0017 λ	193	0.5	2 dBi @ 2 GHz
[6]	15 × 29 × 0.787	0.032 λ × 0.063 λ × 0.0017 λ	168	0.65	~ 0 dBi @ 0.65 GHz
[8]	149 × 107.3 × 1.524	0.204 λ × 0.147 λ × 0.0021 λ	182	0.41	0.4 dBi @ 1 GHz
[12]	156.3 × 150 × 0.5	0.333 λ × 0.32 λ × 0.001 λ	185	0.64	4 dBi @ 2 GHz
[14]	97.8 × 136.9 × 1.524	0.15 λ × 0.21 λ × 0.0021 λ	170	0.46	~ 0 dBi @ 1 GHz
[15]	132 × 132 × 29	0.33 λ × 0.33 λ × 0.0725 λ	112	0.75	/
[16]	130 × 130 × 29	0.316 λ × 0.316 λ × 0.071 λ	137	0.73	2.5 dBi @ 0.75 GHz
[18]	56.2 × 113 × 33	0.135 λ × 0.271 λ × 0.079 λ	133	0.72	Average: 5.7dBi
Proposed antenna	55.5 × 113 × 48.5	0.109 λ × 0.222 λ × 0.095 λ	111	0.6	Average: 7.43dBi

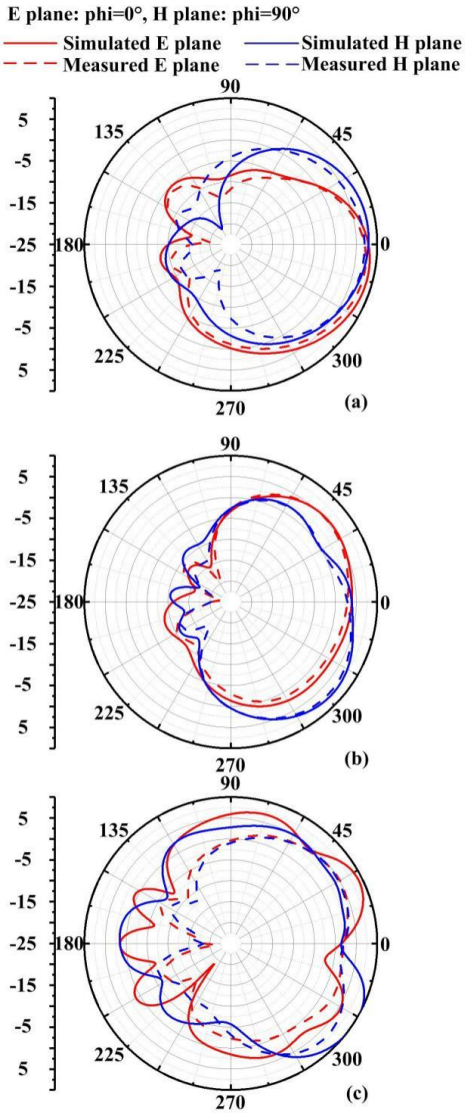

Fig. 7. Radiation patterns at: (a) 1.1 GHz, (b) 1.6 GHz, and (c) 2.1 GHz.

IV. CONCLUSION

By loading the slow-wave metamaterials structure and metal pillars, an improved low-profile high-gain folded patch antenna was demonstrated. The operating frequencies cover from 0.6 GHz to 2.1 GHz with the VSWR<2. Its profile height is only 0.095λ at 0.6 GHz. The measured gain is 4 dBi at 0.6 GHz. The average gain reaches up to 7.43 dBi over the entire bandwidth. The antenna is suitable for the emerging indoor base station applications such as 700MHz, CDMA800, GSM900, DCS1800, PCS1900, UMTS, and IMT2000, etc.

ACKNOWLEDGMENT

This work was supported by the National Natural Science Foundation of China under Grant No. 61971469, and by Science and Technology Commission Shanghai Municipality (STCSM) under Grants No. 18ZR1413500 and SKLSFO2017-05.

REFERENCES

[1] L. Y, J. Song,Y. Gao, K. He, and F. Gao, "Low-profile dual-polarized omnidirectional antenna for broadband indoor distributed antenna system," *Progress in Electromagnetics Research*, vol. 67, pp. 39-45, 2017.

[2] Q. Wu, X. J. Ding, and A. X. Chen, "A broadband dipole antenna for multiservice indoor distributed antenna system (MS-IDAS)," *IEEE Antennas Wireless Propagation Letters*, vol. 14, pp. 839-842, 2015.

[3] L. Zhou, Y. C. Jiao, Y. H. Qi, Z. B. Weng, and L. Lu, "Wideband ceiling-mount omnidirectional antenna for indoor distributed antenna systems," *IEEE Antennas Wireless Propagation Letter*s, vol. 13, pp. 836-839, 2014.

[4] S. Singhal and A. K. Singh, "Modified star-star fractal (MSSF) super-wideband antenna," *Microwave and Optical Technology Letters*, vol. 59, no. 3, pp. 624-630, 2017.

[5] V. Waladi, N. Mohammadi, Y. Zehforoosh, A. Habashi, and J. Nourinia, "A novel modified star-triangular fractal (MSTF) monopole antenna for super-wideband applications," *IEEE Antennas and Wireless Propagation Letters*, vol. 12, pp. 651-654, 2013.

[6] M. Manohar, "Miniaturised low-profile super-wideband Koch snowflake fractal monopole slot antenna with improved BW and stabilised radiation pattern," *IET Microwaves Antennas & Propagation*, vol. 13, pp. 1948-1954, 2019.

[7] C. Y. Huang and W. C. Hsia, "Planar elliptical antenna for ultra-wideband communications," *Electronics Letters*, vol. 41, no. 6, pp. 296-297, 2005.

[8] X. L. Liang, S. S. Zhong, and W. Wang, "Elliptical planar monopole antenna with extremely wide bandwidth," *Electronics Letters*, vol. 42, no. 8, pp. 441-442, 2006.

[9] X. R. Yan, S. S. Zhong, and X. L. Liang, "Compact printed semi-elliptical monopole antenna for super wideband applications," *Microwave and Optical Technology Letters*, vol. 49, no. 9, pp. 2061-2063, 2007.

[10] M. Manohar and U. K. Neani, "A novel super wideband notched printed trapezoidal monopole antenna with triangular tapered feedline," *2014 International Conference on Signal Processing and Communications*, pp. 1-6, 2014.

[11] M. Manohar, R. S. Kshetrimayum, and A. K. Gogoi, "A compact dual band-notched circular ring printed monopole antenna for super-wideband applications," *Radio Engineering*, vol. 26, no. 1, pp. 64-70, 2017.

[12] Y. Dong, W. Hong, L. Liu, Y. Zhang, and Z. Kuai, "Performance analysis of a printed super-wideband antenna," *Microwave and Optical Technology Letters*, vol. 51, no. 4, pp. 949-956, 2009.

[13] M. Alibakhshikenari, C. H. See, B. S. Virdee, R. Abd-Alhameed, A. Ali, F. Falcone, and E. Limiti, "Wideband printed monopole antenna for application in wireless communication systems," *IET Microwaves, Antennas & Propagation*, vol. 12, no. 7, pp. 1222-1230, 2018.

[14] X. R. Yan, S. S. Zhong, and X. L. Liang, "Compact printed semi-elliptical monopole antenna for super wideband applications," *Microwave and Optical Technology Letters*, vol. 49, no. 9, pp. 2061-2063, 2007.

[15] S. L. Zuo, Y. Z. Yin, Z. Y. Zhang, and K. Song, "Enhanced bandwidth of low-profile sleeve monopole antenna for indoor base station application," *Electronics Letters*, vol. 46, no. 24, pp. 1587-1588, 2010.

[16] Z. Y. Zhang, G. Fu, W. J. Wu, J. Lei, and S. X. Gong, "A wideband dual-sleeve monopole antenna for indoor base station application," *IEEE Antennas and Wireless Propagation Letters*, vol. 10, pp. 45-48, 2011.

[17] Z. H. Jiang, L. Zhang, Y. Zhang, C. Yu, L. Cai, S. Zheng, and W. Hong, "A compact triple-band antenna with a notched ultra-wideband and its MIMO array," *IEEE Transactions on Antennas and Propagation*, vol. 66, no. 12, pp. 7021-7031, 2018.

[18] K. L. Lau, S. H. Wong, and K. M. Luk, "Wideband folded feed L-slot folded patch antenna," *IEEE Antennas and Wireless Propagation Letters*, vol. 8, pp. 340-343, 2009.

[19] H. Wong, K. M. Luk, C. H. Chan, Q. Xue, K. K. So, and H. W. Lai, "Small antennas in wireless communications," *Proceedings of the IEEE*, vol. 100, no. 7, pp. 2109-2121, 2012.

[20] A. A. Deshmukh and K. P. Ray, "Analysis of shorted-plate compact and broadband microstrip antenna," *IEEE Antennas and Propagation Magazine*, vol. 55, no. 6, pp. 100-113, 2013.

[21] J. Long, E. Li, H. Zheng, and Y. Tu, "A novel structure for VHF band dipole antenna miniaturization," *2019 IEEE International Symposium on Antennas and Propagation and USNC-URSI Radio Science Meeting*, pp. 1385-1386, 2019.

[22] R. L. Shao, B. Li, L. Yang, and Y. J. Zhou, "Electrically small multiband antenna based on spoof localized surface plasmons," *EPJ Applied Metamaterials*, vol. 6, 2019.

Lu Xu was born in Yangzhou, Jiangsu, China, in 1996. She is currently pursuing the Master's degree of Electronic and Communications Engineering in Shanghai University, Shanghai 200444, China. Her research interests include small antenna, broadband antenna and metamaterials.

Yong Jin Zhou was born in Shandong, China, in 1982. His current research interests include microwave and millimeter antenna, plasmonic metamaterials and applications, millimeter wave and THz functional devices, wireless energy transmission. He received the B.S. degree in Communication Engineering from Shandong University, Jinan, China, in 2006, and Ph.D. degree in Electromagnetic Field and Microwave

Technology from Southeast University, Nanjing, China, in 2011, respectively. From 2009 to 2010, he was a Visiting Scholar of University of Houston. From 2011 to 2012, he was a Software Engineer with EEBU of Marvell Technology (Shanghai) Ltd. From 2012 to 2015, he was an Assistant Professor with School of Communication & Information Engineering, Shanghai University, Shanghai, China. From 2015, he was an Associate Professor with School of Communication & Information Engineering, Shanghai University, Shanghai, China. He has authored and coauthored over 90 papers in peer-reviewed journals and conference proceedings. He is IEEE Member, OSA Member, and Senior Member of Chinese Institute of Electronics. He is serving as a Reviewer for over 20 peer-reviewed journals, such as Nature electronics, Photonic Research, Optics Letter, Optics Express, Appl. Phys. Express, IEEE Access, IEEE MTT, IEEE MWCL, etc. He is serving as a Session Chair for several International Symposiums.

Multi-Beams Waveguide Slot Antennas at X-Band for Wireless Communications Systems

Hatem Oday Hanoosh, M. K. A. Rahim, N. A. Murad, and Yaqdhan Mahmood Hussein

Advanced RF & Microwave Research Group (ARFMRG)
School of Electrical Engineering, Faculty of Engineering
Universiti Teknologi Malaysia (UTM), 81310
UTMJB Johor, Malaysia
Hatem.altaee1990@gmail.com, mdkamal@utm.my, noorasniza@utm.my, Yaqthanm.79@gmail.com

Abstract ─ This paper focuses on the design of a multi-beams antenna using waveguide slots technology at X-band. The multi-beams radiation is proposed to expand the coverage of the single antenna, thus more capacity is enabled. Waveguide slots antenna is a well-known antenna for high power and gain transmission capabilities. Therefore, it is preferred. In this work, four variations of waveguide slots antennas are studied. The slot distribution covers one to four broad and narrow walls of the waveguide. This technique enables multi-beams patterns. The performance of the proposed antennas is simulated using CST microwave software. The simulated responses of the antennas show that a good matched with return loss greater than 10 dB at the desired frequency. The four proposed antennas achieved a good gain between 6.3 and 7.4 dB with directional beamwidth of 15 degree. The proposed antennas are suitable for implementing in radar applications.

Index Term ─ CST, multi-beams, slots antenna, waveguide.

I. INTRODUCTION

The backbone of the proposed cellular technology is changed to form wireless connection by using higher frequency spectrum [1]. Hence, higher spectrum has been assigned for outdoor links due to high path loss at higher frequencies, cost effective components, and other related factors. However, this technology on other hand suffers from severe challenges, including large propagation loss, signal absorbing, low gain of the proposed antenna, and low transmitted power. Waveguide slots antenna technology has been preferred in the past few years as a new inventive solution to allow higher gain, higher data rates, and power efficiency especially in the Cellular [2-5]. Rectangular waveguides have been used for many decades in microwave applications, with standard bands ranging from 1 GHz up to 300 GHz [3]. Slotted antenna arrays on waveguides are popular in navigation, radar and other high-frequency systems. The antenna is of interest due to its' low-loss property especially at high frequencies and thus possessed high efficiency [4].

Recently, a dual-beams waveguide slotted antenna is presented in [6]. The slots are distributed on the broad walls of the waveguides with directivity and gain of 14 dB at 28 GHz. Other types of waveguide slots antenna with implementing in the narrow-wall of the waveguide structure are introduced in [7-9]. The designs suffer from high grating lobes and lower gain than 10 dB. Additionally, dual-band dual-polarization waveguide slots antenna at 30 and 35 GHz is proposed in [10]. The narrow wall is implemented with 9×10 inclined slots array at 35 GHz to form horizontal polarization, and 8×10 longitude slots array is distributed on the broad wall at 30 GHz to form vertical polarization. However, the slots distributed on the narrow wall of the waveguide suffered from side lobes and grating lobes due to the small offset between the slots.

Therefore, this paper focuses on designing the waveguide slotted antenna operating at X-Band, providing a high gain, low side lobes, and multi-beams. Four waveguide slotted antennas are investigated in this paper. The antennas are implemented with 4 slots on narrow and broad walls of the waveguide structure. The performance of the proposed antennas is simulated using Computer Simulation Technology (CST) software. The paper is divided as follows: section 2 presents the design process, Section 3 discusses the results in term of simulation responses, and Section 4 concludes the paper.

II. WAVEGUIDE SLOT ANTENNA DESIGN

Commonly, the slots are represented as shunt elements in transmission line. The circuit for the slot is illustrated in Fig. 1. The *G* represents the conductance of the slot, and *B* represents the susceptance of the slot. The slot used in this research is cut in the longitude direction

Submitted On: February 28, 2020
Accepted On: April 26, 2020

of the waveguide structure. Each slot has length of L and width of *W*, the distance between two centered slots is *d*, and the offset from the center line is *x* as seen in Fig. 2. The distance *d* between the slots is designed to be half the guided wavelength. Thus, it would be 180-degree phase shift between the radiating slots [12-15]. The offset *x* is calculated using the normalized Conductance *Gn* equations [15]:

$$G_n = \sum_{n=1}^{N} g_n = 1, \quad (1)$$

$$g_n = \left[2.09 \frac{\lambda g}{\lambda 0} \cdot \frac{a}{b} \cdot cos^2 \frac{\pi \lambda 0}{2\lambda g}\right] sin^2 \frac{\pi x}{a}, \quad (2)$$

a and *b* are the inner dimensions of the waveguide (as shown in Fig. 3), which is used WR-90 standard waveguide, and λ_0 is the free space wavelength and λg is the guided wavelength, while *N* is the slots number. The antenna physical dimensions with the gain and the beamwidth of the slotted waveguide antenna are calculated using equations below [15]:

$$\lambda_g = \frac{\lambda 0}{\sqrt{1-\left(\frac{\lambda 0}{2a}\right)}}, \quad (3)$$

$$Gain = 10 \times log\left(\frac{N.d}{\lambda 0}\right) \ dB, \quad (4)$$

$$Beamwidth = 50.7 \times \frac{\lambda 0}{\frac{N}{2}.d} \ degree, \quad (5)$$

$$d = \lambda_g/2, \quad (6)$$

$$L = 0.98\ \lambda_0/2, \quad (7)$$

$$W = \lambda_g/20, \quad (8)$$

Where *L* is the slot length, *W* is the slot width, and *d* is the spacing between slots. From equation (3) it can be clearly noticed that the slot parameters are obtained from the center operating frequency and its guided wavelength. In addition, the gain and beamwidth are effected with two important parameters; the wavelength and the number of the slots. Beside the distance between slots (*d*) is also effected to these parameters. For instance, if the number of the slots (*N*) increases, the gain is increased [15]. However, the guided wavelength (λ_g) is increased which leads to increase the distance between slots and size of the waveguide accordingly [15]. Therefore, for this work a four slots are chosen to be implemented on the waveguide walls to maintain a reasonable size and optimal gain.

Generally, the waveguide structure is propagated at TE_{10} mode with both E-field and H-field are positioned within narrow and broad walls of the waveguide as shown in Fig. 2. To allow the slot radiation, a cutting will be made through the H-field lines at maximum flux [15]. This will generate one beam at one of which wall is used. To enable multiple beams (two or more than), the slots are cut on each wall side of the waveguide. For example, if the slot cutting is on broad and narrow walls of the waveguide, it will be generated a dual beam in the direction of the cutting slots. Figure 3 shows the standard distribution of the slots with dimensions on the waveguide structure.

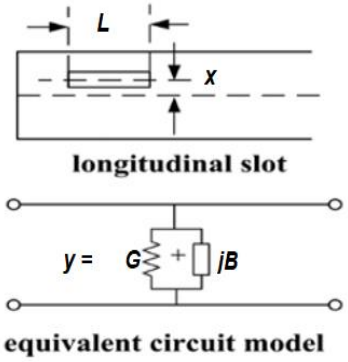

Fig. 1. Slot circuit representations [11].

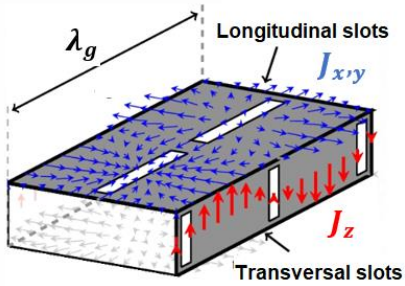

Fig. 2. The E-field and H-field distributed lines in the rectangular hollow waveguide [15].

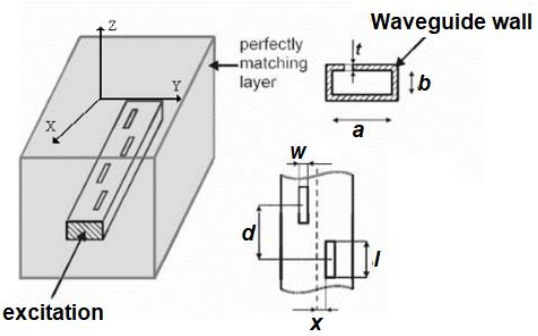

Fig. 3. Waveguide slot antenna. Standard waveguide slots antenna structure [12].

Therefore, a dual, triple, and four beams waveguide slots antennas are designed. Referring to Fig. 4 (a), the first antenna (Antenna 1) is designed by distributing four slots on one broad wall and one narrow wall of the waveguide. This will enable a dual beam generated from two different directions. The slots are distributed in symmetrical offset *x* from the centerline of the waveguide (for all designs). The second antenna (Antenna 2) is implemented with same number of the

slots as in Antenna 1.

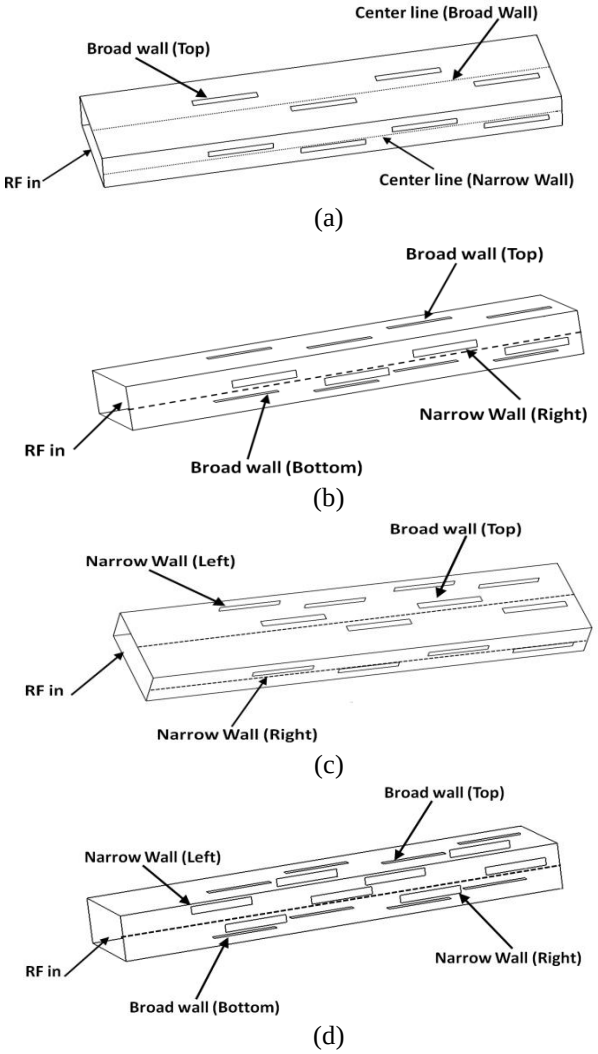

Fig. 4. The proposed antennas: (a) Antenna 1, (b) Antenna 2, (c) Antenna 3, and (d) Antenna 4.

The slots are distributed in two broad walls and one narrow wall of the waveguide. This will enable triple beams. The first two beams from the broad walls is radiated oppositely to each other and the third beam is generated from the narrow wall. The third antenna (Antenna 3) is similar to Antenna 2, whereas the slots distribution are in one broad wall and two narrow walls of the waveguide. The last antenna (Antenna 4) is designed with slots implementation on all the waveguide walls, which allows a four beams generations. Figure 4 and Table 1 shows the proposed antennas with their slots distribution and final dimensions of all the antenna designs respectively.

Table 1: The final dimensions of the proposed antennas at X-band (All dimensions are in mm)

Parameter/ Antennas	Ant.1	Ant.2	Ant.3	Ant.4
Broad Wall				
a	22.86	22.86	22.86	22.86
d	18.69	18.69	18.69	18.69
x	1.5	1.5	1.5	1.5
Slot length (L)	13.4	13.4	13.4	13.4
Slot width (W)	1.72	1.72	1.72	1.72
Narrow Wall				
b	10.16	10.16	10.16	10.16
d	18.69	18.69	18.69	18.69
x	1.5	1.5	1.5	1.5
Slot length (L)	13.4	13.4	13.4	13.4
Slot width (W)	1.72	1.72	1.72	1.72
Wall Distribution				
Sided walls	One broad and one narrow	Two broads and one narrow	One broad and two narrows	All

III. RESULTS AND DISCUSSIONS

The proposed designs are simulated by CST software and the performance in terms of return loss, directivity, gain, efficiency, and radiation patterns are analyzed. Figure 5 shows the simulated return loss of all the proposed designs. From the analysis, Antenna 1 and Antenna 2 have a maximum return loss of 22.7 dB and 22 dB at specific frequency of 9.22 GHz and 9.2 GHz respectively. Antenna 3 has a maximum return loss of 13 dB at 9.012 GHz. The shifting in frequency below the desired frequency happened due to the implementation of the slots on both side of the narrow walls. This is could be caused by the offset *x* from the centerline in the narrow wall of the waveguide, which effects the E-field lines that shifted the frequency. Antenna 4 showed a good return loss of 21 dB at 8.95 GHz. The shifting frequency in Antenna 4 is similar to Antenna 3, since the slots are also distributed within the sides of the narrow walls.

The simulated gain, directivity, and efficiency of the proposed antennas are shown in Fig. 6. Antenna 1 and Antenna 2 has maximum gain of 6.3 dB and 6.58 dB at the desired frequencies correspondingly. These gains are reordered from the radiating slots in the broad walls of the waveguide structure. In the same time, Antenna 3 and Antenna 4 showed a good gain performance of 6.9 dB and 7.4 dB at 9 and 8.95 GHz. Additionally, all antennas are noticed with good efficiency ranging from 75% to 92%.

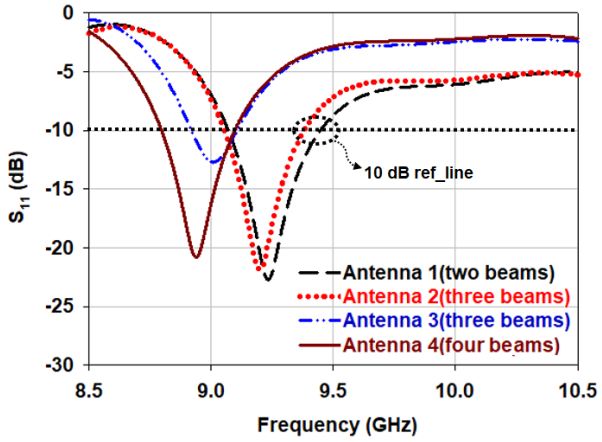

Fig. 5. The return loss of the proposed antennas.

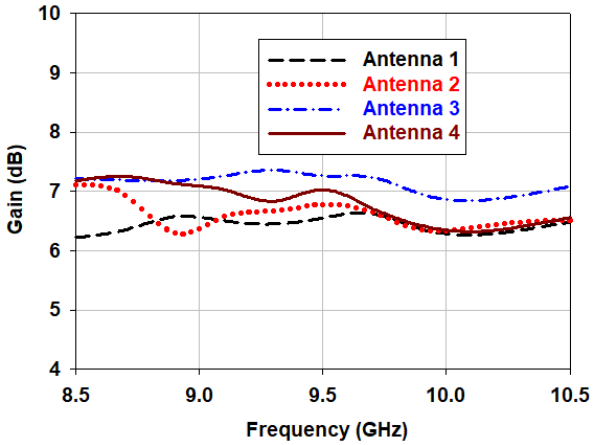

(a)

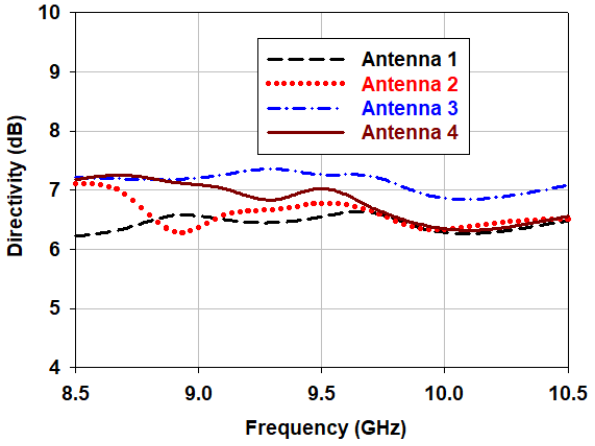

(b)

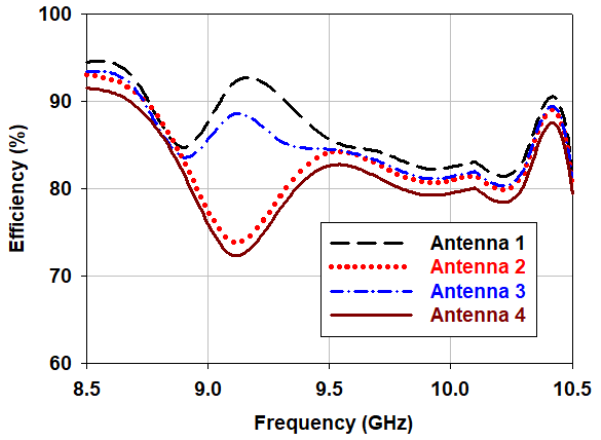

(c)

Fig. 6. The performance of the proposed antennas: (a) gain, (b) directivity, and (c) efficiency.

The radiation patterns of the proposed antennas are illustrated in Fig. 7. The radiation pattern analysis has performed on each antenna with broad and narrow wall of the waveguide. Firstly, Antenna 1 in Fig. 7 (a) has dual beams from broad and narrow wall. When Phi = 90 degree (broad wall), the beam is in one direction with slidelobes of -5 dB and grating lob of 0 dB. At narrow wall (Phi =0), one beam is noticed with slidelobes of -10 dB and grating lobes of -5 dB. Hence, dual beams are enabled from Antenna 1. Secondly, Antenna 2 (as in Fig. 7 (b)) has dual beams from the broad walls and one beam from the narrow walls. However, a high grating lobes are seen from the broad wall of 5 dB. Despite these grating lobes, a triple beams are clearly observed. Thirdly, Antenna 3 (as in Fig. 7 (c)) showed a good triple beams with low slidelobes of -10 dB at broad wall and -5 dB at narrow walls. The beams are from two sided narrow walls and one broad wall. Nevertheless, Antenna 4 (Fig. 7 (d) showed a high level of grating and slidelobes of 5 dB and 0 dB respectively. This could be due to the slots radiation from all the walls which makes it difficult to differentiate the four beams from others. Hence, more analysis and investigation should be taken to enhance and reduce these grating and slidelobes.

Table 2 shows the comparison between the four antennas performance, and Table 3 compares this work in respect with other researches. As summary, it can be concluded that multi beams property can be achieved by using one single waveguide structure. Taking the

advantage of signals are confined within the broad and narrow walls of the waveguide

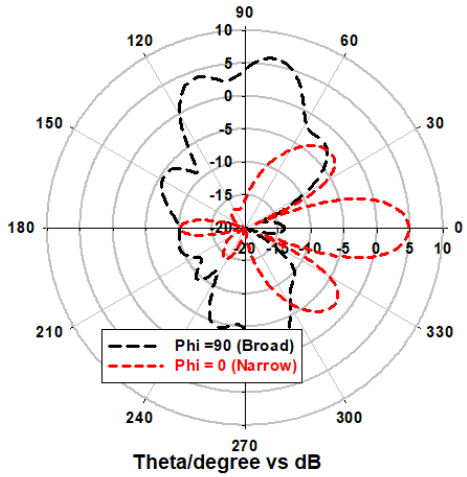

(a)

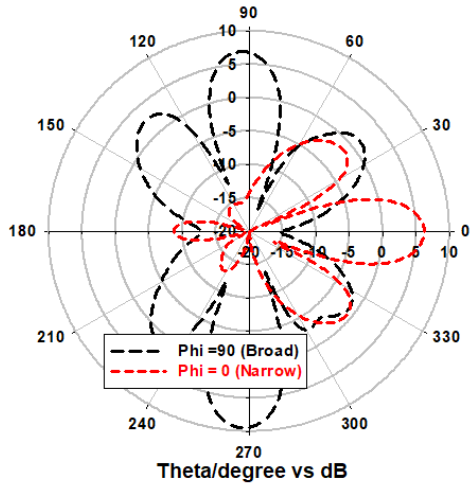

(b)

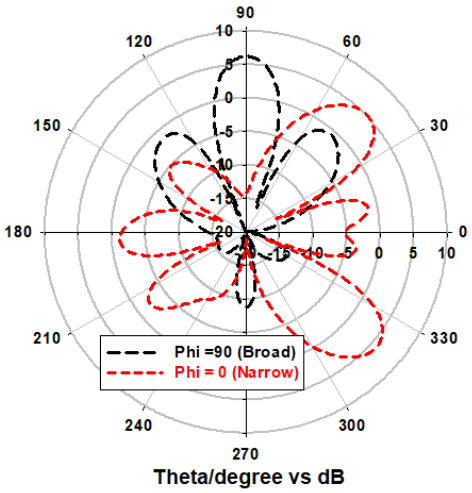

(c)

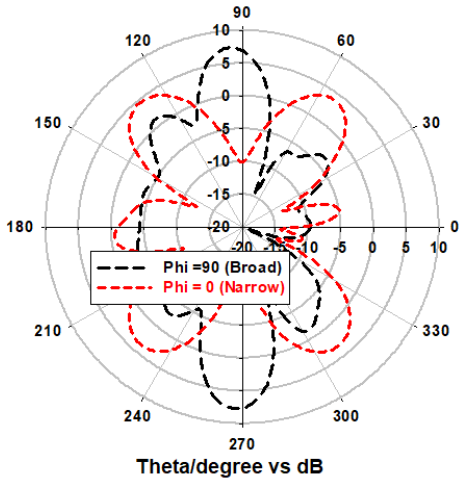

(d)

Fig. 7. The radiation patterns of the proposed antennas. (a) Antenna 1, (b) Antenna 2, (c) Antenna 3, and (d) Antenna 4.

Table 2: The performance of the proposed antennas

Variables	Ant.1	Ant.2	Ant.3	Ant.4
Frequency (GHz)	9.22	9.2	9.012	8.95
Return loss (dB)	22.7	22	13	21
Bandwidth (MHz)	400	400	200	300
Gain (dB)	6.3	6.58	6.9	7.4
Efficiency	92%	75%	87%	84%
Beams	Dual	Triple	Triple	Four

Table 3: Comparison with other works

Waveguide slots Antennas at X-band			
Parameters/Antennas	Ref. [16]	Ref. [17]	This work
Return loss (dB)	16	17	20
Frequency (GHz)	10	9.5	9.2
Gain (dB)	10	18	6.3-7.4
Efficiency (%)	90	84	75-92
Number of beams	One beam	One beam	Dual, triple and four

IV. CONCLUSION

In this work, four types of waveguide slots antennas are presented at X-band. The antennas are implemented on both broad and narrow walls of the waveguide structure to enable dual, triple, and four beams. Four slots are distributed symmetrically on the broad and narrow walls of the waveguide, whereas a total of eight slots implemented at Antenna 1, twelve slots implemented at Antenna 2 and Antenna 3, and sixteen slots implemented

at Antenna 4. The performance of the proposed antennas showed a good return loss of greater than 10 dB and a gain range of 6.3 to 7.4 dB. The dual beams with gain of 6.3 dB are obtained in both H-plane and E-plane. Antenna 2 and antenna 3 has a triple beams with gain of 6.58 dB and 6.9 dB in both broad and narrow walls directions. Antenna 4 has four beams with gain of 7.4 dB. These proposed antennas could be useful for radar and wireless applications at X-band.

ACKNOWLEDGMENT

The authors would like to thank the Ministry of Higher Education (MOHE), School of Postgraduate Studies (SPS), Research Management Centre, Advanced RF and Microwave Research Group, School of Electrical Engineering, and Universiti Teknologi Malaysia (UTM), Johor Bahru, for the support of the research under Grant 09G19/06G15/04G65.

REFERENCES

[1] N. Duc Anh and D. T. Do, "The maximal SINR selection mode for 5G millimeter-wave MIMO: Model systems and analysis," *Indonesian Journal of Electrical Engineering and Computer Scienc*., vol. 7, no. 1, pp. 150-157, 2017.

[2] I. Hosako, N. Sekine, and M. Patrashin, "At the dawn of a new era in terahertz technology," *Proceedings of the IEEE*, vol. 95, no. 8, pp. 1611-1623, 2007.

[3] T. S. Rappaport, J. N. Murdock, and F. Gutierrez, "State of the art in 60-GHz integrated circuits and systems for wireless communications," *Proceedings of the IEEE 2011*, vol. 99, no. 8, pp. 1390-436, 2011.

[4] A. M. Mousa, "Prospective of fifth generation mobile communications," *International Journal of Next-Generation Networks (IJNGN*), vol. 4, no. 3, pp. 203-207, 2012.

[5] S. Chen and J. Zhao, "The requirements, challenges, and technologies for 5G of terrestrial mobile telecommunication," *IEEE Communications Magazine*, 2014.

[6] M. W. Sabri, N. A. Murad, and M. K. A. Rahim, "Highly directive 3D printed dual beam waveguide slotted antenna for millimeterwave apllications," *Microwave and Optical Letters (MOTL*), vol. 61, pp. 1566-1573, 2019.

[7] E. Hossain, "Evolution toward 5G multi-tier cellular wireless networks: An interference management perspective," *IEEE Wireless Communications*, vol. 21, no. 3, pp. 118-127, 2014.

[8] W. Xidong, Y. Fan, and A. Jinfang, "Circularly polarized waveguide antenna with dual pairs of radiation slots at Ka-band," *IEEE Antennas and Wireless Propagation Letters*, vol. 16, pp. 2947-2950, 2017.

[9] D. Ali, S. T. Wayne, and G. Kamran, "Split-ring slot in the broad-wall of a rectangular waveguide," *IEEE Antennas and Wireless Propagation Letters*, vol. 13, pp. 991-994, 2014.

[10] L. Teng, M. Hongfu, and D. Wenbin, "Design and implementation of dual- frequency dual-polarization slotted waveguide antenna array for Ka-band application," *IEEE Antennas and Wireless Propagation Letters*, vol. 13, pp. 1317-132, 2014.

[11] D. S. Ramkiran, B. T. P. Madhav, K. Narasimha Reddy, S. Shabbeer, Pr. Jain, and S. Sowmya, "Coplanar wave guide fed dual band notched MIMO antenna," *International Journal of Electrical and Computer Engineering (IJECE)*, vol. 6, no. 4, pp. 1732-1741, 2016.

[12] K. Sakakibara, T. Watanabe, K. Sato, and K. Nishikawa, "Millimeter-wave slotted waveguide array antenna manufactured by metal injection molding for automotive radar systems," *Ieice Transactions on Communications*, E84-B (9), 2001.

[13] G. P. Le Sage, "3d printed waveguide slot array antennas, *IEEE Access*, vol. 4, pp. 1258-1265, 2016.

[14] J. Tak, A. Kantemur, Y. Sharma, and H. Xin, "A 3-D-printedw-band slotted waveguide array antenna optimized using machine learning," *IEEE Antennas and Wireless Propagation Letters*, vol. 17, no. 11, pp. 2008-2012, 2018.

[15] R. S. Elliott, *Antenna Theory and Design*, Revised Edition, John Wiley & Sons, pp. 305-315, 2003.

[16] Y. E. Yamac and A. Kizilay, "A waveguide slot array antenna design for X-band radar," *2016 9th International Kharkiv Symposium on Physics and Engineering of Microwaves, Millimeter and Submillimeter Waves (MSMW)*, Kharkiv, pp. 1-5, 2016.

[17] P. Kumar, A. Kedar, and A. K. Singh, "Design and development of low-cost low sidelobe level slotted waveguide antenna array in X-band," in *IEEE Transactions on Antennas and Propagation*, vol. 63, no. 11, pp. 4723-4731, 2015.

Modified V-Groove Slot Waveguide for DNA Hybridization Detection

Eman ELDamarawy [1,2], Ahmed M. Heikal [1,3], Salah S. A. Obayya [3*], and Mohamed Farhat O. Hameed [3,4,5*]

[1] Electronic and Electrical Engineering Department, Faculty of Engineering, Mansoura University, 35516, Egypt

[2] Basic Sciences, Higher Future Institute of Engineering and Technology in Mansoura, Mansoura 51, Egypt

[3] Centre for Photonics and Smart Materials, Zewail City of Science and Technology, October Gardens
6th of October City, Giza 12578, Egypt
sobayya@zewailcity.edu.eg*

[4] Nanotechnology and Nanoelectronics Program, Zewail City of Science and Technology, October Gardens
6th of October City, Giza 12578, Egypt
mfarahat@zewailcity.edu.eg*

[5] Mathematics and Engineering Physics Department, Faculty of Engineering, Mansoura University
Mansoura 35516, Egypt

***Abstract* —** Highly sensitive slot waveguides are introduced and studied for DNA hybridization detection. In this investigation, two different configurations based on V-groove silicon on insulator (SOI) waveguides are analyzed using full vectorial finite element method. The suggested designs rely on improving the light confinement through the slot region at an operating wavelength of 1.55 μm. The power confinement, power density (PD), and effective index of the supported modes are studied for the conventional rectangular slot waveguide and proposed designs. Further, the effect of adding a plasmonic layer to the reported slot waveguides is implemented. It has been shown that the plasmonic layer increases the light confinement in the slot region with high potential for DNA hybridization detection with good confinement through the slot region.

***Index Terms* —** DNA biosensors, DNA hybridization, plasmonics, slot waveguides, V-groove.

I. INTRODUCTION

Biosensors have many applications in our daily life such as food analysis [1], biomolecules study [2], drug development [3], crime detection [4] and medical diagnosis [5]. The biomedical sensor can integrate the biological elements with the physiochemical transducer to produce a signal that mimics any small change in the properties of the biological element. There are many kinds of biosensors such as electrochemical biosensors, optical biosensors and piezoelectric biosensors. However, optical biosensors [6] could enable direct and real-time detection of many biological and chemical substances [7]. Further, high sensitivity, compact size, remote sensing and cost-effectiveness could be realized using optical biosensors. The optical detection relies on the interaction of the optical field with a bio-recognition element. Additionally, optical biosensors are based on label free or label-based techniques. The detected signal in label free biosensor is generated by the interaction of the analyte with the transducer. However, label and the optical signal generated by a colorimetric are needed in label based biosensors.

There are many platforms that can be used for optical sensing applications such as photonic crystal [8] and silicon on insulator (SOI) [9]. In this context, SOI microring cavity was proposed for protein concentration detection [10]. Additionally, a label-free integrated biosensor based on Si_3N_4/SiO_2 slot waveguide has been used to detect the Bouie serum albumin (BSA) and anti-BSA molecular [11]. Moreover, SOI ring resonator based biosensor has been presented for protein sensing [12]. However, most optical waveguide biosensors are based on light confinement in the denser medium with limited interaction with the sensing medium. The slot waveguide has an advantage of light confinement in the slot low index region. This will improve the interaction between the light and the sensing medium with enhanced sensor sensitivity.

The DNA hybridization is a molecular biology technique that measures the degree of genetic similarity

Submitted On: December 25, 2019
Accepted On: May 5, 2020

between pools of DNA sequences. It is usually used to determine the genetic distance between two organisms. Through the DNA hybridization process, the single stranded DNA (ssDNA) is transformed into double stranded DNA (dsDNA) when the two complement ssDNA sequences are merged together. DNA hybridization detection [13] is very helpful for several applications such as genetic detection, [14], medicinal bio-engineering [15] and clinical diagnostics [16]. The DNA analysis has been performed using different techniques such as restriction fragment length polymorphism [17], short tandem repeats [18], mitochondria analysis [19] and polymerase chain reaction [20]. The electrochemical sensor [21] is the most popular DNA detection technique [22] with low cost, high sensitivity and high selectivity [23]. There are also several nanomaterials that have been used in DNA biosensors like metallic nanoparticles [24], carbon nanomaterials [25] semiconductor metal oxide [26] and two dimensional transition metal sulfide [27]. Optical biosensors have been recently used for DNA hybridization detection. Most of the DNA biosensors rely on dielectric materials with different configurations [28] such as Mach-Zehnder interferometer [29]. Additionally, the light can be strongly confined in the slot waveguide by using surface plasmon polaritons (SPPs) [30]. The SPPs are resulted from the light interaction with the surface free electrons of the metal. Gold and silver [31] are the widely used metals in sensing applications due to their high conductivity with low Ohmic losses. The silver has high detection accuracy [32] with low chemical stability owing to its oxidation problem. Therefore, it is difficult to obtain reproducible results and hence the silver based sensor is not reliable for practical applications [33].

In this paper, the potential of using V-groove SOI based slot waveguides is introduced for DNA hybridization detection. The rectangular slot biosensor has been previously reported [7] for DNA hybridization detection. In order to increase the confinement of the field in the slot region, V-groove slot types are presented in this work. The V-groove shape can be achieved by etching the edges with an angle θ. This angle has a significant effect on the light confinement through the slot region. Therefore, a modified V-groove design is suggested to simplify the fabrication process and achieve good confinement with a good potential for detecting DNA hybridization. The possibility of adding plasmonic material to the reported designs is also implemented. It is found that the field confinement through the slot region and the power density (*PD*) in the DNA layers are improved significantly using the plasmonic material. Therefore, the DNA hybridization detection could be achieved effectively.

II. DESIGN CONSIDERATIONS

Figure 1 shows schematic diagrams of the conventional rectangular slot waveguide, V-groove and modified V-groove structures. The conventional structure consists of two silicon waveguides with width W, length H and refractive index (RI) of 3.476 [7] at a wavelength of 1550 nm. The silicon nanowires are separated by a distance of SW and are placed over SiO_2 layer with RI = 1.444 as shown in $Fig.$ 1 (a). Further, the silicon waveguides are covered by a linker layer (silanes) with RI and thickness t_{Linker} of 1.42 and 1 nm, respectively [34]. Then, single-stranded DNA (ssDNA) (probe layer) of thickness t_{DNA} = 8 nm and RI= 1.456 is used. The double-stranded DNA (dsDNA) with RI=1.53 [35] will be formed due to the hybridization process with fixed layer thickness. Initially, the silicon waveguides have H = 320 nm, W = 180 nm and SW = 40 nm surrounded by an analyte H_2O with refractive index of 1.31. *Figure* 1 (b) illustrates the V-groove slot waveguide with an angle θ and fixed height (H) similar to the rectangular waveguide. In the modified V-groove, the parameter g shown in $Fig.$ 1 (c) stands for the minimal bottom gap distance between the two layers of the DNA which is taken as g=22 nm.

III. NUMERCAL METHOD

From Maxwell's equations, the vector wave equation of the magnetic field will be as follows:

$$\nabla \times \left(\varepsilon_r^{-1}\nabla \times \vec{H}\right) - \omega^2 \mu_0 \vec{H} = 0, \qquad (1)$$

where ω is the angular frequency, μ_0 is the free space permeability and $\varepsilon = \varepsilon_0\varepsilon_r$ is the permittivity of the waveguide material, ε_0 is the free space permittivity and ε_r is relative permittivity of the composing material. The cross section of the waveguide structure is discretized using vector finite element method [36]. The following eigenvalue equation can be derived:

$$[K]\{H\} - \beta^2[M]\{H\} = \{0\}, \qquad (2)$$

where [K] and [M] are the global stiffness and mass matrices, {H} is the global magnetic field vector, {0} is the null vector and $\boldsymbol{\beta}$ is the propagation constant. The eigenvalue equation can be solved to obtain the eigenvector H, and the corresponding eigenvalue $\boldsymbol{\beta}$. Then, the effectively index of the supported mode is calculated from $n_{eff}=\boldsymbol{\beta}/K$ where K is the free space wave number.

The full vectorial finite element method (FVFEM) via Comsol Multiphysics software package [37] is utilized to study the optical characteristics of the suggested designs. In this study, total number of elements of 55181 is used with perfect matched layer boundary conditions and minimum element size of 0.04 nm.

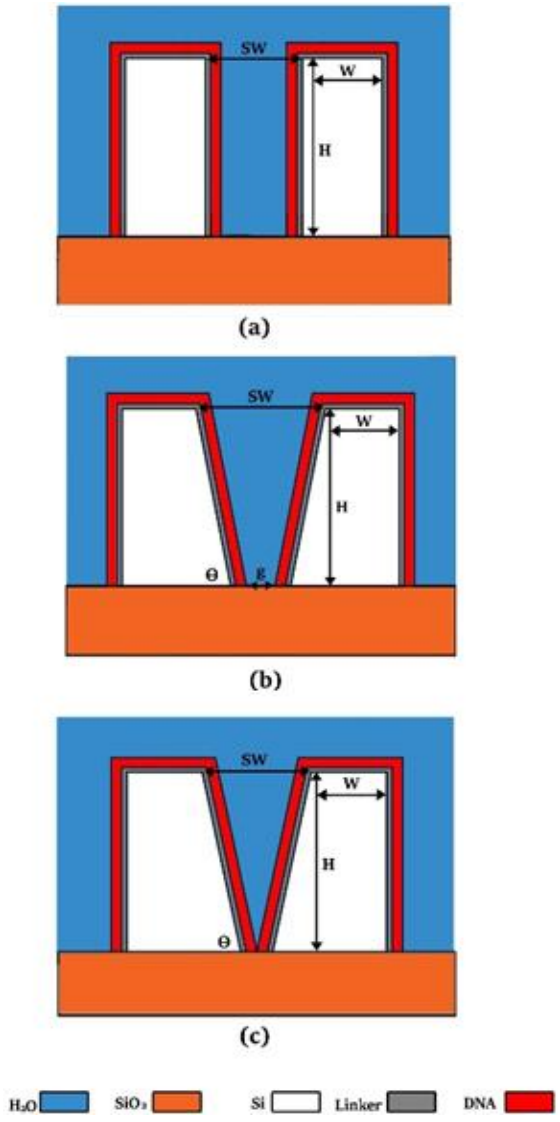

Fig. 1. Schematic diagrams of the: (a) rectangular waveguide, (b) modified V-groove SOI, and (c) V-groove SOI for DNA hybridization detection.

IV. RESULTS AND DISCUSSION

Figure 2 illustrates the E_x field component of the supported transverse electric (TE) mode of the rectangular, V-groove and modified V-groove designs at λ=1.55 μm. Further, the power flow P_z in the z-direction through the studied designs is shown in $Fig.$ 2. It is revealed from this figure that high field confinement is achieved in the low index region due to the high index contrast between the analyte and the silicon nanowires. The highest field confinement is achieved using the V-groove based designs. Therefore, it is expected that the V-groove based biosensors can achieve high sensitivity for DNA hybridization detection. In this work, the power over the DNA region is normalized to the total power through the studied waveguide as shown in equation (3). The power density (*PD*) can be obtained from the normalized power confinement divided by the area of the DNA layer as represented in equation (4). The highest *PD* through the proposed designs is achieved by the V-groove structure which confirms the field confinement shown in $Fig.$ 2.

Normalized power confinement %=

$$\frac{Power\ over\ the\ DNA\ region}{Total\ power\ over\ the\ waveguide}\times 100\%, \quad (3)$$

$$\text{Power density}=\frac{Normalized\ power\ confinement\ \%}{Area\ of\ the\ DNA\ reion}. \quad (4)$$

The main purpose of these designs is to improve the light confinement in the slot region. Therefore, the DNA hybridization detection capability can be increased. Consequently, the geometrical parameters of the V-groove and modified V-groove structures will be studied. First, the effect of the silicon waveguide width W is investigated. In this study, the silicon waveguide height is taken as 320 nm, θ = 77, and g = 22 nm. Figures 3 (a) and (c) show the effective index n_{eff} and δn_{eff} dependence of the quasi-TE mode for the ssDNA and dsDNA cases on the silicon waveguide width W for the V-groove and modified V-groove, respectively. Additionally, Figs. 3 (b), and (d) illustrate the dependence of the *PD* on the width (W). The change in the effective index δn_{eff} of the supported mode can be defined as $\delta n_{eff}= n_{eff-dsDNA} - n_{eff-ssDNA}$. The δn_{eff} is obtained by simulating the proposed design with ssDNA layer (n=1.456) above the linker layer. Then, the ssDNA is replaced by dsDNA with n=1.53. It may be seen that the maximum δn_{eff} is obtained at W = 210 nm of the V-groove as shown in Fig. 3 (a). Further, maximum PD also occurs at $W = 210\ nm$ as shown in Fig. 3 (b) due to the well confinement of the mode in the slot region. Therefore, a good light interaction with the analyte in the slot region can be achieved with expected high sensor sensitivity. It is worth noting that the ssDNA has a smaller refractive index than that of the dsDNA. Consequently, the PD through the ssDNA case is greater than that of the dsDNA as revealed from Fig. 3. It is also evident from Figs. 3 (c) and (d) that the maximum δn_{eff} and PD of the modified V-groove are achieved at W = 200 nm and 170 nm, respectively. Therefore, $W = 170\ nm$ is chosen for the next simulations of the modified V-grove design to have good light interaction with the studied analyte.

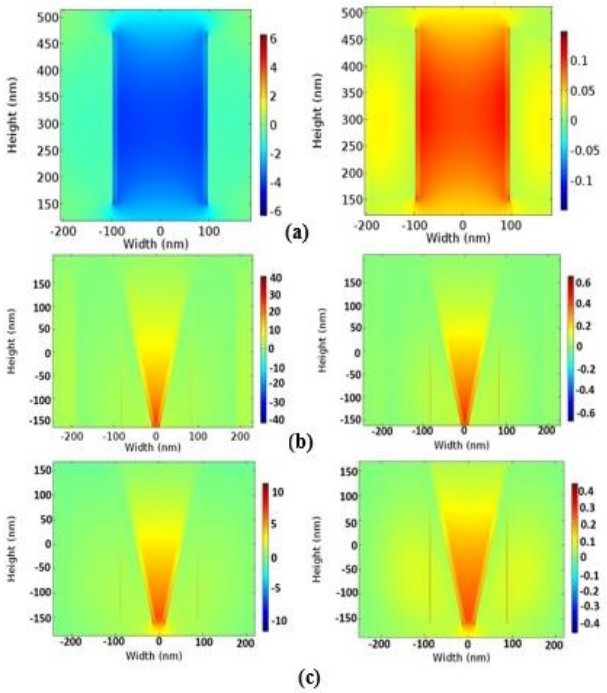

Fig. 2. The E_x field component and the power flow P_z of the quasi-TE mode at λ = 1.55 µm of the: (a) rectangular waveguide, (b) V-groove, and (c) and modified V-groove structures.

The effect of the waveguide height H is next studied at $W = 210\ nm$ for the V-groove design and at $W = 170\ nm$ for the modified V-groove. Figures 4 (a) and (b) show the dependence of the PD through the $ssDNA$ and $dsDNA$ layers on the silicon waveguide height of the V-groove and modified V-groove designs. It is evident from $Fig.$ 4 that the maximum PD is obtained at H = 220 nm of the V-groove and modified V-groove with high field confinement through the slot region. It should be noted that a height of 220 nm is chosen according to the well-known standard height of the SOI waveguide to simplify the fabrication process. Additionally, H >220 nm is studied to ensure the etching feasibility of the suggested design.

The effect of the angle θ is then studied through $Figs.$ 5. (a) and (b). In this investigation, W = 210 nm and H = 220 nm for the V-groove design. However, the modified V-groove design has W = 170 nm, H =220 nm and g = 12 nm. It may be seen that an angle $\theta = 86^{o}$ results in maximum PD for both the V-groove and modified V-groove which could achieve high DNA hybridization detection. $Figure$ 5 (c) shows the effect of the distance g of the modified V-groove at $\theta = 86^{o}$ where maximum PD occurs at g= 12 nm. If the gap is decreased to 5 nm, the PD will be significantly decreased to 2.26 for ssDNA and 2.13 for dsDNA cases.

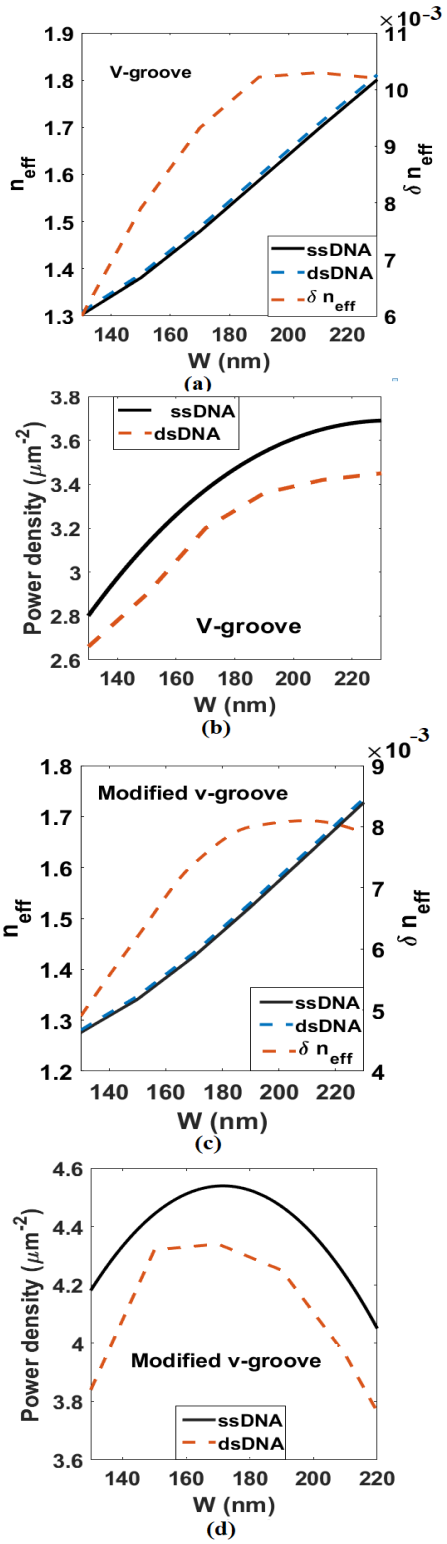

Fig. 3. Dependence of the n_{eff}, δn_{eff} and PD of the quasi-TE mode on the width (W) of the: (a), (b) V-groove, and (c), (d) modified V-groove designs using $ssDNA$ and $dsDNA$ layers.

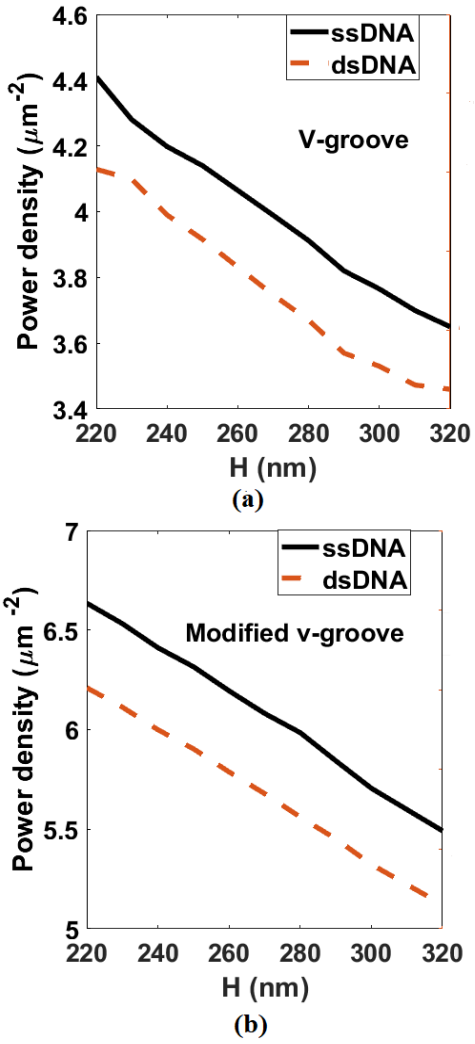

Fig. 4. Dependence of the *PD* of the quasi-TE mode with $ssDNA$ and $dsDNA$ layers on the height (H) of the: (a) V-groove and (b) modified V-groove designs using ssDNA and dsDNA layers.

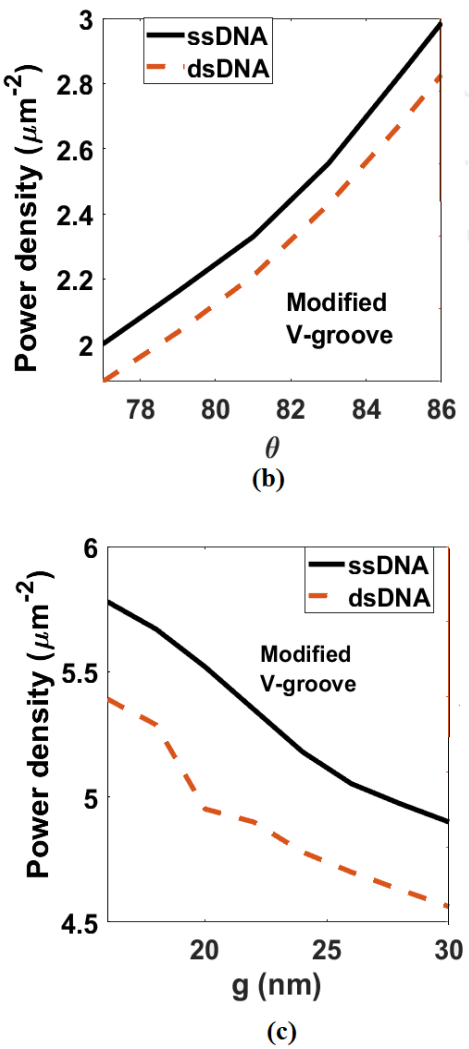

Fig. 5. Dependence of the *PD* of the quasi-TE mode of the proposed designs on the angle θ for the: (a) V-groove, and (b) modified V-groove using ssDNA and dsDNA layers. Fig. 5 (c) illustrates the *PD* of the quasi-TE mode variation with the distance (g) nm of the modified V-groove structure.

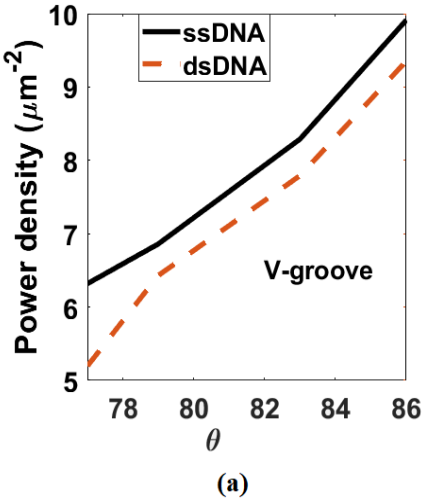

Next, a gold layer is added above the SiO_2 material to improve the light confinement in the slot region as shown in Fig. 6. Then, the DNA hybridization detection capability could be improved. The gold layer with thickness (t) has the following relative permittivity [38,39]:

$$\varepsilon_{Au}(\omega) = \varepsilon_{\infty} - \frac{\omega_p^2}{\omega(\omega + i\omega_\tau)}, \quad (5)$$

where ε_∞ = 9.75, ω_p = 1.36 × 10^{16} (rad/sec) and ω_τ = 1.45 × 10^{14} (rad/sec). In this investigation, the V-groove design has H = 220 nm, t (gold thickness) = 50 nm and θ = 86°. The *PD* dependence on the silicon width is first studied as shown in $Fig.$ 7. The figure shows that the V-

groove has high light confinement at W = 240 nm which differs from the geometrical parameters of the V-groove without plasmonic material. *Figure* 7 (b) shows that the appropriate width for the modified V-groove is equal to W = 250 nm with maximum *PD*.

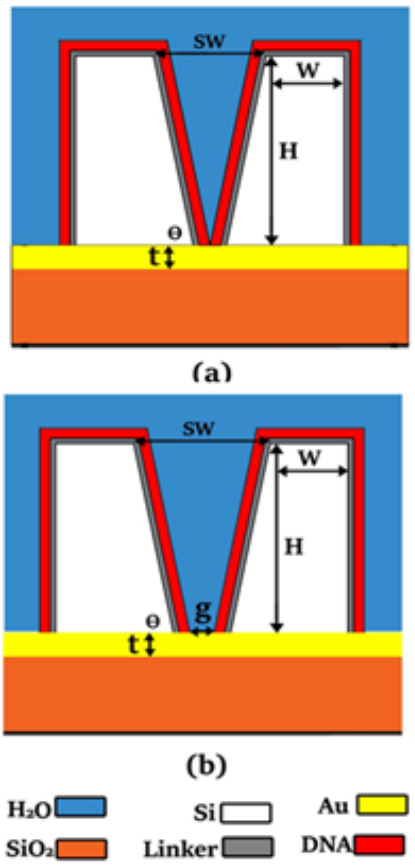

Fig. 6. Schematic diagram of the plasmonic: (a) V-groove and (b) modified V-groove designs.

The effect of the angle θ will be studied for the two suggested designs; V-groove and modified V-groove. As θ increases, the light confinement through the slot region and the *PD* of the supported quasi TE mode are increased for the V-groove and modified V-groove designs as shown in $Fig.9$. The highest *PD* of the V-groove and modified V-groove designs are obtained at θ =80° with high field confinement in the slot region. It may be also seen that the ssDNA has higher *PD* than that occurs for the dsDNA case. This is because of the smaller RI of the ssDNA than the dsDNA.

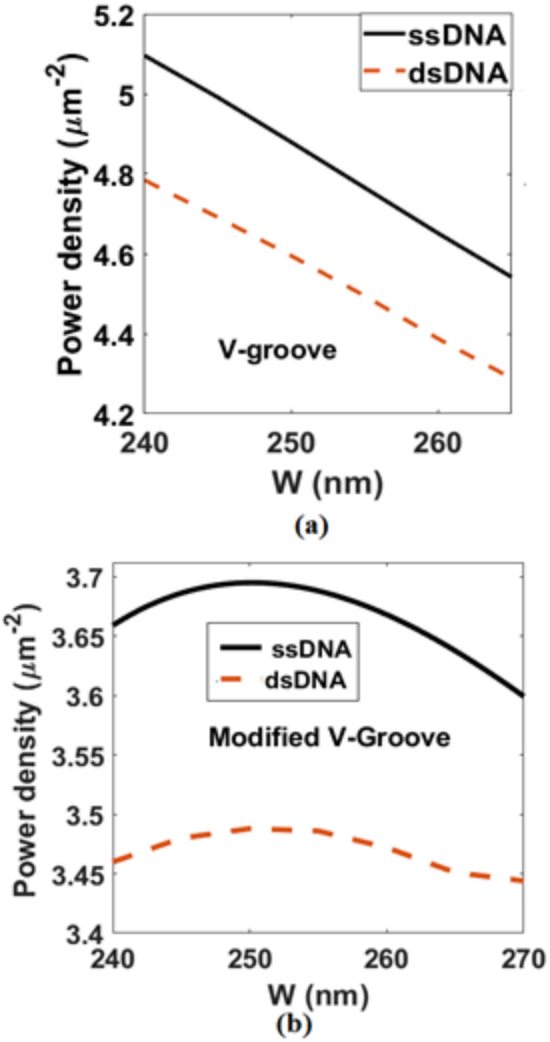

Fig. 7. Dependence of the *PD* of the quasi-TE mode of the plasmonic designs with $ssDNA$ and $dsDNA$ layers and gold layer with t=50nm on the width (W) of the: (a) V-groove and (b) modified V-groove designs.

The impact of the waveguide height H is next studied at W = 240 nm for the plasmonic V-groove design. For the modified V-groove design, $W = 250\ nm$ is taken for this study. The dependence of the *PD* though the plasmonic designs with $ssDNA$ and $dsDNA$ layers on the silicon waveguide height of the V-Groove and modified V-groove designs is shown in *Fig.* 8 at t=50 nm. *Figure* 8 (a) shows that the highest *PD* occurs at H = 220 nm of the V-groove and at $H = 240\ nm$ for the

modified V-groove with high field confinement through the slot region.

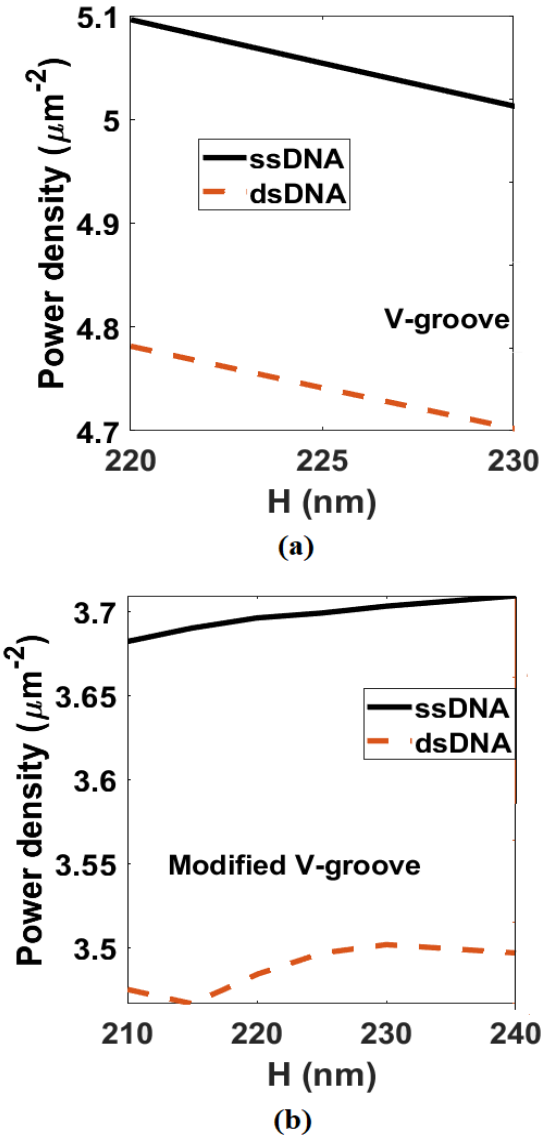

Fig. 8. Variation of the *PD* at t= 50nm with width (H) and its *PD* of the: (a) V-groove and (b) modified V-groove designs with ssDNA and dsDNA layers.

The effect of the distance $g\ (nm)$ in the modified V-groove is also introduced at $t = 50\ nm$ as shown in $Fig.10$. It can be seen that the maximum *PD* occurs at $g = 50\ nm$ for high filed confinement through the slot region. Finally, the thickness (t) of the plasmonic layer is studied to enhance the field confinement in the slot region. $Figure\ 11$ shows that the best thickness for both V-groove and modified V-groove will be obtained at $t = 50\ nm$ which will be appropriate for the fabrication process. The optimum geometrical parameters of the plasmonic V-groove designs are summarized in Table 1 to obtain maximum *PD* and maximum confinement.

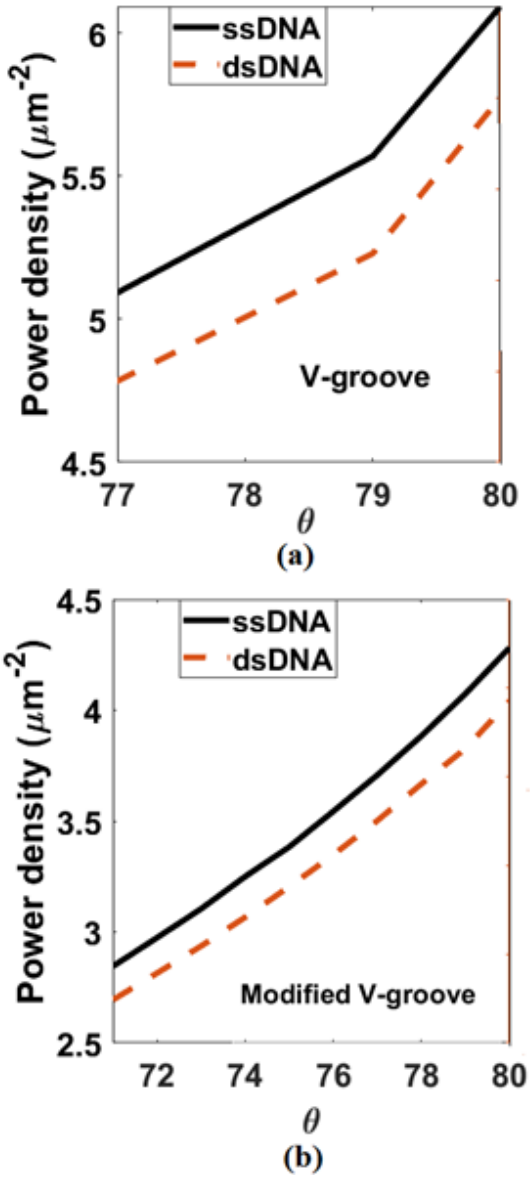

Fig. 9. Variation of the *PD* at t= 50 nm with an angle (θ) and its *PD* for the: (a) V-groove and (b) modified V-groove designs with ssDNA and dsDNA layers.

The fabrication of the suggested designs can be achieved using the standard SOI fabrication technology [40]. In this context, conventional rectangular slot waveguide is previously implemented in [41]. Additionally, the fabrication of V-groove structure has been reported in different applications [42, 43, 44]. Further, the deposition of plasmonic materials over SOI waveguides can be realized by atomic layer deposition [45]. Therefore, the suggested designs can be realized using the current technology.

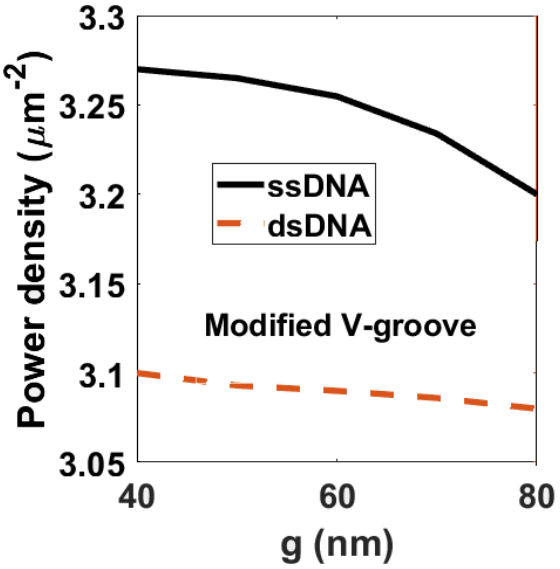

Fig. 10. Variation of the *PD* at $t = 50\,nm$ with the distance $(g)nm$ for modified v-groove design with ssDNA and dsDNA layers.

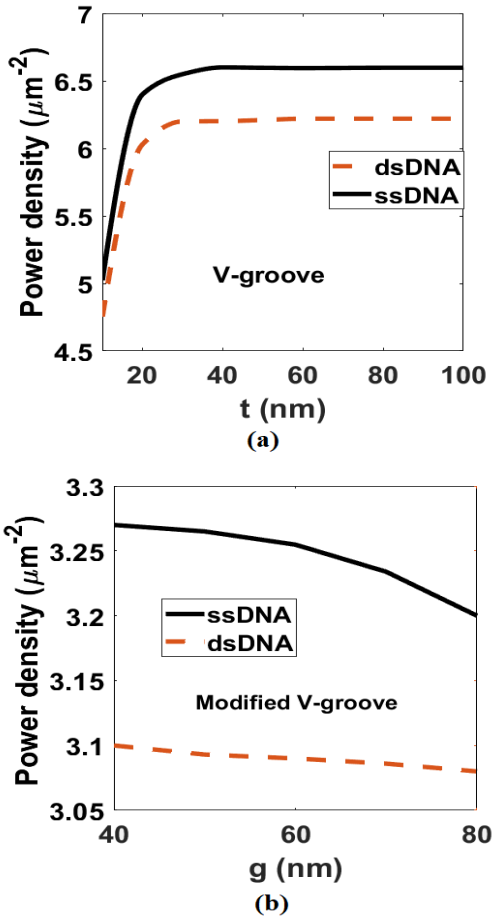

Fig. 11. Variation of the *PD* with the gold layer thickness (t) nm for the: (a) V-groove and (b) modified V-groove designs with ssDNA and dsDNA layers.

Table 1: The optimized parameters of the plasmonic V-groove and modified V-groove SOI structures

Parameter	V-groove	Modified V-groove
t	50 nm	50 nm
W	240 nm	250 nm
H	220 nm	240 nm
θ	80°	80°
g	-	40 nm

V. CONCLUSION

Modified slot waveguides are suggested and optimized for DNA hybridization detection capabilities. This is due to the dependence of the refractive index of the DNA layer on the hybridization process. In this investigation, three designs are studied including rectangular waveguide, V-groove and modified V-groove structure based on SOI platform. It is found that the power confinement and *PD* of the V-groove slot waveguide is higher than those of the other designs. However, the modified V-design is easier for real implementation. Further, the addition of plasmonic layer increases the light confinement in the low index region with high potential for DNA hybridization detection with good confinement through the slot region.

REFERENCES

[1] A. Agrawal, R. A. Tripp, L. J. Anderson, and S. Nie, "Real-time detection of virus particles and viral protein expression with two-color nanoparticle probes," *J. Virol.*, vol. 79, no. 13, pp. 8625-8628, 2005.

[2] K. Kneipp, *et al.*, "Single molecule detection using surface-enhanced Raman scattering (SERS),"

Phys. Rev. Lett., vol. 78, no. 9, p. 1667, 1997.

[3] M. D. Hämäläinen, *et al.*, "Characterization of a set of HIV-1 protease inhibitors using binding kinetics data from a biosensor-based screen," *J. Biomol. Screen.*, vol. 5, no. 5, pp. 353-359, 2000.

[4] S. Sumriddetchkajorn and A. Somboonkaew, "Thermal analyzer enables improved lie detection in criminal-suspect interrogations," *SPIE Newsroom Def. Secur.*, 2011.

[5] L. Heinemann and G. Schmelzeisen-Redeker, "Non-invasive continuous glucose monitoring in Type I diabetic patients with optical glucose sensors," *Diabetologia*, vol. 41, no. 7, pp. 848-854, 1998.

[6] M. F. O. Hameed, Y. K. A. Alrayk, A. A. Shaalan, W. S. El Deeb, and S. S. A. Obayya, "Design of highly sensitive multichannel bimetallic photonic crystal fiber biosensor," *J. Nanophotonics*, vol. 10, no. 4, 2016 .

[7] T. Dar, J. Homola, B. M. A. Rahman, and M. Rajarajan, "Label-free slot-waveguide biosensor for the detection of DNA hybridization," *Appl. Opt.*, vol. 51, no. 34, pp. 8195-8202, 2012.

[8] N. F. F. Areed, M. F. O. Hameed, and S. S. A. Obayya, "Highly sensitive face-shaped label-free photonic crystal refractometer for glucose concentration monitoring," *Opt. Quantum Electron.*, vol. 49, no. 1, 2017.

[9] M. F. O. Hameed, A. S. Saadeldin, E. M. A. Elkaramany, and S. S. A. Obayya, "Label-free highly sensitive hybrid plasmonic biosensor for the detection of DNA hybridization," *J. Light. Technol.*, vol. 35, no. 22, pp. 4851-4858, 2017.

[10] K. De Vos, I. Bartolozzi, E. Schacht, P. Bienstman, and R. Baets, "Silicon-on-Insulator microring resonator for sensitive and label-free biosensing," *Opt. Express*, vol. 15, no. 12, pp. 7610-7615, 2007.

[11] C. A. Barrios, *et al.*, "Label-free optical biosensing with slot-waveguides," *Opt. Lett.*, vol. 33, no. 7, pp. 708-710, 2008.

[12] T. Claes, J. G. Molera, K. De Vos, E. Schacht, R. Baets, and P. Bienstman, "Label-free biosensing with a slot-waveguide-based ring resonator in silicon on insulator," *IEEE Photonics J.*, vol. 1, no. 3, pp. 197-204, 2009.

[13] J. Guo, J. Wang, J. Zhao, Z. Guo, and Y. Zhang, "Ultrasensitive multiplexed immunoassay for tumor biomarkers based on DNA hybridization chain reaction amplifying signal," *ACS Appl. Mater. Interfaces*, vol. 8, no. 11, pp. 6898-6904, 2016.

[14] Z. Cheglakov, T. M. Cronin, C. He, and Y. Weizmann, "Live cell microRNA imaging using cascade hybridization reaction," *J. Am. Chem. Soc.*, vol. 137, no. 19, pp. 6116-6119, 2015.

[15] S. X. Chen and G. Seelig, "An engineered kinetic amplification mechanism for single nucleotide variant discrimination by DNA hybridization probes," *J. Am. Chem. Soc.*, vol. 138, no. 15, pp. 5076-5086, 2016.

[16] N. S. Gabr, A. K. Ahmed, U. S. Belal, R. A. M. Abd Rabou, R. F. Ahmed, and E. H. Abdel-Hafeez, "Molecular characterization of Cryptosporidium isolates from humans by nested polymerise chain reaction-restriction fragment length polymorphism (nPCR-RFLP) analysis in Egypt," *Trop. Biomed.*, vol. 36, no. 1, pp. 1-10, 2019.

[17] R. Yano, O. Shimoda, T. Okitsu, M. Sakurada, and Y. Ueno, "Development of a modified p-dimethylaminocinnamaldehyde solution for touch DNA analysis and its application to STR analysis," *Forensic Sci. Int. Genet.*, vol. 38, pp. 86-92, 2019.

[18] T. Devièse, *et al.*, "Compound-specific radiocarbon dating and mitochondrial DNA analysis of the Pleistocene hominin from Salkhit Mongolia," *Nat. Commun.*, vol. 10, no. 1, p. 274, 2019.

[19] E. T. Lagally, C. A. Emrich, and R. A. Mathies, "Fully integrated PCR-capillary electrophoresis microsystem for DNA analysis," *Lab Chip*, vol. 1, no. 2, pp. 102-107, 2001.

[20] S. Z. Mousavisani, J. B. Raoof, R. Ojani, and Z. Bagheryan, "An impedimetric biosensor for DNA damage detection and study of the protective effect of deferoxamine against DNA damage," *Bioelectrochemistry*, vol. 122, pp. 142-148, 2018.

[21] H. Gao, M. Sun, C. Lin, and S. Wang, "Electrochemical DNA biosensor based on graphene and TiO2 nanorods composite film for the detection of transgenic soybean gene sequence of MON89788," *Electroanalysis*, vol. 24, no. 12, pp. 2283-2290, 2012.

[22] A. A. Ensafi, N. Kazemnadi, M. Amini, and B. Rezaei, "Impedimetric DNA-biosensor for the study of dopamine induces DNA damage and investigation of inhibitory and repair effects of some antioxidants," *Bioelectrochemistry*, vol. 104, pp. 71-78, 2015.

[23] M. Y. Azab, M. F. O. Hameed, A. M. Nasr, and S. S. A. Obayya, "Label free detection for DNA hybridization using surface plasmon photonic crystal fiber biosensor," *Opt. Quantum Electron.*, vol. 50, no. 2, 2018.

[24] M. Fojta, A. Daňhel, L. Havran, and V. Vyskočil, "Recent progress in electrochemical sensors and assays for DNA damage and repair," *TrAC Trends Anal. Chem.*, vol. 79, pp. 160-167, 2016.

[25] H. Huang, W. Bai, C. Dong, R. Guo, and Z. Liu, "An ultrasensitive electrochemical DNA biosensor based on graphene/Au nanorod/polythionine for human papillomavirus DNA detection," *Biosens. Bioelectron.*, vol. 68, pp. 442-446, 2015.

[26] M. R. Saidur, A. R. A. Aziz, and W. J. Basirun, "Recent advances in DNA-based electrochemical

biosensors for heavy metal ion detection: A review," *Biosens. Bioelectron.*, vol. 90, pp. 125-139, 2017.

[27] J. Lee, M. Morita, K. Takemura, and E. Y. Park, "A multi-functional gold/iron-oxide nanoparticle-CNT hybrid nanomaterial as virus DNA sensing platform," *Biosens. Bioelectron.*, vol. 102, pp. 425-431, 2018.

[28] C. Viphavakit, M. Komodromos, C. Themistos, W. S. Mohammed, K. Kalli, and B. M. A. Rahman, "Optimization of a horizontal slot waveguide biosensor to detect DNA hybridization," *Appl. Opt.*, vol. 54, no. 15, pp. 4881-4888, 2015.

[29] S. A. Maier, "Plasmonics: Metal nanostructures for subwavelength photonic devices," *IEEE J. Sel. Top. quantum Electron.*, vol. 12, no. 6, pp. 1214-1220, 2006.

[30] M. Y. Azab, M. F. O. Hameed, and S. S. A. Obayya, "Multi-functional optical sensor based on plasmonic photonic liquid crystal fibers," *Opt. Quantum Electron.*, vol. 49, no. 2, 2017.

[31] K. A. Willets and R. P. Van Duyne, "Localized surface plasmon resonance spectroscopy and sensing," *Annu. Rev. Phys. Chem.*, vol. 58, pp. 267-297, 2007.

[32] K. Q. Le, J. Bai, Q. M. Ngo, and P.-Y. Chen, "Fabrication and numerical characterization of infrared metamaterial absorbers for refractometric biosensors," *J. Electron. Mater.*, vol. 46, no. 1, pp. 668-676, 2017.

[33] E. L. S. Wong and J. J. Gooding, "Charge transfer through DNA: a selective electrochemical DNA biosensor," *Anal. Chem.*, vol. 78, no. 7, pp. 2138-2144, 2006.

[34] M. D. Malinsky, K. L. Kelly, G. C. Schatz, and R. P. Van Duyne, "Chain length dependence and sensing capabilities of the localized surface plasmon resonance of silver nanoparticles chemically modified with alkanethiol self-assembled monolayers," *J. Am. Chem. Soc.*, vol. 123, no. 7, pp. 1471-1482, 2001.

[35] X. Li *et al.*, "Sensitive label-free and compact biosensor based on concentric silicon-on-insulator microring resonators," *Appl. Opt.*, vol. 48, no. 25, pp. F90-F94, 2009.

[36] S. S. A. Obayya, B. M. A. Rahman, and H. A. El-Mikati, "New full-vectorial numerically efficient propagation algorithm based on the finite element method," *J. Light. Technol.*, vol. 18, no. 3, pp. 409-415, 2000.

[37] C. Multiphysics, "Introduction to COMSOL Multiphysics®," *COMSOL Multiphysics, Burlington, MA*, accessed Feb., vol. 9, p. 2018, 1998.

[38] A. M. Heikal, M. F. O. Hameed, and S. S. A. Obayya, "Improved trenched channel plasmonic waveguide," *J. Light. Technol.*, vol. 31, no. 13, pp. 2184-2191, 2013.

[39] S. Obayya, M. F. O. Hameed, and N. F. F. Areed, *Computational Liquid Crystal Photonics: Fundamentals, Modelling and Applications*. John Wiley & Sons, 2016.

[40] G. K. Celler and S. Cristoloveanu, "Frontiers of silicon-on-insulator," *J. Appl. Phys.*, vol. 93, no. 9, pp. 4955-4978, 2003

[41] P. Steglich, C. Villringer, S. Pulwer, M. Casalboni, and S. Schrader, "Design optimization of silicon-on-insulator slot-waveguides for electro-optical modulators and biosensors," in *Photoptics 2015*, Springer, pp. 173-187, 2016.

[42] A. d'Alessandro, B. Bellini, D. Donisi, R. Beccherelli, and R. Asquini, "Nematic liquid crystal optical channel waveguides on silicon," *IEEE J. Quantum Electron.*, vol. 42, no. 10, pp. 1084-1090, 2006.

[43] http://www.o-eland.com/passive/FiberArray/vgroove.htm

[44] H.-L. Hsiao, *et al.*, "Compact and passive-alignment 4-channel× 2.5-Gbps optical interconnect modules based on silicon optical benches with 45 micro-reflectors," *Opt. Express*, vol. 17, no. 26, pp. 24250-24260, 2009.

[45] S.-B. Kang, Y. Chae, C. Park, and S. Lee, "Method for forming metal layer using atomic layer deposition." *Google Patents*, Jan. 16, 2001.

Integrated Simulation and Analysis of Super Large Slotted Waveguide Array

Chang Zhai, Yingyu Liu, Shugang Jiang, Zhongchao Lin, and Xunwang Zhao

Shaanxi Key Laboratory of Large Scale Electromagnetic Computing
Xidian University, Xi'an, Shaanxi 710071, China
zaishuiyifang131@126.com

Abstract ─ Aiming at the simulation problem of the super large slotted waveguide array antenna, the parallel higher-order method of moment is used and the coupling effect between each slot element is taken into account to perform the integrated and accurate simulation. In order to ensure that the algorithm is efficient and stable in the parallel process, the BDPLU strategy is introduced to reduce the communication pressure and eliminates the redundant communication of the equation solving when pivoting, which speeds up the process of matrix equation solving. According to different types of waveguide port forms, the computation of rectangular wave port and coaxial wave port is studied, and a new parallel matrix filling technique of wave port is used to accelerate the matrix filling process. Numerical examples calculated at "Tianhe-2" supercomputer show that the algorithm can efficiently and accurately handle the simulation analysis of most types of complex slotted waveguide array.

Index Terms ─ BDPLU algorithm, higher-order MoM, parallel algorithm, slotted waveguide array antenna, wave port.

I. INTRODUCTION

Slotted waveguide array antennas are widely used in microwave communication, military radar and other fields because of its low side-lobe and high gain characteristics [1,2,15]. In the military field, slotted waveguide array antennas are often used as receiver and transmitter in large radar systems. Such as the airborne radars for various types of aircraft, the guidance radars in weapon guidance systems and missile defense systems. In the civilian field, the high-speed development of 5G communication has increasingly higher performance requirements for base station antennas. As a kind of antenna with low ohmic loss in high-frequency, slotted waveguide array antennas are gradually being used as a new generation of 5G antennas. Therefore, with the development of computer technology, accurate and rapid simulation can effectively shorten the antenna design cycle and improve the antenna design efficiency. As one of the important method of antenna design, numerical simulation has been paid more attention in the design of slotted waveguide array antennas. For the simulation of slotted waveguide array antenna, the mainstream research methods are divided into two categories: high frequency and low frequency. High-frequency methods include Physical Optics (PO), Uniform Theory of Diffraction (UTD), Shooting and Bouncing Ray (SBR), etc. The advantages of those methods are faster calculation and low resource consumption. But the disadvantage is that those methods cannot calculate the coupling effect between the units, so the accuracy of those methods are lower and the error between simulation and practice is larger. Low frequency methods include Method of Moments (MoM), Finite Element Method (FEM), Finite-Difference Time-Domain (FDTD), etc. The advantage of those methods is that the calculation is accurate, but the disadvantages are that they need long calculation time and high resource consumption. Therefore, the paper [3, 4] proposed a hybrid method of high frequency method and low frequency method for antenna simulation, which can increase the scale of the problem and improve the efficiency of the solution while losing some accuracy. The paper [5] uses the parallel domain decomposition method to analyze the slotted waveguide array antennas, and achieves the accuracy requirements by combining the finite element method, the boundary element method and the fast multiple method (FMM). The paper [13] combines MoM with the method of generalized equivalent circuit to carry out a computational study of broadband waveguide. However, so far in the published paper, there are still few mentions of accurately integrated simulation of super large slotted waveguide array antennas with more than 4000 units.

Traditional simulation algorithms use the fast approximation algorithms such as the iterative algorithms (like the multilevel fast multipole algorithm) and the high-low frequency hybrid algorithms (like PO-MoM and PO-FEM). But when dealing with such super large slotted waveguide array antennas, the convergence of the algorithm cannot be guaranteed and

Submitted On: March 5, 2020
Accepted On: May 13, 2020

the accuracy of engineering applications is difficult to achieve. Therefore, in order to solve this problem, this paper uses the previously completed parallel higher-order MoM kernels [6-8], which uses the higher-order basis functions instead of the traditional RWG (Rao-Wilton-Glisson) basis functions that can greatly reduce the unknowns of MoM. At the same time we introduce parallel computing technology to expand the solution scale of MoM and break the frequency limit. So the MoM can solve high-frequency complex electromagnetic simulation problems. In order to ensure the efficiency and stability of the solution of the matrix equation of the large-scale electromagnetic simulation problems, a new matrix equation solving algorithm BDPLU (Block Diagonal Pivoting LU Decomposition) is proposed by studying the matrix characteristics of the higher-order MoM. This algorithm can alleviate the problem of communication congestion when solving very large matrices. The BDPLU algorithm changes the traditional principal component selection strategy, completely eliminating the communication of the process of the principal component selection in the LU decomposition process, speeding up the process of the matrix equation solution, and avoiding the unstable factors caused by dense and frequent decomposition matrix communication. The comparison results for a single waveguide slot antenna between this algorithm and the commercial software FEKO are given to prove the accuracy of this algorithm. With the help of the "Tianhe II" supercomputer, a wide-side waveguide slot array antenna and a narrow-side waveguide slot array antenna are simulated by this algorithm using 19200 CPU cores. The number of the units of the two slotted array antenna are both more than 4000 and the computing time of them are both about 4.5h. Numerical examples show that the algorithm used in this paper can stably and efficiently solve the simulation problems of different types of super large slotted waveguide array antenna. And this algorithm provides an effective and reliable guarantee for the future analysis and design of super large slotted waveguide array antenna.

II. THEORETICAL ANALYSIS

A. Higher-order moment of method

For the electrically large scale problem, the traditional RWG MoM will produce a huge complex dense matrix. Therefore, large resource consumption and long calculation time make MoM difficult to effectively deal with such problems. Compared with the traditional RWG basis functions to establish the current continuity equation on the surface of a pair of triangulars, higher-order MoM introduces a higher-order polynomial basis functions and the equation is established by using a bilinear surface. The increase of the basis functions' order can use fewer basis functions to simulate the current distribution, thereby greatly reducing the unknown quantity of the complex dense matrix produced by the higher-order MoM. The number of unknowns produced by the higher-order MoM is about one tenth of the traditional RWG MoM, and there is almost no loss of accuracy. The storage complexity and computation complexity of the LU decomposition of MoM matrix are $O(N^2)$ and $O(N^3)$ respectively, where N is the number of unknowns, and the trend of N is increasing exponentially. Therefore, under the premise of ensuring accurate simulation, the cost of storage and the computation time of the higher-order MoM compared with the traditional RWG MoM will be greatly reduced.

The bilinear surface is a non-planar surface quadrilateral that can be determined with four vertices, as shown in Fig. 1. Its parametric equation is:

$$\begin{aligned} \mathrm{r}(p,s) = \frac{1}{\Delta p \Delta s}[&r_{11}(p_2 - p)(s_2 - s) + r_{12}(p_2 - p)(s - s_1) \\ &+ r_{21}(p - p_1)(s_2 - s) + r_{22}(p - p_1)(s - s_1)] \\ \Delta p = p_2 - p_1,\ \Delta s = s_2 - s_1,\ &p_1 \le p \le p_2,\ s_1 \le s \le s_2 \end{aligned} \quad (1)$$

where r_{11}, r_{12}, r_{21} and r_{22} are the position vectors of the four vertices, respectively; p and s represent local coordinate systems; p_1 and p_2 are the starting and ending coordinates along the p direction; s_1 and s_2 are the starting and ending coordinates along the s direction.

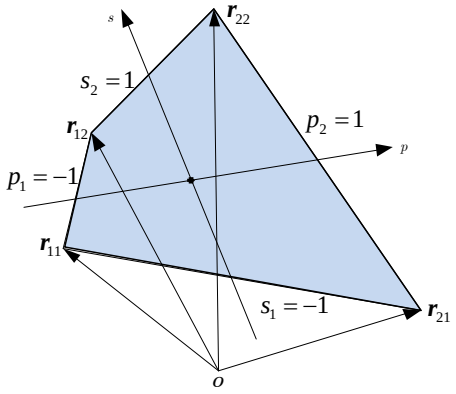

Fig. 1. Bilinear surface.

B. BDPLU algorithm

The commercial math library needed in the matrix solving process, such as Intel MKL [16] and the open source library ScaLapack [17]. However, these libraries fail or deteriorates on supercomputers with special architectures, such as Tianhe-2 system from Guangzhou in China. Therefore, our previous work developed a direct solver using the CALU algorithm to improve the performance of the panel factorization in parallel LU decomposition [18]. Due to reduced communication of CALU, it has better scalability than Intel MKL and ScaLapack. However, those parallel LU solvers are

general-purpose solvers for solving matrix equations, without considering the specific features of the MoM impedance matrices. Under this situation, based on our previous studies, we introduce a new pivoting scheme based on diagonally dominant matrices of MoM, which named as Block Diagonal Pivoting LU.

The matrix generated by the higher-order MoM can be divided into two parts: self-impedance element and mutual impedance element. From the perspective of physical concepts, diagonal elements represent the self-action of the same basis functions, and non-diagonal elements represent the interactions between the various basis functions [10]. Generally speaking, the self-effect is greater than the mutual effect, so that the complex dense matrix produced by the higher-order MoM has the characteristic of diagonal dominance, and this characteristic has been maintained during the LU decomposition process, as shown in Fig. 2. Utilizing the diagonal-dominant property of MoM, the diagonal block of the matrix is always guaranteed during the parallel matrix filling process and the parallel matrix equation solving process. Therefore, the operation of pivoting during the LU decomposition process can be omitted, and the time of pivoting is saved. At the same time, the communication between processes in the LU decomposition process is avoided, which improves the efficiency of the algorithm and ensures the stability of the algorithm.

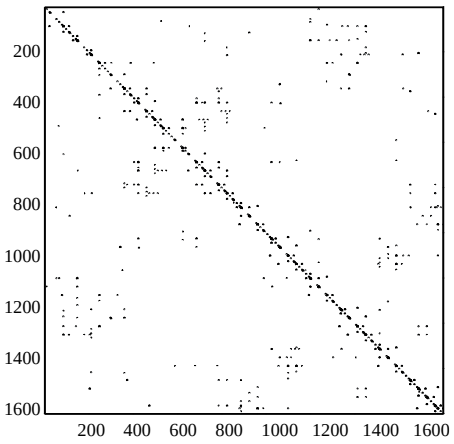

Fig. 2. Diagonally dominant of matrix.

The performance of the parallel LU decomposition solver can be further improved, with the diagonal dominance characteristic of impedance matrices taken into account. Compared with the traditional LU solver, the communication and computation time of the new pivoting scheme is analyzed.

Assume that the communication latency is α and the communication bandwidth is *1/β*. Thus, the communication time *T* taken to send a message of size *L* is:

$$T = \alpha + \beta L . \tag{2}$$

The process of pivoting in the BDPLU solver is given in Fig. 3. As we can see that there is no internodes communication during the *k*th panel column rotation. For every column in the panel, those should perform n_b size binary-exchange. The total communication time is:

$$\begin{aligned} T_{comm,BDPLU} &= \alpha \times \log_2 P_r + n_b \times (n_b \beta) \times \log_2 P_r \\ &= \alpha \log_2 P_r + \beta n_b^2 \log_2 P_r , \end{aligned} \tag{3}$$

where n_b is the number of columns in the panel, $log_2 P_r$ is complexity of binary-exchange.

The total communication time of the traditional LU is:

$$\begin{aligned} T_{comm,traditional\ lu} &= n_b \times (\alpha + 2 \times n_b \beta) \times \log_2 P_r \\ &= n_b \alpha \log_2 P_r + 2\beta n_b^2 \log_2 P_r . \end{aligned} \tag{4}$$

And the computation time of both is:

$$T_{comp,lu} = (m - \frac{n_b}{3}) n_b^2 \gamma . \tag{5}$$

Comparing the formula (4) and (5), it can find that DBPLU requires less communication time than traditional LU.

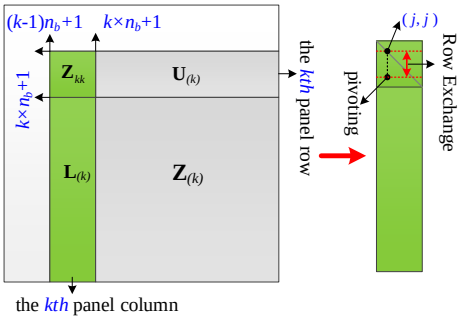

Fig. 3. Block diagonal pivoting LU scheme.

C. Wave port theory

The wave port theory of MoM is developed based on the pattern matching theory and the aperture coupling equivalent principle. Two types of the ports used in this paper are rectangular wave port and coaxial wave port. The normalized tangential vectors of the electric field of them are different, and the electromagnetic fields generated by the equivalence principle of LOVE are different.

For a rectangular waveguide, the normalized tangential vector of the electric field in the TE model is:

$$\boldsymbol{e}_i = \begin{cases} -\sqrt{\frac{2}{ab}}\sin\left(\frac{n\pi}{b}y\right)\hat{\boldsymbol{a}}_x & m=0,\ n\neq 0 \\ \sqrt{\frac{2}{ab}}\sin\left(\frac{m\pi}{a}x\right)\hat{\boldsymbol{a}}_y & m\neq 0,\ n=0 \\ \sqrt{\frac{2}{ab}}\sqrt{\frac{2}{(an)^2+(bm)^2}}\begin{bmatrix} bm\sin\left(\frac{m\pi}{a}x\right)\cos\left(\frac{n\pi}{b}y\right)\hat{\boldsymbol{a}}_y & m\neq 0 \\ -an\cos\left(\frac{m\pi}{a}x\right)\sin\left(\frac{n\pi}{b}y\right)\hat{\boldsymbol{a}}_x & n\neq 0 \end{bmatrix} \end{cases}, \quad (6)$$

where a and b are the length and width of the rectangular waveguide, respectively; $\hat{a}_x$ and $\hat{a}_y$ are the direction vectors in the local coordinate system on the port surface, as shown in Fig. 4 (a).

For a coaxial waveguide, its main model is the TEM model, and its normalized tangential vector of the electric field is:

$$\boldsymbol{e}_1 = \frac{1}{\sqrt{2\pi\ln\left(\frac{b}{a}\right)}}\frac{1}{r}\cdot\hat{\boldsymbol{a}}_r, \quad (7)$$

where b is the outer diameter of the coaxial, a is the inner diameter of the coaxial, and r is the distance from any point on the port surface to the center of the coaxial, as shown in Fig. 4 (b).

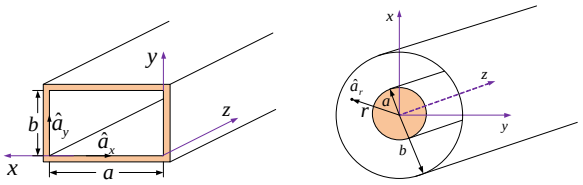

Fig. 4. Two port models: (a) rectangular model and (b) coaxial model.

D. Parallel port matrix filling

The MoM is a method that discretizes continuous equations into algebraic equations. The problem is discretized into an algebraic equation and then transformed into a matrix equation. Finally, the solution of the problem is obtained through the process of matrix inversion. Therefore, the size of the matrix generated by MoM will affect the calculation speed.

In order to speed up the port matrix filling process, this paper adopts a new parallel matrix filling strategy based on [9]. The strategy allocates the impedance matrix generated by the port to each process in parallel in the form of a circular block distribution, and introduces local index information. On the basis of retaining the feature of renumbering common edges, the new impedance matrix is filled into the existing impedance matrix in parallel according to the sequence of each process, which reduces the reordering time and improves the matrix filling efficiency. The filling strategy is as shown in Fig. 5.

```
Do k = 1,nel                          ! loop geometric elements for basis functions
  Do kp = 1,nep(k)                    ! loop p-direction subdivisions of kth geometric element
    Do ks = 1,nes(k)                  ! loop s-direction subdivisions of kth geometric element
      Do l = 1,nel                    ! loop geometric elements for testing functions
        Do lp = 1,nep(l)              ! loop p-direction subdivisions of lth geometric element
          Do ls = 1,nes(l)            ! loop s-direction subdivisions of lth geometric element
            find_Zmn_index(k,kp,ks,l,lp,ls)
            flag(ls)=0
            If (m,n belongs to this process) then
              If (flag(ls)==0) then   ! if flag is false, then perform integration
                Compute_integral
                flag(ls)=1
              Endif
              Calculate the value of Z(m,n)
            Endif
            … inner loops end here …
          Enddo
        Enddo
      Enddo
    Enddo
  Enddo
Enddo
```

Fig. 5. HOMoM filling strategy.

III. INTRODUCTION TO COMPUTING PLATFORMS

The computing platform used in this paper is the Tianhe II supercomputer at the National Center for Supercomputing Guangzhou, with a peak computing speed of 54.9 PFlops (PetaFlops) and a double-precision floating-point continuous computing speed of 33.9 PFlops. And the platform won the top spot in the world's supercomputer rankings six times in a row.

The Tianhe II supercomputer is composed of 16,000 computing nodes, each node contains 2 E5-2692 processors based on the Ivy Bridge architecture, with a total of 32,000 Ivy Bridge processors and 768,000 CPU cores. The operating system is Kirin operating system and Ubuntu Linux. Programming language environments include C, C ++, Fortran, Java, MPI, OpenMP. This paper uses a maximum of 19,200 cores with 800 nodes.

IV. NUMERICAL EXAMPLES

This paper uses the computing platform as the "Tianhe II" supercomputer platform, the higher-order MoM is used for waveguide slot array antenna simulation, and BDPLU algorithm is used to speed up the calculation. The algorithm reliability of parallel higher-order MoM has been verified in previous work [11,12,14]. The verification results of a single waveguide and a small waveguide array are given firstly. Secondly, the simulations are performed for K-band wide-side slotted waveguide array and Ka-band narrow-side slotted waveguide array, and the calculation results and resource consumption are given. It is proved that the method in this paper can efficiently, reliably and stably solve the simulations of the radiation problem of the super large slotted waveguide array antennas.

A. Correctness verification

To verify the correctness of the algorithm, a single narrow-side waveguide antenna is simulated. The working frequency of the waveguide is 9.375GH. There are 10 slot units, and the size of each unit is 22.86mm×10.16mm×266.58mm. The port is a rectangular wave port feed, and the other end is matched. The antenna model is shown in Fig. 6 (a). This method is compared with the RWG MoM of the commercial software FEKO, and the result is shown in Fig. 6 (b).

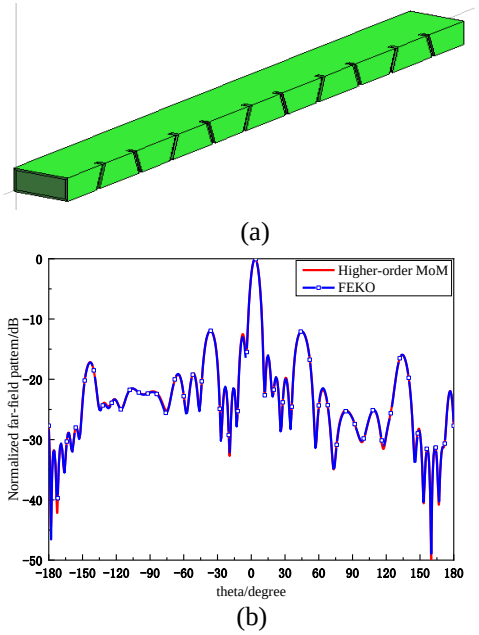

Fig. 6. (a) Model of single narrow-sided waveguide, and (b) result comparison.

The red solid line in Fig. 6 (b) is the result of this method, and the blue dashed line is the FEKO simulation result. It can be seen that the results of the two methods are in good agreement, with slight differences in some angles. The maximum difference does not exceed 0.5dB, which means the accuracy of this method meeting the requirements of engineering applications.

A small narrow slotted waveguide array is used to verify the accuracy of the coupling between units. This array is composed of 10 single waveguides described above. The antenna model is shown in Fig. 7 (a). The radiation pattern of the antenna array is calculated by using higher-order MoM and FEKO-RWG MoM respectively. For HOMoM, the unknown is 26.090, which requires about 10.9GB of memory; for the FEKO-RWG MoM, the unknown is 135,367, which requires about 293.1GB of memory. The HOMoM unknown is 1/5.19 of the FEKO-RWG MoM. The result comparison is shown in Fig. 7 (b). It can be seen that the two methods basically agree. The results show that the method is effective and feasible in dealing with the coupling between waveguides.

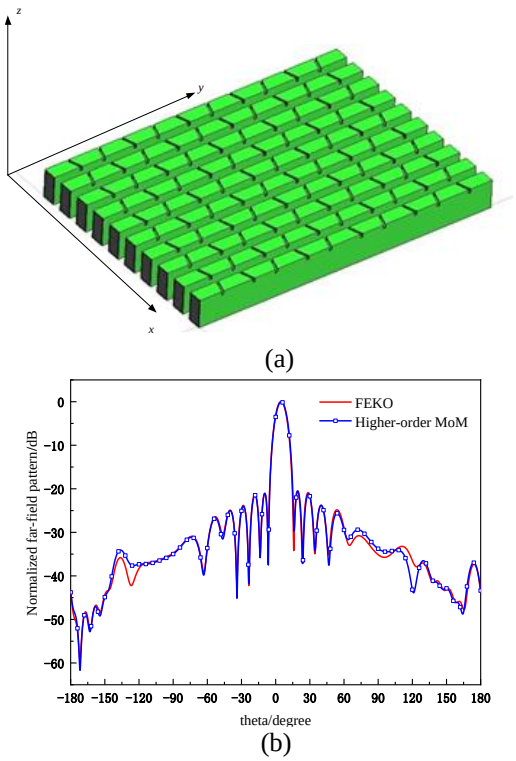

Fig. 7. (a) Model of narrow-sided waveguide array, and (b) result comparison.

B. Narrow-sided waveguide array

Narrow-side slotted waveguide array is a two-sided array composed of two waveguide arrays. Each array contains 2068 slot units, a total of 4136 slot units, and its model is shown in Fig. 8. The working frequency of the antenna is in Ka-band, and the port is fed by the rectangular port. The number of unknowns generated by the higher-order MoM is 1,167,436, and the required memory is 19.83TB. A total of 19200 CPU cores of 800 nodes are used for simulation. The results are shown in Fig. 8, and the resource consumption is shown in Table 1.

Table 1: Resource consumption of narrow-side waveguide array

Unknowns	Number of CPU Cores	Process Grid	Matrix Filling /s	Matrix Solving /s
1,167,436	19200	168×100	322.17	14749.02

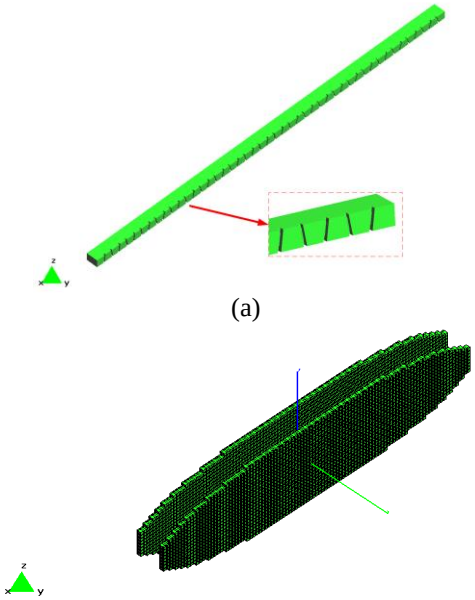

(a)

(b)

Fig. 8. Model of narrow-sided waveguide array: (a) single and (b) total.

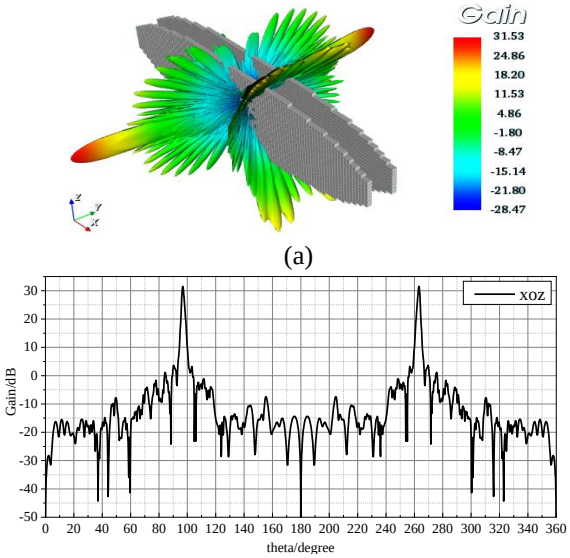

(a)

(b)

Fig. 9. Radiation pattern of narrow-sided waveguide array: (a) 3D and (b) 2D.

C. Wide-side waveguide array

The wide-edge slotted waveguide array consists of 64 waveguides, each of waveguide has 64 slots, a total of 4096 unit, and the model is shown in Fig. 10. The working frequency of the antenna is in K-band, and the port is fed by the coaxial port. Taylor synthesis is used to feed the port. The number of unknowns generated by the higher-order MoM is 1,190,950, and the required memory is 20.64TB. The calculation results are shown in Fig. 11, and the resource consumption is shown in Table 2.

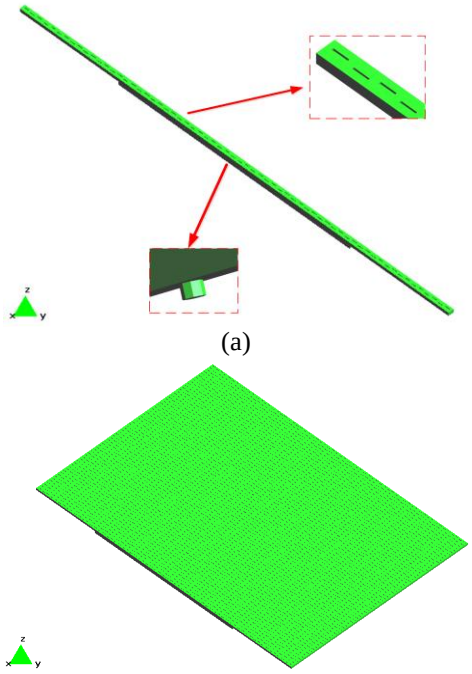

(a)

(b)

Fig. 10. Model of wide-sided waveguide array: (a) single and (b) total.

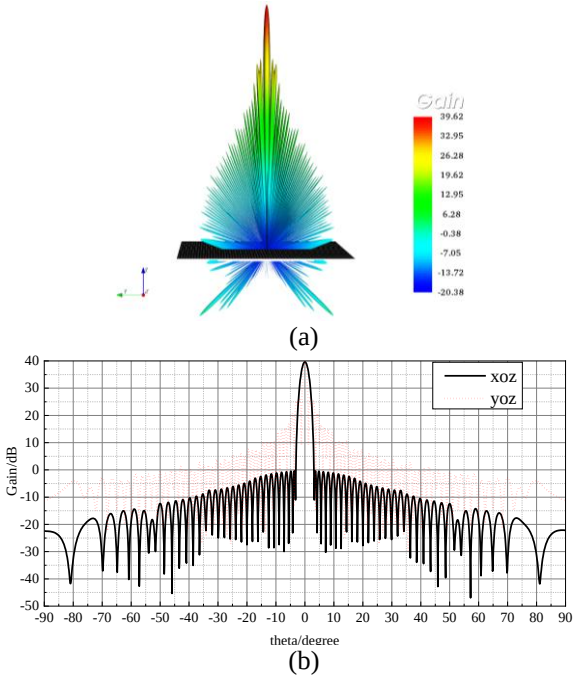

(a)

(b)

Fig. 11. Radiation pattern of wide-sided waveguide array: (a) 3D and (b) 2D.

Table 2: Resource consumption of wide-side waveguide array

Unknowns	Number of CPU Cores	Process Grid	Matrix Filling /s	Matrix Solving /s
1,190,950	19200	168×100	344.01	15582.85

V. CONCLUSION

This paper focuses on the accurate simulation of super large slotted waveguide arrays. The parallel higher-order MoM is used to solve this problem, and the BDPLU algorithm is used to accelerate the matrix equation solving to ensure the computation process is efficient and stable. Meanwhile, a new parallel matrix filling strategy of wave port is proposed to accelerate the process of matrix filling by studying the characteristics of the wave port matrix. Finally, two kinds of typical super large slotted waveguide array antennas are simulated with the help of "Tianhe II" supercomputer platform. The numerical example proved that the method can completely finish the accurate simulation and analysis in 4.5h for any type of waveguide slot array antenna within 4000 units in the high frequency band (about K-band). For the design of the next generation of UAV slotted waveguide array antenna, the simulation method proposed in this paper can reasonably provide simulation within the acceptable range of engineering.

ACKNOWLEDGMENT

This work was supported in part by the National Key Research and Development Program of China under Grant 2017YFB0202102, in part by the National Science Foundation of China under Grant 61901323, in part by the Colleges and Universities 20 Terms Foundation of Jinan City under Grant 2018GXRC015, in part by the Fundamental Research Funds for the Central Universities under Grant XJS190210.

REFERENCES

[1] Z. Yefeng, Z. Yongzhong, L. Mingfei, et al., "A low-profile half-mode substrate integrated waveguide circularly polarized antenna," [J]. *Journal of Xidian University (Natural Science Edition)*, vol. 44, no. 6, pp. 169-174, 2017.

[2] Hu Wei, "Research on waveguide slot array antenna and printed slot unit antenna," [D]. *Xidian University*, 2013.

[3] W. Zhiwei, "Research on fast hybrid algorithm of antenna radiation characteristics of complex electrical platform," [D]. *Southeast University*, 2016.

[4] M. Yi, "Research and application of high and low frequency hybrid algorithm," [D]. *Xidian University*, 2013.

[5] S. Xumin, Y. Minglin, and S. Xinqing, "Integration and efficient and accurate analysis of large waveguide slot array and radome," [J]. *Journal of Radio Science*, vol. 31, no. 4, 2016.

[6] Y. Wang, Y. Li, X. Zhao, et al., "Analysis of electrically large slotted waveguide array using high-order MoM," [C] *IEEE International Symposium on Antennas and Propagation & Usnc/ursi National Radio Science Meeting. IEEE*, pp. 975-976, 2015.

[7] Y. Li, Y. Wang, and Y. Zhang, "Analysis of large waveguide slotted antenna array using symmetry techniques," [C] *Radar Conference 2015, IET International. IET*, vol. 4, no. 4, 2016.

[8] Y. Li, S. Zuo, Y. Wang, et al., "Analysis of geometric structure and wave port symmetry in higher-order moment method," *[J]. Journal of Xidian University (Natural Science Edition)*, vol. 43, no. 6, pp. 34-38, 2016.

[9] Y. Chen, S. Zuo, Y. Zhang, et al., "Large-scale parallel method of moments on CPU/MIC heterogeneous clusters," [J]. *IEEE Transactions on Antennas & Propagation*, vol. 65, no. 7, pp. 3782-3787, 2017.

[10] F. X. Canning, "Solution of impedance matrix localization form of moment method problems in five iterations," *Radio Science*, vol. 30, no. 5, pp. 1371-1384, Sept.-Oct. 1995. doi: 10.1029/95RS01457.

[11] Q. Chang, Y. Wang, Y. Zhang, and X. Zhao, "Higher-order MoM combined waveport analysis of circular waveguide problems," [C] *IET International Radar Conference*, Hangzhou, pp. 1-4, 2015.

[12] S. Zuo, Y. Li, and Y. Zhang, "Analysis of the perturbation characteristics of airborne antennas with parallel outer-core high-order moment method," [J]. *Journal of Terahertz Science and Electronic Information*, vol. 6, 2016.

[13] A. Nouainia and T. Aguili, "Analysis of shielding of metallic rectangular waveguide using new implementation of the MoM-GEC method based on wave concept," [C] *2017 13th International Wireless Communications and Mobile Computing Conference (IWCMC)*, Valencia, pp. 830-835, 2017.

[14] Y. Wang, X. Zhao, Y. Zhang, S. W. Ting, T. K. Sarkar, and C. H. Liang, "Higher order MoM analysis of traveling-wave waveguide antennas with matched waveports," [J]. *IEEE Transactions on Antennas and Propagation*, vol. 63, no. 8, pp. 3718-3721, Aug. 2015.

[15] Y. Kimura, F. Nonaka, S. Shimamori, and S. Saito, "Design of microstrip antenna arrays fed by slots on broad and narrow walls of the rectangular waveguide," [C] *2018 IEEE International Workshop on Electromagnetics: Applications and Student Innovation Competition (iWEM)*, Nagoya, pp. 1-1, 2018.

[16] Intel Copyright (2015) Intel Math Kernel Library for Linux OS User's Guide, Intel Corporation. Available: https://software.intel.com/sites/default/files/anaged/df/1e/mkl_11.3_lnx_userguide.pdf

[17] L. S. Blackford, J. Choi, and A. Cleary, "ScaLAPACK: A portable linear algebra library for distributed memory computers - Design issues and performance," *Proceedings of the 1996 ACM/IEEE Conference on Supercomputing, IEEE*, pp. 1-20, 1996.

[18] Y. Zhang, Y. Chen, G. Zhang, X. Zhao, Y. Wang, and Z. Lin, "A highly efficient communication avoiding LU algorithm for methods of moments," *2015 IEEE International Symposium on Antennas and Propagation & USNC/URSI National Radio Science Meeting*, pp. 1672-1673, 2015.

Double-layer Chessboard AMC Surface for RCS Reduction in an Ultra-wide Band

Xueyan Song [1], Lei Chen [2], Zehong Yan [2], Yunqi Zhang [1], and Haitao Song [3]

[1] School of Electronic Engineering
Xi'an University of Posts & Telecommunications, Xi'an, 710121, China
xysong6597@126.com, johnny_5@126.com

[2] National Key Laboratory of Antennas and Microwave Technology
Xidian University, Xi'an, 710071, China
leichen@mail.xidian.edu.cn, zhyan@mail.xidian.edu.cn

[3] Complex Systems Research Center, Shanxi University
Taiyuan, Shanxi, 030006, China
htsong@sxu.edu.cn

Abstract ─ A novel chessboard surface is proposed for ultra-wideband radar cross section (RCS) reduction. The designed artificial magnetic conductor (AMC) surface is arranged by two different double-layer AMC unit cells, bringing in destructive reflection phase difference (180°±37°) in an ultra-wide band ranging from 5.8 to 16.1 GHz (94.06%). Each double-layer unit cell consists of a substrate layer loaded with metal patches and a PEC layer, in between of which is a 2-mm-thick air gap, which results in smooth phase curves of the two AMC units. One of the metal patches is composed of an octagonal ring and a Union Jack cross, and the other one is a Jerusalem cross. With chessboard arrangement by the two units, the RCS of the proposed surface can be reduced by more than 10 dB over a 90.22% frequency range (6.23-16.47 GHz) for both x and y polarizations. And the 20-dB RCS reduction frequency band ranges from 12.3 GHz to 15.9 GHz (25.5%). Then, the proposed AMC surface is fabricated and measured, and the measured 10-dB RCS reduction frequency band ranges from 6.66 to 16.42 GHz (84.58%) for x polarization and from 6.65 to 16.5 GHz (85.1%) for y polarization, which verifies that the presented AMC configuration may achieve potential applications on low-RCS platforms in an ultra-wide band.

Index Terms ─ Artificial Magnetic Conductor (AMC), Radar Cross Section (RCS) reduction, ultra-wideband.

I. INTRODUCTION

With the development of new electromagnetic metamaterials, the study on AMC has gradually been a hot research in fields of microwave. Thanks to their unique in-phase reflection properties, planar AMCs have been found many applications, such as suppression of surface waves in antenna designs [1], reducing the mutual coupling of units in antenna array designs [2], being utilized as artificial ground planes to achieve low-profile and gain-enhanced antennas [3], and reducing the RCS of platforms to achieve stealth in military fields [4]. Among them, contributing to solving the problems on thickness and bandwidth of traditional materials, such as Salisbury screen [5], metamaterial absorbers [6], etc., the application of AMC surfaces in RCS reduction [7-15] has recently been paid more and more attention. Radar cross section (RCS) is integral to the development of radar stealth technology [15]. RCS reduction (RCSR) means reducing the electromagnetic backscattered waves, which is essential in stealth technology [13]. An EBG checkerboard surface can result in a redirecting of the scattered fields [16], which bringing about a decrease in RCS.

In 2007, a planar structure combined of AMC and perfect electric conductor (PEC) unit cells in a chessboard is designed for RCS reduction applications [4]. Based on the opposite reflection phase of AMC and PEC, the reflections in normal direction cancel out, thus reducing the RCS. However, the bandwidth of the chessboard is limited by the narrow in-phase reflection (±37°) frequency band of AMC. In order to enhance the RCS reduction bandwidth, PEC can be substituted by another AMC, and surfaces consisting of AMC structures [7-12] have gradually been presented. In [7], two different types of AMC unit cells are periodically designed to form a planar surface, which achieve a +143° ~ +217° phase difference in the band from 13.25 to 24.2 GHz for boresight RCS reduction. After that, composite surfaces, consisting of two kinds of AMC

Submitted On: January 11, 2020
Accepted On: May 21, 2020

units, are proposed in [8] and [9], which achieve a nearly 10 dB RCS reduction over a 32% and 40% bandwidth, respectively. Moreover, combined by two Jerusalem Crosses with different sizes, a planar chessboard structure is proposed [10] and obtained about 42% bandwidth for 10 dB RCS reduction. With the same method, a miniaturized AMC reflecting screen combined by square unit cells with different sizes is recently designed [11] and the RCS is reduced in the band from 13.4 GHz to 26.9 GHz (67%).

Nevertheless, the bandwidth of RCS reduction in the previous researches needs to be furtherly widened to meet the requirements of objects for stealth in an ultra-wide band. For the purpose of a further increase in the bandwidth, double-layer AMC structure is proposed in [12]. By using an air layer, a novel double-layer chessboard surface is presented, and 73% bandwidth for 10 dB RCS reduction is obtained. The top layer is formed by substrate and substrate printed with a circular patch, and the bottom layer is PEC ground. Loading with the air gap, two smooth phase curves of the AMC units can be obtained, resulting in a wide phase difference bandwidth. Then, double-layer and multi-layer AMC surfaces are proposed in succession [13-15]. In [13], a three-layer chessboard-like AMC structure formed by two crossed ellipses with different sizes is proposed and obtain wide 10 dB RCS-reduction bandwidth from 8.11 to 23.32 GHz. In addition, a chessboard AMC surface based on the quasi-fractal structure is proposed in [14], and realizes a 10-dB RCS reduction band ranging from 5.4 GHz to 14.2 GHz. In 2019, a double-layer checkerboard AMC structure with two kinds of AMC elements is designed [15] and observe 10 dB RCS reduction in the band from 3.77 to 10.14 GHz.

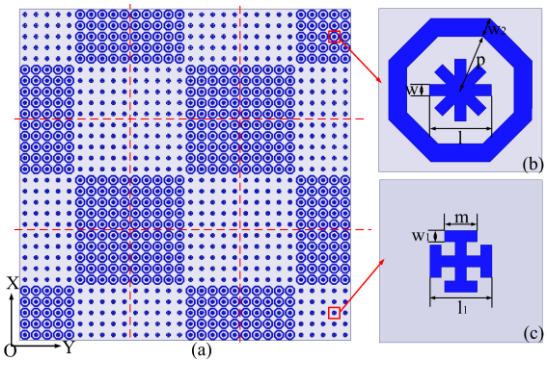

Fig. 1. Top view of the proposed AMC surface and unit cells. (a) Chessboard AMC surface, (b) AMC unit cell$_1$, and (c) AMC unit cell$_2$. Dimensions (unit: mm): l=3.8, p=3.55, w=0.7, w_2=1.2, l_1=4.0, w_1=0.8, m=2.

In this paper, a novel double-layer AMC configuration is designed here to further improve the bandwidth and increase the RCS reduction value. On the top layer, the patch array is composed of two kinds of AMC patches instead of combination by AMCs and PECs. One kind of AMC patches is an octagonal ring with a Union Jack cross, and the other one is a Jerusalem Cross. The simulated results show that the frequency band of reflection phase difference (180°±37°) between the two AMC unit cells ranges from 5.8 to 16.1 GHz (94.06%). And a 90.22% fractional bandwidth (6.23-16.47 GHz) for both x and y polarizations is obtained for 10 dB RCS reduction. In addition, a 20-dB RCS reduction frequency band ranging from 12.3 GHz to 15.9 GHz (25.5%) can be obtained for both x and y polarizations. The measured RCS reduction frequency bands are 6.66-16.42 GHz for x polarization and 6.65-16.5 GHz for y polarization, which agree well with the simulated ones.

II. AMC DESIGN AND SIMULATED RESULTS

A. Design principle of broadband AMC surface

From reference [16], the expression of the AMC surface for RCS reduction can be obtained from the following formula [17-18]:

$$\text{RCS reduction} = 10\log_{10}\left|\frac{A_1 e^{j\varphi_1} + A_2 e^{j\varphi_2}}{2}\right|^2, \qquad (1)$$

where, A_1 and A_2 is the reflection magnitude of AMC$_1$ and AMC$_2$, respectively; φ_1 and φ_2 are their reflection phases. Generally, a 10 dB RCS reduction in boresight direction compared to PEC sheet with the equal size is set as a criterion [19]. Therefore, from formula (1), the effective reflection phase difference of the AMC surface is

$$143° \le \left|\varphi_2 - \varphi_1\right| \le 217°. \qquad (2)$$

For this reason, 180°±37° is considered as the effective phase difference for analysis in follows.

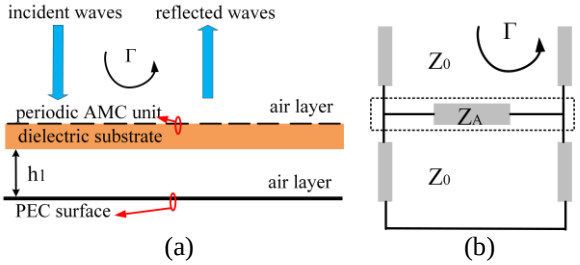

Fig. 2. (a) Double-layer AMC structure, and (b) its equivalent transmission line model.

Therefore, to achieve ultra-wideband 10 dB RCS reduction, two AMC units, which can generate 180°±37°

phase difference in an ultra-wide band, need to be designed firstly. Because of the excellent performances, double-layer AMC structure is finally chosen for wideband 10-dB RCS reduction. Based on the research in reference [15], the double-layer AMC structure and its equivalent transmission line model can be depicted as Fig. 2. Z_A and Z_0 refer to the equivalent impedance of the periodic structure and the intrinsic impedance of air layer, respectively. h1 is the height between the top layer and the PEC layer. Z_A can be approximately expressed as $Z_A \approx jX_A$. The impedances can be replaced by the admittances. Therefore, $Y_A = 1/Z_A \approx jB_A$, and $Y_0 = 1/Z_0$.

According to [15], the reflection coefficient and phase of an AMC can be expressed as:

$$\Gamma = \frac{Y_0(j\sin(\beta_0 h_1) - \cos(\beta_0 h_1)) - jY_A \sin(\beta_0 h_1)}{Y_0(j\sin(\beta_0 h_1) + \cos(\beta_0 h_1)) + jY_A \sin(\beta_0 h_1)}, \quad (3)$$

$$\varphi = 2\arctan\left(\frac{Y_0 \sin(\beta_0 h_1)}{-Y_0 \cos(\beta_0 h_1) + B_A \sin(\beta_0 h_1)}\right), \quad (4)$$

where, $\beta_0 = 2\pi f / c$ refers to the phase constant in vacuum, and f is the operation frequency. Moreover, for total cancellation, the susceptance of the AMC periodic structure can be calculated as:

$$B_A = Y_0 \cot(\beta_0 h_1) + Y_0 \tan(sf + a), \quad (5)$$

Where s is related to rate of reflection phase and a is related to initial value of reflection phase, and the unit of frequency (f) is gigahertz. And the independence of periodic structure for AMC unit1 and unit2 can be written as:

$$Z_{A1} = \frac{1}{jB_{A1}} = \frac{-jZ_0}{\cot(\beta_0 h_1) + \tan(sf + a)}, \quad (6)$$

$$Z_{A2} = \frac{-jZ_0}{\cot(\beta_0 h_1) - \cot(sf + a)}. \quad (7)$$

From (6) and (7), AMC unit1 can be approximately parallel resonance when AMC unit2 is series resonance. Or, AMC unit1 can be approximately series resonance when AMC unit2 is parallel resonance.

B. Design and analysis of AMC surface

After sufficiently analyzing the frequency behaviors of various AMC units, the two unit cells in Fig. 1 are selected to constitute the proposed AMC surface. Using a Floquet port and Master/Slave boundaries, a full-wave analysis is carried out by ANSYS HFSS. And Figs. 3 (a) and (b) demonstrate the simulated configuration of the two units, both of which are double-layer structures with dimensions of 10×10 mm^2. The top layer is a metal patch etched on a 2-mm-thickness F4BM-2 dielectric substrate (ε_r=2.2, tanδ=0.0007), and the bottom layer is a PEC sheet. Between two layers is an air gap with height of h1, which contributes to smooth phase curves of the two AMC units. An octagonal ring with a Union Jack cross patch constitutes AMC unit cell1 and a Jerusalem Cross patch comprises AMC unit cell2. Figures 3 (c) and (d) depict the equivalent circuit models for the two AMC units [20]. It can be seen from the equivalent circuit models that the AMC unit cell1 can is a series resonance circuit and the AMC unit cell2 is a parallel resonance circuit, which accords with the cancelation conditions mentioned above.

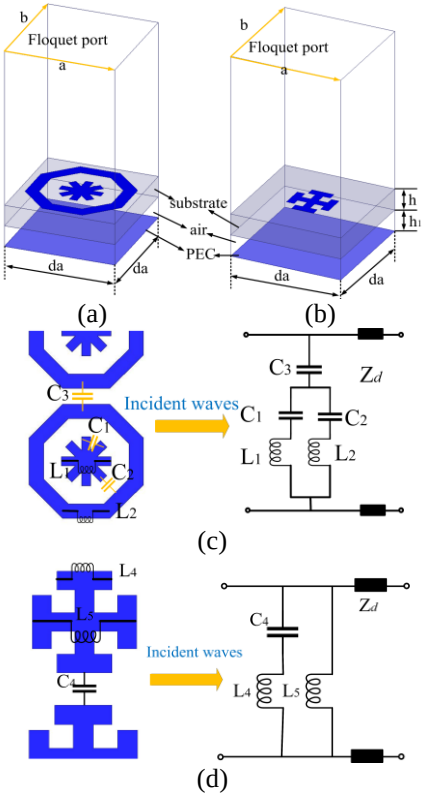

Fig. 3. Simulation model and equivalent circuit models of the proposed AMC unit cells. (a) AMC unit cell$_1$ and (b) AMC unit cell$_2$. h=2mm, h$_1$=2mm, da=10mm. (c) Equivalent circuit model for AMC unit cell$_1$, and (d) equivalent circuit model for AMC unit cell$_2$.

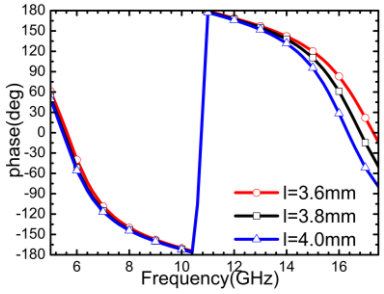

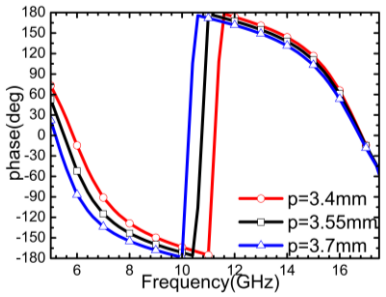

(b)

Fig. 4. Impact of parameters (a) l and (b) p on the reflection phase of AMC unit cell$_1$.

Figure 1 depicts dimensions of the two designed unit cells. Of all the parameters, parameters l and p have a great impact on the reflection phase property of the two AMC unit cells, which can be seen in Figs. 4 (a-b). The values of l and p determine the two resonances of unit cell1 in the high and low frequency band, respectively. When l increases from 3.6mm to 4mm, the equivalent inductance L1 and capacitance C2 in Fig. 3 (c) increase, which leads to a decrease in the resonances in the low frequency band, as can be seen in Fig. 4 (a). Similarly, with an increase in p, the circumference of the square loop increases, bringing about the increase in the inductance L2 of the octagonal loop the mutual coupling capacitance C3. Therefore, the resonant frequency in low band decreases, which corresponds to the simulated results in Fig. 4 (b). To obtain a wide phase difference band, the values of l and p are finally decided to be 3.8mm and 3.55mm, respectively.

Figure 5 demonstrates the simulated reflection phase and difference of two AMC unit cells. Consisting of an octagonal ring and a Union Jack cross patch, AMC unit cell1 can generate two resonances in the low and high frequency band, respectively, as depicted in Fig. 4 (a), thus arising two different 0° phase reflection frequencies (5.5 GHz and 17.8 GHz) and a 180° phase reflection at 10.8 GHz. Whereas, AMC unit cell2 exhibits 0° phase reflection value at 11.6 GHz, which is close to the 180° phase reflection frequency of AMC unit cell1, thus giving birth to an ultra-wide reflection phase difference (180°±37°) band from 5.8 to 16.1 GHz for normal incidence. Hence, an ultra-wideband 10 dB RCS reduction with a percentage bandwidth of 94.06% can be expected.

In addition, the phase differences under different incident angles are also simulated and depicted in Fig. 6. It can be obtained that the bandwidths of phase difference keep stable when the incident angle is lower than 15°, and when the incident angle is increased to 30° and 45° the phase difference band changes to double bands. And with the increase in incident angle, the phase difference bandwidth decreases.

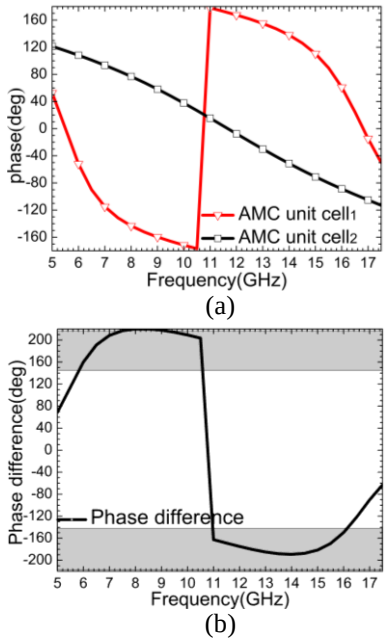

Fig. 5. Simulated reflection phase and difference of AMC unit cells. (a) Reflection phase and (b) reflection phase difference.

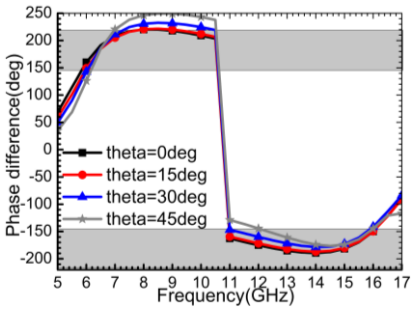

Fig. 6. Reflection phase difference for different incident angles.

For the sake of low RCS property in an ultra-wide band, the surface is combined by 3×3 chessboard's cell arrays, as demonstrated in Fig. 1 (a). Each chessboard cell array is made up of 10×10 unit cells, and arranged by 5×5 AMC unit cell1 and 5×5 AMC unit cell2. Dimensions of the proposed AMC surface are 300×300×4 mm^3. To calculate the RCS reduction bandwidth of the designed chessboard surface, the monostatic RCS of the AMC surface and PEC surface with equal size for normal incidence is simulated. As depicted in Fig. 4, parameters l and p have a great influence on the reflection phase property. To investigate the effect of those two parameters on the RCS reduction of AMC surface, the RCS reduction of AMC surface with

different l or p is simulated, and Fig. 7 shows the simulated results. It can be obtain from Fig. 7 that the change in parameter l has an influence on the 10-dB RCS reduction bandwidth and the largest reduction value in the high frequency band, and parameter p affects the largest reduction value in low frequency band and the RCS reduction bandwidth, which corresponds to the results in Fig. 4. In compromising of the value and bandwidth of RCS reduction, l and p is finally selected as 3.8mm and 3.55mm, respectively.

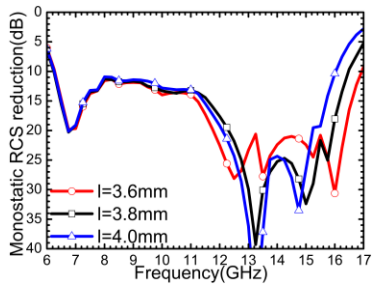

(a)

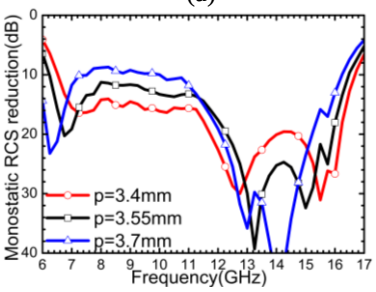

(b)

Fig. 7. Impact of parameters (a) l and (b) p on the simulated monostatic RCS reduction.

Then, Fig. 8 depicts the final simulated monostatic RCS and RCS reduction of proposed AMC surface under normal incidence for both x and y polarizations. From the simulated results, an ultra-wide 10-dB RCS reduction frequency band ranging from 6.23 GHz to 16.47 GHz (90.22%) is achieved. And the maximum RCS reduction, which is more than 35 dB, is obtained at 13.4 GHz. Compared with references [12-15], the AMC surface can achieve larger RCS reduction value and wider 20-dB RCS reduction frequency band ranging from 12.3 GHz to 15.9 GHz (25.5%). Furthermore, Fig. 9 demonstrates the normalized 2-D bistatic RCS of PEC sheet and the proposed AMC configuration under different incidences for both x and y polarizations at 13.4 GHz. Compared with the bistatic RCS of the PEC surface in Fig. 9, the proposed AMC surface can achieve low RCS in boresight direction and reflects the scattering energy in other directions.

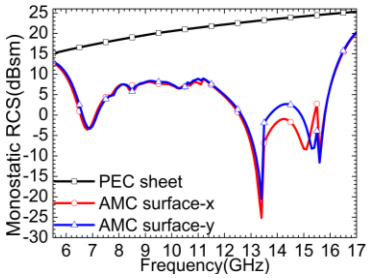

(a)

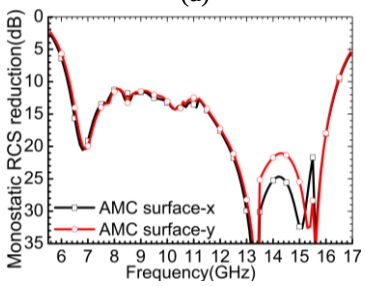

(b)

Fig. 8. Simulated monostatic RCS and RCS reduction of proposed chessboard AMC surface under normal incidence for both *x* and *y* polarizations. (a) Monostatic RCS and (b) RCS reduction.

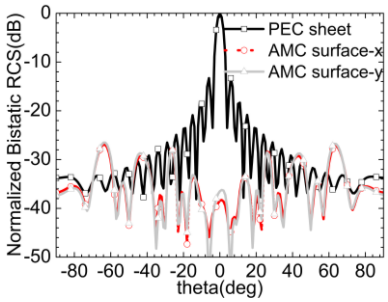

Fig. 9. Simulated normalized 2-D bistatic RCS pattern of proposed AMC surface and PEC sheet under different incidences for both *x* and *y* polarizations at 13.4GHz.

In order to investigate the change of RCS reduction with different incident angles, Fig. 10 demonstrates the simulated bistatic RCS reduction under different incident angles for both x and y polarizations. From the simulated results, it can be obtained that the values of RCS reduction decrease with the increase in incident angle, which is corresponding to the simulated phase differences under different incident angles. And the changes in RCS reduction values are related with the instability of the AMC structure with incident angles.

In view of the good RCS reduction property of the proposed AMC surface, the proposed AMC unit cells can be arranged periodically around the antenna on the

same plane when an antenna need to be obtained low RCS performance, just as the structures in references [9] and [11].

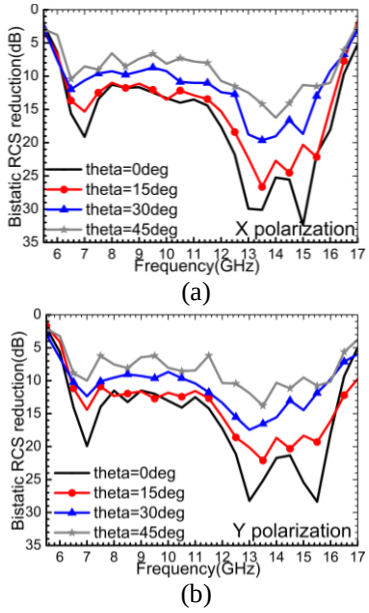

Fig. 10. Simulated bistatic RCS reduction under different incident angles for (a) x and (b) y polarizations.

III. FABRICATION AND MEASURED RESULTS

To verify the simulated results, the proposed chessboard surface is fabricated, as shown in Fig. 11. 30×30 unit patches are etched on a 2-mm-thickness F4BM-2 dielectric substrate. Separated by a 2-mm-thickness air gap, a PEC sheet (a replacement by a thin aluminum sheet) is installed beneath the substrate layer. The total dimensions of the proposed structure are 300×300×4 mm^3. To show the ability for RCS reduction, the RCS values of the proposed AMC surface are normalized by the PEC sheet with the identical physical dimensions. The measured and simulated monostatic RCS of the proposed AMC surface and PEC sheet is depicted in Fig. 12 (a). And Fig. 12 (b) illustrates the measured and simulated RCS reduction of the designed chessboard configuration.

From the measured results depicted in Fig. 12, the RCS of the designed AMC surface can be reduced by more than 10 dB in the band ranging from 6.66 to 16.42 GHz (84.58%) for x polarization and from 6.65 to 16.5 GHz (85.1%) for y polarization under normal incident waves. Due to the fabricated and measured errors and the error in the height between the top and the bottom layers, there is a little frequency shifting in the measured RCS reduction frequency band compared with the simulated results and the measured values of RCS reduction are a little higher than the simulated ones.

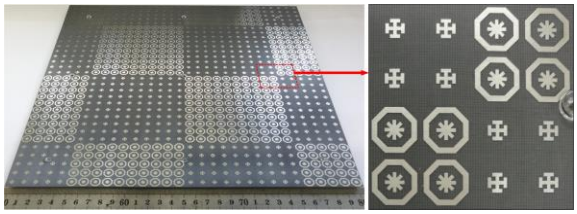

Fig. 11. Photograph of fabricated chessboard surface.

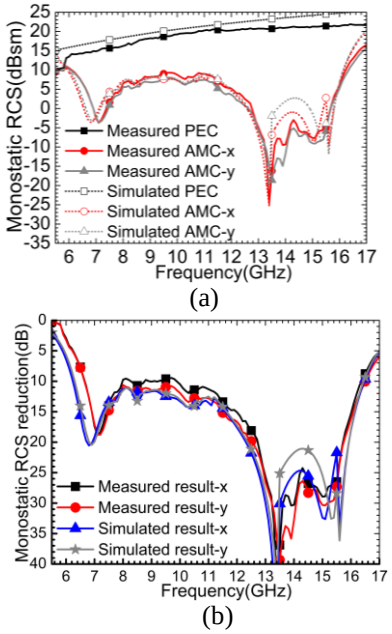

Fig. 12. Measured and simulated monostatic RCS and RCS reduction of proposed chessboard AMC surface under normal incidence for both *x* and *y* polarizations. (a) monostatic RCS and (b) RCS reduction.

IV. CONCLUSION

In this letter, a novel double-layer chessboard AMC surface is presented for RCS reduction in an ultra-broad band. In the expectation of a wider RCS reduction frequency band, the proposed chessboard configuration is formed by two different double-layer AMC unit cells. The patch printed on the substrate of one unit is an octagonal ring with a Union Jack cross, and that of the other one is a Jerusalem cross. With the two different unit cells, an ultra-broad reflection phase difference (180°±37°) band from 5.8 to 16.1 GHz can be obtained. Arranged by the two double-layer unit cells, the designed AMC surface achieves an ultra-wide frequency band ranging from 6.23 to 16.47 GHz (90.22%) for 10 dB RCS reduction under normal incidence for both x and y polarizations. In the band from 12.3 GHz to 15.9 GHz (25.5%), the RCS can be reduced for more than 20 dB. The measured results show that the fabricated prototype can achieve a 10-dB RCS reduction frequency band of 6.66-16.42 GHz for x

polarization and of 6.65-16.5 GHz for y polarization, which validates that the designed AMC surface can be utilized for ultra-wideband RCS reduction applications.

ACKNOWLEDGMENT

This work is supported by the National Natural Science Foundation of China (61671304 and 11601291) and the Scientific Research Program Funded by Shaanxi Provincial Education Department (18JK0701).

REFERENCES

[1] X. C. Wei, Y. F. Shu, J. B. Zhang, and D. Wang, "Applications of high impedance surfaces for surface wave elimination," *2016 URSI Asia-Pacific Radio Science Conference (URIS AP-RASC)*, Seoul, South Korea, pp. 1458-1461, 2016.

[2] L. Mouffok, L. Damaj, X. Begaud, A. C. Lepage, and H. Diez, "Mutual coupling reduction between dual polarized microstrip patch antennas using compact spiral artificial magnetic conductor," *Proceedings of the 5th European Conference on Antennas and Propagation (EUCAP)*, Rome, Italy, pp. 909-912, 2011.

[3] B. Zhang, P. Yao, and J. Duan, "Gain-enhanced antenna backed with the fractal artificial magnetic conductor," *IET Microwaves Antennas Propag*., vol. 12, pp. 1457-1460, 2018.

[4] M. Paquay, J. C. Iriarte, I. Ederra, R. Gonzalo, and P. Maagt, "Thin AMC structure for radar cross-section reduction," *IEEE Trans. Antennas Propag*., vol. 55, pp. 3630-3638, 2007.

[5] K. L. Ford and B. Chambers, "Tunable single layer phase modulated radar absorber," *2001 Eleventh International Conference on Antennas and Propagation*, Manchester, UK, pp. 588-592, 2001.

[6] Y. Ishii, T. Masaki, N. Michishita, H. Morishita, and H. Hada, "RCS reduction characteristics of thin wave absorbers composed of flat and curved metasurfaces," *2016 International Symposium on Antennas and Propagation (ISAP)*, Okinawa, Japan, pp. 192-193, 2016.

[7] Y. Zhang, R. Mittra, B. Z. Wang, and N. T. Huang, "AMCs for ultra-thin and broadband RAM design," *Electron. Lett*., vol. 45, pp. 484-485, 2009.

[8] Y. Fu, Y. Li, and N. Yuan, "Wideband composite ANC surfaces for RCS reduction," *Microwave Opt. Technol. Lett*., vol. 53, pp. 712-715, 2011.

[9] Y. J. Zheng, J. Gao, X. Y. Cao, Z. Yuan, and H. Yang, "Wideband RCS reduction of a microstrip antenna using artificial magnetic conductor structures," *IEEE Antennas Wireless Propag. Lett.*, vol. 14, pp. 1582-1585, 2015.

[10] J. C. I. Galarregui, A. T. Pereda, J. L. M. Falcón, I. Ederra, R. Gonzalo, and P. Maagt, "Broadband radar cross-section reduction using AMC technology," *IEEE Trans. Antennas Propag*., vol. 61, pp. 6136-6143, 2013.

[11] Y. Pei, B. Zhang, and J. Duan, "A broadband artificial magnetic conductor reflecting screen and application in microstrip antenna for radar cross-section reduction," *IEEE Antennas Wireless Propag. Lett*., vol. 17, pp. 405-409, 2018.

[12] M. Mighani and G. Dadashzadeh, "Broadband RCS reduction using a novel double layer chessboard AMC surface," *Electron. Lett*., vol. 52, pp. 1253-1255, 2016.

[13] R. Zaker and A. Sadeghzadeh, "Wideband radar cross section reduction using a novel design of artificial magnetic conductor structure with a triple-layer chessboard configuration," *International Journal of RF and Microwave Computer‐Aided Engineering*, e21545, 2018.

[14] J. Xue, W. Jiang, and S. Gong, "Chessboard AMC surface based on quasi-fractal structure for wideband RCS reduction," *IEEE Antennas and Wireless Propagation Letters*, vol. 17.2, pp. 201-204, 2018.

[15] D. Sang, Q. Chen, L. Ding, M. Guo, and Y. Fu, "Design of checkerboard AMC structure for wideband RCS reduction," *IEEE Transactions on Antennas and Propagation*, pp. 2604-2612, 2019.

[16] W. Chen, C. A. Balanis, and C. R. Birtcher, "Checkerboard EBG surfaces for wideband radar cross section reduction," *IEEE Trans. Antennas Propag*., vol. 63, pp. 2636-2645, 2015.

[17] A. Y. Modi, C. A. Balanis, C. R. Birtcher, and H. N. Shaman, "Novel design of ultrabroadband radar cross section reduction surfaces using artificial magnetic conductors," *IEEE Trans. Antennas Propag*., vol. 65, pp. 5406-5417, 2017.

[18] W. Q. Chen, C. A. Balanis, C. R. Birtcher, and A. Y. Modi, "Cylindrically curved checkerboard surfaces for radar cross section reduction," *IEEE Antennas Wireless Propag. Lett*., vol. 17, pp. 343-346, 2018.

[19] Y. Zhao, X. Y. Cao, J. Gao, X. Yao, and X. Liu, "A low-RCS and high-gain slot antenna using broadband metasurface," *IEEE Antennas Wireless Propag*., vol. 15, pp. 290-293, 2016.

[20] D. Singh, A. Kumar, S. Meena, and V. Agarwala, "Analysis of frequency selective surfaces for radar absorbing materials," *Progress in Electromagnetics Research B*, vol. 38, pp. 297-314, Feb. 2012.

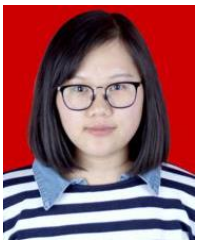

Xueyan Song was born in Henan Province, China, 1989. She received the B.E. degree in Electronic and Information Engineering from Xidian University, Xi'an, China, in 2012. She received the Ph.D. degree in Electromagnetic Fields and Microwave Technology from Xidian University, Xi'an, China, in 2018.

She joined the School of Electronic Engineering, Xi'an University of Posts and Telecommunications in 2018. Her research interests include artificial magnetic conductors, low RCS antennas, low-profile antennas, frequency selective surfaces, and reflector antennas.

Lei Chen was born in Shaanxi Province, China, 1982. She received the Ph.D. degrees in Electromagnetic Fields and Microwave Technology from Xidian University, Xi'an, China, in 2010.

She is an Associate Professor at Xidian University. Her research interests include retrodirective array, reflectarray and smart antenna.

Zehong Yan was born in Hubei Province, China, 1964. He received the B.E. degree in Antenna and Microwave from Xidian University, Xi'an, China, in 1984. He received the Ph.D. degree in Electromagnetic Fields and Microwave Technology from Northwestern Polytechnical University, Xi'an, China, in 1996.

He joined the School of Electronic Engineering, Xidian University in 1987 and was promoted to Associate Professor and Professor in 1996 and 2000, respectively, where he is currently a Doctoral Supervisor with the School of Electronic Engineering. His research interests include communication antennas, satellite tracking antennas, and microwave devices.

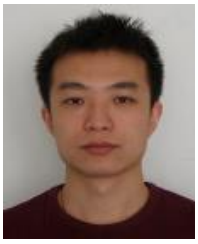

Yun-Qi Zhang was born in BaoTou, Inner Mongolia, China. He received the Ph.D. degree from Xidian University, Xi'an, China in 2015. He is currently working in the Xi'an University of Posts & Telecommunications. From 2017 he joined the school of Physics and Optoelectronic Engineering, Xidian University, as a Post Doctor. His research interests include GPS antenna, CP antenna, omnidirectional antenna and antenna array designs.

Haitao Song was born in Henan Province, China, 1986. He received the Ph.D. degree in Mathematics from Harbin Institute of Technology, Harbin, China, in 2014. He was a Postdoctoral Fellowship in York University, Toronto, Canada, from 2016 to 2018.

He is and Associate Professor at Shanxi University. His research interests include functional differential equations, dynamical system and theirs' applications.

A Compact Tri-band Miniaturized Antenna with Parasitic Elements Loading

Yan Deng, Xue-Fei Li, and Jing-Song Hong

Institute of Applied Physics
University of Electronic Science and Technology of China, 610054 Chengdu, China
dengyanabc@gmail.com, 13668740942@163.com, cemlab@uestc.edu.cn

Abstract ─ A compact tri-band miniaturized antenna with parasitic element loading is proposed for small form factor devices. Firstly, the dual-band antenna is proposed. Based on the theory of characteristic mode (TCM), the resonant of the metal loop decreases by adding three identical square monopole on the other side of the substrate. By exciting one of three square monopoles, the other two monopole treating as parasitic units, can lower the Q factor of the monopole and enhance the bandwidth of the antenna. Then, the tri-band antenna is proposed. By adding metal patches on the side of the parasitic elements, the higher order of the metal loop is excited and the new resonant point is created. With the adoption of the TCM, two degenerate modes are separated by adding metal strips on the metal loop to enhance the bandwidth of the low band. Also, the same way is carried out to decrease the electric size of the antenna and the size of the proposed structure meets the requirement of the electric small antenna. To verify the performance, the proposed antenna is fabricated and tested. The measured results are in agreement with simulated results.

Index Terms ─ Bandwidth enhancement, electrically small antenna (ESAs), miniaturized size, tri-band.

I. INTRODUCTION

In our daily life, many wireless devices have been successfully deployed in a wireless communication system such as laptops, Global Positioning System, Bluetooth. Recently, many researchers attach more attention to the electric small antenna for a huge demand for the small form factor devices applied in the smart city.

A widely recognized fact is that the electric small antenna possesses the characteristic of $k \cdot a < 1$. Many technologies have been developed to decrease the size of the antenna. Grounding on the analysis and calculation of CRLH LT theory [1], the antenna designed based on CRLH metamaterial possesses the characteristic of electric small size. Folded patch [2-4], defected ground plane [5-7], and virtually shorting pin [8,9] are three techniques to decrease the size of the antenna. By combining three approaches, the antenna in [8] achieves size reduction more than 80% compared to the conventional half-wave patch antenna. Moreover, the employed of a high permittivity substrate to miniaturize the size of antenna report in [10] and a size reduction more than 80% is achieved.

Also, the multi-band antenna is required to satisfy the requirement of the equipment in different applications. Till now, the variously printed antenna has manufactured for the multi-band application. In paper [11-13], the different shapes of metal were printed on the front and back sides of the substrate to produce diverse resonance. The diode serving as a configuration structure makes the antenna resonance in the upper and low band [14]. With high and low voltage, the resonant frequency of the antenna is varied to generate different resonant modes. In terms of Babinet theory, slot [15] is treated as the dipole. Therefore, the same way is carried out in the slot antenna to generate multi-band.

Although many methods have been adopted in multi-band miniaturized antenna, there still exist some problems. In [16-19], various complex printed shapes were employed to achieve multi-band characteristics. With those shapes utilized, it's difficult to design and optimize the antenna. In [20], the dual-band patch antenna achieves a 74% miniaturized ratio at 2.4 GHz, but the -6 dB impedance bandwidth of the antenna is 40 MHz at the 2.4 GHz and 1.5 GHz at 5.2 GHz.

In this paper, a compact tri-band miniaturized antenna is proposed to reduce the electric size and enhance the bandwidth of the antenna. With the TCM adopted, it's easy and accurate to design and optimize the antenna. With three square monopoles adding, the resonant point of the antenna in the low band decrease, and the bandwidth of the antenna in the high band increase. In addition, two metal patches add on the side of the parasitic elements to generate the high order mode of the metal loop. Finally, the performance of the antenna in each band can be efficiently controlled by adding strips on the metal loop. The proposed antenna possesses with simple structure meeting the requirement of the WLAN/WiMAX application.

Submitted On: April 2, 2020
Accepted On: May 16, 2020

II. ANTENNA DESIGN

A. Antenna geometry and evolution steps

Figure 1 is the drawing of the proposed antenna (26.4×26.4×1mm^3). The dielectric serving as the substrate of the antenna is FR-4. The height of substrate and copper are 1mm and 0.018mm respectively. Figure 2 depicts the four steps to designing the proposed compact tri-band miniaturized antenna. The curves presenting in Fig. 3 (b) are the reflection coefficient of the antenna with a different structure. The label of curves in Fig. 3 (b) corresponds to the label in Fig. 2. To explore the working principle of the proposed antenna, the characteristic mode analysis (CMA) use here to analyze the performance of the antenna with the adoption of CST MICROWAVE STUDIO.

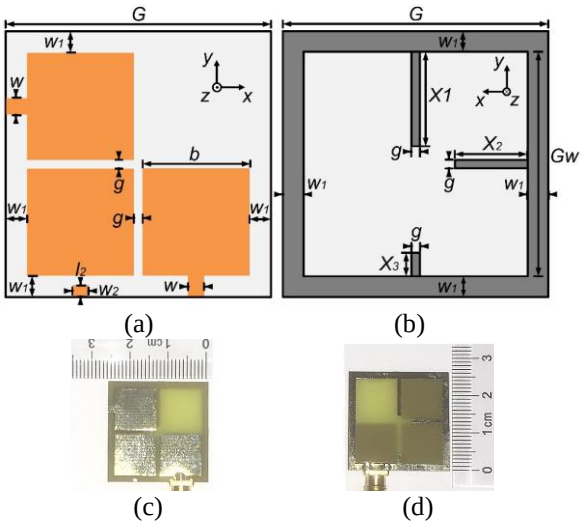

Fig. 1. Topology of the proposed antenna: (a) top view, (b) bottom view, (c) top view of the fabricated antenna, and (d) bottom view of the fabricated antenna.

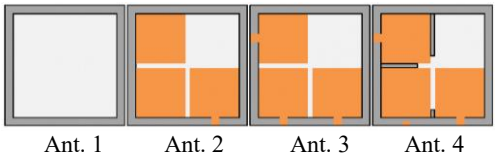

Fig. 2. Four steps to design the proposed antenna.

B. Theory of characteristic mode

Basing on the method of moment (MOM) which is the mathematical concept, a unified matrix approach treating for field problems is given in [21]. And, the theory and the computation of CMs for conducting bodies are given in [22] and [23]. Then, TCM applied in a dielectric and magnetic material is given in [24].

To summary, the TCM gives three important indices λ_n , α_n and Modal significance (MS) to judge the performance of the characteristic mode.

λ_n called eigenvalue represent the degree of resonant at *n*th modes. The value of λ_n is calculated by equation: $X(J_N) = \lambda_N R(J_N)$, where $X(J_N)$ and $R(J_N)$ are the imaginary and real parts of the impedance at the corresponding mode in matrix *Z*. The corresponded mode is likely to resonate when λ_n approaches zero.

α_n called the weighting coefficient obtain from the equation: $J = \sum \alpha_N J_N$, where *J* is current on conducting bodies when an electric field impress and J_N is a series of complete orthogonality eigenfunctions.

The resonant frequency and the resonant degree of characteristic mode can also be judged from the value of MS. The value of MS is calculated by the equation: $MS = |1/(1 + j\alpha_N)|$. The corresponded mode is likely to resonate when MS approaches one.

C. The mechanism of Ant. 1

The loop antenna widely applies to the wireless communication system. Here, we put a loop on the surface of the substrate.

The value of *Gl* is determined by:

$$Gl \approx \frac{c}{4\times f_0}, \tag{1}$$

where c is the speed at which light travels in a vacuum, f_0 is the frequency where the eigenvalues of the Ant.1 equal to zero. The value of *Gl* is related to the value of *G* and *Gw* giving by:

$$Gl = \frac{G+Gw}{2}. \tag{2}$$

Figure 3 (a) shows the eigenvalues of the proposed structure Ant. 1 with the adaptation of TCM. We can notice that the curves of the two eigenvalues coincide with each other and the value of eigenvalues equal to zero at 3.1 GHz. Therefore, the metal loop possesses two degenerate modes at 3.1 GHz.

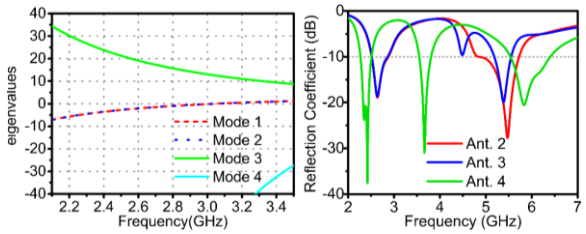

Fig. 3. The curve of the antenna: (a) eigenvalues of the metal loop, and (b) reflection coefficient of antennas.

D. The mechanism of Ant. 2

By adding three square metal patches in Ant. 1, the electrical size of the antenna decreases, and the bandwidth of the antenna in the upper band increases. The size of the square metal patch is determined by:

$$b \approx \frac{3 \times c}{8 \times f_1 \times \sqrt{\varepsilon_{rd}}}, \quad (3)$$

where f_1 is the resonant frequency of the Ant. 2 in the upper band.

As showing in Fig. 4 (a), with three monopoles loading, the point where eigenvalues equal to zero, varies from 3.1 GHz to 2.7 GHz in the low band. When three monopoles loading on the surface of the substrate, it can change the impedance characteristic of the metal loop leading to the resonant point decrease.

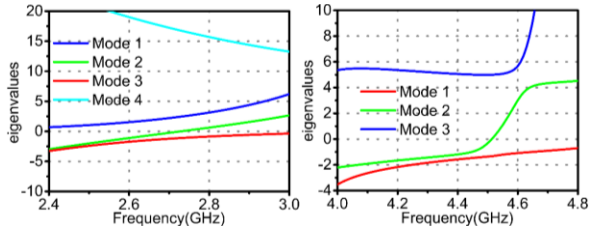

Fig. 4. Eigenvalues of the antenna: (a) Ant. 2 in the low band, and (b) Ant. 3 in the middle band.

Fig. 5. Simulated eigencurrent distribution of Ant. 2 at 2.7 GHz: (a) Mode 1, (b) Mode 2, and (c) Mode 3.

To enhance the impedance bandwidth in the upper band, the parasitic loading technique studying in paper [25] use here. By exciting one of three square metal patches, the other two metal patches treating as parasitic units, can lower the Q factor of the monopole and enhance the bandwidth of the antenna in the upper band.

The -10dB impedance bandwidth of Ant. 2 covering the frequency of 2.52 GHz-2.87 GHz (WiMAX band) and 4.84 GHz-5.72 GHz (WLAN band) is shown in Fig. 3 (Ant. 2). Moreover, the antenna possesses with omnidirectional radiation pattern in the low band. For the upper band, the antenna is provided with a 4.09 dBi peak gain at 5.5 GHz.

E. The mechanism of Ant. 3

In the process of CMA [26], the shorting pin and capacitance are traditional ways to modulate the performance of the antenna. Here, we add the patches on the side of the parasitic metal patches to vary the performance of the Ant. 2. In comparison with the curve of Ant. 2 in Fig. 3 (b), the curve of Ant. 3 changes greatly in the middle and up band, while the curve of Ant. 3 remains the same in the low band.

For the low band, the current distribution of the characteristic mode presents in Fig. 5. Few currents distribute on the right side of the PEC where two metal patches are added. Therefore, the metal patches have less influence on the current distribution of Mode 2, and the performance of the antenna remains unchanged.

For the upper band, the antenna work in monopole mode. The metal patches adding to the side of the monopole influence the impedance of two parasitic radiators. Therefore, the impedance matching of the antenna becomes worse and the impedance bandwidth of the antenna becomes narrow in the upper band.

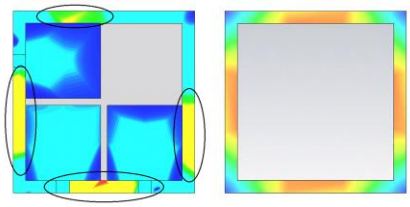

Fig. 6. Simulated eigencurrent distribution: (a) Mode 2 of Ant. 3 at 4.5 GHz, and (b) Mode 4 of Ant. 1.

In the middle band, the CMA uses here to figure out the new mode. Judging from the eigenvalues in Fig. 4 (b), we can conclude that Mode 2 contributes to the antenna resonant in the middle band. Furthermore, the eigencurrent of the metal loop's high-order is given to prove that Mode 2 is the high-order mode of the metal loop. As we can see from Figs. 6 (a) and (b), the primary current distribution of two modes is similar by contrasting the maximum current in each arm. However, the current distribution is unbalanced in each arm of the Mode 2 showing in Fig. 6 (a). And, the monopole and metal patches loading are the main reasons leading to the unbalanced distribution of the current.

F. The mechanism of Ant. 4

The curve of the reflection coefficient in Fig. 3 (b) illustrates that the Ant. 3 is a tri-band antenna and possesses narrow bandwidth in the upper band. Therefore, we can take some measures to improve the impedance bandwidth in the upper band. The strips adding on the metal loop is shown in Fig. 2 (Ant. 4) for changing the impedance of monopole. With the adaptation of CAM, we figure out the function of strips adding in the different places separately.

In the low band, Mode 2 and Mode 3 contribute to the resonance of the antenna according to the eigenvalues in Fig. 4. As we can see from Fig. 5, the strip X_1 and X_3 add to the maximum current distribution of Mode 2 and the minimum current distribution of Mode 3 while the strip X_2 adds to the minimum current

distribution of Mode 2 and the maximum current distribution of Mode 3. With the strip adding to the minimum of current distribution, the impedance of the metal loop changes leading to the mode resonant point shifts to low frequency.

Therefore, the performance of Mode 2 has a relation to the strip X_2. Also, the performance of Mode 3 has a relation to the strip X_1 and X_3. To verify this point of the view, the strips X_1, X_2 and X_3 add separately in Ant. 3. And the reflection coefficient and modal significance of Ant. 3 with strips X_1, X_2 and X_3 adding separately shows in Fig. 7.

The strip X_1 with the length of 10mm adds in Ant. 3. In Fig. 7 (b), the frequency of Mode 3 shifts to low band equal to 2.34 GHz which corresponded to the resonant point showing in the red line of Fig. 7 (a). Moreover, the frequency of Mode 2 shifts lightly.

Add a strip X_2 with a length of 8mm to Ant. 3. In Fig. 7 (c), the frequency of Mode 2 shifts to low band equal to 2.42 GHz which corresponded to the resonant point showing in the blue line of Fig. 7 (a). Furthermore, the frequency of Mode 3 shifts lightly.

Owing to the length of the X_3 is short so that the resonant point of Mode 2 and Mode 3 shift lightly.

And the middle band of the antenna is the high order mode of the metal loop. Therefore, the resonant frequency shifts as the low band.

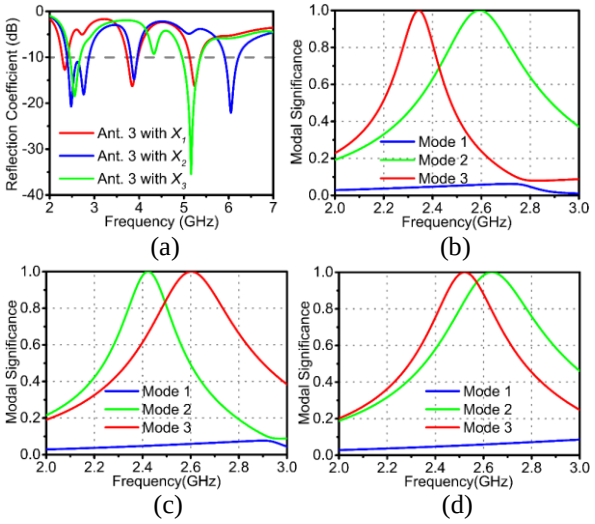

Fig. 7. The simulated results of Ant. 3 with strip loading separately: (a) reflection coefficient, (b) modal significance with X_1 loading, (c) modal significance with X_2 loading, and (d) Modal significance with X_3 loading.

G. Parametric study

Parametric studies are carried to improve the performance of Ant. 3 with the strips X_1, X_2 and X_3 loading.

In Fig. 8, two degenerate modes in the low band coincide with the increasing of X_2 and separate with the increasing of X_1 and X_3. Therefore, the changes in Fig. 8 are consistent with the changes in Fig. 7.

As we can see from Fig. 8 (a), two resonant points shift to the low frequency and become closer with increasing the length of X_1 in the upper band. Furthermore, with increasing of X_2, the first resonant point in the upper band still unchanged and the second resonant point in the upper band shifts to the low band showing in Fig. 8 (b). According to Fig. 8 (c), the performance of the antenna in the upper band is better with the shorter length of X_3.

In Fig. 8 (d), the performance of the Ant. 4 in the upper band is getting better with the value of the w_2 and l_2 changing.

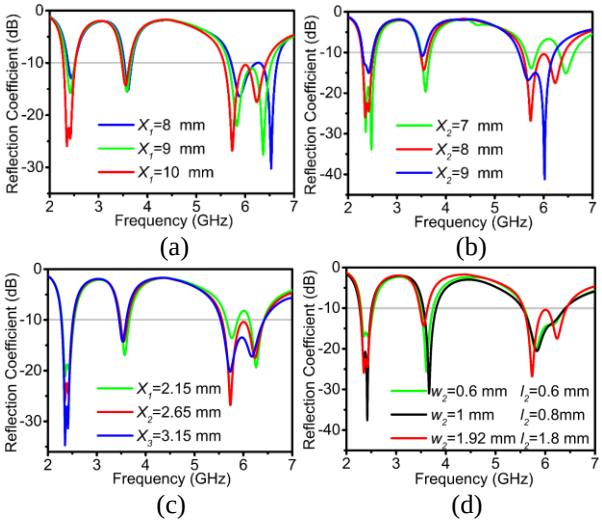

Fig. 8. Reflection coefficient of Ant. 4 with different parameters' value: (a) X_1; (b) X_2; (c) X_3; (d) w_2 and l_2.

Table 1: The optimized parameters of the Ant. 4

Parameter	Value (mm)	Parameter	Value (mm)
G	26.4	b	10.9
Gw	22.8	h	1
g	1	l_2	0.8
w	1.92	X_1	10
w_1	1.8	X_2	8
w_2	1	X_3	2.65

III. MEASURED RESULTS

The optimized parameters are given in Table 1. And, to confirm the validity of the design, the proposed Ant. 4 is fabricated and measured as shown in Fig. 9.

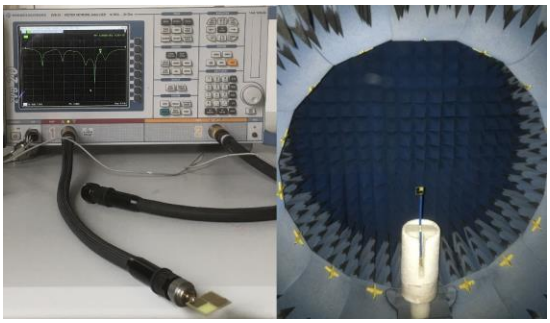

Fig. 9. Measured environment.

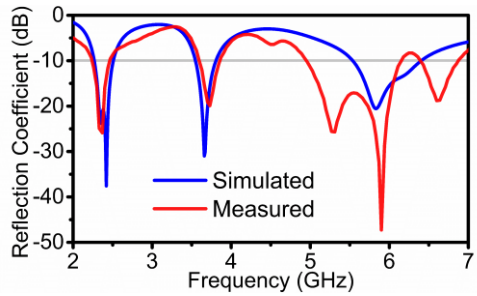

Fig. 10. The measured and simulated S_{11}.

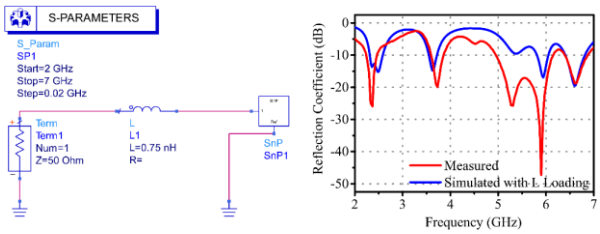

(a) (b)

Fig. 11. The influence of the inductor on the reflection coefficient of the antenna: (a) Simulated model considering the SMA, and (b) The results of the measured and simulated reflection coefficient.

A. S-parameters

The measured and simulated value of the reflection coefficient is presented in Fig. 10. The solid red line shows the result of the measured reflection coefficient, while the solid blue line exhibits the consequence of the simulated reflection coefficient. The measured bandwidth where S_{11}<-10dB covers 2.24-2.48 GHz, 3.60-3.85 GHz, 4.94-6.15 GHz, and 6.40-6.86 GHz. The relative bandwidth of the proposed antenna is 10.2%, 6.7%, 21.8%, and 6.9%.

The difference between simulated and measured results is primarily due to the adding of feeding SMA in measurement. The soldering and the adding of the SMA introduce extra inductors leading to the reflection coefficient of antenna change greatly in the upper band. To verify it, the simulated model and result exhibits in Fig. 11. As we can see from Fig. 11 (b), the simulated result corresponds to the measured result.

B. Radiation performance

The antenna measurement system SATIMO [27] is employed to calculate the performance of the antenna. With this equipment, the 2-D electric field data, the realized peak gain and the total efficiency are calculated. In Fig. 12, the radiation pattern at frequencies of 2.37, 3.73, 5.31, 5.90 GHz are selected to represent the radiation performances of the antenna. In Fig. 12, we can come up with that the antenna can achieve omnidirectional radiation in the low and middle band. For the upper band, the antenna cannot achieve the omnidirectional radiation but still acceptable. And this phenomenon caused by the strips adding on the metal loop to enhance the impedance bandwidth.

The total efficiency and peak gain are exhibited in Fig. 13. For the low band, the measured value of peak gain is lower than the simulated gain of 0.8 dBi owing to lower efficiency.

According to [28], the total efficiency of the antenna is determined by the reflection efficiency at the input terminals of the antenna, conduction efficiency and dielectric efficiency of the antenna.

And, SATIMO [27] measures the efficiency of the antenna according to this principle. This equipment measures radiation characteristics and the reflection coefficient of the antenna. Then, it calculates radiation efficiency by the definition in [28].

The antenna is electrically small in the lower band. Therefore, the small size of the ground plane leading to the currents flows back to the outer conductor surface of the cable. According to [29], this phenomenon will cause ripples in the radiation pattern. To improve the accuracy of the measured results, the feeding cable cover with an EM suppressant material [30] to absorb the currents flowing back to the outer conductor surface by SATIMO. The radiation energy absorbed by an EM suppressant material causes a decrease in the measured gain and efficiency.

To verify this point of view, the model of the feeding cable used in the Starlab System is built-in HFSS according to [30]. The simulated and measured efficiency of the antenna in the low band shows in Fig. 13. Owing to the feeding cable effects described above, the curve of the measured efficiency is corresponding to the simulated efficiency with the employ of the cable model in the low band. Therefore, we can conclude that the feeding cable used in the Starlab System absorbs the energy leading to the decreasing of the radiation efficiency in the low band. However, this part of the energy which absorbs by an EM suppressant material is radiated by antenna according to [29] and the gain of antenna approach to the simulated value in the application.

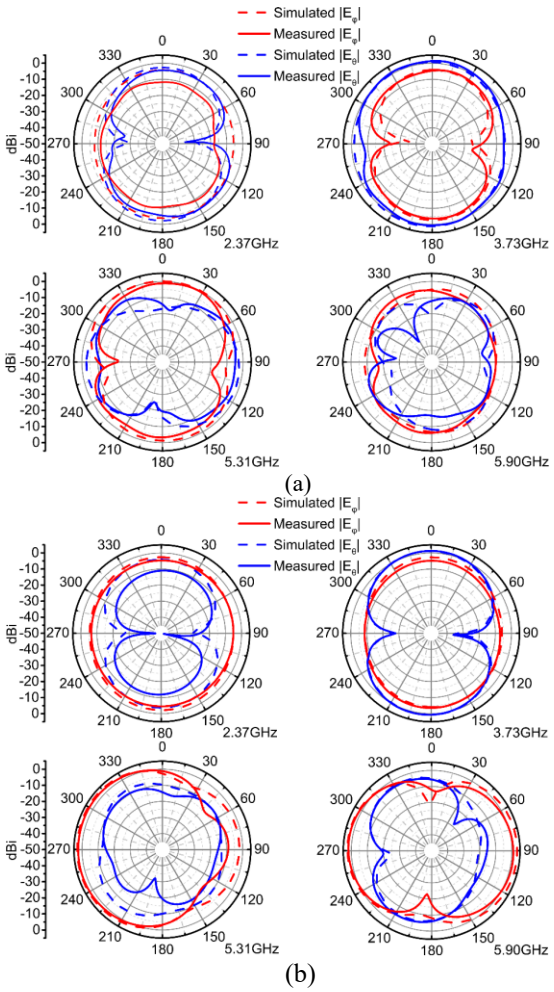

Fig. 12. The radiation pattern of the proposed antenna: (a) *xoz* plane and (b) *yoz* plane.

In Fig. 13, the curves of simulated and measured results are corresponding better. For the middle band, the measured value of peak gain lies between 2.4 and 2.9 dBi company with total efficiency vary from 69% to 75%. For the upper band, the measured value of peak gain ranges from 1.5 to 3.3 dBi with the total efficiency fluctuation between 53% and 62%.

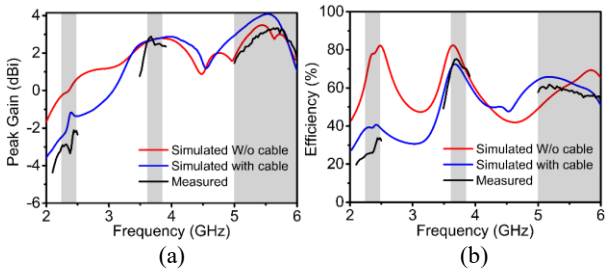

Fig. 13. The simulated and measured results of the antenna: (a) peak gain and (b) efficiency.

Table 2: Performance comparison

Reference	$k \cdot a$	First Band Bandwidth	Total Bandwidth
[9]	1.8	0.8%	3%
[16]	1.6	4.2%	12.4%
[17]	1.4	11.2%	20.4%
[31]	0.9	6%	20.7%
[32]	1.4	20.3%	32%
Proposed	0.9	10.2%	45.6%

The measurement characteristics of the proposed antenna are utilized to compare with previous works in Table 2. All of those multi-band antenna focus on the electrical small characteristic in the first band. The proposed antenna possesses the lowest value of $k \cdot a$ equal to 0.9 when we consider the first band frequency. Despite the impedance bandwidth restricted by antenna circumscribed sphere's radius, the proposed antenna achieves wider impedance bandwidth up to 10.2% in the low band with the smallest electrical size. Besides, the proposed antenna also exhibits a wider impedance bandwidth compared to the other five antennas when we consider the summation of each impedance bandwidth.

IV. CONCLUSION

A single fed novel structure with wide impedance bandwidth and miniaturized size is presented for small form factor wireless devices. The monopole serving as the radiator in the upper band is properly placed nearby the metal loop to decrease the electric size of the antenna. Moreover, the metal patches add to excite higher-order mode of metal loop leading to another resonance point achieved. To realize the better performance in each band, the metal strips are introduced to enhance bandwidth and decrease the electric size of the antenna. It is observed that by altering the performance of the monopole and metal loop, the antenna resonant in the WiMAX band and achieves better performance in the WLAN band. The prototype achieves the miniaturized structure with a size of $0.21 \times 0.21 \times 0.008$ λ3 and the 10.2% impedance bandwidth in the low band. For a middle and upper band of the antenna, the measured impedance bandwidth equal to 6.7% and 21.8% respectively.

REFERENCES

[1] A. Lai, C. Caloz, and T. Itoh, "Composite right/left-handed transmission line metamaterials," *IEEE Microw. Mag.*, vol. 5, no. 3, pp. 34-50, Sep. 2004.

[2] L. Zaid, G. Kossiavas, J. Y. Dauvignac, J. Cazajous, and A. Papiemik, "Dual-frequency and broad-band antennas with stacked quarter wavelength elements," *IEEE Trans. Antennas Propag.*, vol. 47, no. 4, pp. 654-660, Apr. 1999.

[3] C. Y. Chiu, K. M. Shum, C. H. Chan, and K. M.

Luk, "Bandwidth enhancement technique for quarter-wave patch antennas," *IEEE Antennas Wirel. Propag. Lett.*, vol. 2, pp. 130-132, 2003.

[4] S. H. Yeung, K. F. Man, K. M. Luk, and C. H. Chan, "A trapeizform U-slot folded patch feed antenna design optimized with jumping genes evolutionary algorithm," *IEEE Trans. Antennas Propag.*, vol. 56, no. 2, pp. 571-577, 2008.

[5] H. D. Chen, "Compact circularly polarised microstrip antenna with slotted ground plane," *Electron. Lett.*, vol. 38, no. 13, pp. 616-617, 2002.

[6] J. S. Kuo and G. B. Hsieh, "Gain enhancement of a circularly polarized equilateral-triangular microstrip antenna with a slotted ground plane," *IEEE Trans. Antennas Propag.*, vol. 51, no. 7, pp. 1652-1656, July 2003.

[7] D. Wang, H. Wong, and C. H. Chan, "Small circularly polarized patch antenna," *in 2011 International Workshop on Antenna Technology (iWAT)*, Hong Kong, China, pp. 271-273, 2011.

[8] H. Wong, K. K. So, K. B. Ng, K. M. Luk, C. H. Chan, and Q. Xue, "Virtually shorted patch antenna for circular polarization," *IEEE Antennas Wirel. Propag. Lett.*, vol. 9, pp. 1213-1216, 2010.

[9] A. Boukarkar, X. Q. Lin, Y. Jiang, and Y. Q. Yu, "Miniaturized single-feed multiband patch antennas," *IEEE Trans. Antennas Propag.*, vol. 65, no. 2, pp. 850-854, Feb. 2017.

[10] H. M. Chen, Y. K. Wang, Y. F. Lin, C. Y. Lin, and S. C. Pan, "Microstrip-fed circularly polarized square-ring patch antenna for GPS applications," *IEEE Trans. Antennas Propag.*, vol. 57, no. 4, pp. 1264-1267, Apr. 2009.

[11] B. Li, J. S. Hong, and B. Z. Wang, "A novel circular disc monopole antenna for dual-band WLAN applications," *Appl. Comput. Electromagn Soc. J.*, vol. 27, no. 5, pp. 441-448, May 2012.

[12] S. A. Rezaeieh and A. M. Abbosh, "Compact planar loop–dipole composite antenna with director for bandwidth enhancement and back radiation suppression," *IEEE Trans. Antennas Propag.*, vol. 64, no. 8, pp. 3723-3728, Aug. 2016.

[13] D. L. Jin, T. T. Bu, J. S. Hong, J. F. Wang, and H. Xiong, "A tri-band antenna for wireless applications using slot-type SRR," *Appl. Comput. Electromagn Soc. J.*, vol. 29, no. 1, pp. 47-53, Jan. 2014.

[14] G. M. Zhang, J. S. Hong, B. Z. Wang, and G. B. Song, "A novel frequency reconfigurable monopole antenna using PIN diode for WLAN/WIMAX applications," *Appl. Comput. Electromagn Soc. J.*, vol. 27, no. 3, pp. 256-260, Mar. 2012.

[15] C. T. Lee, S. W. Su, S. C. Chen, and C. S. Fu, "Low-cost, direct-fed slot antenna built in metal cover of notebook computer for 2.4-/5.2-/5.8-GHz WLAN operation," *IEEE Trans. Antennas Propag.*, vol. 65, no. 5, pp. 2677-2682, May 2017.

[16] M. P. Jayakrishnan, K. Vasudevan, M. Ameen, P. Mohanan, and S. Mathew, "Compact dual polarised V slit, stub and slot embedded circular patch antenna for UMTS/WiMAX/WLAN applications," *Electron. Lett.*, vol. 52, no. 17, pp. 1425-1426, Aug. 2016.

[17] S. Mathew, R. Anitha, U. Deepak, C. K. Aanandan, P. Mohanan, and K. Vasudevan, "A compact tri-band dual-polarized corner-truncated sectoral patch antenna," *IEEE Trans. Antennas Propag*., vol. 63, no. 12, pp. 5842-5845, Dec. 2015.

[18] M. C. Tang and R. W. Ziolkowski, "A study of low-profile, broadside radiation, efficient, electrically small antennas based on complementary split ring resonators," *IEEE Trans. Antennas Propag.*, vol. 61, no. 9, pp. 4419-4430, Sep. 2013.

[19] S. Verma and P. Kumar, "Printed Newton's egg curved monopole antenna for ultrawideband applications," *IET Microw. Antennas Propag.*, vol. 8, no. 4, pp. 278-286, Mar. 2014.

[20] A. A. Salih and M. S. Sharawi, "A dual-band highly miniaturized patch antenna," *IEEE Antennas Wirel. Propag. Lett.*, vol. 15, pp. 1783-1786, 2016.

[21] R. F. Harrington, "Matrix methods for field problems," *Proc. IEEE*, vol. 55, no. 2, pp. 136-149, 1967.

[22] R. Harrington and J. Mautz, "Theory of characteristic modes for conducting bodies," *IEEE Trans. Antennas Propag.*, vol. 19, no. 5, pp. 622-628, Sep. 1971.

[23] R. Harrington and J. Mautz, "Computation of characteristic modes for conducting bodies," *IEEE Trans. Antennas Propag.*, vol. 19, no. 5, pp. 629-639, Sep. 1971.

[24] R. Harrington, J. Mautz, and Y. Chang, "Characteristic modes for dielectric and magnetic bodies," *IEEE Trans. Antennas Propag.*, vol. 20, no. 2, pp. 194-198, Mar. 1972.

[25] C. Wood, "Improved bandwidth of microstrip antennas using parasitic elements," *IEE Proc. H Microw. Opt. Antennas UK*, vol. 127, no. 4, pp. 231-234, 1980.

[26] C. Deng, Z. Feng, and S. V. Hum, "MIMO mobile handset antenna merging characteristic modes for increased bandwidth," *IEEE Trans. Antennas Propagat.*, vol. 64, no. 7, pp. 2660-2667, July 2016.

[27] [Online]. Available: https://www.mvg-world.com/

[28] C. A. Balanis, *Antenna Theory–Analysis and Design*. 3rd ed. Hoboken, NJ, USA: John Wiley & Sons, 2005.

[29] L. Liu, S. W. Cheung, Y. F. Weng, and T. I. Yuk, "Cable effects on measuring small planar UWB monopole antennas," *in Ultra Wideband - Current Status and Future Trends*, M. Matin, Ed. InTech, pp. 274-294, 2012.

[30] L. Liu, Y. F. Weng, S. W. Cheung, T. I. Yuk, and L. J. Foged, "Modeling of cable for measurements of small monopole antennas," *in 2011 Loughborough Antennas & Propagation Conference*, Loughborough, United Kingdom, pp. 1-4, 2011.

[31] P. S. Bakariya, S. Dwari, M. Sarkar, and M. K. Mandal, "Proximity-coupled microstrip antenna for bluetooth, WiMAX, and WLAN applications," *IEEE Antennas Wirel. Propag. Lett.*, vol. 14, pp. 755-758, 2015.

[32] M. P. Jayakrishnan, K. Vasudevan, M. Ameen, P. Mohanan, and S. Mathew, "Compact dual polarised V slit, stub and slot embedded circular patch antenna for UMTS/WiMAX/WLAN applications," *Electron. Lett.*, vol. 52, no. 17, pp. 1425-1426, Aug. 2016.

Design of a Printed Metamaterial-Inspired Electrically Small Huygens Source Antenna for Cognitive Radio Applications

Imen Ben Trad [1], Hatem Rmili [1], Muntasir Sheikh [1], Bandar Hakim [1], and Jean-Marie Floch [2]

[1] King Abdulaziz University, Electrical and Computer Engineering Department
P.O. Box 80204, Jeddah 21589, Saudi Arabia
imen.bentrad@gmail.com, hmrmili@kau.edu.sa, mshaikh@kau.edu.sa, bmhakim@kau.edu.sa

[2] IETR, INSA, 20 Avenue des Buttes de Coësmes, 35708 Rennes, France
jean-marie.floch@insa-rennes.fr

Abstract **–** Metamaterial-inspired electric- and magnetic-based near-field resonant parasitic (NFRP) elements are electrically coupled to a coaxial-fed printed monopole to realize an electrically small, ka = 0.49 ($\lambda_0/9.41 \times \lambda_0/14.11 \times \lambda_0/104.18$) Huygens source antenna that operates at the GSM1800 frequency. The electric NFRP element is a meander patch; the magnetic element is a Capacitively Loaded Loop (CLL). The individual electric- and magnetic-based antennas were studied numerically to ensure they had overlapping frequency behavior near the GSM frequency 1.8 GHz; high radiation efficiency; and very good matching to their 50 Ω sources. They were combined together and retuned to create a three metal – two dielectric layer Huygens source antenna. A 20 nH inductor was inserted between the driven monopole and the SMA connector in order to enhance the input impedance matching. A prototype of this antenna was fabricated and experimentally characterized. The measurements confirmed the Huygens source nature of the prototype antenna.

Index Terms **–** CLL-NFRP element, electric NFRP element, ESAs, Huygens source, metamaterial-inspired antenna.

I. INTRODUCTION

Electrically small antennas (ESAs) continue generate increasing interest from both academic and industrial communities. Tremendous amount of research has been conducted to enhance and exploit various ESA properties, including high efficiency, stable radiation properties, ease of fabrication and integration, low cost, compactness and low-profile. These performance characteristics are attractive features typically desired in modern wireless communication systems, RFID tags, biomedical monitoring sensors, and other internet of things devices [1-6].

One of proposed approach to meet several these desirable aspects is the design of electrically small, highly efficient, Huygens source antennas [7-11]. Huygens source antennas are attractive for wireless communication and other mobile platforms because a significant amount of power is radiated away from their source into a prescribed hemisphere. For instance, such an antenna in a mobile phone could be designed to radiate away from the head, significantly reducing the specific absorption rate (SAR), leading to fewer health concerns and less power consumption (hence, more battery life). Theoretically, a Huygens source is a particular combination of electric and magnetic dipole antennas. It has been demonstrated that a realizable single Huygens source can achieve a directivity near to its theoretical limit of 4.77 dB [7]. This antenna was constructed as a particular combination of electrically small electric- and magnetic-near-field resonant parasitic (NFRP) elements coupled to a driven dipole antenna. It radiated its maximum directivity in the plane containing the NFRP elements and away from its feed point. Another recent design radiates its maximum directivity in the direction broadside to the plane containing the NFRP and driven elements [12]. In both cases, a single input port was employed, thus avoiding difficulties associated with multiple feeds and matching multiple input impedances.

In this letter, an electrically small Huygens source antenna based on a combination of metamaterial-inspired electric- and magnetic-NFRP elements is reported that radiates its maximum directivity in the plane of those NFRP elements, but orthogonal to the feed direction. Antennas associated with the electrically small electric- and magnetic-NFRP elements and a coax-fed printed monopole antenna were designed and numerically studied individually to be efficient, to be well matched to a 50 Ω source, and to have an overlapping frequency behavior around the GSM1800 frequency. Then, by coupling them to the same driven monopole and adjusting their relative responses to be equal, a three metal – two dielectric layered Huygens source antenna

Submitted On: January 11, 2020
Accepted On: May 9, 2020

having high efficiency, high directivity, and large bandwidth was obtained. A prototype of this Huygens source antenna was fabricated and tested. The measured results were in good agreement with their simulated values.

All of the design simulations were performed with the ANSYS-ANSOFT High Frequency Structure Simulator, HFSS-V15. They all took into account the realistic material properties of the copper and dielectric components. The SMA connector was included in all of the simulations for higher accuracy between the simulated and the measured results.

II. ELECTRICALLY SMALL NRFP DIPOLE ANTENNAS

A printed monopole antenna of length L_M and width W_M is introduced to act as the driven element for both the magnetic and electric NFRP antennas. It is fed by a 50Ω SMA connector. Each antenna, i.e., the monopole and a NFRP element, was printed on a W×L Rogers Duroid™ 5880 substrate of thickness 0.7874 mm, relative permittivity $\varepsilon_r = 2.2$, relative permeability $\mu_r = 1.0$ and loss tangent $\tan\phi = 0.0009$. The copper thickness is 0.017 mm.

A. Magnetic NFRP antenna

The metamaterial-inspired capacitively loaded loop (CLL)- based NFRP antenna introduced previously [13-16] was used as the core design to achieve the requisite magnetic dipole antenna. The CLL NFRP element and the ground strip line were printed in the top side of the Duroid substrate. The driven monopole and the extra-strip line of dimensions L_S and W_S (to achieve the maximum directivity in the horizontal direction [13]) were printed on its back side as exhibited in Fig. 1. The optimized design parameters of this antenna are summarized in Table 1. This CLL based NFRP antenna is electrically small with ka=0.49 (where "k=2π/λ" is the free space wavenumber, and "a" is the radius of the smallest sphere circumscribing the maximum dimensions of the antenna).

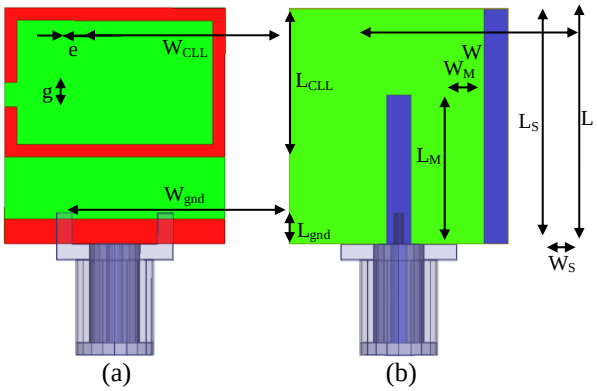

Fig. 1. The magnetic NFRP antenna geometry: (a) front side and (b) back views.

Table 1: Magnetic NFRP antenna parameters

Parameter	Value (mm)	Parameter	Value (mm)
W	18	**W_{CLL}**	18
L	19	**L_{CLL}**	12
W_M	2	**W_{gnd}**	18
L_M	12	**L_{gnd}**	2
W_S	2	**e**	1
L_S	19	**g**	2

The proposed structure dimensions were rescaled from those in [13, 14] so that the antenna would radiate at the GSM1800 frequency. As illustrated in Fig. 2, nearly complete input impedance matching $|S_{11}|_{min}$ = -21.35 dB was achieved at 1.815 GHz. The simulated total directivity pattern at this resonance frequency is shown in Fig. 3 and verifies that the antenna radiates as a magnetic dipole oriented, along the y-axis with its maximum directivity orthogonal to the feed structure. The simulated performance characteristics are: front-to-back ratio: FTBR=1.0 (0dB); accepted power: AP=0.992W; total radiated power: RP=0.754W, giving the radiation efficiency RE=76%; the maximum directivity: D_{max} = 2.22dB; and the peak realized gain RG_{max}=1dB. The 3dB bandwidth is 27 MHz.

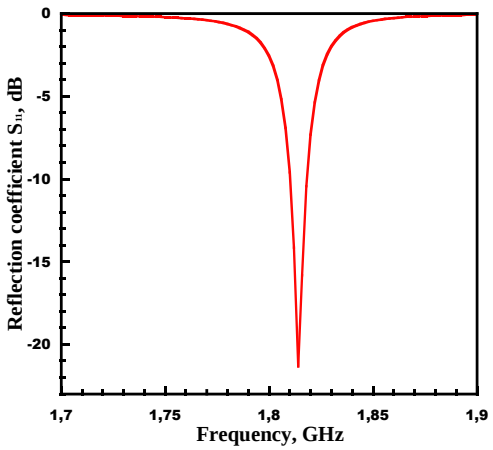

Fig. 2. Simulated $|S_{11}|$ values of the magnetic antenna versus the source frequency.

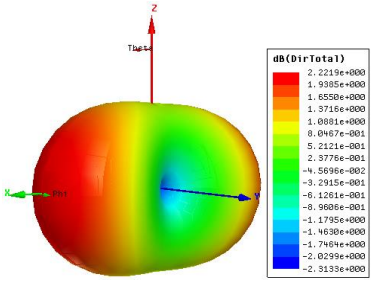

Fig. 3. Simulated 3D total directivity pattern at the resonance frequency of the magnetic NFRP antenna, 1.815 GHz.

B. Electric NFRP antenna

The other component of the Huygens source antenna is a metamaterial-inspired electric NFRP dipole antenna. With the driven printed monopole, it is an adaptation of the 2D electric EZ antenna [17]. The electric NFRP element is a meandered strip; it was printed on the same Rogers Duroid™ 5880 substrate and with the same overall dimensions as the magnetic dipole. The electric NFRP dipole antenna geometry and its optimized design parameters are shown in Fig. 4 and given in Table 2, respectively.

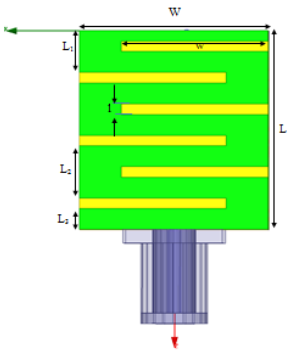

Fig. 4. Front side view of the electric NFRP antenna.

Table 2: Electric NFRP antenna parameters

Parameter	Value (mm)
L_1	4
L_2	5
L_3	2
l	1
w	14
L	19
W	18

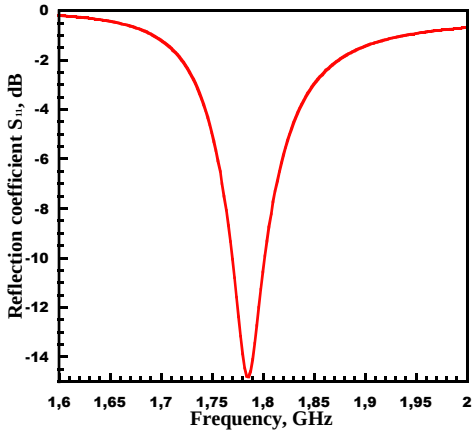

Fig. 5. Simulated $|S_{11}|$ values of the electric NFRP antenna versus the source frequency.

The electric dipole was designed to have a resonance behavior that overlaps with that of the CLL-based NFRP element. It radiates at 1.78GHz as presented in Fig. 5. The proposed NFRP element remains electrically small with ka = 0.49. Figure 6 show that the antenna behaves as an electric dipole oriented along the z-axis. The antenna performance characteristics are: FTBR = 1.0 (0dB), AP = 0.967W, RP = 0.862W (giving RE = 89.14%), D_{max} = 2.23dB, and RG_{max} = 1.58dB. The 3dB bandwidth is 120 MHz (FBW = 6.74%).

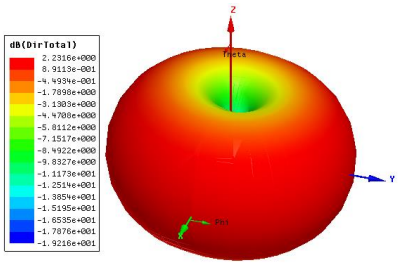

Fig. 6. Simulated 3D total directivity pattern at the resonance frequency of the electric antenna, 1.78 GHz.

III. HYUGENS SOURCE ANTENNA

The Huygens source antenna was obtained by combining the meandered NFRP and CLL based NFRP designs as shown in Fig. 7. Two Rogers Duroid™ 5880 substrates were used. The CLL NFRP element and the ground strip line were printed in the top side of the first substrate; the driven monopole and the extra-strip line were printed on its back side. The electric NFRP element was printed on the back side (outside face) of the second substrate. The two substrates were combined so that the electric and magnetic NFRP elements were on the external sides and the driven monopole was in the middle. The gap between the two substrates was G=0.9mm, it was filled with foam in order to easily maintain the structural integrity of the whole structure.

The structure dimensions were readjusted to construct the Huygens source while operating at the GSM frequency. However, the input impedance matching was poor. In order to fix this problem, a 20 nH inductor was introduced between the driven monopole and the source feed line. The driven monopole was offset upwards of 4mm from the bottom side as presented in Fig. 7 (c) to accommodate this lumped element. The resulting simulated minimum values of $|S_{11}|$ were significantly improved at the GSM frequency. Figure 8 exhibits the prototyped metamaterial-inspired Huygens source antenna. The simulated and measured values of $|S_{11}|$ as functions of the source frequency are compared in Fig. 9. The prototype antenna radiated at 1.77GHz with nearly complete input impedance matching $|S_{11}|_{min}$=-22.91dB. The difference between the measured and simulated values is attributed to small variations in the design parameters that resulted from fabrication errors and the measurement setup, which did not include any ferrite beads nor matching balun to isolate the

antenna from the VNA cables.

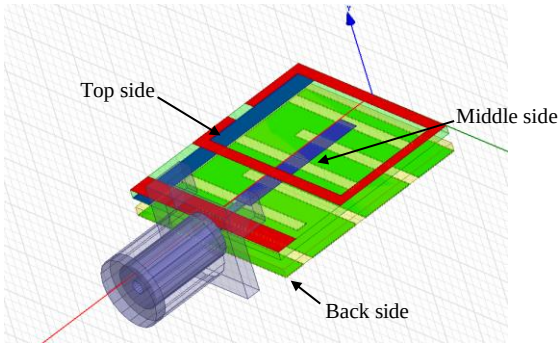

(a)

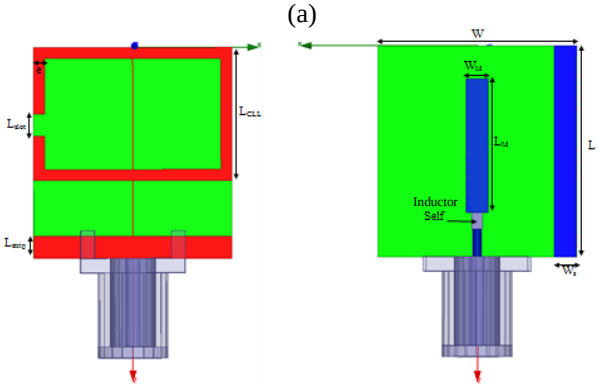

(i) (ii)

(b) Duroid sheet 1: (i) front side view (outside face), and (ii) back side view (middle face)

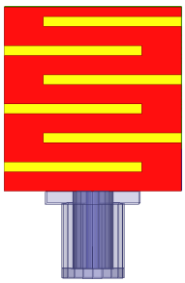

(c) Duroid sheet 2: back side (outside face)

Fig. 7. The Huygens source antenna geometry: (a) perspective view, (b) Duroid sheet 1, and (c) Duroid sheet 2.

Fig. 8. Photos of the fabricated prototype Huygens source antenna.

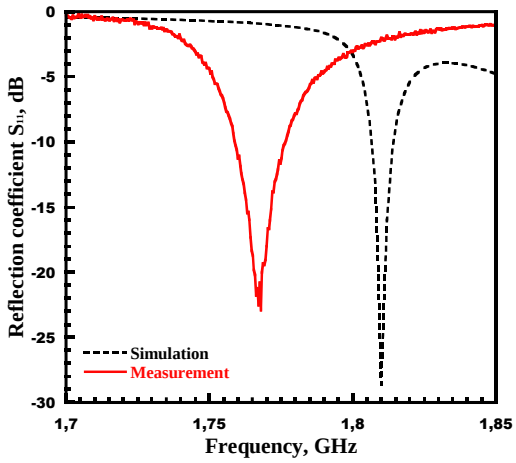

Fig. 9. Simulated and measured $|S_{11}|$ values of the Huygens source antenna versus the source frequency.

The simulated performance characteristics of the prototype Huygens source antenna were: AP = 0.99W; RP = 0.6W; giving RE = 60.19%; D_{max} = 4.38dB and RG_{max} = 2.17dB. The measured values were: RE = 31.05%; D_{max} = 3.39dB; and RG_{max}=1.67dB. The 3dB bandwidth is 60MHz.

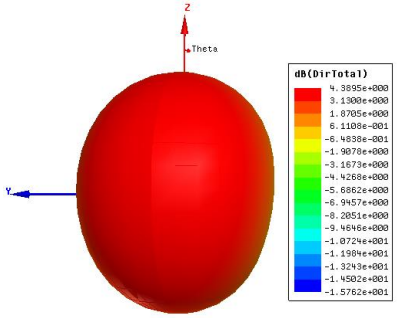

(a)

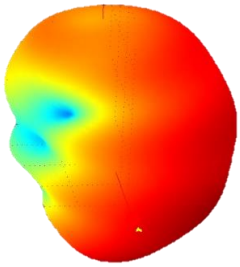

Maximum Value (dB)	Minimum Value (dB)
3.399	-95.18

(b)

Fig. 10. (a) Simulated and (b) measured 3D total directivity pattern.

One can note that the overall measured antenna performance characteristics were lower than predicted. The differences between the simulated and measured results are due to inaccuracies in the measurements and

in the manufacturing of the prototype antenna:

- The gap between the two substrates was filled using with a 1.0 mm thick foam rather than the simulated 0.9 mm value.
- The inductor model used in the simulations was ideal; losses were not taken into consideration.

Despite the fact that the realized antenna is not as efficient as predicted, the Huygens source behavior is well obtained along the x-axis as illustrated in Fig. 10.

IV. CONCLUSION

A metamaterial-inspired electrically small Huygens source antenna was numerically studied, manufactured and tested. It was fed with a single 50 Ω coaxial cable. The electric- and magnetic-based NFRP designs were designed first to have overlapping frequency behaviors at the GSM 1.8 GHz frequency. The two designs were then combined to achieve the desired electrically small Huygens source antenna. The input impedance matching was significantly improved by inserting a 20 nH inductor between the driven monopole and the SMA connector. The measured antenna efficiency, the maximum directivity and realized gain were much lower than predicted. This degradation of the antenna performance could be corrected to obtain the predicted values by taking into consideration the actual antenna design specifications.

ACKNOWLEDGMENT

The project was funded by the Deanship of Scientific Research (DSR), King Abdulaziz University, Jeddah, Saudi Arabia under grant no. KEP-Msc-3-135-39. The authors, therefore, acknowledge with thanks DSR technical and financial support.

Finally, the authors would like to acknowledge Prof. Richard Ziolkowski, from the University of Arizona, USA, for his helps and constructive discussions.

REFERENCES

[1] O. S. Kim, "Low-Q electrically small spherical magnetic dipole antennas," *IEEE Trans. Antennas Propag.*, vol. 58, no. 7, pp. 2210-2217, July 2010.

[2] J. J. Adams and J. T. Bernhard, "A modal approach to tuning and bandwidth enhancement of an electrically small antenna," *IEEE Trans. Antennas Propag.*, vol. 59, no. 4, pp. 1085-1092, Apr. 2011.

[3] N. Zhu and R. W. Ziolkowski, "Broad-bandwidth, electrically small antenna augmented with an internal non-Foster element," *IEEE Antennas Wireless Propag. Lett.*, vol. 11, pp. 1116-1120, 2012.

[4] M.-C. Tang and R. W. Ziolkowski, "Efficient, high directivity, large front-to-back-ratio, electrically small, near-field-resonant-parasitic antenna," *IEEE Access*, vol. 1, pp. 16-28, May 2013.

[5] J. Zhang and Y. Long, "A novel metal-mountable electrically small antenna for RFID tag applications with practical guidelines for the antenna design," *IEEE Trans. Antennas Propag.*, vol. 62, no. 11, pp. 5820-5829, Nov. 2014.

[6] H. Maema and T. Fukusako, "Radiation efficiency improvement for electrically small and low-profile antenna by stacked elements," *IEEE Antennas Wireless Propag. Lett.*, vol. 13, pp. 305-308, 2014.

[7] P. Jin and R. W. Ziolkowski, "Metamaterial-inspired, electrically small Huygens sources," *IEEE Antennas Wireless Propag. Lett.*, vol. 9, pp. 501-505, 2010.

[8] S. R. Best, "Progress in the design and realization of an electrically small Huygens source," *Proc. International Workshop on Antenna Technologies* (iWAT 2010), Lisbon, Portugal, Mar. 2010.

[9] P. Alitalo A. O. Karilainen T. Niemi C. R. Simovski S. A. Tretyakov, "Design and realisation of an electrically small Huygens source for circular polarisation," *IET Microwaves Antennas Propag.*, vol. 5, iss. 7, pp. 783-789, May 2011.

[10] T. Niemi, P. Alitalo, A. O. Karilainen, and S. A. Tretyakov, "Electrically small Huygens source antenna for linear polarisation," *IET Microwaves Antennas Propag.*, vol. 6, iss. 7, pp. 735-739, May 2012.

[11] C. Pfeiffer and A. Grbic, "Realizing Huygens sources through spherical sheet impedances," *Proc. 2012 IEEE AP-S International Symposium and USNC/URSI National Radio Science Meeting*, Chicago, IL, July 2012.

[12] R. W. Ziolkowski, "Low profile, broadside radiating, electrically small Huygens source antennas," *IEEE Access*, vol 3, pp. 2644-2651, Dec. 2015.

[13] O. Turkmen, G. Turhan-Sayan, and R. W. Ziolkowski, "Metamaterial inspired, electrically small, GSM antenna with steerable radiation patterns and high radiation efficiency," 2013. *Proc. 2013 IEEE AP-S International Symposium and USNC/URSI National Radio Science Meeting*, Orlando FL, July 2011.

[14] O. Turkmen, G. Turhan-Sayan, and R. W. Ziolkowski, "Single, dual and triple-band metamaterial-inspired electrically small planar magnetic dipole antennas," *Microw. Opt. Techn. Lett.*, vol. 56, no. 1, pp. 83-87, Jan. 2014.

[15] D. Chaturvedi and S. Raghavan, "A compact metamaterial-inspired antenna for WBAN application," *Wireless Pers. Commun.*, vol. 105, pp. 1449-1460, 2019. doi:10.1007/s11277-019-06153-z.

[16] A. Ashyap, Z. Zainal Abidin, S. Dahlan, H. Majid, and G. Saleh, "Metamaterial inspired fabric antenna for wearable applications," *International*

Journal of RF and Microwave Computer-Aided Engineering, vol. 29, no. 3, 2019.

[17] A. Erentok and R. W. Ziolkowski, "Metamaterial-inspired efficient electrically-small antennas," *IEEE Trans. Antennas Propag.*, vol. 56, no. 3, pp. 691-707, Mar. 2008.

Imen Ben Trad received a degree in Electronics, Computer and Information Science from the University Tunis El Manar, Tunisia in 2008 and the Master thesis in System of Communications from the Faculty of Science of Tunis, Tunisia in 2011. She received the Ph.D. in Engineering Sciences from the University of Tunis El Manar and, INSA Rennes, France 2017. From April 2017 to August 2019, she was a Post-Doctoral Researcher with IETR at INSA Rennes, in collaboration with King Abdulaziz University, Saudi Arabia. Her research mainly focuses on the development of design of antennas for wireless applications.

Hatem Rmili received the B.S. degree in General Physics from the Science Faculty of Monastir, Tunisia in 1995, and the DEA diploma from the Science Faculty of Tunis, Tunisia, in Quantum Mechanics, in 1999. He received the Ph.D. degree in Physics (Electronics) from both the University of Tunis, Tunisia, and the University of Bordeaux 1, France, in 2004. From December 2004 to March, 2005, he was a Research Assistant in the PIOM Laboratory at the University of Bordeaux 1. During March 2005 to March 2007, he was a Postdoctoral Fellow at the Rennes Institute of Electronics and Telecommunications, France. From March to September 2007, he was a Postdoctoral Fellow at the ESEO Engineering School, Angers, France. From September 2007 to August 2012, he was an associate professor with the Mahdia Institute of Applied Science and Technology (ISSAT), department of Electronics and Telecommunications, Tunisia. Actually, he is Full Professor with the Electrical and Computer Engineering Department, Faculty of Engineering, King Abdulaziz University, Jeddah, Saudi Arabia.

Rmili's research interests concern applied electromagnetic applications involving antennas, metamaterials and métasurfaces. The main targeted applications are reconfigurable antennas for multi-standard wireless communications systems, security of chipless RFID systems with fractal tags, terahertz photoconductive antennas for infra-red energy harvesting, UWB nano rectennas for collection of solar energy, phase shifters for low-cost 5G communication systems, and microwave absorbing materials for stealth technologies.

Muntasir Sheikh received his B.Sc. from King Abdulaziz University, Saudi Arabia, in Electronics and Communications Engineering, M.Sc. in RF Communications Engineering from the University of Bradford, U.K., and Ph.D. from the University of Arizona, U.S.A. Since then he has been teaching in the Electrical and Computer Engineering Dept. in KAU. His research interests are Antenna Theory and Design, Radar applications, and electromagnetic metamaterials.

Bandar Hakim Bandar Hakim is an Assistant Professor of Electrophysics at KAU. He received his Ph.D. degree in Electrophysics from the University of Maryland. He worked with the Medical Robotics Group at the École Polytechnique Fédérale de Lausanne in Switzerland, the Center for Devices and Radiological Health at the Food and Drug Administration in Washington DC and the Neurology department at Mount Sinai School of Medicine in the New York NY. He served as an industrial consultant in the US, Switzerland and Germany.

Jean Marie Floch received his Ph.D. in Electronics in 1992 from the INSA Rennes, France. He joined the IETR Institute as Research Engineer where he supervised Master and Ph.D. Students, in addition to the execution of many research projects with collaboration of the industry. His research interests concern the design of different type of antennas for wireless applications.